Title
Shaping Galaxy Evolution with Galaxy Structure

Author
Cheung, Edmond

Publication Date
2014

UNIVERSITY OF CALIFORNIA
SANTA CRUZ

SHAPING GALAXY EVOLUTION WITH GALAXY STRUCTURE

A dissertation submitted in partial satisfaction of the
requirements for the degree of

Doctor of Philosophy

in

ASTRONOMY & ASTROPHYSICS

by

Edmond Cheung

June 2014

The Dissertation of Edmond Cheung
is approved:

Professor Sandra M. Faber, Chair

Professor David C. Koo

Professor Charlie Conroy

Dean Tyrus Miller
Vice Provost and Dean of Graduate Studies

Table of Contents

List of Figures

List of Tables

Abstract

Shaping Galaxy Evolution with Galaxy Structure

by

Edmond Cheung

A fundamental pursuit of astronomy is to understand galaxy evolution. The enormous scales and complex physics involved in this endeavor guarantees a never-ending journey that has enamored both astronomers and laymen alike. But despite the difficulty of this task, astronomers have still attempted to further this goal. Among of these astronomers is Edwin Hubble. His work, which includes the famous Hubble sequence, has immeasurably influenced our understanding of galaxy evolution.

In this thesis, we present three works that continues Hubble's line of study by using galaxy structure to learn about galaxy evolution. First, we examine the dependence of galaxy quiescence on inner galactic structure with the AEGIS/ DEEP2 survey at $0.5 < z < 0.8$. We developed a method to compare the efficacy of several parameters at distinguishing star-forming galaxies from quiescent galaxies. Our method indicates that the inner stellar mass is the most correlated parameter of quenching, implying that the process that quenches galaxies must also buildup their inner structure. Second, we explore the relationship between galactic bars and their host galaxies with Galaxy Zoo 2 at $z \sim 0$. The correlations of bar properties and galaxy properties are consistent with simulations of bar formation and evolution, indicating that bars affect their host galaxies. Finally, we investigate whether bars can drive supermassive black hole growth with data from Chandra and Galaxy Zoo: Hubble at $0.2 < z < 1.0$. Comparing a sample of active galaxies to a matched sample of inactive, control galaxies shows that there is no statistically significant excess of bars in active hosts. Our result shows that bars are not the primary fueling mechanism of supermassive black hole growth.

To mother, sister, father,

and friends,

for their continual support.

Acknowledgments

To my advisors Sandy Faber and David Koo, I wouldn't be completing my doctorate if it were not for both of your unflinching candidness, unending advice, and continued support. Thank you both from the bottom of my heart.

To all the graduate students and postdocs that I have had the pleasure to meet during my time at UC Santa Cruz, thank you for the support and encouragement. Without your help, I wouldn't know how to use IDL, extract data, or present my science in a somewhat coherent manner.

To my collaborators, thank you for helping me develop into the scientist that I am today. Without the countless comments and suggestions, my papers wouldn't be half as good (nor half as long).

To my teachers, especially Mr. Kearney, thank you for believing that a little boy from Atlantic City could do whatever he wanted to do. In a city where a casino job was the expectation, my teachers helped me strive for more, and I thank them with all of my heart.

To my friends from Atlantic City, especially Ratha, thank you for keeping me down-to-earth. Without your influence, I would have turned out to be an insufferable idiot.

To my girlfriend, Alex, thank you for supporting me throughout my entire career at UC Santa Cruz. I love you.

To my mom, although she can't read this, thank you for always putting me and my sister first; thank you for working tirelessly through double shifts, graveyard shifts, and countless job changes; thank you for your love and support; thank you for everything. Although you always wanted me to be a doctor, I'm glad you never forced me. Funny how things work out though—at the end I did become a doctor. I love you mom.

To my sister, Maggie, thank you for always supporting me. You are always there when I need a kick in the right direction. Thank you for giving me two beautiful nieces. And thank you for being my sister.

The text of this dissertation includes reprints of the following previously published material: (i) Cheung, Edmond; Faber, S. M.; Koo, David C.; Dutton, Aaron A.; Simard, Luc; McGrath, Elizabeth J.; Huang, J.-S.; Bell, Eric F.; Dekel, Avishai; Fang, Jerome J.; Salim, Samir; Barro, G.; Bundy, K.; Coil, A. L.; Cooper, Michael C.; Conselice, C. J.; Davis, M.; DomŠnguez, A.; Kassin, Susan A.; Kocevski, Dale D.; Koekemoer, Anton M.; Lin, Lihwai; Lotz, Jennifer M.; Newman, J. A.; Phillips, Andrew C.; Rosario, D. J.; Weiner, Benjamin J.; Willmer, C. N. A. 2012, The Astrophysical Journal, 760, 131 (Chapter 2), and (ii) Cheung, Edmond; Athanassoula, E.; Masters, Karen L.; Nichol, Robert C.; Bosma, A.; Bell, Eric F.; Faber, S. M.; Koo, David C.; Lintott, Chris; Melvin, Thomas; Schawinski, Kevin; Skibba, Ramin A.; Willett, Kyle W. 2013, The Astrophysical Journal, 779, 162 (Chapter 3). Small changes in the text have been made to fit these chapters in the context of this document. The author was supported through the NSF Grant AST 08-08133.

Chapter 1

Introduction

In 1936, Edwin Hubble created the Hubble sequence (see Fig. 1.1), a morphological classification scheme for galaxies that is ingrained in the field of galaxy evolution. The origin of this scheme comes from his observations of galaxies outside our Milky Way galaxy, which in itself deserves special mention—Hubble was among the first to realize that some of the "nebulae" that he was observing were actually galaxies outside our own. From his extragalactic observations, he noticed that galaxies tend to resemble either a smooth ellipsoid or a disk with spiral arms. Using these two classes as the main categories—elliptical (early-type) galaxies and spiral/disk (late-type) galaxies—Hubble aimed to create a classification scheme that encompassed all galaxies.

In Hubble's scheme, elliptical galaxies were situated to the left and spiral galaxies to the right. In the elliptical galaxies section, he subdivided them by their ellipticity, placing the most elliptical galaxies to the right, and the least elliptical galaxies, i.e., the most circular galaxies, to the left. Within the spiral section, he subdivided them by the tightness of the spiral

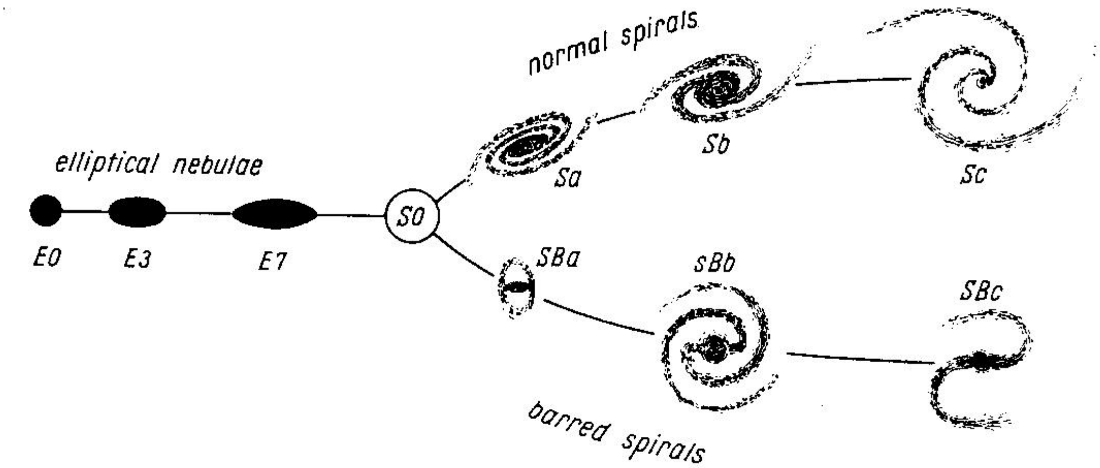

Figure 1.1: The original diagram of the Hubble sequence as published in Hubble (1936).

arms, with the loosest placed on the right, and the tightest placed on the left. Hubble further observed that among the spirals, many contained linear structures that stretched across their centers; he called them “barred galaxies.” Since barred galaxies appeared indistinguishable from non-barred spirals, sans the bar, he placed barred galaxies in a parallel branch to the non-barred spirals. At the middle of the Hubble sequence are the lenticulars—a type of galaxy that seemed to show an equal balance of an elliptical and a disk morphology. The original Hubble sequence diagram is reproduced in Fig. 1.1.

While Hubble tried to include all types of galaxies, there were some that just did not fall into the elliptical or spiral category. These types of galaxies, e.g., merging systems, would eventually be labelled “irregular" or “peculiar,” and were not represented in the original Hubble sequence. But as we discuss below, these types of galaxies play an important role in the evolution of galaxies.

Contrary to common perception, Hubble did not intend the Hubble sequence to represent an evolutionary sequence (Hubble, 1936; Baldry, 2008). But despite his intentions, the Hubble sequence has turned out to be a reasonable evolutionary model. Recent works show that the morphologies of massive galaxies at $z > 2$ are dominated by peculiars and irregulars, while at $z < 2$, the morphologies of massive galaxies are dominated by disks and ellipticals (Buitrago *et al.*, 2013; Mortlock *et al.*, 2013). This change in the morphological mix of galaxies with time implies that peculiar and irregular galaxies evolve into disk and elliptical galaxies, i.e., into the ordered morphologies represented by the Hubble sequence.

Within these ordered morphologies, evidence indicates that galaxies evolve statistically from spirals into ellipticals. Bell *et al.* (2004b) and Faber *et al.* (2007) show that the number density of red galaxies has doubled since $z = 1$, while the number density of blue galaxies has remained constant. Since red galaxies tend to be ellipticals and blue galaxies tend to be spirals (Holmberg, 1958), these results indicate that blue spirals evolve statistically into red ellipticals. In other words, galaxies evolve from right to left in the Hubble sequence.

The Hubble sequence is the prime example of how studies on galaxy structure, albeit unintentional, impacted our theory of galaxy evolution. Below, I briefly discuss a couple of other significant works that have used galaxy structure to reveal new aspects of galaxy evolution.

In the early 1900s, several works found that the fraction of early-type galaxies increases with projected number density of galaxies, i.e., with proximity to the core of a galaxy cluster, while the fraction of late-type galaxies decreases with projected number density (e.g., Hubble and Humason, 1931; Dressler, 1980). A popular interpretation of this correlation, known as the “morphology-density” relationship, was that cluster environments transform infalling late-type galaxies into early-type galaxies. The exact environmental mechanisms may be ram pressure stripping (Gunn and Gott, 1972), harassment (Moore *et al.*, 1996), and/or strangulation (Larson *et al.*, 1980).

A test of this scenario was conducted decades later, when works studied the morphology-density relationship at $z = 1$. If environmental processes were transforming late-type galaxies into early-type galaxies, then one would expect that there would be a lower early-type fraction in cluster cores at earlier times compared to today. And indeed, the $z = 1$ early-type fraction at the highest densities was lower than that at $z = 0$ (Smith *et al.*, 2005; Postman *et al.*, 2005). Furthermore, since $z = 1$, the fraction of early-type galaxies has steadily increased in cluster cores, while the fraction of early-type galaxies has remained constant in cluster outskirts. These results showed that environment is an important factor of galaxy evolution.

Another significant work utilizing galaxy structure is the observed change of galaxy size over cosmic time. At fixed stellar masses, it has been shown that galaxies at $z \sim 3$ are more compact than galaxies at $z = 0$ (Daddi *et al.*, 2005; Trujillo *et al.*, 2006, 2007; Buitrago *et al.*, 2008). This finding implies that the outer parts of galaxies are built after the formation of their inner regions, i.e., galaxies grow inside-out. The favored process that drives this evolution is minor mergers, which is consistent with the currently favored hierarchical model of the universe.

These works demonstrate the influence that galaxy structure has had on our current theory of galaxy evolution. In this thesis, we continue this line of exploration by: (1) examining the connection between the inner structure of galaxies and galaxy quiescence (Chapter 2); (2) investigating the effects of bars on galaxy evolution (Chapter 3); (3) determining whether bars are a dominant fueling mechanism for supermassive black hole growth (Chapter 4).

In Chapter 2, we explore how galaxies quench their star formation. We know that galaxies must quench because of two pieces of evidence: (1) the colors and star formation rates of galaxies have been bimodal since at least $z \sim 1$, with star-forming galaxies making up the blue cloud, and quiescent galaxies making up the red sequence (e.g., Strateva *et al.*, 2001); (2) number counts have revealed that blue cloud galaxies have been statistically transitioning onto the red sequence since $z \sim 2$ (Bell *et al.*, 2004b; Faber *et al.*, 2007; Ilbert *et al.*, 2010). These two results indicate that galaxies must shut down, or "quench," their star formation. One of the largest mysteries in galaxy evolution is the identity of this quenching mechanism.

We explore this mystery by searching for the parameter that best separates star-forming galaxies from quiescent galaxies. In our analysis, we considered stellar mass and galaxy structure parameters such as Sérsic index, half-light radius, and a brand-new non-parametric measure, the central surface stellar mass density $\Sigma^*_{1\ \mathrm{kpc}}$. We present a method that finds the best parameter, and conclude that $\Sigma^*_{1\ \mathrm{kpc}}$ is the best. We use our findings to constrain possible quenching mechanisms.

In Chapter 3, we study the relationship between bars and their host galaxies. Bar-driven secular evolution of disk galaxies is predicted to be an important evolutionary process that affects a number of galaxy properties, including morphology, chemical abundance gradients, star formation, and nuclear activity (Kormendy and Kennicutt, 2004). While there have been many searches for evidence of bar-driven secular evolution, conclusive proof has been elusive, mainly due to the small samples sizes of barred galaxies.

To overcome this shortcoming, we collaborated with Galaxy Zoo 2, a citizen science project that produces the largest sample of barred galaxies to date. With this data set, we aim to find the best evidence of bar-driven secular evolution by comparing measurements of bar likelihood and bar length to state-of-the-art simulations of bar formation and evolution.

And finally, in Chapter 4, we investigate if bars are a major fueling mechanism for the growth of supermassive black holes. Recent works have shown that most galaxy hosts of active galactic nuclei (AGN) have a disk-dominated morphology, implying that the process that triggers AGN must not visibly disturb the disky structure of AGN hosts. Among the many possible mechanisms, one that has received attention is bar-driven secular evolution.

Previous works, however, have shown no evidence that bars fuel AGN. But a limitation of these works has been that they were all conducted in the local universe, where the number density of AGN is low. A link between bars and AGN might still be found at earlier epochs, where the number density of AGN is higher. Therefore, our goal in this chapter is to find if there is an excess of bar structures among AGN hosts compared to non-AGN hosts.

Chapter 2

The Dependence of Quenching upon the Inner Structure of Galaxies at $0.5 \leq z < 0.8$ in the DEEP2/AEGIS Survey

2.1 Introduction

With the advent of large galaxy surveys, the color bimodality of the galaxy population has become well-characterized (Lin *et al.*, 1999; Strateva *et al.*, 2001; Im *et al.*, 2002; Blanton *et al.*, 2003; Kauffmann *et al.*, 2003c; Bell *et al.*, 2004b). Galaxy counts back in time revealed that the number of red galaxies has at least doubled since $z \sim 1$ while the number of blue galaxies has remained relatively constant (Bell *et al.*, 2004b; Bundy *et al.*, 2006; Faber *et al.*, 2007; Arnouts *et al.*, 2007; Brown *et al.*, 2007; Ilbert *et al.*, 2010; Domínguez *et al.*, 2011). A natural interpretation is that galaxies evolve from blue to red with time, i.e., from star-forming to 'quenched'. Later measurements of star formation rates confirmed that blue galaxies create stars at a high rate while red galaxies show little to no star formation (Salim *et al.*, 2005, 2007; Noeske *et al.*, 2007; Zheng *et al.*, 2007). Moreover, star formation rates in blue galaxies correlate well with stellar mass, forming the 'Main Sequence' of star formation. In non-dusty red galaxies, however, star formation is generally much lower than that of blue ones (Salim *et al.*, 2005). This abrupt jump in star formation rate across colors motivates the search for a quenching process. For simplicity, we define quenching to be a process that permanently turns a blue star-forming galaxy into a red non-star-forming one.[1]

Many quenching mechanisms have been proposed, but they can generally be categorized into two classes. The first class is internal processes; these act to either expel the gas already in a galaxy or render it inert to star formation. Examples of internal processes include feedback from starbursts and active galactic nuclei (AGN), both of which may be triggered by mergers. They act to heat the surrounding gas and/or drive winds out of the galaxy (e.g., Sanders *et al.*, 1988; Springel *et al.*, 2005; Murray *et al.*, 2005; Cox *et al.*, 2008; Ciotti *et al.*, 2009; Alexander *et al.*, 2010). Another example of an internal process is morphological quenching (Martig *et al.*, 2009). In this model, the presence of a dominant bulge stabilizes the gaseous disk against gravitational instabilities needed for star formation.

The second class contains external processes, which we define as acting to prevent gas from accreting onto a galaxy in the first place. The main external process is halo mass quenching (Silk, 1977; Rees and Ostriker, 1977; Blumenthal *et al.*, 1984; Birnboim and Dekel, 2003; Kereš *et al.*, 2005; Dekel and Birnboim, 2006; Cattaneo *et al.*, 2006); this posits that dark

---

[1] Rejuvenation of star formation in quiescent spheroids through gas and/or satellite infall has been proposed to explain the observed blue spheroids seen in various works (e.g., Kannappan *et al.*, 2009; Schawinski *et al.*, 2009a). In this paper, we do not consider this process.

matter halos above a critical halo mass establish virial shocks that stop the flow of cold gas onto their central galaxies. Additional examples are AGN 'radio mode' feedback (Croton *et al.*, 2006) and gravitational heating (Khochfar and Ostriker, 2008; Birnboim and Dekel, 2011), both of which can be considered as variants of halo mass quenching since both mechanisms require massive halos.

According to our definition, mergers do not qualify as an external process since they act to exhaust and/or remove existing gas already within a galaxy. By the same token, ram pressure stripping (Gunn and Gott, 1972) is also not considered an external process since it strips gas from a galaxy. Furthermore, this paper only concentrates on quenching processes that affect the central galaxy of a halo. According to Gerke *et al.* (2005), who used a sample of DEEP2 galaxies ($\sim 25\%$ of the total DEEP2 sample), only $\sim 32\%$ of DEEP2 galaxies are in groups, meaning $\sim 68\%$ of these galaxies are in the field. These field galaxies would be centrals and additionally, since each group contains one central, the percentage of centrals in this DEEP2 sample is at least $\sim 68\%$. Assuming this sample is representative of the entire DEEP2 dataset, we can conclude that most of our galaxies are centrals. Thus we will not consider mechanisms that affect satellites, i.e., strangulation and harassment (Larson *et al.*, 1980; Moore *et al.*, 1996).

These quenching processes may imprint themselves on the structure of a galaxy, e.g., major majors can create highly concentrated galaxies. The prospect of detecting quenching mechanisms at work via observable changes in structural parameters has motivated many previous works. One of the first parameters explored was luminosity. Using an early SDSS sample, Strateva *et al.* (2001) found that galaxies are bimodal in color, i.e., galaxies generally lie within the red sequence or the blue cloud. However, while galaxies are well separated in color, they overlap over almost the entire range of luminosity, indicating that luminosity is not the main driver of galaxy color.

Later, stellar mass was explored; hereafter, mass refers to stellar mass unless otherwise stated. For a sample of local SDSS galaxies, Kauffmann *et al.* (2003c) found that the correlations between the star formation history indicators $D_n(4000)$ and $H\delta_A$ (which can also be thought of as a proxy for galaxy color) and mass are significantly better than that of the g-band luminosity. They further found that galaxies divide into two distinct families at a stellar mass of 3×10^{10} $M_\odot$.

Recently, additional structural parameters have been introduced. Using an SDSS sample, Kauffmann *et al.* (2006) found that the galaxy surface mass density ($\sim M_*/r_e^2$) produced an even sharper division in specific star formation rate (SSFR) than stellar mass (see also Brinchmann *et al.*, 2004; Maier *et al.*, 2009). They suggested that high surface stellar mass density is connected to the creation of a bulge and the quenching of a galaxy.

Franx *et al.* (2008) intercompared several of the aforementioned color-parameter correlations in the redshift range $0 < z < 3$ using data from the FIREWORKS catalog (Wuyts *et al.*, 2008). Confirming Kauffmann *et al.* (2006)'s result, they showed that surface mass density better separates red and blue galaxies than stellar mass alone. Franx *et al.* (2008) also examined a second structural parameter, the "inferred velocity dispersion" ($\sim M_*/r_e$), and found that the inferred velocity dispersion also better distinguishes red and blue galaxies than mass.

Besides these structural parameters, Sérsic index (n) has also been explored. Driver *et al.* (2006) and Allen *et al.* (2006) observed a clear bimodal distribution in both the rest-frame $u-r$ color and n in the Millennium Galaxy Catalog. A similar trend with SDSS galaxies was seen by Blanton *et al.* (2003) and Schiminovich *et al.* (2007). Bell (2008) showed that n is an even better color discriminator than surface mass density. However, several outliers were noted, and he concluded that high n is a necessary (but not sufficient) condition for quiescence. Recently, Wuyts *et al.* (2011) and Bell *et al.* (2012) found that the correlation between quenching and n was in place since at least $z \sim 2.5$.

A study by Mendez *et al.* (2011) supports the implications of the relationship between Sérsic index and quiescence. Using a sample of DEEP2/AEGIS galaxies at $0.4 < z < 1.2$, they compared the morphological parameters (CAS, G/M_{20}, and B/T) of galaxies in the green valley – galaxies with colors that lie between the blue and red peak in the color bimodality – to those in the blue cloud and red sequence. They found that most green valley galaxies are still disks but are building up their central bulge, in that they have higher concentrations and higher B/T ratios than blue galaxies and less than red galaxies. In other words, they found that the bulges of galaxies are being created or augmented in the evolution of a galaxy from the blue cloud, through the green valley, and finally onto the red sequence.

A recent study by Wake *et al.* (2012b) adds SDSS central velocity dispersion to the list of previously considered structural parameters. It is also the first study to compare the efficacy of Sérsic indices head to head versus other variables. They find that central velocity dispersion leaves the weakest residual color trends with other parameters and conclude quenching correlates most strongly with central velocity dispersion.

The dependence of quiescence on halo properties has thus far been measured only statistically, by looking at the probability that a galaxy is quenched as a function of some mass and/or surrounding density. Peng *et al.* (2010) found that just two processes – “stellar mass quenching", which correlates directly with galaxy stellar mass, and "environmental quenching", which correlates directly with local environmental density – can accurately describe the quenching probabilities of SDSS galaxies. A later paper (Peng *et al.*, 2012) divided centrals from satellites and found that central quenching – of relevance here – had no environment dependence but related only to stellar mass. A similar study by Woo *et al.* (2013) introduced halo mass, which Peng *et al.* (2010) had not considered, and found that central quenching correlated better with halo mass than with stellar mass. However, it is important to note that, regardless of whether halo mass is better than stellar mass, it is clearly not as predictive as structural variables such as Sérsic index or central velocity dispersion. We expound on this statement in the discussion of this paper, but a cursory examination of the SSFR as a function of halo mass from Conroy and Wechsler (2009) (Fig. 8) shows that star formation only gradually changes as a function of halo mass. Whereas the plots of color as a function of Sérsic index and central velocity dispersion from Wake *et al.* (2012b) (Fig. 1) show that color changes quite sharply as a function of both these parameters. Thus a central challenge has emerged for the halo mass quenching picture, namely, why do galaxy structural parameters predict the outcome of halo mass quenching better than halo mass itself does? We return to this question below.

While correlations do not necessarily imply causality, they are strong hints, all of which has led to a rather complicated picture of galaxy evolution. Quenching may well involve a mix of complex processes that are likely to be dependent on several parameters that are themselves correlated. However, several themes emerge from the results discussed. The conditions of the bulge and perhaps the very center of the galaxy appear to be important. Indeed, Kauffmann *et al.* (2006) suggested that bulge-building is the underlying cause of their correlation between color and surface mass density. And several authors, cited above, concluded that high n is necessary to quench a galaxy, providing further evidence for bulges. Moreover, since a hallmark of bulges is high central density, it is notable that Wake *et al.* (2012b) find that central velocity dispersion is the single most correlated parameter of all with galaxy color. And finally, since bulges and high central densities are closely associated with black holes (Magorrian *et al.*, 1998; Gebhardt *et al.*, 2000), it is tempting to conclude that this mounting chain of evidence is simply a "smoking gun" pointing to AGN feedback.

In total, these works suggest that internal processes, and specifically central processes, are responsible for shutting down star formation. As noted, this poses a problem at first sight for halo mass quenching, since halo properties are seen to correlate more weakly with quenching than do variables such as Sérsic index and central velocity dispersion. However, a key element in the halo picture is radio mode, which depends on AGN feedback (Dekel and Birnboim, 2006; Croton *et al.*, 2006), and thus possibly on internal/central conditions. Perhaps it will be possible to link these various processes in a plausible causative chain that explains all of the data. We return to this possibility in the discussion section.

In this paper, we build on previous works and consider the possibility of multiple physical processes acting together in concert to quench star formation in galaxies. Whereas most works have only explored global structural parameters, we explore both global and central structural parameters. Our data set is AEGIS galaxies possessing HST/ACS imaging, similar to Mendez *et al.* (2011) but over a narrower redshift range, $0.5 \leq z < 0.8$. Like them, we use color as a proxy for quenching and structural parameters derived from the same GIM2D fits. However, we focus on different structural parameters and, importantly, convert luminous quantities of subcomponents to stellar mass using color-derived M/L ratios.

Our ultimate goal is to identify that parameter, or combination of parameters, that seems to be the best discriminant between star-forming and quenched galaxies. Having found that combination, we compare its efficacy (or sharpness) to studies focusing on halo parameters (e.g., Woo *et al.*, 2013) in order to assess whether the primary driver of quenching is conditions that exist inside a galaxy or outside it.

A major result of this paper is that the Sérsic index, n, displays the sharpest break between star-forming and quenched galaxies, i.e., it looks most like a quenching threshold. However, n does not really distinguish red and blue galaxies all that well – $\approx 40\%$ of AEGIS galaxies with high n have blue colors. Suspecting contamination from starbursts, AGN, or errors of measurement, we introduce a novel parameter that is closely related to n but is more robustly measured, namely, central surface mass density, $\Sigma^*_{1\mathrm{kpc}}$. Under this parameter, we find that the number of outliers is dramatically reduced, implying that the innermost structure of galaxies may be most fundamentally related to quenching. Moreover, using stellar mass measurements of the bulge and inner 1 kpc region of galaxies, we show that at $z \sim 0.65$, most blue galaxies cannot simply fade onto the red sequence; they must instead undergo a significant restructuring of their innermost stellar density profiles en route to quenching.

These results are compared to various theoretical models. The first major conclusion is that the quenching sharpness found with our new parameter, central surface mass density, far exceeds that found with halo mass, highlighting a major tension with the halo quenching picture. Looking at alternative theories, we find several striking points of agreement with the major-merger picture, but also some important caveats. These concerns suggest that bulge-building may just proceed quite naturally because galaxies at these redshifts are not yet very axisymmetric and non-central torques are constantly being generated. Finally, the very close connection between quenching state and central conditions that we find in this paper looks like a "smoking gun" for AGN feedback, yet not all aspects of the data are fully explained by that model either.

Finally, we place online[2] one of the most comprehensive datasets available, comprised of 11,223 galaxies at $0.2 < z < 1.2$, with a mean redshift of $z \sim .75$. One powerful aspect of this dataset is the use of multi-color HST/ACS V- and I-band imaging, which allows the accurate conversion of light to stellar mass. It also includes GIM2D bulge-disk decompositions (Simard *et al.*, 2002), which provide photometric and structural measurements of the bulges and disks separately; these intermediate redshift galaxy decompositions are only possible thanks to the high resolution HST imaging. Additionally, stellar masses are derived for the subcomponents using their V, I colors.

This paper is organized as follows: §2 describes our data and derivation of the analyzed quantities. In §3, we explain our sample selection criteria and discuss sample completeness. §4 presents our main results – the correlations between structural parameters and color. In §5, we compare our results with several theoretical models and present our two-stage scenario of galaxy evolution. Finally, we list our conclusions in §6. A cosmology with H_0 = 70 km s^{-1} Mpc^{-1}, Ω_m = 0.30 and Ω_Λ = 0.70 is used throughout this paper. All magnitudes are on the AB system.

---

[2] http://people.ucsc.edu/ echeung1/data.html

2.2 Data

We start with a description of all the main sources of data used in this paper, which come from AEGIS, and then discuss the sample selection in §2.3. For an overview of the AEGIS data, please see Davis *et al.* (2007).

2.2.1 CFHT *BRI* Photometric Catalog

The fist photometric data are we use from the Canada-France-Hawaii Telescope (CFHT) *BRI* imaging catalog. The CFHT 12k camera has a 12,288 × 8192 pixel CCD mosaic array and a plate scale of $0\farcs207$ per pixel, providing a field of view of $0.70° \times 0.47°$. Five separate fields, with one to five distinct CFHT 12k pointings per field, were observed from 1999 September to 2000 October. The integration time for each points was ~ 1 hour in B and R and for ~ 2 hours in I, broken down to individual exposures of 600 s. The data are complete to ~ 25.25 in B, 24.75 in R, and ~ 24.25 in I (see Coil *et al.*, 2004 for more details).

These *BRI* magnitudes were used with k-correct v4.2 (Blanton and Roweis, 2007) to obtain the rest-frame color $(U-B)$ and absolute magnitudes (M_B) used throughout this paper.

2.2.2 HST ACS V+I Imaging and SExtractor Photometry

The main photometric catalog from which the sample was selected is based on HST/ACS images taken as part of the AEGIS survey (Davis *et al.*, 2007) under program GO-10134 (PI: M. Davis). The exposures were taken between 2004 June and 2005 March over 63 tiles covering an area approximately $10\farcm1 \times 70\farcm5$ in size. Each tile was observed for a single orbit in F606W (V) and F814W (I) using a four-point dither pattern. These pointings were combined with the

STSDAS Multidrizzle package using a square kernel. The final images have a pixel scale of $0\farcs03$ per pixel and a point-spread function (PSF) of $0\farcs12$ FWHM. The 5σ limiting magnitudes for a point source are $V = 28.14$ and $I = 27.52$ within a circular aperture of radius $0\farcs12$($\sim$ 50-pixel area). For an extended object, the 5σ limiting magnitudes are $V = 26.23$ and $I = 25.61$ for a circular aperture of radius $0\farcs3$ ($\sim$ 314 pixel area).

SExtractor (Bertin and Arnouts, 1996) is used to detect objects in summed ACS V+I images and to construct initial galaxy segmentation maps. A detection threshold of 1.5σ and 50 pixels is chosen. These detection maps and the ACS zero points (Sirianni *et al.*, 2005) were applied to each band separately to create the ACS photometric catalogs. We selected all nonstellar objects with SExtractor CLASS_STAR < 0.9 and $I < 25.0$ that did not lie within 50 pixels of a tile edge for our automated morphology analysis, covering an effective area of 710.9 arcmin^2 in the ACS images (see Lotz *et al.*, 2008a, for more details).

This high resolution catalog was used to generate the galaxy sample comprising the GIM2D bulge+disk catalogs.

2.2.3 GIM2D

Structural parameters of the HST/ACS imaged galaxies were measured using GIM2D, a 2D bulge+disk decomposition program (Simard *et al.*, 2002). Three separate fits were made: a single Sérsic fit with floating n, a bulge + disk fit with $n_{bulge} = 2$ and $n_{disk} = 1$, and a bulge + disk fit with $n_{bulge} = 4$ and $n_{disk} = 1$ The three fits were done simultaneously using both the V and I HST/ACS images according to the procedure in Simard *et al.* (2002). The bulge surface brightness profile is parameterized by:

$$\Sigma(r) = \Sigma_{\rm e}\exp\{k[(r/r_{\rm e})^{1/n} - 1]\}, \tag{2.1}$$

as given by (Sersic, 1968). Here, the parameter k is set equal to $1.9992n - 0.3271$, so $r_{\rm e}$ remains the projected radius enclosing half the light (Capaccioli, 1989). The disk profile is a simple exponential:

$$\Sigma(r) = \Sigma_0 \exp(-r/r_{\rm d}), \tag{2.2}$$

where Σ_0 is the face-on central surface brightness and $r_{\rm d}$ is the semimajor axis scale length. For the single Sérsic fit, Eqn. 2.1 is used to fit the whole galaxy.

GIM2D also measures concentration, which, unlike the SDSS definition, is defined as the ratio of the inner and outer isophote fluxes of normalized radii α and 1; we follow Abraham *et al.* (1994) and use $\alpha = 0.3$. Additionally, the GIM2D models produce galaxy, bulge, and disk V, I magnitudes – these are the primary magnitudes used throughout this paper.

Throughout this paper, most of our results utilize the single Sérsic fits (Table A.3). When examining the bulge and disk properties, we use the best-fitting, two-component decomposition, i.e., either $n_{bulge} = 4$ or $n_{bulge} = 2$ (Tables A.4 and A.5), for each galaxy as indicated by χ^2. We only use bulge measurements of $B/T > 0.1$ galaxies, as the low signal-to-noise makes measurements of systems with $B/T < 0.1$ uncertain. Our subcomponent sample with GIM2D measurements of the bulge and disk separately is comprised of $\approx 60\%$ from the $n_{bulge} = 2$ and $\approx 40\%$ from the $n_{bulge} = 4$ fits. Comparing the $n_{bulge} = 4$ fit to the $n_{bulge} = 2$ fit shows a median offset of log $M_{*,\rm bulge}$ to be ≈ 0.10 dex with a dispersion of ≈ 0.23 dex while log $r_{\rm e,bulge}$ has a median offset of ≈ 0.15 dex with a dispersion of ≈ 0.28 dex; both parameters are offset toward higher values in the $n_{bulge} = 4$ fit.

2.2.4 DEEP2 + DEEP3 Redshift Survey

Spectroscopic redshifts were measured in the DEEP2 redshift survey using the DEIMOS spectrograph (Faber *et al.*, 2003) on the Keck II telescope (Davis *et al.*, 2003; Newman *et al.*, 2013). Targets were selected for DEEP2 spectroscopy from the CFHT *BRI* imaging described in §2.2.1. Most of DEEP2 used the *BRI* photometry to screen out low-redshift galaxies, but this screening was not applied in the AEGIS region, and so the resulting sample is representative from $z = 0$ to $z \sim 1.4$. Eligible targets must have $18.5 \leq R \leq 24.1$ and surface brightness brighter than $\mu_R \leq 26.5$ (Davis *et al.*, 2003; Newman *et al.*, 2013).

Additional spectroscopic redshifts are available in the recently completed DEEP3 redshift survey (Cooper *et al.*, 2011, 2012). This survey shares many of the same characteristics of DEEP2, i.e., they both use the DEIMOS spectrograph and were both preselected using CFHT *BRI* photometry. However, while DEEP2 used a 1200 line/mm grating in DEIMOS, DEEP3 employed a 600 line/mm grating, resulting in spectra of lower resolution. The quality of the redshifts, however, are unaffected.

Taking only spectroscopic redshifts with quality code of $Q = 3$ or $Q = 4$ and cross matching it to the HST/ACS catalog yields a sample of 6310 galaxies; these galaxies make up the spectroscopic sample.

2.2.5 Photometric Redshifts

The DEEP2+DEEP3 survey is approximately 65% complete to $R = 24.1$ in AEGIS (Newman *et al.*, 2013). For those galaxies without spectroscopic z and to extend the sample to fainter limits, we utilized photometric redshifts (J. Huang et al., in prep) derived from the Artificial Neural Networks method (ANNz, Collister and Lahav 2004) using the multi-wavelength AEGIS photometry that includes 12 unique bands in the wavelength range from u to 8 μm, with deep Spitzer/IRAC photometry (Davis *et al.* 2007; Barmby *et al.* 2008; Zheng et al., in prep) as the base. This sample was 3.6 μm selected ($f_{3.6} > 2\mu$Jy) with a color cut to isolate $z < 1.5$ galaxies. The redshift catalog is complete down to log $M_*/M_\odot = 9.5$ for $0.4 < z < 1.2$, and the rms accuracy is $\Delta z/(1+z) = 0.025$. Cross matching this sample to the HST/ACS catalog that does not have a quality spectroscopic redshift yields 4913 galaxies; these galaxies make up the photometric sample. The total number of galaxies in our initial sample, consisting of the spectroscopic and photometric sample, is 11,223.

2.2.6 Rest-frame Absolute B Magnitudes and $U-B$ Colors

Rest-frame absolute M_B magnitudes and $U-B$ colors are needed for both integrated galaxies and for bulge and disk subcomponents separately. For galaxies, these quantities are obtained through k-correct v4.2 (k-corrected down to $z = 0$; Blanton and Roweis, 2007) with CFHT *BRI* photometry and redshift as inputs.

For bulges and disks, however, CFHT *BRI* photometry is not available, but there is HST/ACS V and I photometry modeled by GIM2D. In order to be consistent with the galaxy values, we derive a calibration for M_B and $U-B$ from V, I, and redshift. We use the galaxy rest-frame magnitudes from *k*-correct as fiducial values to derive this calibration, which was then used to calculate M_B and $U-B$ for the subcomponents sample.

The functional form we use for M_B is (Gebhardt *et al.*, 2003)[3]:

$$M_B = I_{814} - DM(\Omega_m, \Omega_\Lambda, \Omega_K) + K_{IB}, \tag{2.3}$$

where DM is the distance modulus for the adopted cosmology and

$$\begin{aligned} K_{IB} &= 1.490 - 18.266z + 94.056z^2 \\ &\quad - 229.782z^3 + 294.741z^4 - 189.892z^5 + 48.034z^6 \\ &\quad + (2.233 - 5.448z + 3.187z^2 - 0.082z^3)(V-I) \\ &\quad + (0.592 - 0.540z - 0.036z^2)(V-I)^2. \end{aligned} \tag{2.4}$$

The functional form for $U-B$ is (Gebhardt *et al.*, 2003):

$$\begin{aligned} U-B &= -0.882 + 16.627z - 84.798z^2 \\ &\quad + 212.831z^3 - 286.211z^4 + 195.256z^5 - 52.584z^6 \\ &\quad + (0.492 + 0.380z + 0.415z^2 - 0.493z^3)(V-I) \\ &\quad + (0.751 - 1.609z + 0.739z^2)(V-I)^2 \end{aligned} \tag{2.5}$$

Fig. 2.1a and 2.1b compares the values of M_B and $U-B$ from Eqn. 2.3-2.5 to those derived from

---

[3] We use Gebhardt *et al.* (2003)'s form but fit for our own coefficients

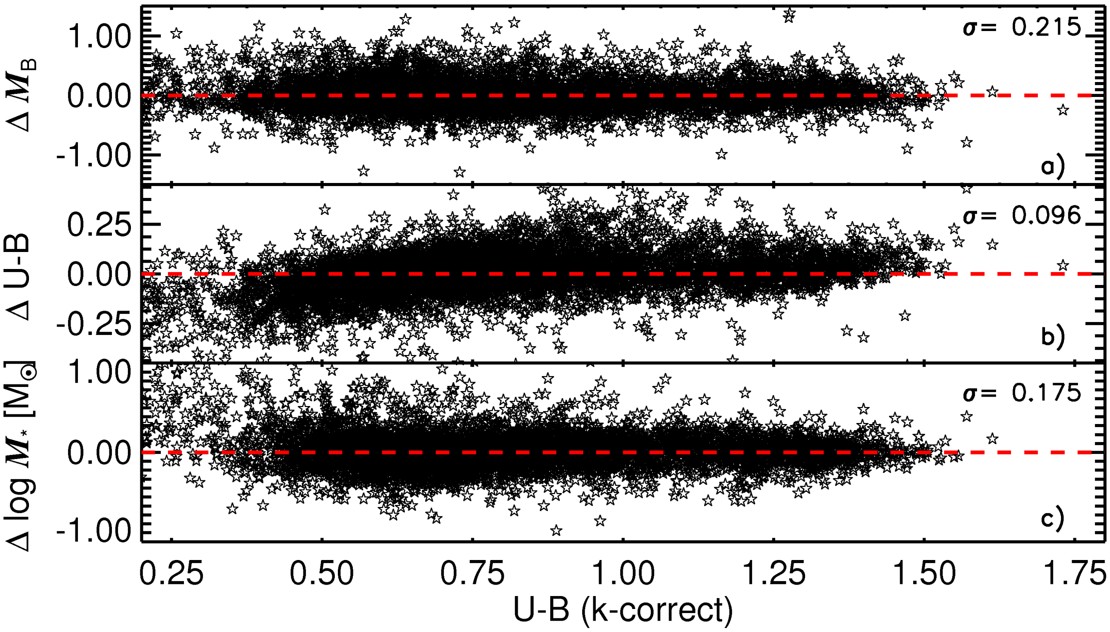

Figure 2.1: We plot the residuals of rest-frame absolute B-band magnitude M_B, rest-frame $U-B$, and stellar mass M_* against rest-frame $U-B$ from k-correct. Panel a shows the difference between M_B computed from k-correct v4.2 (Blanton and Roweis, 2007) using CFHT BRI and redshift and M_B computed from Eqn. 2.3 and 2.4. Panel b plots the residuals of $U-B$ from k-correct to $U-B$ from Eqn. 2.5. Panel c shows the residuals of M_* from J. Huang et al., (in prep) and M_* obtained using Eqn. 2.3 and 2.6. From the one-to-one red dashed line in each panel, it is clear that values derived from our fits are consistent with the fiducial values. The dispersion σ is displayed on the top of each panel.

k-correct. The relations are nicely linear with $\sigma(M_B) = 0.215$ mag and $\sigma(U-B) = 0.096$ mag. We use these relations to compute M_B and $U-B$ for the subcomponent sample. We also use these equations for the galaxies in our sample that have ill-measured CFHT BRI measurements, characterized by large errors ($\approx 7\%$).

2.2.7 Stellar Masses

Stellar masses for most of our sample are available from J. Huang et al., (in prep.). Using a Salpeter initial mass function (IMF), the multi-wavelength AEGIS photometry (with deep Spitzer/IRAC photometry as the base (Davis *et al.* 2007; Barmby *et al.* 2008; Zheng et al., in prep; J. Huang et al., in prep) were fit to a grid of synthetic SEDs from Bruzual and Charlot (2003), assuming solar metallicity. These synthetic SEDs span a range of ages, dust content, and exponentially declining star formation histories. The typical widths of the stellar mass probability distributions are $0.1-0.2$ dex.

To obtain stellar masses for the subcomponent samples we utilize the well-known correlation between mass-to-light ratio (M_*/L) and optical colors (e.g., Bell and de Jong, 2001). To account for our large redshift range, we add a redshift-dependent term to the relationship, similar to the approach in Lin *et al.* (2007) and Weiner *et al.* (2009). Options are to use either rest-frame $U-B$ (from k-correct) or observed $V-I$. To aid our choice, we make fits using both colors and compare them to the M_*/L_B values in Fig. 2.2. The left panels display M_*/L_B vs. observed $V-I$ while the right panels plot M_*/L_B vs. rest-frame $U-B$. Each row represents a different redshift range. Overplotted in each panel is a red dashed curve that represents our fit. The fit for M_*/L_B as a function of $V-I$ is a better match than the fit to $U-B$, especially at high redshifts. The final adopted expression for M_*/L_B is:

$$\begin{aligned} \log\, M_*/L_B &= -0.340-2.593z+1.195z^2 \\ &\quad 1.908(V-I)-0.432(V-I)^2 \end{aligned} \tag{2.6}$$

Together with the absolute B magnitudes measured from Eqns. 2.3 and 2.4, we are now in a position to calculate stellar masses for any object with a measured V, I, and redshift. These calibrated fits are used to obtain M_* values for the subcomponent samples. For the galaxies in our sample that do not have stellar masses from J. Huang et al., (in prep) ($\approx 10\%$), their M_* are also obtained this way; these stellar masses are shown in Table A.1. We make a final check of our method by comparing these derived stellar masses to those calculated by J. Huang et al., (in prep); this is shown in Fig. 2.1c, where the relationship is well-behaved with an rms scatter of 0.175 dex.

2.2.8 Error Estimates

All error estimates measured by GIM2D, i.e., the structural parameters such as r_e and n, are 99% confidence limits (Simard *et al.*, 2002); we convert these into 1-σ limits assuming a Gaussian distribution. There are two sources of stellar mass: those from the SED-fitting and those from our mass fits. The errors for the former are the typical widths of the stellar mass probability distribution ($0.1-0.2$ dex). The errors for masses obtained from Eqn. 2.6, 2.3, and 2.4 are the standard deviation of the residual distribution between the fitted masses and those of J. Huang et al., (in prep) (see Fig. 2.1c; $\sigma \approx 0.175$). Errors for $U-B$ and M_B obtained from k-correct are estimated by measuring the 1-σ dispersion from the HST/ACS V and I in the redshift range $0.64 < z < 0.68$ and $0.82 < z < 0.86$, respectively. Within these redshift ranges, rest-frame U and B approximately redshifts into observed V and I, which when combined with the high resolution of HST, gives us an accurate photometric error estimate. The average errors are ≈ 0.07 mag (U) and ≈ 0.05 mag (B). Errors for $U-B$ and M_B obtained from Eqn. 2.3 and 2.5 are taken to be the standard deviation between our fits and k-correct. For the mass-radius combinations, e.g., M_*/r_e, we propagate the errors from the masses and the GIM2D confidence limits.

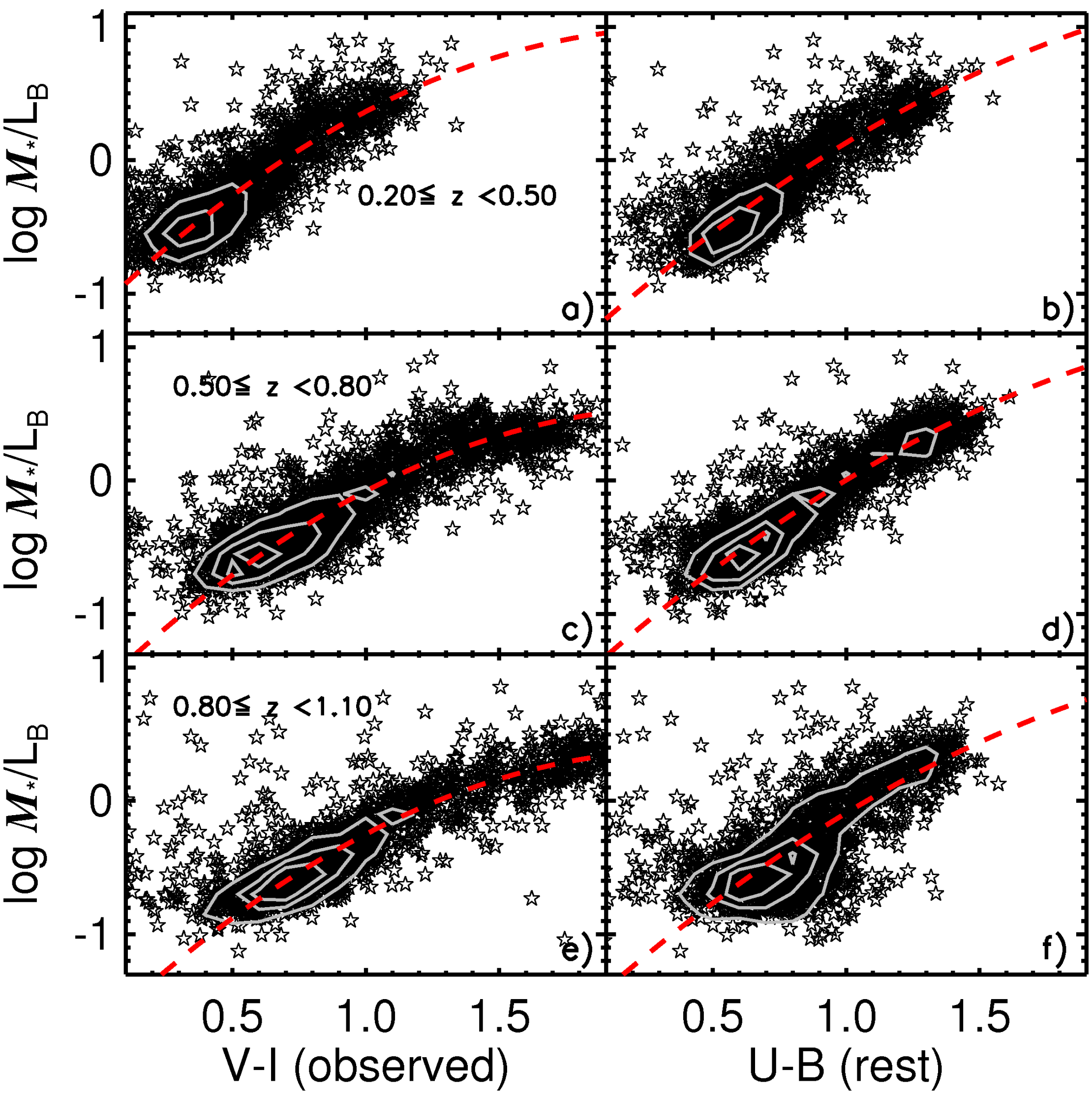

Figure 2.2: M_*/L_B ratio (mass from J. Huang et al., in prep and B-band luminosity from *k*-correct) vs. observed $V-I$ (left column) and rest frame $U-B$ (right column) in three redshift bins: a)-b) $0.20 \le z < 0.50$, c)-d) $0.50 \le z < 0.80$, and e)-f) $0.80 \le z < 1.10$. Contours are shown to give a sense of the relative number densities. The red dashed curve in each panel represents our fit; the fit for M_*/L_B as a function of observed $V-I$ is better than the fit to rest-frame $U-B$, hence we adopt it.

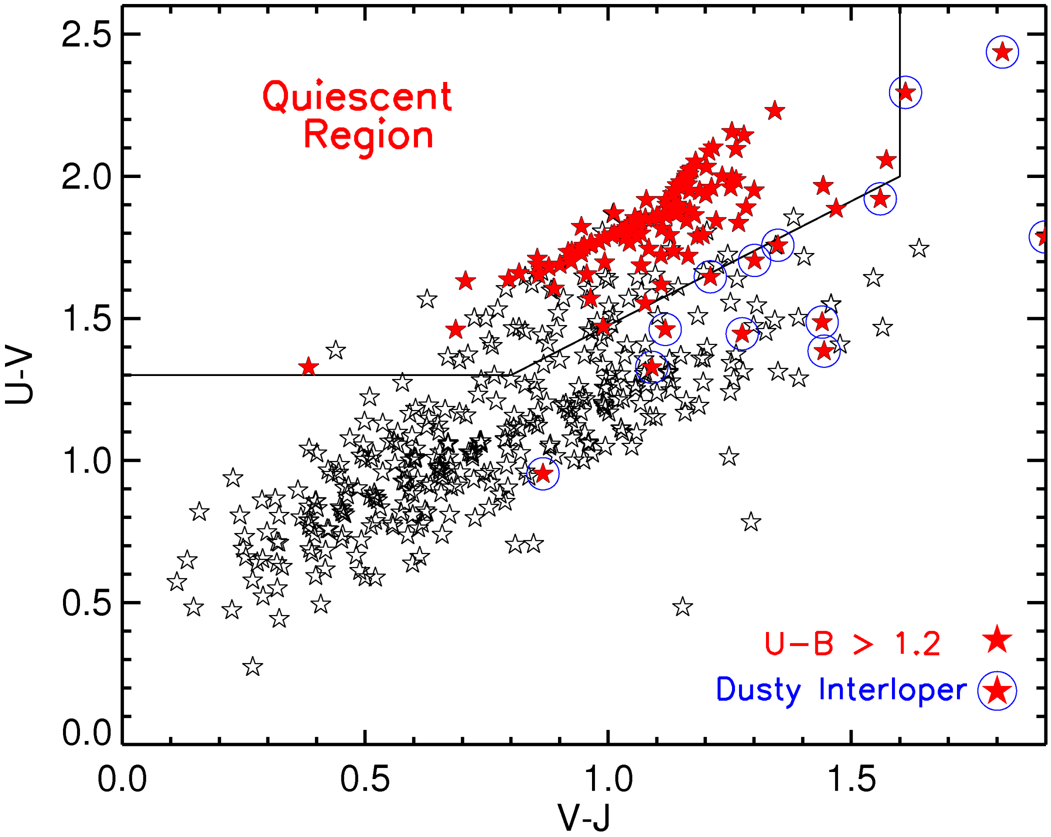

Figure 2.3: To address dust, we plot our sample in the rest-frame UVJ diagram. The quiescent population lie within the quiescent region as defined by Williams *et al.* (2009). Red points represent red sequence galaxies, defined to have $U-B > 1.20$. Almost all of the red sequence lies within the quiescent area. $U-B > 1.20$ galaxies outside the quiescent area is only $\approx 3\%$ of the defined red sequence. These are the dusty star-formers, and we eliminate them from the sample so that the red sequence galaxies are truly quiescent.

2.3 Sample Selection

Within the AEGIS region, $\approx 30,000$ objects have both HST/ACS imaging and GIM2D decompositions; this is the master GIM2D sample. Only 11,223, however, have either a spectroscopic or photometric redshift (see §2.2). Moreover, although our redshift coverage is from $0.2 < z < 1.2$, in order to minimize k-corrections, we restrict our sample to $0.5 \leq z < 0.8$; this cuts our sample down to 3,426, this will be referred to as the 'starting' sample. To reduce the

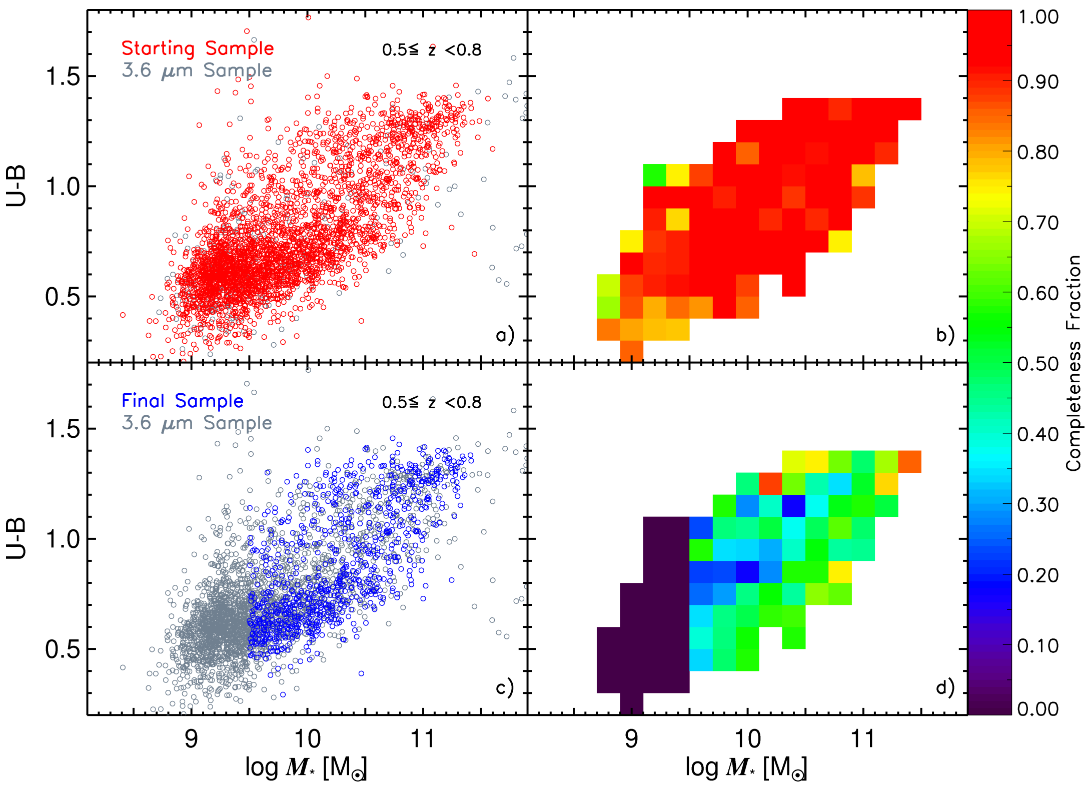

Figure 2.4: *Left column* : Rest-frame $U-B$ vs. log M_* is plotted for the 'starting' sample (red; top row) and the 'final' sample (blue; bottom row). For comparison, the Spitzer/IRAC 3.6 μm-selected sample (J. Huang et al., in prep) in our redshift range $0.5 \leq z < 0.8$ is plotted in the background. *Right column* : $U-B$ vs. log M_* is binned with lengths in $U-B$ and log M_* that correspond roughly to their 1–σ error; we only show bins with more than 5 galaxies. Within each bin, the fraction of the number of galaxies in that row's sample to that of the 3.6 μm-selected sample is computed and displayed as the corresponding color indicated by the color bar to the right. The completeness of the 'starting' sample is uniformly complete above log $M_*/M_\odot = 9.5$. The completeness of the 'final' sample is $\sim 50\%$ and is largely uniform. See text for discussion.

effects of dust, we only choose galaxies with axis ratios (b/a; as measured from the single n fit) greater than 0.55, furthering reducing our sample to 1,567 galaxies.

Although GIM2D was run for every galaxy, not every decomposition is reliable. For example, galaxies with effective radii r_e less than half the full width at half-maximum (FWHM) of the point-spread function (PSF; 2 pixels) are not well fit. Additionally, galaxy models created by GIM2D that are offset from the center of the HST/ACS image by more than 3.5 pixels are similarly ill-fit. There are also instances where the fitting failed; eliminating these leaves us with 1,427 objects. Note that we are only using the single Sérsic fit values for global galaxy parameters, and hence this sample consists of values only from the single n fit.

GIM2D was also used to produce measurements of every galaxy's bulge and disk through two different fits – the $n_{bulge} = 4$ and $n_{bulge} = 2$ decompositions with the disk being $n = 1$ for both (see §2.2.3). Note that GIM2D bulge+disk decompositions do allow for a galaxy to have $B/T = 0$, i.e., a pure disk galaxy, if that is the optimal fit according to the Metropolis fitting algorithm ($\approx 22\%$ of the subcomponent sample have $B/T = 0$; see Simard *et al.*, 2002 for more details). For each galaxy, we use the bulge+disk fit with the smallest χ^2. We only use the subcomponent measurements of the 'final' sample, which we define below.

To reduce the effects of dust, we applied an axis ratio cut of $b/a > 0.55$.. While this cut eliminates many edge-on dusty galaxies (Martin *et al.*, 2007), it does not affect dusty face-on galaxies. To clean these from out sample, we calculate UVJ rest-frame magnitudes. The resultant $U-V$ vs. $V-J$ two color plot enable us to separate dusty red galaxies from truly quiescent red galaxies (Williams *et al.*, 2009). We use the *Rainbow* software described in Barro *et al.* (2011a,b). Briefly, the software applies a χ^2 minimization algorithm to find the best fitting galaxy template from the multi-wavelength photometry of AEGIS. Then several filters (U Bessel, V Bessel, J Johnson) are convolved with the best template to estimate synthetic fluxes assuming a luminosity distance of 10 pc. Our results can be seen in the UVJ diagram (Fig. 2.3). The upper-left region bounded by the solid lines within the UVJ diagram represents the quiescent region, as defined by Williams *et al.* (2009). Comparing the quiescent galaxies to the red sequence galaxies, which we define to be galaxies with $U-B > 1.20$ and are shown in red in Fig. 2.3, shows excellent agreement; only 17[4] (6%) of the $U-B > 1.20$ galaxies lie outside the quiescent area. These are presumed to be dusty, star-formers and are discarded from our sample. There is an additional reduction of 8 $U-B > 1.20$ galaxies because we were unable to obtain their UVJ magnitudes. Since we do not know whether these galaxies are truly quiescent or simply dusty, we take the conservative route and discard them. To sum, we require our quiescent galaxies to have $U-B > 1.20$ and to lie within the quiescent region of the UVJ diagram. With this criterion, our galaxy sample has 1,402 galaxies.

2.3.1 Completeness

Finally, we must discuss our sample's completeness. Because the DEEP2+3 spectroscopic survey is limited by an R-band magnitude of 24.1[5], there is a selection bias against low-mass galaxies. Fortunately, the photometric sample goes deeper, down to an IRAC 3.6 μm flux of 2 μJy. Details of the photometric sample can be found in J. Huang et al., (in prep), but we will briefly summarize the key characteristics. The 3.6 μm-selected sample spans the redshift range of $0.4 < z < 1.2$, where 3.6 μm also probes the rest-frame NIR ($1.2-2.5$ μm). Galaxies of all types have very similar SEDs in the NIR band. Therefore a rest-frame NIR-selected sample suffers no bias against either blue or red galaxies (Cowie *et al.*, 1996; Huang *et al.*, 1997). Galaxy NIR luminosities also trace their underlying stellar mass, in other words, this sample is very close to a mass-selected sample. The K-band absolute magnitudes for galaxies in this sample are calculated with the 3.6 μm flux densities. The IRAC-to-K-band k-correction

---

[4] 4 of these galaxies are not visible because they have UVJ magnitudes that are identical to those that are visible.

[5] There are some DEEP3 targets fainter than this limit (Cooper *et al.*, 2011, 2012)

is adopted from De Propris *et al.* (2007). The absolute K-band magnitude range for this sample is $-19 < M_K < -25$. This translates into a limiting stellar mass of log $M_*/M_\odot = 9.5$. Therefore, cross-matching to the photometric sample has essentially eliminated the selection bias against low-mass galaxies of the DEEP2+3 surveys.

To illustrate our sample completeness, we compare the color-mass diagrams of our ‘starting’ sample (red) to the Spitzer/IRAC 3.6 μm-selected sample (gray) in Fig. 2.4a. There are hardly any gray points, indicating that the ‘starting’ sample contains almost all the galaxies in the 3.6 μ-selected sample. This is further illustrated in Fig. 2.4b where we bin up the color-mass diagram with lengths in $U-B$ and log M_* that roughly correspond to their distributions’ $1-\sigma$ error; we only show bins with more than 5 galaxies. Within each bin, the fraction of the number of galaxies in the ‘starting’ sample to that of the 3.6 μm-selected sample is computed and displayed as the corresponding color indicated by the color bar to the right. Confirming what was seen in Fig. 2.4a, the completeness is almost perfect, and most importantly, the completeness is uniform, especially for log $M_*/M_\odot > 9.5$, the mass limit of the 3.6 μm-selected sample. Thus, our ‘starting’ sample is uniformly complete down to the mass limit of the 3.6 μm-selected sample.

However, our ‘starting’ sample is not the ultimate sample we use. To get rid of bad data and dusty galaxies, we have imposed several requirements (see §2.3). To obtain our ‘final’ sample, we impose one final requirement, log $M_*/M_\odot > 9.5$. This last cut ensures that our ‘final’ sample is complete above log $M_*/M_\odot = 9.5$. Thus finally, we have our ‘final’ sample, consisting of 943 galaxies. The ‘final’ sample is what is plotted in all subsequent figures unless stated otherwise. The completeness of the ‘final’ sample is illustrated in Fig. 2.4c and Fig. 2.4d.

Fig 2.4d (calculates bins of completeness like in Fig. 2.4b) shows that the completeness of the 'final' sample is $\sim 50\%$, with a dearth of galaxies on the top of the blue cloud, i.e., the green valley, and a surplus of galaxies on the upper red sequence. These features are due to the b/a criterion, which is meant to eliminate edge-on galaxies that are presumably dusty. Indeed, according to Martin *et al.* (2007), dusty galaxies do primarily reside on top of the blue cloud, which explains why there is a lack of galaxies on top of the blue cloud in the 'final' sample compared to the 3.6 μm sample. The surplus of galaxies on top of the red sequence is also understandable since the reddest galaxies are elliptical galaxies that have intrinsically high axis ratios. Although there are some biases introduced into the 'final' sample by these various cuts, we have tested the effects of removing them and find that it does not affect our conclusions. But we stress that these cuts are necessary; they remove bad data. Our 'final' sample is a culmination of the best data from our available resources. For an extra discussion of our samples' surface brightness limits, data quality, and possible Sérsic index bias, please see Appendix A.1, A.2, A.3.

All our data, including those that were not presented in this paper, are available online at: `http://people.ucsc.edu/~echeung1/data.html`. Tables A.1-A.5 present the key parameters we use in our paper for twenty randomly selected galaxies in our catalog. Table A.1 presents basic information of our galaxies, including their unique IDs, derived photometric quantities, and stellar masses both from k-correct and Eqn. 2.6, 2.3, and 2.4. Table A.2 presents much of the same information in Table 1, but only for the subcomponents. Tables A.3, A.4, and A.5 present the three GIM2D catalogs: the single Sérsic fit, $n_{bulge} = 4$ fit, and $n_{bulge} = 2$ fit, respectively. These GIM2D catalogs provides many measurements, including V, I, and r_{e}

for both the galaxy and its subcomponents. The rest of the measurements and galaxies can be obtained online.

2.4 Results

2.4.1 The Most Discriminating Color Parameter

We begin by intercomparing the various global structural parameters discussed in the introduction to find which is the best predictor of color. Fig. 2.5 plots $U-B$ rest-frame color against six quantities for the final galaxy sample: rest-frame absolute B-band magnitude M_B, stellar mass M_*, stellar mass divided by semimajor axis effective radius M_*/r_e (sometimes called the "inferred velocity dispersion")[6], M_*/r_e^2 (nominal surface density)[7], Sérsic index n, and inner stellar mass surface density $\Sigma^*_{1\mathrm{kpc}}$ (we defer discussion of $\Sigma^*_{1\mathrm{kpc}}$ to §2.4.3.3). The 1-σ error bars are given in the top right of each panel (see §2.2.8 for details). The spectroscopic sample and photometric sample are shown in open stars and open circles, respectively; we use this scheme throughout the rest of the paper. As stated in the introduction, the amount of color overlap is one measure of how well a parameter separates red sequence and blue cloud galaxies, and parameters that reduce this overlap are better discriminators of galaxy quenching. The sample considered is the 'final' sample, which is complete only in stellar mass, as defined in §2.3. Thus the results of the following analysis is only applicable for the 'final' sample. The

---

[6] The true stellar velocity dispersion is $\sigma^2 \propto GM/r_\mathrm{e}$, where M is the total mass including stars, gas, and dark matter. Franx *et al.* (2008) provide a value of the coefficient through the fitting of a sample of SDSS galaxies: $\sigma^2 = 0.3GM_*/r_\mathrm{e}$. Recently, Taylor *et al.* (2010) and Bezanson *et al.* (2011) showed that the addition of a Sérsic dependent term to the "inferred velocity dispersion" of Franx *et al.* (2008) provides a better estimate of the true velocity dispersion. We choose not to use this updated "inferred velocity dispersion" because we want to compare the color correlations of these parameters independently.

[7] Surface mass density is actually $M_*/2\pi r_\mathrm{e}^2$, but we omit the constants.

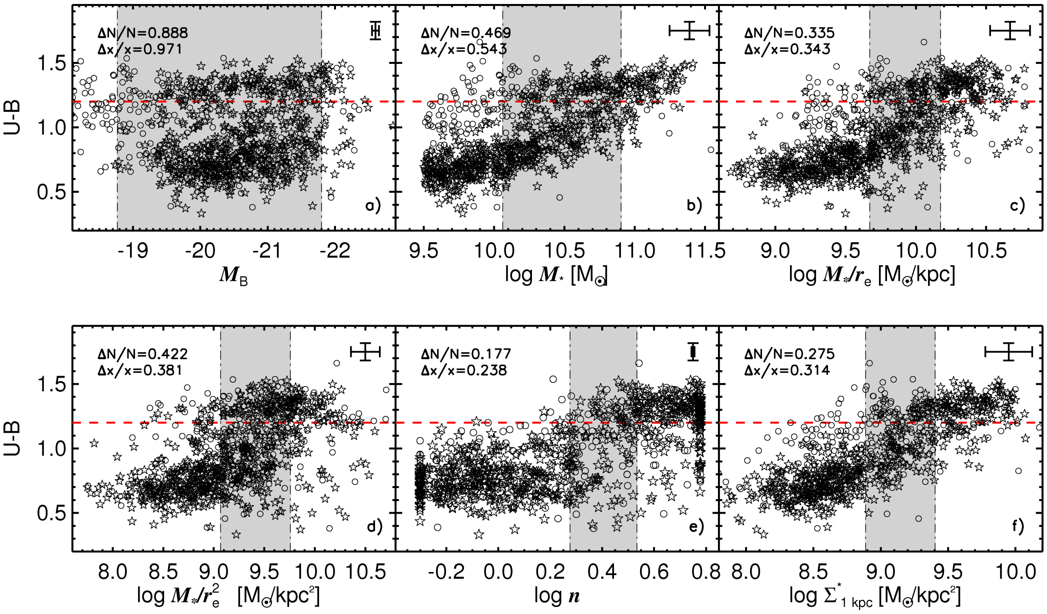

Figure 2.5: Rest-frame $U-B$ color is plotted against: a) rest-frame absolute B-band magnitude M_B, b) stellar mass M_*, c) stellar mass divided by semimajor axis effective radius M_*/r_e, d) M_*/r_e^2 (surface density), e) Sérsic index n, and f) stellar mass surface density within 1 kpc Σ^*_1kpc. M_* is in solar masses and r_e is in kpc. The stars and circles represent galaxies with spectroscopic redshifts and photometric redshifts, respectively. 1-σ error bars are displayed in the upper right of each panel. The overlap region of each parameter is highlighted in gray. Overlap regions are defined as regions in which the fraction of red galaxies is between 15%−60% (see §2.4.1). The red horizontal line represents the division between red and blue galaxies. The top left corner of each panel shows two measures of the size of the overlap region: the fractional number of galaxies within the overlap region ΔN/N and the fractional extent of the region Δx/x, where x contains 90% of the points (see text). This analysis was done on the 'final' sample, which is complete only in stellar mass (down to log $M_*/M_\odot = 9.5$; see §2.3.1). By both measures, M_*/r_e outperforms other parameters of the form M_*/r_e^p, which we have confirmed by studying intermediate values of p. Sérsic index and Σ^*_1kpc do even better, hinting that the distribution of mass in the inner parts of galaxies may play a fundamental role in quenching star formation.

goal of this section is to quantify the amount of overlap in order to determine the single best color discriminant among the traditional parameters.

As in Strateva *et al.* (2001), the color-magnitude diagram (Fig. 5a) shows a clear red sequence and blue cloud. However, these two groups overlap greatly over the entire range of absolute magnitude. This confirms the well-known result that the B-band magnitude is a poor predictor of galaxy color.

Fig. 2.5b shows the color-mass diagram. As shown by Kauffmann *et al.* (2003c) and Borch *et al.* (2006), mass is better correlated with star-formation history than is luminosity. Although the relationship with color is improved, the range of color overlap is still large, extending over ~ 0.8 dex in mass. Fig. 2.5c and 2.5d add powers of r_e in the denominator to M_*, in the form of M_*/r_e^p. The smallest overlap by eye is given by M_*/r_e in Fig. 2.5c, while mass surface density M_*/r_e^2 in Fig. 2.5d looks slightly worse. Thus, this new DEEP2 sample indicates that M_*/r_e is a superior color discriminator to surface mass density M_*/r_e^2.

To summarize, effective radius r_e tightens the basic color-mass relation because red galaxies at fixed mass are smaller than blue galaxies, and the tightest correlation is obtained using M_*/r_e.

We plot in Fig. 2.5e color vs. Sérsic index n. The character of this plot is markedly different from the others – rather than a smooth trend with color within the blue cloud as in, for example, M_*/r_e, the color jump is more abrupt, with color remaining constant above and below what appears to be a critical value of n around $\log\, n = 0.36$ ($n = 2.3$). This behavior is intriguing because it might signal a real physical threshold in Sérsic index, above which star formation shuts down. As stated in the introduction, n likely plays an important role in quenching star-formation. Blanton *et al.* (2003) and Schiminovich *et al.* (2007) demonstrated a trend between n and color for SDSS galaxies. Driver *et al.* (2006) and Allen *et al.* (2006) also showed this relationship with their Millennium catalog. And Wuyts *et al.* (2011) demonstrated that this relationship persists out to $z \sim 2.5$. Bell (2008) and Bell *et al.* (2012) explored this correlation and showed that high n is necessary for quenching but not sufficient – there are many galaxies that are blue despite having high n. We see something similar in our data with the scattering of aberrant points in the lower-right-hand corner of Fig. 2.5e. We term these aberrant points "outliers" and discuss them further in §2.4.3.2.

The above conclusions are based mainly on visual assessment of Fig. 2.5. To quantify our results, we now present two new quantities that are designed to measure the size of the overlap regions. These measurements can be applied to rank the predictive power of the various structural parameters and also to identify galaxies within the overlap regions for further study. To define these quantities, we first bin the sample by the parameter of interest. Then, within each bin, we find the fraction of galaxies that are red, i.e., galaxies with $U-B > 1.20$, which we have ensured to be genuinely quiescent and not dusty (see §2.3). The locations where this fraction equals 15% and 60% mark the beginning and end of the overlap region, respectively; these percentages were adjusted to match the core of the overlap regions as judged by eye and are a compromise over all diagrams. We varied the overlap definition with various permutations of starting boundaries in the red fraction range of 5% to 20% and ending boundaries from 40% to 60% and found that the results are unchanged. To find the locations of the edges of the overlap regions, we fit a fourth-order polynomial to the red fraction bins and interpolate to find where the fit reaches the desired fractions. Each parameter has been divided into 25 bins, and each edge value is examined to ensure that the choice is sensible. The edge locations depend only weakly on the choice of bin width – for example, in the case of M_*/r_e, bin sizes in the range $0.07-0.25$ dex produce similar results.

We define two measures to quantify the sizes of the overlap regions. The first is the fractional number of galaxies in the region, ΔN/N, where N is the total number of galaxies and ΔN is the number within the overlap region. The second is the fractional extent of the region, Δx/x, where Δx is the width of the overlap and x is the range that includes 90% of the data (excluding 5% at either end). The resulting overlap regions for each parameter are demarcated in gray in Fig. 2.5, and the upper left corner of each panel shows the two measures ΔN/N and Δx/x. These quantitative measures confirm what was seen by eye, namely, that M_*/r_e gives the smallest values of both $\Delta\mathrm{N}/\mathrm{N}$ and Δx/x among all the mass-radius combinations. Note that the relative extent of M_B is Δx/x=0.971; this simply means that the overlap region is almost equal to the entire range that encompasses 90% of the data, again agreeing with our previous qualitative assessment. Furthermore, we find that Sérsic index performs considerably better than even M_*/r_e in minimizing both $\Delta\mathrm{N}/\mathrm{N}$ and Δx/x.

We also point out the extremely tight relation that is produced when plotting color vs. M_*/r_e or M_* for blue-cloud galaxies alone (Fig. 2.5b and 2.5c). This has been pointed out before and is referred to as the 'Main Sequence' of star formation (Noeske *et al.*, 2007). Previous work on quenching has focused on the relationship between red sequence vs. blue cloud galaxies and not so much on the properties of galaxies within the blue cloud itself. However, the tightness of the relation between M_*/r_e (or M_*) and color for star-forming galaxies alone could be an important clue to the physics of quenching, and we return to this point in §2.5.

2.4.2 Properties of Galaxies in the M_*/r_e Overlap Region

We have shown that our AEGIS data duplicate previous findings showing that M_*/r_e and n correlate strongly with quenching, but we have also shown that neither parameter alone

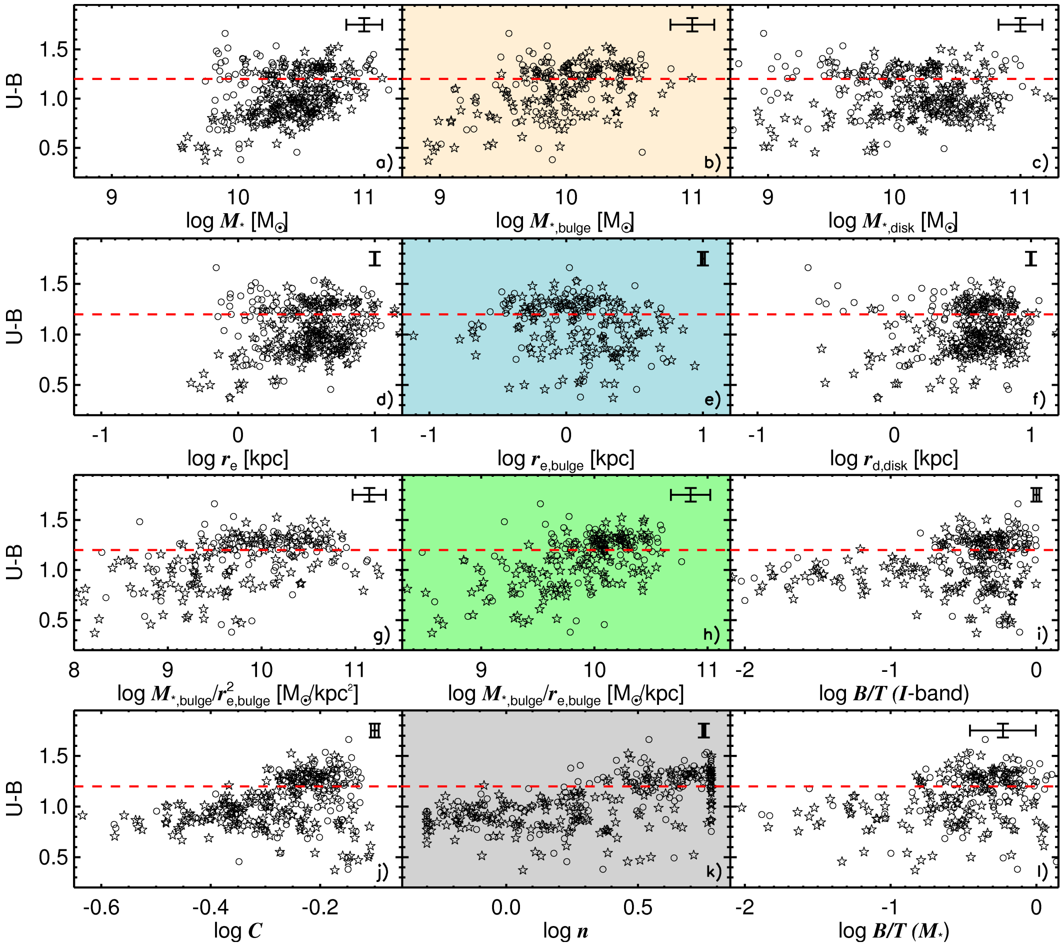

Figure 2.6: Galaxies in the overlap region of $M_*/r_{\rm e}$ (containing 316 galaxies) from Fig. 2.5c are isolated to examine possible second-parameter color correlations with both global and disk/bulge properties. $U-B$ rest-frame color is plotted against: a) global stellar mass M_*, b) bulge stellar mass $M_{*,\rm bulge}$, c) disk stellar mass $M_{*,\rm disk}$, d) global semimajor axis effective radius $r_{\rm e}$, e) bulge semimajor axis effective radius $r_{\rm e,bulge}$, f) disk semimjaor axis exponential scale length $r_{\rm d,disk}$, g) $M_{*,\rm bulge}/r^2_{\rm e,bulge}$, h) $M_{*,\rm bulge}/r_{\rm e,bulge}$, i) bulge-to-total ratio B/T in the I-band, j) concentration C, k) global Sérsic index n, and l) B/T based on stellar mass M_*. The 1-σ error bars are displayed in the upper right of each panel. The red horizontal line in each panel represents the division between red and blue galaxies. Global properties hardly differ between red and blue galaxies (white panels), but bulge properties, disk scale length, and n show key differences (colored panels and panel c). Specifically, red sequence bulges are physically smaller, yet more massive, than those of the blue cloud. Moreover, red sequence disks are less massive than their blue cloud counterparts. These trends cannot be produced by simple disk fading but require a concentration of inner stellar mass.

is close to being a perfect predictor of it. In this section and the next, we take a further look at the properties of galaxies in the overlap region and outliers to find out whether multiple parameters can be used in concert to predict quenching, and whether this interplay sheds light on the physical processes involved.

Fig. 2.6 investigates residual trends within the M_*/r_e overlap region of Fig. 2.5c by plotting color versus various structural parameters for overlap galaxies alone. In exploring this slice of M_*/r_e, we are assuming a general evolutionary sequence such that the blue galaxies evolve into the red galaxies within this overlap region. However, this assumption is not without proof. Bell *et al.* (2004b) and Faber *et al.* (2007) have shown that the red sequence has increased by ~ 2 while the blue cloud has remained relatively stable from $z \sim 1$ to $z = 0$. Moreover, Hopkins *et al.* (2010b) showed that $\sim 65-80\%$ of the observed mass density of bulge-dominated galaxies formed since $z \sim 1$. Thus our redshift range ($0.5 \leq z < 0.8$) peers directly into the epoch when the majority of red sequence galaxies are being formed. We choose M_*/r_e as the base parameter because it is the tightest $M_* - r_\mathrm{e}$ combination in Fig. 2.5, but similar results are obtained when M_* is used.

Panels a, d, j, and k of Fig. 2.6 plot integrated quantities, while the remaining panels introduce structural parameters (e.g., M_* and r_e) for bulges and disks separately. Among the integrated properties, virtually no trend is seen in either stellar mass (panel a) or r_e (panel d), but a mild "step function" is seen with Sérsic index in that n is significantly higher for quenched galaxies (panel k, gray). Concentration, C, shows similar behavior, albeit less cleanly (panel j). A similar trend with n was seen for all galaxies (Fig. 2.5e), but it is important to see the same effect for overlap galaxies alone. This establishes beyond doubt that M_*/r_e alone does not fully encapsulate the processes needed to quench star formation. A possible interpretation is that some galaxies are "ripe" for quenching based on M_*/r_e and that a second process, which drives galaxies to high n, ultimately quenches star formation. We return to this idea later in §2.5.

The remaining panels in Fig. 2.6 focus on the properties of bulge and disk components separately (the subcomponent sample; see §2.2.3). These parameters are derived from GIM2D photometric fits and M_*/L_B values from the $V-I$ colors of bulges and disks separately (§2.2.7), for which high-resolution two-color HST imaging is required. The striking result from the subcomponent panels in Fig. 2.6 is the marked differences in disk mass, bulge mass, and bulge effective radius between blue and red overlap galaxies (panels b, c, and e). The disks of red sequence galaxies are less massive by about 0.2 dex than the blue cloud galaxies (panel c) while the bulges of red sequence galaxies are more massive by about 0.3 dex than the blue cloud galaxies (panel b, in light tan). At the same time, disk sizes remain constant but bulge sizes decrease by about 0.3 dex as blue cloud galaxies transition to the red sequence (panel e, in blue). These differences between red sequence bulges and blue cloud bulges amount to a difference of 0.6 dex in bulge $M_{*,\mathrm{bulge}}/r_{\mathrm{e,bulge}}$ (panel h, in green). A similar trend is seen in B/T ratios, but it is weaker due to the large spread of blue galaxies.

These trends collectively demonstrate a real structural difference between the inner stellar mass distributions of quenched vs. star-forming galaxies, and furthermore, that this difference exists even within a narrow range of M_*/r_e. Higher central stellar mass densities in quenched galaxies have been inferred in previous work from higher integrated Sérsic values (Weiner *et al.*, 2005; Bundy *et al.*, 2010), but photometric data by themselves do not rule out a simple fading picture in which disks decline in brightness, permitting an underlying high-

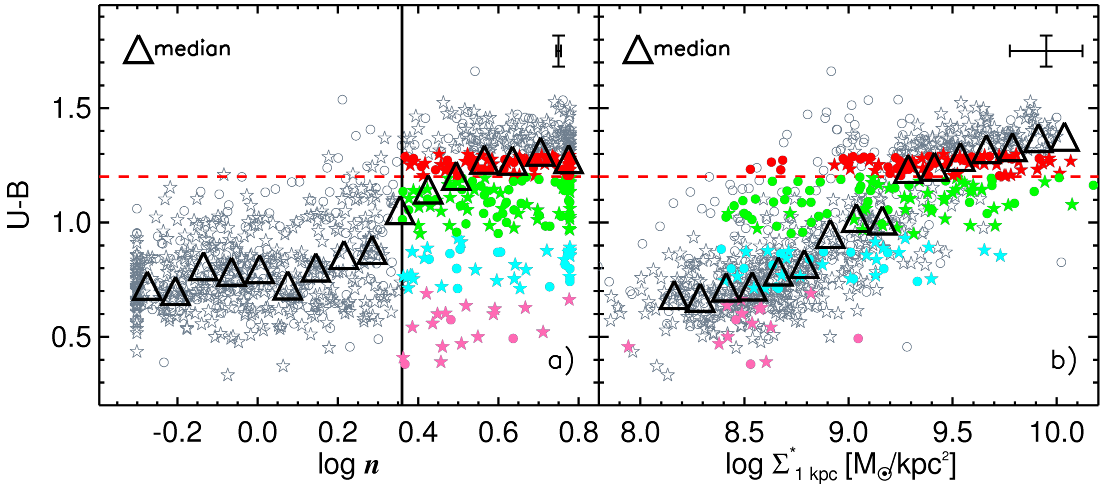

Figure 2.7: a) The $U-B$ vs. n diagram is reproduced from Fig. 2.5e with median values of color in each n bin plotted as open black triangles. The red horizontal line represents the division between red and blue galaxies, while the black vertical solid line at log $n = 0.36$ represents the point at which the median is half way between the red and blue values. The medians show a step-like behavior in $U-B$ vs. n, suggestive of a physical threshold in n. Exceptions to the step function are the blue "outlier" galaxies in the lower right. These are highlighted in strips of color for further discussion in §2.4.3.2 and Fig. 2.9: pink points encompass $U-B < 0.70$, cyan points encompass $0.70 \leq U-B < 0.95$, and green points encompass $0.95 \leq U-B < 1.20$. Bluish red-sequence galaxies are highlighted for comparison and lie within $1.20 \leq U-B < 1.30$. Images of these outliers are shown in Fig. 2.9. Roughly 40% of the log $n > 0.36$ galaxies are outliers. b) $U-B$ color vs. inner stellar mass surface density $\Sigma^*_{1\mathrm{kpc}}$. Note that some galaxies do not have $\Sigma^*_{1\mathrm{kpc}}$ measurements due to insufficient signal-to-noise. Most outliers now fall into line, suggesting that inner stellar mass surface density is a cleaner predictor of quenching than n.

n bulge to emerge. Actual stellar masses for bulges and disks separately are needed to rule out fading. An important new insight from our work is that evolution to the red sequence appears to be accompanied by a significant rearrangement of inner stellar mass in which existing stars move to the centers of galaxies, and/or new stars are formed there. We discuss processes whereby that might happen in §2.5.

2.4.3 Sérsic Index and Inner Surface Density

2.4.3.1 A threshold in n?

The previous section considered M_*/r_e as the main quenching parameter and looked at scatter around it to discover secondary effects. In this section, we use a similar tack but focus on Sérsic index n. An enlarged version of the color-n plot is shown in Fig. 2.7a, which indicates median $U-B$ in bins of n. The medians illustrate the striking step-like behavior previously mentioned. Defining the riser of the step to be where the medians are half-way between their red and blue values, we place this point at $\log\ n = 0.36$, which is marked with the vertical black line. This value corresponds to $n = 2.3$, which is similar to the value of n often used to distinguished quenched (or early-type) galaxies from star-forming ones locally (e.g., Shen *et al.*, 2003; Bell *et al.*, 2004a; Schawinski *et al.*, 2007a; Drory and Fisher, 2007).

The medians also emphasize how flat the color trends are above and below the threshold n value. Evidently, in the extreme high-n and low-n regimes, star formation history is independent of n. This differs markedly from the behavior of M_*/r_e; Fig. 2.5c shows a strong correlation between M_*/r_e and color for star-forming galaxies below the overlap region.

The lack of importance of n above and below the threshold is further emphasized by the large color scatter in both of these regimes. This scatter is, however, of two types. At low n, there is a rather uniform spread in color, i.e., specific star-formation rate can assume any value within a large range, and n does not predict what SSFR will be. At high n, n predicts color much better, i.e., the color distribution is strongly peaked toward red (quenched) colors, but a significant tail of outliers with blue colors exists (colored points, except the red in Fig. 2.7).

The existence of these outliers was seen at both low and high redshifts by Bell (2008) and Bell *et al.* (2012), who expressed the role of n in quenching as "necessary but not sufficient", i.e., all quenched galaxies have high n, but not all high-n galaxies are quenched. We see the same thing.

Unlike Fig. 2.5c (which plotted color vs. M_*/r_e), there is no interval in n where the color scatter is markedly larger than elsewhere (Fig. 2.7a), and thus no impetus to search for a second parameter within a narrow region of n. To investigate the scatter, we have replotted Fig. 2.7, this time highlighting galaxies within narrow bins of various second parameters. The results are shown in Fig. 2.8, where galaxies are divided into bins of stellar mass (top row), M_*/r_e (middle row), and M_*/r_e^2 (bottom row), collectively termed M_*/r_e^p. The outlier region from Fig. 2.7a is outlined in blue. In each row, the behavior is the same. Galaxies with low values of M_*/r_e^p are seen to be mainly blue. A few leak into the high-n "outlier" regime, but their blue colors always agree with other galaxies in the same parameter bin, i.e., their star formation rates are not depressed by having high n. As M_*/r_e^p increases, the mean color of low-n galaxies becomes redder while the number of outliers remains relatively constant. Again, the colors of the outliers still agree with the average color of all galaxies in the same M_*/r_e^p bin. At the highest values of M_*/r_e^p, virtually all galaxies are quenched and the fraction of outliers is negligible. Two points are clear: dividing galaxies into bins has not destroyed the basic step-like nature of the behavior in that galaxies within each bin still trend smoothly but sharply (apart from outliers) from their "native" star-forming state to a quenched state. The second point is that all trends with color at low n remain flat within each bin of M_*/r_e^p. This shows that the strong trend of color vs. M_* or M_*/r_e within the blue cloud (Fig. 2.5b and 2.5c) is not caused by some hidden dependence on n.

To summarize, we have reproduced findings by previous authors that indicate that high n typically predicts a quenched galaxy, and we have set the half-power point between blue and red galaxies at $n_{crit} = 2.3$. This value is very near the SDSS value, implying no large evolution in n_{crit} from $z \sim 0.65$ down to $z \sim 0$. The rise in color near the critical value is sharp, while above and below this value there is no trend in color with n, even within narrow slices of M_*/r_{e}^{p}. At high n, most galaxies are quenched with red colors, but a non-negligible fraction of objects is blue despite having high n. We turn to the nature of these outliers next.

2.4.3.2 Outliers

Although n acts like a threshold for the vast majority of galaxies, there are obvious exceptions, namely the blue, high-n ($\log n \geq 0.36$) "outliers" highlighted in Fig. 2.7a and elsewhere. Understanding these objects is clearly crucial for unraveling the quenching mechanism – why are they blue when their photometric structure resembles that of quenched objects? We have highlighted 151 outliers in Fig. 2.7 using color to indicate their $U-B$ ranges; they make up $\approx 40\%$ of all $n > 2.3$ galaxies (the red points immediately above the red horizontal dashed line at $U-B = 1.20$ are not outliers, they are quiescent red sequence galaxies shown for comparison).

Several possibilities come to mind to explain these objects. One possibility is that they are artifacts due to the presence of bright point-like AGNs. Adding a blue AGN to a normal star-forming galaxy would make the global colors bluer and increase n (and concentration) (Pierce *et al.*, 2010). To pursue this, we have cross-matched the outliers to two AGN samples selected using X-ray and optical line-emission data. The AEGIS region is covered by a deep 800 ksec

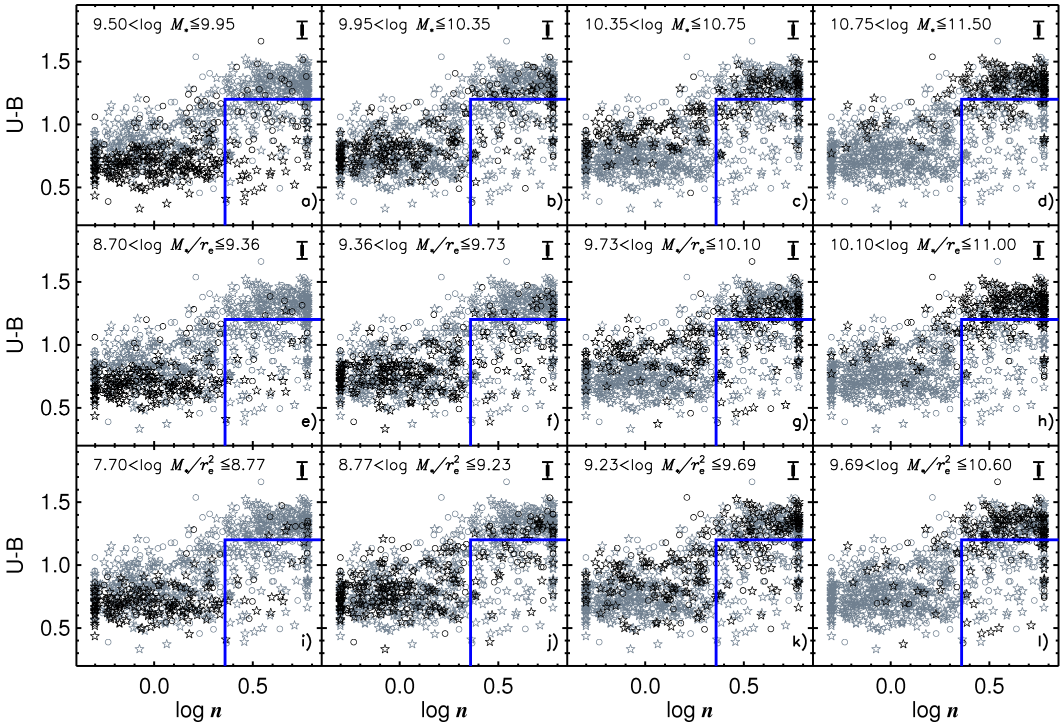

Figure 2.8: The $U-B$ vs. n diagram from Fig. 2.7a is replotted to separate the roles of M_*, M_*/r_e, and M_*/r_e^2 from n in driving color evolution. Galaxies are divided into bins of M_*/r_e^p and plotted as the black points. Bin boundaries are shown in the upper left of each panel. The rectangles outlined in blue indicate the outlier region from Fig. 2.7a. The panels demonstrate that the step-function-like behavior near $\log\, n = 0.36$ ($n = 2.3$) seen in Fig. 2.7a is replicated separately in each range of M_*/r_e^p independent of p. Color rises rapidly near $\log\, n = 0.36$ ($n = 2.3$), but there is little impact of n on color above and below this value. This shows that the trends in color with M_* and M_*/r_e in the blue cloud (Fig. 2.5b and 2.5c) are not caused by a hidden dependence on n.

Chandra X-ray mosaic (Laird *et al.*, 2009). We find that only 11 of the outliers have X-ray luminosities above 10^{42} erg s^{-1}, or 7%. We have also used an optical method for selecting AGN based on a modified version of the classical "BPT" diagram (Baldwin *et al.*, 1981) that plots [O III]/Hβ versus $U-B$ rather than [N II]/Hα (Yan *et al.*, 2011). This adds only 14, bringing the total to 21 AGN, or 14% of the outliers. Thus, it seems that the vast majority of these objects are unlikely to be AGN hosts.

Another possibility is a bright blue clump of recently formed stars at the centers of the outliers, which might skew the colors and Sérsic indices as an AGN would. We would like to remind the reader that the single Sérsic GIM2D model does not fit for any substructure, such as clumps. Hence asymmetric structures may affect the n measurements. To explore this, we constructed V and I color images of all outliers using the HST/ACS data and inspected them; a montage of 20 galaxies is shown in Fig. 2.9, where each row represents a different range of $U-B$ color according to the color-coding in Fig. 2.7a. The bluest outliers are in the bottom row. These tend to be lumpy, asymmetric, and/or small – their fitted Sérsic values are somewhat questionable. Moving up one row to the cyan points, we find a mix of genuinely concentrated galaxies plus more small galaxies like the ones in the previous row. The third row contains larger objects of intermediate color but with convincingly high concentrations. Finally, we show a sample of red sequence galaxies in the top row as a comparison; they are all red and highly concentrated spheroids.

To summarize, the blue, high-n outliers are a mix of different types. Some may have doubtful Sérsic indices, being small or with off-centered clumps of star formation or AGN, but a fair fraction seem to be genuinely blue yet high-n galaxies. These genuine exceptions tend to be located at intermediate values of $U-B$. The existence of such outliers has been noticed before. An important class of candidates is poststarburst galaxies (e.g., Dressler and Gunn, 1983; Couch and Sharples, 1987; Poggianti *et al.*, 1999; Goto *et al.*, 2003). These objects possess blue colors and strong Balmer absorption yet weak Hα, signifying recent quenching, and their Sérsic indices are high (Quintero *et al.*, 2004; Yang *et al.*, 2008). A second class of objects is the blue spheroidal galaxies; like poststarbursts, they have smooth, centrally concentrated, elliptical-like profiles but they are different in having active star formation (Menanteau *et al.*, 2001; Im *et al.*, 2001; Koo *et al.*, 2005; Schawinski *et al.*, 2009a; Kannappan *et al.*, 2009). Their masses tend to be small (Im *et al.*, 2001), and there appear to be several objects in our outlier population that fit this description in the bottom row of Fig. 2.9.

A quick calculation of the percentage of outliers within a volume-limited SDSS sample at $z \sim 0$ shows that it has dropped from $\approx 40\%$ for our sample at $z \sim 0.65$ to $\approx 10\%$ at $z \sim 0$. This difference seems consistent with the higher levels of gas at higher redshifts, which could give rise to more clumpy star formation asymmetrically distributed throughout the galaxy, skewing the Sérsic values.

For completeness, in passing we also mention satellite processes. Processes such as ram pressure stripping (Gunn and Gott, 1972) and strangulation (Larson *et al.*, 1980) do not by themselves change n. However, other satellite mechanisms involving tidal interactions (such as "harassment" e.g., Moore *et al.* 1996) may induce a morphological transformation. If satellite galaxies are first harassed, they might attain a high n while still forming stars. While we do not expect most of the DEEP2 galaxies to be satellites (see introduction), a more thorough investigation is needed to confirm this.

2.4.3.3 Inner Surface Density: An Improvement on n?

From the above, it is clear that in n we have found a remarkable, but still imperfect, structural predictor of quenching. The main criticism of n is the presence of outliers; if they could be removed, the correlation, and hence the prediction, would be nearly exact.

There are two obvious weaknesses with n. First, it is based on light, not stellar mass, and hence is subject to the vagaries of star formation history and dust. Second, it relies on a fit to the entire light profile and is thus at least partially dependent on the outer light distribution, which may be disturbed or irregular. In contrast, trends discovered using bulge properties in Fig. 2.6 hint that the structure of the inner regions of galaxies is more important at predicting quiescence.

Accordingly, we introduce a new parameter that attempts to remove both of these weaknesses, namely the stellar mass surface density within 1 kpc. This is defined as $\Sigma^*_{1\mathrm{kpc}} \equiv M^*_{1\mathrm{kpc}}/\pi r^2_{1\mathrm{kpc}}$, where $r_{1\mathrm{kpc}} \sim 1$ kpc[8]. The actual diameter used is 12 pixels ($0\farcs36$), which is set by the smallest radius that our HST images can conveniently resolve; it spans a radius of $1.08-1.35$ kpc at our redshifts. The quantities I and $V-I$ are measured within this aperture, and L_B, M_*/L_B, and M_* are estimated using Eqns. 2.3, 2.4, and 2.6.

The quantity $\Sigma^*_{1\mathrm{kpc}}$ was already included for completeness in Fig. 2.5 (panel f), where its performance is seen to be mixed. It seems to predict color less well than the global quantities M_* and M_*/r_e in the blue cloud, but it does much better than n in removing outliers. This is even better illustrated in Figs. 2.7a and 2.7b, which compare outliers directly. Using $\Sigma^*_{1\mathrm{kpc}}$, almost all the pink and cyan points have receded back into the blue cloud, and only a few green outliers remain. This suggests that the outliers in n are largely artifacts caused by poor GIM2D fits[9] and that using a more secure quantity like inner mass surface density can remove them. It is still true that using $\Sigma^*_{1\mathrm{kpc}}$ by itself is not perfect and that n somewhat outperforms it on the overlap criteria seen in Figs. 2.5e and 2.5f. That a genuine spread exists in $\Sigma^*_{1\mathrm{kpc}}$ is confirmed

---

[8] Note that here we include the π, so these are physical surface densities.

[9] GIM2D only models a galaxy into either a bulge+disk model or a single Sérsic model. More complex structures like spiral arms, bars, and clumps are not modeled. Thus a galaxy with these features are potentially ill-fit.

by ongoing work with higher-S/N SDSS data (Fang et al., in prep), which however reveals some additional striking regularities. Our point for now is that using $\Sigma^*_{1\mathrm{kpc}}$ removes the large number of outliers that are present with n. Furthermore, the definition of $\Sigma^*_{1\mathrm{kpc}}$ as an inner mass density directs our attention even more strongly to the fact that it is conditions near the center of the galaxy that drive quenching.

2.5 Discussion

In this paper, we have found that the most discriminating parameter of quiescence, according to the measures of the overlap region, is the Sérsic index, and that a plot of color vs. Sérsic index shows a step-like behavior near $n = 2.3$, suggestive of some sort of genuine quiescence threshold. About 40% of the $n > 2.3$ galaxies, however, are "outliers" that fall outside this behavior. These outliers have central mass densities much lower than those of the red sequence and fully consistent with those of the blue cloud. In other words, under this new parameter, $\Sigma^*_{1\mathrm{kpc}}$, the outliers now fall in line, suggesting that a galaxy's central structure may be even more physically related to quiescence than Sérsic index.

Both n and $\Sigma^*_{1\mathrm{kpc}}$ corroborate our second major finding, that most blue cloud galaxies at the observed epoch cannot simply fade onto the red sequence. We have shown through stellar mass measurements of bulges and disks that the red sequence galaxies have absolutely higher bulge mass concentrations, i.e., that the jump in n is not due simply to the fading of disks (see §2.4.2). The central mass densities extend this conclusion to the very centers of galaxies. In other words, the transition to the red sequence involves a significant restructuring of a blue cloud galaxy's innermost stellar density profile.

Below the critical value of $n = 2.3$, however, Sérsic index shows little to no correlation with star formation, and color is more closely correlated with M_*/r_e (or perhaps with M_*, see Fig. 2.5).

This two-pronged behavior suggests that the star-formation history of a galaxy is shaped by two separate factors at different stages. While the object is still star-forming (in the blue cloud), its star-formation rate depends on global parameters, like M_*/r_e or M_*. Then, a major internal mass reorganization occurs, a dominant bulge forms, and star formation stops. In the following discussion, we compare these results to the predictions of the standard merger model for bulge-building and quenching and find reasonable agreement, but also several issues. To alleviate these issues, we also consider other models, specifically, violent disk instability (Noguchi, 1999; Elmegreen *et al.*, 2008; Dekel *et al.*, 2009), secular evolution (Kormendy and Kennicutt, 2004), morphological quenching (Martig *et al.*, 2009), and halo quenching (Silk, 1977; Rees and Ostriker, 1977; Blumenthal *et al.*, 1984; Birnboim and Dekel, 2003; Kereš *et al.*, 2005; Dekel and Birnboim, 2006; Cattaneo *et al.*, 2006). We end with a brief discussion on an unresolved concern.

2.5.1 Merger Model

Major mergers[10] have been linked to the formation of spheroids since Toomre and Toomre (1972), with considerable work in the years since (see Hopkins *et al.* 2009b and ref-

---

[10] According to Hopkins *et al.* (2010a), major mergers dominate the formation and assembly of $\sim L_*$ bulges and the total spheroid mass density. Thus, we only consider major mergers in this discussion. However, it should be noted that minor mergers can create bulges (Bournaud *et al.*, 2007) and do contribute a non-negligible amount ($\sim 30\%$) to the total spheroid mass density (Hopkins *et al.*, 2010a).

erences therein). The process of bulge formation in classical merger models occurs through both the violent relaxation of pre-existing stars to the center and a gaseous dissipation-induced nuclear starburst (Hopkins *et al.*, 2009b).

Comparison of the bulge-dominated products of these simulations to observed early-type galaxies shows good agreement. The Sérsic indices of the merger products from Hopkins *et al.* (2008) are high, $n \gtrsim 2.5$. Similarly, Naab and Trujillo (2006) showed that their disk mergers (with bulges) created galaxies with $3 < n < 4$ [11]. Both of these works produce spheroids with Sérsic indices in the range of our red sequence spheroids and of other observations (e.g., Kormendy and Kennicutt, 2004; Drory and Fisher, 2007; Fisher and Drory, 2008).

The properties of quenching induced by mergers are also consistent with our data. The merger model predicts that quenching occurs through the nuclear starburst (Mihos and Hernquist, 1994), in which a large portion of the gas[12] is exhausted (depending on gas fraction; see Springel and Hernquist 2005; Okamoto *et al.* 2005; Robertson *et al.* 2006; Cox *et al.* 2008; Governato *et al.* 2007, 2009), and through subsequent feedback, from supernovae and/or AGN (Springel *et al.*, 2005; Murray *et al.*, 2005; Ciotti *et al.*, 2009). Note that both sources of quenching originate from the center of the galaxy, suggesting that the conditions at the center may correlate better with the quenching state than global properties. This is what we find. Furthermore, the central surface mass densities of the simulated spheroids from Hopkins *et al.* (2009a) match our observations of the red sequence spheroids in Fig. 2.7b – with values of $\log\ \Sigma = 9-10\ \mathrm{M_{\odot} kpc^{-2}}$ at 1 kpc.

---

[11] Naab and Trujillo (2006) conducted a collisionless simulation that does not include gas, and thus does not model a nuclear starburst component. That is why their pure disk-disk mergers only have $n \approx 1.5$, because they lack the high central surface brightness typical of dissipative gas-rich mergers.

[12] In the following discussion, gas is assumed to be cold gas unless otherwise stated

A further success of the merger hypothesis is the good match between it and the stellar mass range where bulge-building is observed to occur. A major point is that the efficiency of bulge-building from major mergers is expected to be highly dependent on the pre-merger gas fraction, such that decreasing gas content increases the potential to form bulges (Springel and Hernquist, 2005; Robertson *et al.*, 2006; Hopkins *et al.*, 2009b). This dependence is consistent with the assumption that gas content gradually falls as galaxies age in the blue cloud, making them ultimately ripe for spheroid formation via mergers. Because more massive galaxies exhaust their gas quicker due to the phenomenon known as "downsizing" (e.g., Cowie *et al.*, 1996), there is a strong color-mass relation in the blue cloud, meaning that the reddest blue cloud galaxies at any epoch have the least amount of gas. According to the merger model, this means that they are also on the threshold of forming bulges.

Evidence for this hypothesis is strong in Fig. 2.5b, which shows a remarkably tight correlation between stellar mass and color in the blue cloud in the sense that more massive galaxies are the reddest. Further data come from Catinella *et al.* (2010) and Saintonge *et al.* (2011), who presented H I and CO data in the GASS and COLD GASS survey, respectively. These works illustrate that the average atomic and molecular gas fraction of galaxies do decrease with increasing stellar mass and increasing NUV-r color. Although these surveys do not fully sample the blue cloud (these surveys only observe $M_* > 10^{10}$ $\mathrm{M}_\odot$ galaxies), extrapolating these seemingly linear trends to lower masses indicate that total gas fraction does indeed decrease with mass along the blue cloud. Theoretically, Hopkins *et al.* (2010a) showed that the most effective bulge-building major mergers are clustered around log $M_* \sim 10.5$ $\mathrm{M}_\odot$ at $z \sim 1$, which is in the center of overlap region of M_*. This behavior is due in part to exactly the same reason, namely, decreasing gas content as galaxies age within the blue cloud. In a general way, then, theory predicts that galaxy colors and gas contents should both age within the blue cloud, causing galaxies to become more prone to bulge-building mergers at higher mass and low gas level, and these trends broadly agree with the observations.

In detail, however, the data indicate that M_*/r_e is a better predictor of quenching than M_* alone (cf. overlap regions in Fig. 2.5b vs. 2.5c). This may be because M_*/r_e is related to velocity dispersion (Franx *et al.* 2008; see footnote 26), which, based on a new study by Wake *et al.* (2012a), is the galaxy property most closely related to halo mass. This finding could then be a manifestation of the dependence of quenching on a critical halo mass. Alternatively, it may reflect the fact that radii are shrinking as stellar mass builds up in the centers of quenching galaxies and thus reflects a property of the galaxies themselves rather than of their halos. We elaborate further on these thoughts in §2.5.5.

Although there are some aspects of the merger model that match our data, general agreement upon the validity of this model has not been reached. One controversial issue is whether major mergers can actually quench galaxies. There have been various works that support this idea (e.g., Schawinski *et al.*, 2007b; Alexander *et al.*, 2010; Cano-Díaz *et al.*, 2012; Farrah *et al.*, 2012). In particular, Cano-Díaz *et al.* (2012) obtained VLT-SINFONI integral-field spectroscopy for one quasar at $z = 2.4$ and showed a suppression of narrow Hα emission, a tracer of star formation, in the region with the highest outflow velocity and highest velocity dispersion. But this is only one example and does not erase the contradicting evidence others have offered. For example, using a sample of X-ray and post-starburst galaxies from SDSS and DEEP2 at $0.2 < z < 0.8$, Coil *et al.* (2011) found winds with velocities that are insufficient to shut down star formation, indicating that the presence of an AGN does not produce faster winds nor does it seem to play a major role in quiescence. And Ammons *et al.* (2011) fail to find any correlation between host galaxy color and X-ray hardness ratio among $z = 0.5 - 1.5$ galaxies, as might be expected from the blowout model.

Another important concern is whether there are enough mergers to account for the bulge density in the universe. Studies that have measured the galaxy merger rate often present different results (e.g., Bell *et al.*, 2006; Conselice, 2006; Lin *et al.*, 2008; Lotz *et al.*, 2008b; Bundy *et al.*, 2009; Xu *et al.*, 2012; Bluck *et al.*, 2012). Lotz *et al.* (2011) addressed the issue of disparate observational merger rates; they found that the major reason for these differences is the assumed timescale in which a merger is observable. Using a suite of hydrodynamic merger simulations, they constrained the observable timescales of three common merger rate estimators – close galaxy pairs, G/M_{20}, and asymmetry – and found that if a physically motivated average observability timescale was adopted to calculate the merger rates, then these rates become largely consistent. The remaining differences between the merger rates are explained by the differences in the ranges of mass ratio measured by different techniques and the differing parent galaxy selection.

Additionally, for mass-limited samples ($M_* > 10^{10}$ $M_\odot$), they found excellent agreement between their merger rates from close pairs to several theoretical merger rates. Specifically, they agreed with the merger rates of Hopkins *et al.* (2010a), who, using a combination of semi-empirical models and high-resolution merger simulations, concluded that there are enough major mergers, to within a factor of ~ 2, to account for the observed growth of the bulge population. They argue that previous studies reached different conclusions because they assumed incorrect merger timescales, rather, if a uniform simulated-calibrated merger timescale is used, then many of these works actually come to their conclusion (see also Robaina *et al.*, 2010).

An alternative way to address whether there are enough mergers is to examine the phase in galaxy evolution that is predicted to correspond to the period of mergers. Adopting a simplified model in which blue star-forming galaxies merge and transform into red quiescent galaxies, one would expect a short period in which galaxies have intermediate colors, i.e., they are in the green valley. A recent study on the morphologies of green valley galaxies by Mendez *et al.* (2011) found that only 14% of their sample are identified as on-going major or minor mergers (using G/M_{20} and asymmetry parameters), which is lower than the 19% merger rate in the blue cloud. They further found that most green valley galaxies have disks and that 21% have $B/T < 0.05$, implying that they were unlikely to have experienced a recent major merger.

To conclude, while the merger model fits many aspects of our data, there are serious open questions, including whether major mergers are able to quench, whether there are enough of them, and whether they are consistent with the color and morphologies of green valley galaxies. In the remaining discussion, we explore other models that may alleviate these problems.

2.5.2 Disk Instabilities: Violent and Otherwise

An alternative bulge-building process involves the growth of giant clumps formed via gravitational instability in gas-rich disks (Noguchi, 1999; Elmegreen *et al.*, 2008; Dekel *et al.*, 2009; Ceverino *et al.*, 2010). These clumps migrate inward and coalesce to form a bulge, and simulations suggest that galaxies can develop classical bulges with $n \approx 4$ during this process[13]

---

[13] However, a recent paper by Inoue and Saitoh (2012a) claims that these clump-origin bulges are more akin to pseudobulges in that they exhibit $n < 2$.

(Elmegreen *et al.*, 2008). Recent simulations also show that the these clump-origin bulges have central surface mass densities comparable to that of our red sequence galaxies (Ceverino et al., in prep). The effectiveness of this instability, however, is highly dependent on the gas inflow rate onto the galaxy (Dekel *et al.*, 2009), which declines with time. Thus, we expect this process to be more important at redshifts higher ($z \sim 2$) than that of our sample.

Although this process may have operated strongly at $z \sim 2$, we stress that this paper concerns a different sample of galaxies at lower redshift when conditions may have changed. Bell *et al.* (2004b) and Faber *et al.* (2007) found that the number of red sequence galaxies has at least doubled from $z \sim 1$ to $z \sim 0$, indicating that a fraction of our galaxies at $z \sim 0.65$ are actively migrating to the red sequence as we view them. Using the NEWFIRM survey, Brammer *et al.* (2011) found that the mass density of quiescent galaxies with $M_* \gtrsim 3 \times 10^{10}$ $\mathrm{M}_\odot$ increased by a factor of ~ 10 from $z \sim 2$ to the present day. Similarly, Hopkins *et al.* (2010b) argue that the vast majority of ellipticals/spheroids do not form through high redshift channels. They state that the observed mass density of bulge-dominated galaxies at $z \sim 2$ is only $\sim 5\%$ of its $z = 0$ value, and at $z \sim 1$, is still only $\sim 20-35\%$ of its $z = 0$ value. Thus, most bulges are formed at $z \lesssim 1$, meaning the majority of our red sequence galaxies are recent arrivals.

Although we expect violent disk instabilities to be increasingly less frequent at decreasing redshift, owing to lower gas fraction, the actual bulge contribution due to this mechanism at $z < 1$ is presently unknown. Hints at intermediate redshift suggest that the process may not be limited to high z. For example, Bournaud *et al.* (2012) found that half of a sample of $z \sim 0.7$ disk galaxies are clumpy without any merger signatures, implying that disk instabilities could still be important at that redshift.

Perhaps we need to think more broadly and to recognize that the settling of matter to form regular, axisymmetric disks is a very lengthy process lasting many billions of years. When any non-axisymmetric forces exist, an inevitable outcome is that some mass will be driven to the center. Furthermore, in a general way the higher the degree of non-axisymmetry in the potential, the higher the rate of matter inflow will be. At late times, non-axisymmetry has become small and the flow rate is low, a process that we call "secular evolution", which we discuss next.

Future studies will resolve this question.

2.5.3 Secular Evolution

Secular evolution (Kormendy and Kennicutt, 2004) constitutes the weak end of the spectrum of non-axisymmetric processes in disk evolution. This complex of processes involves the slow rearrangement of gas (and stellar) mass due to gravitational interactions between the gas and stars within a disk galaxy. A variety of relatively weak non-axisymmetric disturbances, such as bars, ovals, and spiral structure in the stellar component, can create non-central gravitational forces that add or subtract angular momentum from the gas, which responds by moving inward or outward depending on radius. The process sweeps inner gas into the center, where it forms stars, and pushes gas farther out to larger radii, where it can accumulate in tightly wrapped spiral arms or a ring (Simkin *et al.*, 1980; Kormendy and Kennicutt, 2004). Separately, the gas itself may become mildly gravitationally unstable, which raises the velocity dispersion and causes the gas to radiate. This net loss of energy must come from somewhere, and the gas responds by sinking slowly to the center, increasing its (negative) potential energy (Forbes *et al.*, 2012). Overall, these processes push some mass to the center and other mass to the outskirts, thus increasing n. The forces are, however, weak and the process is slow, hence the term "secular evolution". The total time required would be many dynamical timescales, and thus at least several Gyr (Kormendy and Kennicutt, 2004; Fisher *et al.*, 2009).

Although secular evolution may contribute to some of the bulge-building taking place at $z \sim 0.65$, we do not believe it is the major factor. According to Kormendy and Kennicutt (2004), bars are a major driver of secular evolution at the current epoch. Assuming that bars are also the main drivers at higher redshifts, comparing the bar fraction from the past, which is 10%-25% among late-types at $z > 0.8$ (Jogee *et al.* 2004; Sheth *et al.* 2008, Herrington et al., in prep), to the current epoch, which is 30-60% at $z \sim 0$ (Sheth *et al.*, 2008; Cameron *et al.*, 2010; Masters *et al.*, 2011), implies that secular evolution was not a major bulge-building process at $z \sim 0.65$. Additionally, Koo *et al.* (2005) showed that 85% of luminous field bulges within this redshift range are red, arguing against secular evolution being the dominant bulge-building process since they are expected to mainly produce blue bulges (Kormendy and Kennicutt, 2004).

Finally, the physical structure of bulges built by secular evolution differs strongly from ones built by mergers, as reviewed by Kormendy and Kennicutt (2004). The so-called "classical" bulges built by mergers resemble small ellipticals embedded in disk galaxies. They have high stellar velocity dispersion and high vertical extent above the plane, having been "fluffed up" by the merger – in other words, they are true spheroids. They can also be very massive and contain a considerable fraction of the total mass of the galaxy. In contrast, the "bulges" built by secular evolution are relatively flat, have effective radii of only a few hundred pc, and have low fractional masses. Because of these differences, Kormendy and Kennicutt (2004) term these structures "pseudobulges". Drory and Fisher (2007) directly compare the properties of these two types of bulges. They isolated a sample of nearby, massive, disk galaxies and classified them into classical bulges and pseudobulges based on the morphology of the central regions. Confirming their disparate nature, they found a clear bimodality in that pseudobulge galaxies are much bluer (in the blue cloud or green valley), have low central surface brightness, and have low global Sérsic index ($n < 2.5$).

For these reasons, we conclude that the pseudobulges cannot be an important contributor to our intermediate redshift, high n, red sequence galaxies. They may, however, certainly help build the bulges seen in late-type galaxies, becoming increasingly more important with decreasing redshifts, where the bar fraction can be as high as 60% (Sheth *et al.*, 2008)[14]. In fact, Fisher and Drory (2011) show that, by number, 80% of the bulges within 11 Mpc of the Milky Way are actually pseudobulges. But, by mass, they only make up $\lesssim 10\%$ of the total mass density in local spheroids (Allen *et al.*, 2006; Driver *et al.*, 2007).

In conclusion, we find it helpful to think of the entire family of bulge-building mechanisms as ordered along a "disturbance continuum" from severe to mild, with corresponding timescales from short to long and bulge-building rates from fast to slow. The members of this continuum consist of major to minor mergers at the strong end, through violent disk instabilities, to milder disk instabilities, and finally to weak, secular instabilities like bars, spiral arms, and normal star formation. The dividing line between an externally triggered process like mergers and internally triggered dynamical instabilities is fairly clear, but there is no such dividing line among the internal processes – each one shades smoothly into the next. However, since every disk is sooner or later subject to one or more of these processes, the central densities of disks

---

[14] This number is controversial, recent studies by Nair and Abraham (2010b); Masters *et al.* (2011); Lee *et al.* (2012a) show that the local bar fraction is $\sim 30\%$.

inevitably tend to increase – the only question is, how fast?

We note that this disturbance continuum is also a continuum in time, with early galaxies experiencing disturbances at the strong end of the spectrum and later galaxies settling down to slower, more secular rates. Our AEGIS galaxies exist somewhere near the middle of the time continuum, when disky galaxies as a class were considerably more disorganized and more non-axisymmetric than they are today. This logic further supports our conclusion above that secular processes were probably not the major bulge-building process in these galaxies, with a combination of mergers and stronger disk instabilities being more likely. However, the exact balance of these two processes remains for further study.

2.5.4 Morphological Quenching

The preceding sections focused on mechanisms to increase the central densities of disk galaxies, and thus account for one of our major findings, namely, higher central stellar densities in quenched galaxies. Even though a variety of stellar build-up mechanisms were identified, including mergers and internal instabilities, we tacitly assumed regardless of process that high density would always lead to the creation of a black hole and that feedback from the black hole would quench star formation. However, the discussion in §5.1 noted a lack of conclusive evidence that AGN feedback actually quenches star-formation in disk galaxies. In this section and the next, we review two other quenching mechanisms that have been proposed to operate in central galaxies.

The first of these is morphological quenching (Martig *et al.*, 2009), whereby the steep potential well of a bulge is able to drive the Toomre Q parameter above unity and stabilize the gas disk against star formation. An attractive aspect of morphological quenching is that it sets in when n is high, which jibes with the structure of quenched galaxies. This mechanism is unique because it does not require the removal of gas or the suppression of the cold-gas supply onto the galaxy. Instead, gas can continue to accrete onto a galaxy yet remain inert to star formation owing to the strong central mass concentration. A recent analysis of a set of three high-resolution AMR simulations at $z \simeq 2.3$ by Ceverino *et al.* (2010) demonstrates this process. From $z \simeq 2.3$ to $z \sim 1$, two of these galaxies are shown to evolve from a gravitationally unstable and turbulent disk into a stable system; they attribute this change to presence of a dominant stellar bulge.

An explicit prediction of morphological quenching is that red, early-type galaxies should frequently host significant cold gas in the amount of a few percent of their baryonic mass, and in fact comparable to gas fractions in normal star-forming galaxies (Martig *et al.*, 2009). However, this prediction is not consistent with observed H I properties of nearby early-type galaxies. Though H I is frequently detected, especially in field galaxies (Morganti *et al.*, 2006; Oosterloo *et al.*, 2010), the amounts are nearly always low. This is confirmed by the GASS H I survey at Arecibo of ~ 1000 slightly more distant massive galaxies with $M_* > 10^{10}$ $\mathrm{M}_\odot$ (Catinella *et al.*, 2010), which shows that the average H I fractions of red sequence galaxies are at least ten times lower than galaxies of similar mass on the star-forming main sequence (Schiminovich *et al.*, 2010; Fabello *et al.*, 2011). The same result applies to molecular H_2 in the same galaxies (Saintonge *et al.*, 2011). These recent studies simply confirm what has been known for a long time about early-type galaxies, that their absolute gas contents are low compared to star-forming galaxies (e.g., van Driel and van Woerden, 1991; Roberts and Haynes, 1994; Noordermeer *et al.*, 2005). Hence, in order to achieve quenching, it is necessary to reduce the fractional gas content, either by expelling gas or preventing new gas from falling in – morphological quenching alone cannot do the job.

For the nearest galaxies it is possible to map the H I distributions (van Driel and van Woerden, 1991; Noordermeer *et al.*, 2005; Morganti *et al.*, 2006; Oosterloo *et al.*, 2010). Normal lenticular galaxies typically have H I in an outer ring with an empty hole in the middle. Several authors (van Driel and van Woerden, 1991; Cortese and Hughes, 2009; Oosterloo *et al.*, 2010) have stressed that the surface density of gas in these rings is well below the critical threshold for star formation (Kennicutt, 1989; Schaye, 2004; Bigiel *et al.*, 2008), which represents the threshold for molecular H_2 formation, a tracer of gravitationally unstable gas (e.g. Krumholz *et al.*, 2011). Moreover, the predicted star formation efficiency at such low densities is ten times lower than in normal star-forming galaxies (Krumholz *et al.*, 2012), which agrees well with the low star-formation efficiencies seen in the Arecibo GASS survey (Schiminovich *et al.*, 2010; Fabello *et al.*, 2011). Such low-level star formation has recently been detected in the outer disks of normal green-valley S0 galaxies in HST U imaging (Salim and Rich 2010; Salim *et al.* 2012; Fang et al., in prep).

Hence, we reach a very important conclusion about the evolutionary track of quenching: low gas content is the underlying cause of quenching, but star formation shuts down even faster as gas content falls below the threshold value, owing to the nonlinear relation between cold gas surface density and star formation rate. This fall in star-formation efficiency causes galaxies to redden even faster than expected, propelling them rapidly to the red sequence[15].

---

[15] An interesting corollary comes from the fact that UV colors are more sensitive to weak star formation than optical colors, and thus galaxies can be on the red sequence according to $U-B$ but in the green valley according

It is fair to point out that all of the data cited above to evaluate morphological quenching comes from nearby galaxies, some of which are members of virialized clusters and dense groups that are subject to environmental processes such as ram-pressure stripping or strangulation. However, many of the nearest galaxies are known not to be in clusters (e.g., Oosterloo *et al.*, 2010), and there must also be many field objects amongst the thousand or so galaxies in GASS, yet the trends are the same. In short, we cannot think of any reason why morphological quenching would be the key causative agent for quenching at higher redshift when it does not appear to play that role (even for field galaxies) today.

2.5.5 Critical Halo Mass

The termination of the cold gas supply due to a critical halo mass is commonly referred to as 'halo quenching' (Silk, 1977; Rees and Ostriker, 1977; Blumenthal *et al.*, 1984; Birnboim and Dekel, 2003; Kereš *et al.*, 2005; Dekel and Birnboim, 2006; Cattaneo *et al.*, 2006). Halos below $\sim 10^{12}$ $M_\odot$ are able to accrete gas through cold flows while halos above the threshold mass experience a virial shock that heats the gas. The hot, diluted gas in massive halos is vulnerable to feedback from AGN, which effectively halts star formation. An interesting outcome of this theory is the ability to generate a hot halo atmosphere that allows for AGN 'radio mode' feedback (Croton *et al.*, 2006; Dekel and Birnboim, 2006). This mechanism provides a way to permanently quench a galaxy, which is desirable since the stellar populations of most local ellipticals show no signs of recent star formation (since at least $z \sim 1$; Thomas

---

to $NUV - r$; this is actually seen (e.g., Salim and Rich, 2010; Salim *et al.*, 2012). Since galaxies in this paper are classified using $U - B$, it is possible that some of our red sequence objects would appear in the green valley if near-UV color were used.

et al. 2005), despite continual gas infusion by stars.

Various studies have explored this theory. For example, using a data-driven, halo-abundance matching technique that spans $0 < z < 1$, Conroy and Wechsler (2009) found a gradual transition of galaxy properties – including specific star formation rate – across a halo mass of $\sim 10^{12}$ $M_\odot$. Recently, More *et al.* (2011) inferred the halo mass-stellar mass relation based on kinematics of SDSS satellite galaxies and found that red, central galaxies, on average, occupy more massive halos than blue centrals for fixed luminosity, but show a less appreciable difference for fixed stellar mass. Woo *et al.* (2013) study the quenched fraction of central galaxies as a function of halo mass and find that the span of halo masses between 20% quenched fraction and 60% quenched fraction is a whole 1.5 dex. This agrees well with the width of 0.8 dex seen here in the overlap region using stellar mass (and the same quenched fractions) in Fig. 2.5b and the theoretical scaling law between central and halo mass (Kang *et al.*, 2005; Cattaneo *et al.*, 2006). By contrast, the width using our preferred parameter, inner surface density, is only 0.5 dex (cf. Fig. 5f). An interpretation that emerges from these works is that halo mass has a gradual and probabilistic effect upon galaxy properties, which is therefore very consistent with a wide overlap region in halo mass. Instead of a sharp transition at $\sim 10^{12}$ $M_\odot$, galaxies seem to become ready for star-formation quenching around this critical value, followed by some type of event that ultimately triggers quenching.

This scenario ties in well with our two-stage picture in which galaxies “ripen” along the blue cloud, becoming more and more susceptible to quenching as they age. In §2.5.1, we associated this ripening with decreasing gas content with stellar mass in the blue cloud, which is also seen in our data as an increase in $U-B$ with stellar mass (Fig. 2.5b). Lower gas content means that less gas needs to be removed in quenching, which means in turn that more massive blue cloud galaxies are more vulnerable to quenching. Their lower gas content stems from the fact that their halo masses are closer to the critical value $\sim 10^{12}$ $\mathrm{M}_{\odot}$, the neighborhood where cold accretion shuts down. This basic picture does not change if M_*/r_e (Franx *et al.*, 2008) or central velocity dispersion (Wake *et al.*, 2012a) is substituted for stellar mass – any parameter that tracks halo mass reasonably well can serve as a ripeness indicator.

This logic leads to a picture in which the changes in gas fraction, color, and star formation rate along the blue cloud are caused by the gradual dominance of shock-heated gas over cold streams as galaxies near the critical halo mass. A tougher challenge, though, is to explain why the actual quenching state relates so closely to conditions at the center of the galaxy – why is this link so close if the primary governor of cooling is out in the halo?

We have no firm answer to this but offer some speculations. Evidently the central conditions either signal, or even trigger, a second quenching mechanism and this, plus "natural" halo quenching, is what tips a galaxy over the edge. The obvious candidate for this second process is AGN feedback, but we have stressed that direct evidence for this is still weak. It is good to be cautious since the ERIS Milky Way simulation (Guedes *et al.*, 2011) develops a red bulge and high central stellar density quite naturally through mergers and/or internal disk evolution. Its star formation rate is falling and it seems well on its way to the red sequence, all without benefit of AGN feedback.

Ideal would be some mechanism that both correlates with central density and can switch a halo quickly from cold mode to hot mode. Some possibilities come to mind. Perhaps AGN feedback helps to heat the halo. Perhaps exhaustion of gas at the center enhances the ability of stellar winds to sweep gas out of the galaxy. Finally, perhaps a merger simultaneously builds up central stellar density and triggers a full standing shock. Such a transformation is seen in simulations (Dekel et al., in prep) where a minor merger triggers a shock that expands from the halo center to the virial radius and heats the medium. The larger point is that quenching is probably not just one factor but a combination of factors that build to some critical threshold.

2.5.6 The Relationship Between Color and Star Formation

In this section, we broach the lingering issue of the relationship between color and star formation. Throughout this paper, we have constantly interchanged these two parameters, suggesting that color is a good representation of specific star formation rate. However, the issue of dust has not been thoroughly addressed in our colors. Although we have excluded edge-on galaxies (that are presumably highly affected by dust) and ensured that our red sequence galaxies are truly quiescent (using the UVJ diagram; see §4.3), we have not actually made any dust correction to our rest-frame $U-B$ colors. Therefore, the color trends that we have examined throughout this paper may not exactly translate into star formation trends. The analysis most affected would be our interpretation of how the star formation rates of galaxies behave within the blue cloud. We remarked on the tight trend between color and M_*/r_e (and M_*) within the blue cloud in Figs. 2.5b (and 2.5c) and we proposed that star formation must decrease with M_*/r_e (or M_*). However, this color trend may instead be due to more dust in larger galaxies. If this is the case, then a galaxy's star formation would be independent of M_*/r_e (or M_*) within the blue cloud. However, work using dust-corrected or dust-robust multi-wavelength data (e.g., Noeske *et al.*, 2007; Salim *et al.*, 2007; Schawinski *et al.*, 2007a; Zheng *et al.*, 2007) have shown that specific star formation rate does indeed decrease with increasing stellar mass, which is what we have inferred from our color-mass diagram (Fig. 2.5b). Thus, these works justify our subtle assertion that color is a proxy for star formation. Most importantly though, our lack of dust-corrected $U-B$ colors do not affect our main result that the inner stellar structure of galaxies is most related to quiescence, since our quenching analysis is based on differentiating galaxies on the blue cloud from those on the red sequence, which we have ensured to be unaffected by dust (see §4.3).

2.6 Conclusion

In this paper, we analyze a sample of DEEP2/AEGIS galaxies in the redshift range $0.5 \leq z < 0.8$ using HST/ACS V,I images. Our sample has been run through GIM2D, a bulge+disk decomposition program that gives us information on the subcomponents of intermediate redshift galaxies. Using these data, which we provide at `http://people.ucsc.edu/~echeung1/data.html`, our goal is to address how quenching depends on galactic structure.

Our methodology is to assess the color correlations of several structural parameters – M_*, M_*/r_e, M_*/r_e^2, n, and Σ^*_1kpc – by computing an 'overlap region', which is the band in color-parameter space that encompasses both red and blue galaxies. To quantify overlap regions, we calculate the fractional number of galaxies within the overlap region ΔN/N and the fractional extent of the region Δx/x; the parameter with the smallest overlap region is considered to be the best predictor of quiescence. Finding that no parameter is a perfect predictor of quenching, we explore the overlap region of M_*/r_e for secondary color correlations amongst a variety of other parameters, including those of bulge and disk. We also consider the number of severe outliers from the best predictor of quiescence, n. Our results are the following:

1. The Sérsic index (n) most sharply discriminates between the red sequence and the blue cloud. Eliminating dusty, red sequence contaminants ensures that n targets quiescent galaxies, not merely red ones. Moreover, the color-n diagram resembles a step function, suggesting that n is related to a physical quenching threshold.

2. However, there are exceptions to this general behavior – blue galaxies make up $\approx 40\%$ of our $n > 2.3$ galaxies. Suspecting contamination from starbursts, AGNs, and/or other sources of error, we measured central surface stellar mass densities, which revealed that these outliers do not truly belong with the red sequence – their Σ^*_1kpc are much lower. Central surface density corrects these outliers and hints that it is the inner structure of galaxies that is most related to quiescence.

3. Red sequence bulges are roughly twice as massive as blue cloud bulges at the same galaxy stellar mass (and M_*/r_e), yet also roughly twice as small. This structural difference shows that most blue galaxies at the observed epoch do not simply fade onto the red sequence. Rather, the high values of n and Σ^*_1kpc on the red sequence must reflect a net migration of existing stars toward the center of the system or the formation of new stars at the center. This restructuring either causes quenching itself or is closely related to the process that does.

4. While in the blue cloud before quenching, a galaxy's star formation rate is most closely

correlated with M_*/r_e (or with M_*).

These results suggest that galaxies evolve toward the red sequence in a two-stage process. In stage one, a galaxy is star-forming in the blue cloud at a rate that correlates with global parameters like M_*/r_e (or M_*). Since these in turn reflect halo mass, a broad conclusion might be that star-formation is controlled by the galaxy's halo while stars are still forming. As stellar mass increases, the halo mass also increases, ultimately approaching the critical value $\sim 10^{12}$ $\mathrm{M}_\odot$, where cold flows begin to give way to hot gas, which cannot accrete. The gas content of the galaxy begins to fall as it nears this critical value, and colors redden.

The result of stage one is a galaxy that is increasingly vulnerable as time goes by to the onset of a second quenching process. This second process must be closely associated with bulge-building, and central stellar density, Σ^*_{1kpc}, must increase. AGN feedback is an obvious candidate for this second process, but direct evidence for this is still weak. Also unclear is the exact mechanism that leads to the central mass build-up at the center of the galaxy. We have stressed that galaxies, particularly at high redshift, are far from axially symmetric and that any non-axisymmetry leads inevitably to an exchange of angular momentum and/or loss of energy, which causes some stars and gas to move inward. Major mergers sit at the strong end of this "disturbance continuum", secular evolution processes sit at the other end, and minor mergers, violent disk instabilities, and milder disk instabilities sit in the middle. Given that our galaxies lie at $z \sim 0.65$, where galaxies are still moderately disturbed, it is unlikely that secular evolution plays a major role in them. More likely is some combination of mergers and disk instabilities, which collectively are probably strong enough and frequent enough to do the job. Mergers in particular have several well known advantages: they build bulges at the right stellar mass, they naturally build a concentrated stellar spheroid, they drive a lot of gas quickly to the center that can power an AGN or starburst, and they may be able to quickly switch a marginally cooling halo into hot mode. A problem for major mergers is the large fraction of galaxies in the green valley that are disky, but these might be explained by the other mechanisms or they might be reddened members of the blue cloud.

One conclusion seems clear, and that is that moving into the green valley and thence to the red sequence requires a lowering of fractional cold gas content. This can only be achieved either by expelling gas or by preventing its infall. Exactly how this happens is still not clear, but at least some of the parameters surrounding the process are better known.

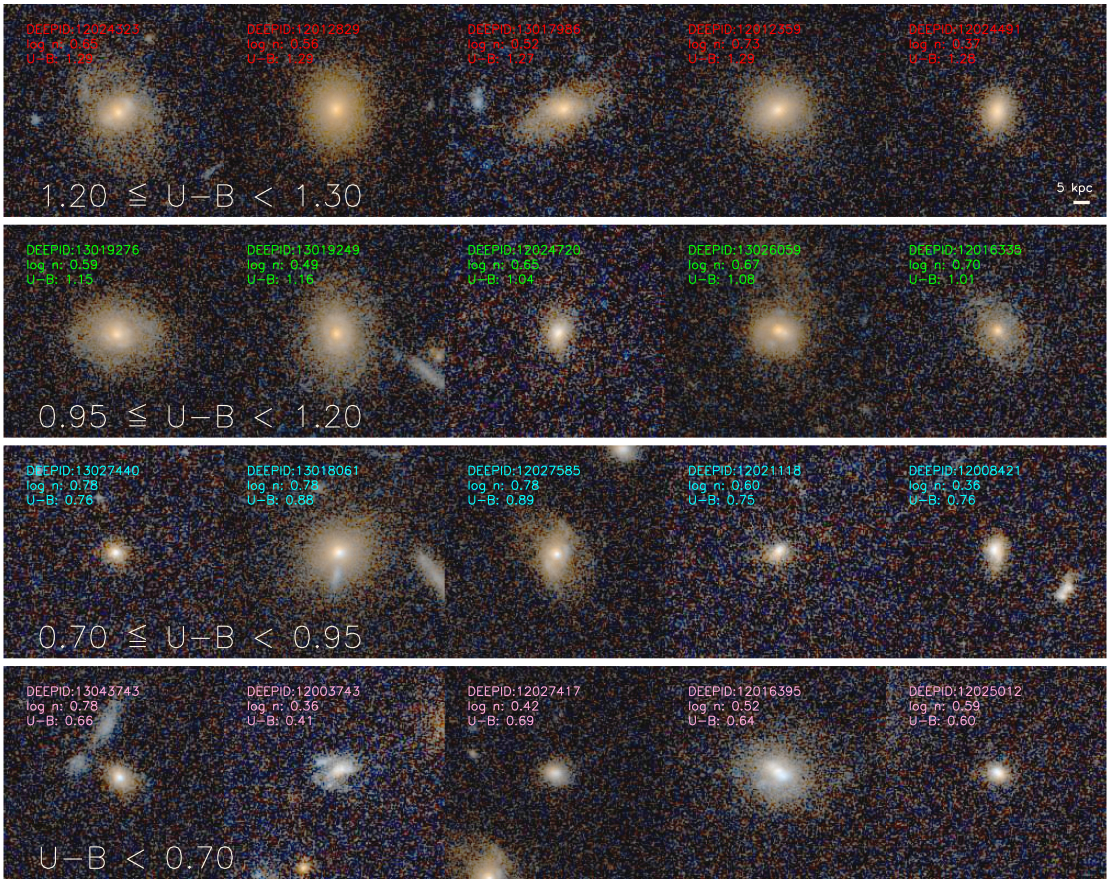

Figure 2.9: HST/ACS V and I color images for a selection of high-n outlier galaxies from Fig. 2.7a. Objects are arranged in rows according to $U-B$ color with bluer galaxies at the bottom. The bottom row corresponds to the pink points in Fig. 2.7a with $U-B < 0.70$; the next row up corresponds to cyan points with $0.70 \leq U-B < 0.95$; and the following row is the green points with $0.95 \leq U-B < 1.20$. The top row contains red sequence galaxies shown for comparison; they are represented by the red points in Fig. 2.7a and have $1.20 \leq U-B < 1.30$. A scale of 5 kpc at the average redshift ($z \approx 0.68$) of our sample is shown as a reference in the upper right picture. Many of these blue high-n objects seem to have Sérsic indices perturbed by small size, irregular structure, central starbursts, and/or AGN and are cured as outliers if inner stellar surface density $\Sigma^{*}_{1\mathrm{kpc}}$ is used instead of n, as shown in Fig. 2.7b.

Chapter 3

Galaxy Zoo: Observing Secular Evolution Through Bars

3.1 Introduction

Stellar bar-shaped structures within galaxies, or more simply ‘bars’, have been known to exist since the days of Edwin Hubble. With only the 100 inch telescope at Mount Wilson, Hubble accurately surmised that bars were abundant in the local universe. So abundant, that he devoted a major part of his classification scheme, the Hubble sequence of galaxies (Hubble, 1936), to barred galaxies. Decades later, infrared and optical studies have confirmed that many galaxies have bars. Indeed, among local disk galaxies, as many as two thirds are barred (e.g., Mulchaey and Regan, 1997; Knapen *et al.*, 2000; Eskridge *et al.*, 2000; Kormendy and Kennicutt, 2004; Menéndez-Delmestre *et al.*, 2007; Sheth *et al.*, 2008).

Bars have an important influence on galaxy evolution. The presence of bars has been linked to the existence of spiral arms, rings (Sanders and Huntley, 1976; Simkin *et al.*, 1980; Schwarz, 1981), and/or disky pseudobulges[16] (Kormendy and Kennicutt, 2004; Athanassoula, 2005). Bars have also been associated with an increase in central star formation (Hawarden *et al.*, 1986; Dressel, 1988; Giuricin *et al.*, 1994; Huang *et al.*, 1996; Martinet and Friedli, 1997; Martin and Friedli, 1997; Ho *et al.*, 1997; Ellison *et al.*, 2011; Oh *et al.*, 2012; Wang *et al.*, 2012), the flattening of galactic chemical abundance gradients (Vila-Costas and Edmunds, 1992; Zaritsky *et al.*, 1994; Martin and Roy, 1994; Williams *et al.*, 2012), and, perhaps, active galactic nuclei (AGN) activity (Noguchi, 1988; Shlosman *et al.*, 1989; Mulchaey and Regan, 1997; Laine *et al.*, 2002; Martini *et al.*, 2003; Laurikainen *et al.*, 2004; Jogee, 2006; Hao *et al.*, 2009; Oh *et al.*, 2012).

Given that bars have an important influence on galaxy evolution, two natural questions are “how do bars form and evolve?” and “how do they affect their host galaxies?” A review of the theoretical work on bars is given by Athanassoula (2013), so we will only summarize here the parts that are most relevant to this work (see also Sellwood and Wilkinson, 1993; Sellwood, 2014). Many past theoretical works have shown that bars can redistribute the angular momentum of the baryons and dark matter of a galaxy (e.g., Sellwood, 1980; Debattista and Sellwood, 2000; Holley-Bockelmann *et al.*, 2005). The angular momentum is emitted mainly by stars at (near-)resonance in the bar region and absorbed mainly by (near-)resonant material in the spheroid (i.e., the halo and, whenever relevant, the bulge) and in the outer disk (Lynden-Bell and Kalnajs, 1972; Tremaine and Weinberg, 1984; Athanassoula, 2003, hereafter A03).

A03 showed that the redistribution of angular momentum is not merely a side-effect

---

[16] Bulges created through secular evolution have been called both “pseudobulges” and/or “disky bulges". For completeness, we will use the term “disky pseudobulges" throughout to represent such bulges in galaxies.

of bars, but is, instead, a process that is closely coupled to the evolution of bars. Specifically, the exchange of angular momentum from the inner disk to the outer disk and/or spheroid (bulge/halo) is the main driver of bar evolution. The efficiency of the angular momentum exchange is primarily dependent upon the mass distribution and velocity dispersion of the disk and spheroid. More angular momentum can be redistributed if the spheroid mass density at the location of the resonances is high, leading to stronger bars (A03). The second factor governing the efficiency of angular momentum exchange is the velocity dispersion. In lower velocity dispersion (lower temperature) disks and spheroids, resonances can emit or absorb more angular momentum than in cases with high velocity dispersion, thereby making the transfer of angular momentum more efficient (A03; Sheth *et al.* 2012).

This redistribution of angular momentum allows bars to drive gas, and to a lesser extent, stars, to the centers of galaxies (Matsuda and Nelson, 1977; Simkin *et al.*, 1980; Athanassoula, 1992; Wada and Habe, 1992a, 1995; Friedli and Benz, 1993; Heller and Shlosman, 1994; Knapen *et al.*, 1995; Sakamoto *et al.*, 1999; Sheth *et al.*, 2005). This process is responsible for the increase of bar length and strength and of the disk scale length (e.g., Hohl 1971, , Debattista and Sellwood 2000, A03, O'Neill and Dubinski 2003, Valenzuela and Klypin 2003, Debattista *et al.* 2006, Martinez-Valpuesta *et al.* 2006, Minchev *et al.* 2011), the formation of a disky pseudobulge (Kormendy and Kennicutt, 2004; Athanassoula, 2005), the increase of central star formation (Friedli and Benz, 1993; Martinet and Friedli, 1997; Martin and Friedli, 1997), and the dilution of abundance gradients (Friedli *et al.*, 1994; Friedli and Benz, 1995; Martel *et al.*, 2013). This process is known as secular evolution (Kormendy and Kennicutt, 2004; Kormendy, 2013).

It has been shown that bar formation and evolution is also dependent on the gas content in the galaxy (e.g., Shlosman and Noguchi, 1993; Berentzen *et al.*, 1998, 2007; Villa-Vargas *et al.*, 2010). More recent simulations – with a multi-phase description of the gas, including star formation, feedback and cooling, and a sufficiently large number of particles to describe adequately the gas flow – have shown that bars form later in simulations with a larger gas fraction (Athanassoula *et al.*, 2013, hereafter AMR13).

Recent observational works have begun to test many of these predictions. For example, Masters *et al.* (2011) used classifications from Galaxy Zoo 2 (see §3.2.2), to show that the fraction of disk galaxies that possess a bar (bar fraction) increases in redder disk galaxies (see also Skibba *et al.*, 2012). This result was confirmed by Lee *et al.* (2012a), who also used a large sample of galaxies from the Sloan Digital Sky Survey (SDSS), but with their own classifications (combining a mix of visual and automated methods). Assuming that galaxy color is closely related to galactic gas content (e.g., Catinella *et al.*, 2010; Saintonge *et al.*, 2011), then this is consistent with the expected effects of gas on bar formation and evolution. Indeed, using a sample of Galaxy Zoo 2 bars with HI measurements from the ALFALFA survey, Masters *et al.* (2012) found that bar fraction correlates strongly with HI content. In that sample, more bars were found in the gas poor disk galaxies, even at fixed color or stellar mass.

Alternatively, Barazza *et al.* (2008) and Aguerri *et al.* (2009) found different results using samples of SDSS galaxies with bars identified from ellipse fitting methods. Both of these works found that bar fractions were larger for the bluer (and presumably more gas rich) galaxies in their samples. However, Nair and Abraham (2010a,b) suggest a way to reconcile these results which came from samples of disk galaxies with very different selections; notably Barazza *et al.*

2008 and Aguerri *et al.* 2009 selected only blue galaxies as disks, and included lower redshift and less massive galaxies than were present in Masters *et al.* 2011, Masters *et al.* 2012, or Lee *et al.* 2012a. The sample of Nair and Abraham (2010a), which probed a wide range of stellar mass, suggested that bar fraction is bimodal with disk galaxy color – having peaks both towards the bluer and redder disk galaxies[17]. Nair and Abraham (2010a) suggest this trend may reveal two distinct types of bars, namely weak bars are predominantly found in lower mass and more gas rich (and bluer) spirals, while stronger bars are more common in massive, redder and gas poor disks.

In addition to the dependence on galaxy color, bar fraction has also been found to depend on inner galactic structure. Masters *et al.* (2011) found that bar fraction was correlated with fracDeV, which is a parameter measured by the SDSS representing the fraction of the best-fit light profile that originates from the de Vaucouleurs fit to the profile, as opposed to an exponential fit. Lee *et al.* (2012a) also found that the bar fraction was highest at moderate central velocity dispersion. However, Barazza *et al.* (2008) found that barred galaxies are most likely to exist in galaxies with low Sérsic indices while Aguerri *et al.* (2009) found that bars are most likely to exist in galaxies with low concentration indices. Although these results appear conflicting, they all show that the presence of a galactic bar is influencing the inner structure of these galaxies.

While the trends of bar fraction can reveal aspects of bar formation and evolution, bar fraction is crude as it hides information on the bar itself. According to A03, the characteristics of a bar (e.g., long or short) can be used as tracers of bar evolution. Therefore, a common bar

---

[17] Masters *et al.* 2011 also commented on a possible upturn in bar fraction for the bluest galaxies in their sample

property that has been studied in the literature is bar length. Athanassoula and Misiriotis (2002) and A03 predicted that the presence of a bulge will result in a longer and more evolved bar. Comparing this prediction to previous observational works shows a good consensus; early-type disk galaxies do indeed have longer bars (Kormendy, 1979; Athanassoula and Martinet, 1980; Martin, 1995; Elmegreen and Elmegreen, 1985; Regan and Elmegreen, 1997). Larger samples and/or infra-red imaging continues this agreement (Laurikainen *et al.*, 2002; Erwin, 2005; Laurikainen *et al.*, 2007; Menéndez-Delmestre *et al.*, 2007; Elmegreen *et al.*, 2007; Aguerri *et al.*, 2009; Gadotti, 2011; Hoyle *et al.*, 2011).

In this paper, we use the Galaxy Zoo 2 dataset (Masters *et al.*, 2011; Hoyle *et al.*, 2011; Willett *et al.*, 2013) to investigate how the likelihood of a galaxy hosting a galactic bar depends on two important factors, namely the gas content of the galaxy and its inner galactic structure. We perform the same investigation with bar length and compare both of these sets of relationships to theoretical predictions, which will not only give us a better understanding of bar formation and evolution, but also a better understanding of how bars affect their host galaxy.

We begin in §2 by describing all the data used in the paper, while the main observational results are presented in §3. We compare our results with several theoretical simulations in §4 and discuss our work, and these comparisons, in §5. We conclude in §6. In Appendix A, we discuss the completeness of our sample. We assume a cosmological model with $H_0 = 70$ km s^{-1} Mpc^{-1}, $\Omega_m = 0.30$ and $\Omega_\Lambda = 0.70$ throughout this paper.

Table 3.1: Sample Selection

Criterion	GZ2D #	BL #
Galaxy Zoo 2*	295,305	3,150
$0.01 < z < 0.06$**	76,336	2,674
$M_r < -20.15$	43,266	2,177
$b/a > 0.5$	28,540	1,753
$\frac{1}{4}$ answers bar question	14,353	1,753
$p_{mg} < 0.4$	14,038	1,734
GIM2D models < $1\farcs0$ offset	13,328	1,655
Quality GIM2D disks	13,328	1,159
MPA cross-match	13,295	1,154

Note. — *See footnote 17. **We only consider galaxies with spectroscopic redshifts.

3.2 Data

This section lists all sources of data that this paper uses. In order to have a fully complementary dataset, we cross-matched every dataset, as described in each subsection, resulting in a successive reduction of the initial sample size. As a guide, our initial dataset is described in §3.2.2, which derives from SDSS DR7 (summarized in §3.2.1). We list the sample totals at the end of each subsection, starting with §3.2.2. Table 3.1 lists every major cut made to our two samples, and the resultant sample sizes.

3.2.1 SDSS

All the galaxies used in our sample are drawn from the Main Galaxy Sample in the Legacy area of the SDSS Data Release Seven (SDSS DR7; Strauss *et al.* 2002; Abazajian *et al.* 2009). Where possible, we use the standard photometric and structural parameters provided by the SDSS pipeline. For example, we use the SDSS information to define a surface stellar mass density within a radius of one kiloparsec of the center of the galaxy, $\Sigma^*_{1\ \mathrm{kpc}}$. We choose one kpc for this density as it matches the typical scale of bulges (Fisher and Drory, 2010) and therefore, should be closely related to the bulges of most galaxies.

In detail, $\Sigma^*_{1\ \mathrm{kpc}}$ is created from the SDSS galaxy surface brightness profiles, `profMean`, which is the mean surface brightness in a series of circular annulii, from the `PhotoProfile` table in the `CasJobs` website[18]. In accordance with the SDSS recommendations[19], we take the inverse hyperbolic sine of each cumulative profile and fit them with a natural cubic spline. After transforming the spline fits back with a sine function, we differentiate the fits and obtain an estimate of the azimuthally averaged surface brightness profile. Finally, we compute the magnitude and color within one kpc for each galaxy from these profiles and convert them into a stellar mass through a color-dependent mass-to-light (M_*/L_g) ratio (e.g., Bell and de Jong, 2001). Our M_*/L_g relationship is derived from a linear fit to the rest-frame $g-r$ color from GIM2D (see §3.2.3) and the M_*/L_g, where the stellar masses are taken from the MPA-JHU catalog (see §3.2.4) and the g-band luminosity is taken from GIM2D models.

One concern is that the one kpc radius aperture is smaller than the typical seeing of SDSS. However, an analysis of angular sizes of galaxies in our sample, which lies within the redshift range $0.01 < z < 0.06$ (see §3.2.2), shows they are typically larger than the full width at half maximum (FWHM) of the SDSS point–spread function ($\sim 1\overset{\prime\prime}{.}3$ in the r-band; Abazajian *et al.* 2009).

---

[18] http://casjobs.sdss.org/CasJobs/

[19] http://www.sdss.org/dr7/algorithms/photometry.html

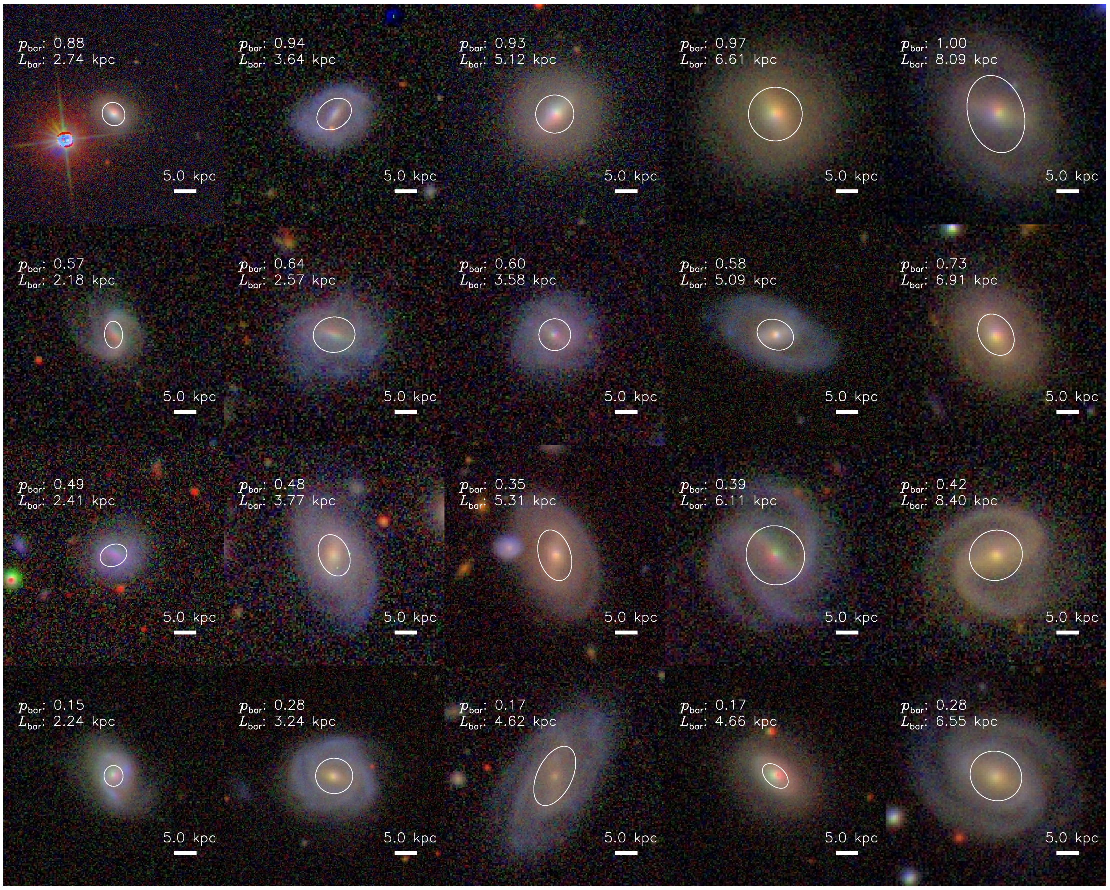

Figure 3.1: A gallery of galaxies with a range of bar likelihood, $p_{\rm bar}$, and bar length, $L_{\rm bar}$. Each row is ordered by increasing bar length. The ellipse drawn over each galaxy represents the GIM2D disk model at $r_{\rm d}$. Visually, the bars generally extend out the disk scale length, consistent with Combes and Elmegreen (1993). The physical scales of every image are the same (± 1 pixel).

3.2.2 Galaxy Zoo

Galaxy Zoo is a citizen science project that enlisted hundreds of thousands of volunteer "citizen scientists" to make morphological classifications of nearly one million galaxies (Lintott *et al.*, 2008, 2011). The initial Galaxy Zoo project asked the public to classify galaxies as elliptical, spiral, or merger. With the Galaxy Zoo 2 project (Willett *et al.*, 2013), the citizen scientists were asked to make more detailed classifications of approximately 304,000 galaxies.

The final product of Galaxy Zoo 2 is a table of morphological likelihoods, including the likelihood that a bar is present in each galaxy, as represented by $p_{\rm bar}$, e.g., if 5 out of 10 scientists classified a galaxy as having a bar, the galaxy would be assigned a bar probability of $p_{\rm bar} = 0.5$. These raw probabilities are then adjusted to account for the reliability of each user through an iterative weighting scheme that "down-weights" classifications from unreliable users (typically a few percent of the population). We also apply a correction to the likelihoods to account for the deterioration of the image quality due to increasing distance of galaxies, i.e., we assume galaxies of a similar luminosity and size will share the same average mix of morphologies regardless of redshifts. This also assumes there is no significant evolution within the SDSS at these low redshifts, which is probably reasonable (Bamford *et al.*, 2009; Willett *et al.*, 2013). Therefore, throughout the paper, we will only use these corrected, or "debiased", bar likelihoods and will calling them $p_{\rm bar}$ for convenience.

In Masters *et al.* (2011) and Masters *et al.* (2012), barred galaxies were selected using $p_{\rm bar} \geq 0.5$. This threshold delivered a high purity of barred galaxies in comparison with other barred galaxies sample, e.g., almost all galaxies with $p_{\rm bar} \geq 0.5$ were classified as possessing a strong bar by Nair and Abraham (2010a) (see Appendix A of Masters *et al.*, 2012). Weaker bars in Nair and Abraham (2010a) were found to correspond to $0.3 \leq p_{\rm bar} \leq 0.5$ (Masters *et al.*, 2012; Willett *et al.*, 2013).

In this work, we choose to use $p_{\rm bar}$ as a bar likelihood, rather than as a bar threshold. This method has been used before with Galaxy Zoo classifications (e.g., Bamford *et al.*, 2009; Skibba *et al.*, 2009, 2012). Our results are in qualitative agreement with other GZ results who used bar fractions, e.g., if we adopt a bar threshold of $p_{\rm bar} = 0.5$, we find an overall bar fraction of $23.6 \pm 0.4\%$, which is similar to Masters *et al.* (2011)[20].

Our initial sample is the Galaxy Zoo 2 dataset[21]. Following Masters *et al.* (2011), we only select galaxies with spectroscopic redshifts in the range of $0.01 < z < 0.06$. In order to have a volume-limited sample, we only include galaxies with $M_r < -20.15$, where M_r is the rest-frame absolute Petrosian r-band magnitude. This limit corresponds to the Galaxy Zoo 2 completeness Petrosian magnitude of 17 in the r-band (Willett *et al.*, 2013) at $z = 0.06$. To ensure that our sample contains relatively face-on galaxies, we applied an axis ratio requirement of $b/a > 0.5$ (this corresponds to inclination angles less than ≈ 60 degrees), where b/a is the axis ratio from the GIM2D single Sérsic model fit (see §3.2.3). This requirement minimizes projection effects and thus results in more reliable bar classifications. This sample also requires that all galaxies have a `Petro90` radius of $> 3\farcs00$. We have tested our results with a larger minimum radius requirement and find that our results are unchanged[22].

We also require that for each galaxy, at least a quarter of all its classifications involved answering the bar question, 'Is there a sign of a bar feature...' (Masters *et al.*, 2011). In order to reach the bar question, however, a user must first classify a galaxy as a non-edge-on galaxy with a disk or some sort of feature (e.g., spiral arms, rings, bars). Assuming that most identified features are associated with a disk, then this last selection effectively ensures we have non-edge-on disk galaxies.

---

[20] The difference between our bar fraction and that of Masters *et al.* (2011) is due to the use of the weighted and debiased bar fractions from Willett *et al.* (2013) which were unavailable at the time of Masters *et al.* (2011).

[21] This Galaxy Zoo 2 sample is comprised of the 'original', 'extra', and 'stripe82' sample in Table 1 of Willett *et al.* (2013). These data are available at http://data.galaxyzoo.org

[22] We find that our results are unchanged when we restrict our sample to galaxies with global half-light radii (as measured by GIM2D) larger than $5\farcs.0$.

Finally, we discard all merging galaxies from the sample since we are only concerned with isolated galaxies that have reliable photometric and structural measurements. According to Darg *et al.* (2010), the Galaxy Zoo merging parameter, p_{mg}, can identify merging galaxies with a cut of $p_{\mathrm{mg}} > 0.4$; we adopt this threshold to eliminate merging galaxies. There is a total of 14,038 galaxies in the resulting sample, which we will call the Galaxy Zoo 2 Disk (GZ2D) sample.

We carefully review here the make-up of our sample to avoid confusion with comparisons with other disk, spiral or late-type selections based on GZ morphologies. The disk galaxy selection presented herein possibly includes a fraction of very early-type disks galaxies (Sa or S0) which would normally be included in a majority of early-type samples selected either by color, or central concentration. This results in our diverse disk galaxy sample showing bimodality in their optical color-mass diagram (Fig. 3.3a). However, other Galaxy Zoo samples, that are more focused on late-type disks or spirals sample (Sb, Sc or later) can be constructed using the GZ1 "clean" spiral criterion as first discussed in Land *et al.* (2008), and most recently used in Schawinski et al. (2013, in preparation), but also through stricter limits in GZ2/GZ Hubble data. This more conservative late-type sample will be more dominated by "blue cloud" spirals and thus show less bimodality of their galaxy properties.

In addition to this sample, we use a Galaxy Zoo 2 subsample that possesses additional bar length measurements. The bar lengths were visually measured by citizen scientists using a Google Maps interface described by Hoyle *et al.* (2011). The bar lengths represent the lengths from one end to the bars to the other. In order to be consistent with previous works, who define it as the semi-major axis of maximum ellipticity in the bar region (e.g., Erwin, 2005), we will take half of the Galaxy Zoo 2 bar lengths and denote it L_{bar}. This catalog requires at least 3 independent bar length measurements per galaxy; the mean of these independent bar length measurements gives L_{bar} of each galaxy. The vast majority of galaxies that were selected for this sample have $p_{\text{bar}} \geq 0.6$, i.e., this sample contains mainly strong bars (Masters *et al.*, 2012; Willett *et al.*, 2013). Of the GZ2D sample, there are 1,734 galaxies that have bar length measurements, which will now be referred to as the Bar Length (BL) sample.

We present a gallery of barred galaxies with a range of p_{bar} and L_{bar} in Fig. 3.1. Each row is ordered by absolute bar length.

3.2.3 GIM2D

Two-dimensional bulge+disk decompositions in the g and r bandpasses of over a million SDSS galaxies were performed with GIM2D by Simard *et al.* (2011). Improvements to the sky background determinations and object deblending over the standard SDSS procedures led to more robust galactic structural parameters than those offered by the standard SDSS pipeline.

Three different models were used in these decompositions: a pure Sérsic model, an $n = 4$ bulge + exponential disk model, and a Sérsic (free-floating n) bulge + exponential disk model. The most important GIM2D parameter for the GZ2D sample is the galaxy Sérsic index, n, from the pure Sérsic model, i.e., the best-fitting single Sérsic index for a given galaxy. The Sérsic index has often been used to separate early-type and late-type galaxies and is widely regarded as a good proxy for bulge dominance (Blanton *et al.*, 2003; Shen *et al.*, 2003; Bell *et al.*, 2004a; Schiminovich *et al.*, 2007; Drory and Fisher, 2007; Bell, 2008; Wuyts *et al.*, 2011; Bell *et al.*, 2012; Wake *et al.*, 2012b; Cheung *et al.*, 2012).

Although a similar parameter, fracDeV from the SDSS database, has been explored by previous works (e.g., Masters *et al.*, 2011; Skibba *et al.*, 2012), n is a more common parameter in the literature and has been thoroughly studied (e.g., Graham and Driver, 2005). It is also the basis of most galaxy fitting programs (e.g., GALFIT, BUDDA, and GIM2D; Peng *et al.* 2002; de Souza *et al.* 2004; Simard *et al.* 2002), which allows for easier and more consistent comparisons to other works. For reference, we compare n and fracDeV in Fig. 3.2 for our GZ2D sample. Clearly, the two parameters are correlated. However, the overdensity of galaxies at fracDeV=1, which accounts for $\sim 15\%$ of the GZ2D sample, indicates that there is a saturation of galaxy structural information in the fracDeV parameter. Indeed, for fracDeV=1, log n ranges from 0.5 to 0.9, corresponding to $n \sim 3-8$. A similar effect occurs at fracDeV=0, which accounts for another $\sim 12\%$ of the GZ2D sample. Our use of Sérsic index in this paper should be more sensitive than fracDeV to the complicated structures of galaxies.

Another similar parameter is the Petrosian concentration index from SDSS. This parameter has been shown by Gadotti (2009) to be a better proxy for bulge fraction than the global Sérsic index. We would like to note, however, that the global Sérsic indices that Gadotti (2009) used were from the New York University Value-Added Galaxy Catalog (Blanton *et al.*, 2005a,b), which fitted one-dimensional profiles extracted from two-dimensional images using circular annuli. The GIM2D fits were done using elliptical annuli, and are two-dimensional fits. As noted by Simard *et al.* (2011), this difference in methodology, i.e., using circular and elliptical apertures, results in a systematic offset between the NYU and GIM2D galaxy half-light radius and galaxy Sérsic index. At the request of the referee, we tested our results using R90/R50 in Appendix B.2 – we find no major impacts to our conclusions.

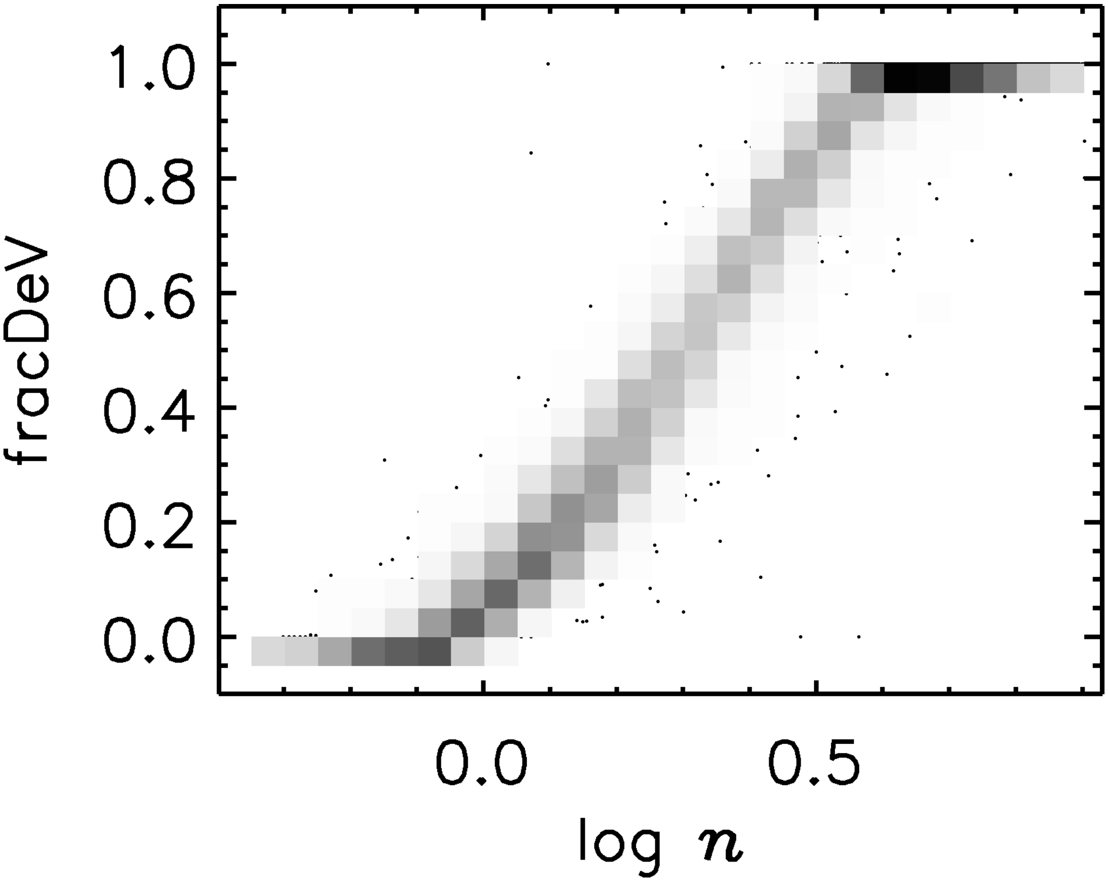

Figure 3.2:]
Comparison of n from the GIM2D single Sérsic model fit and fracDeV (r band) from the SDSS database. The cluster of galaxies at fracDeV=1 and fracDeV=0 accounts for $\sim$ 27% of the total GZ2D sample, indicating that there a loss of galaxy structural information in the fracDeV parameter.

The most important GIM2D parameter for the BL sample is the semi-major axis exponential disk scale length, $r_{\rm d}$; this is needed to properly scale the bar length. The disk scale length is available in both the $n = 4$ bulge + exponential disk model and the Sérsic bulge + exponential disk model; we use the latter model[23]. As is noted in Simard *et al.* (2011), the quality of the GIM2D bulge+disk decompositions is highly dependent on the spatial resolution and signal-

---

[23] We find no change in our main conclusions if we use the $n = 4$ bulge + exponential disk model.

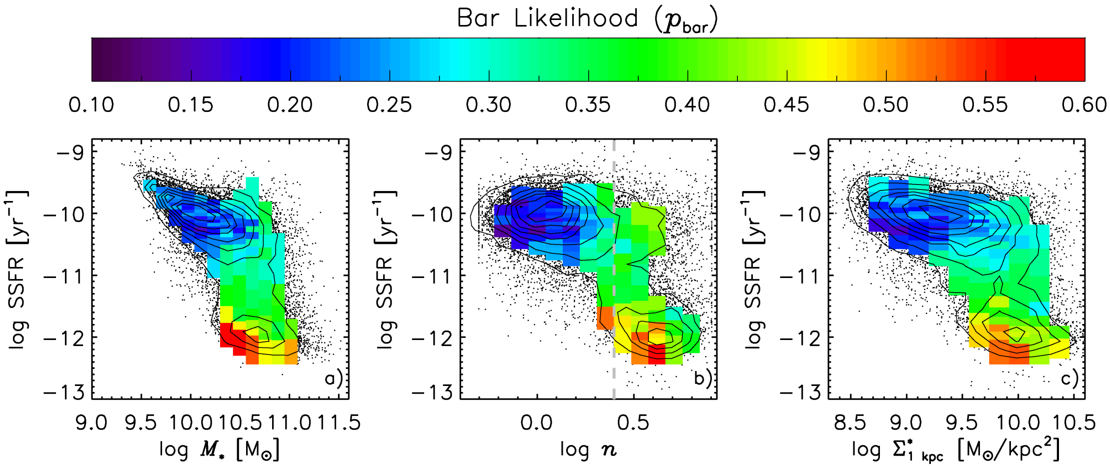

Figure 3.3:]
Average bar likelihood, p_{bar}, in bins of: *a)* SSFR vs. stellar mass M_*, *b)* SSFR vs. Sérsic index n, *c)* SSFR vs. central surface stellar mass density $\Sigma^*_{1\ \mathrm{kpc}}$. Each bin is adjusted so that it contains ~ 100 galaxies (individual points are shown for poorly populated bins). Bin colors indicate the average value of p_{bar} in the bin (see color bar at top), while the contours show the density of points. The gray dashed vertical line in panel b represents the division between galaxies containing disky pseudobulges ($n < 2.5$) and classical bulges ($n > 2.5$; see Drory and Fisher 2007). This plot shows that the trends of bar likelihood with galaxy properties depend on the SSFR of the galaxies. The relationship of p_{bar} with n and $\Sigma^*_{1\ \mathrm{kpc}}$ is bimodal with SSFR.

to-noise of the SDSS images. Therefore, it is important to ensure that we only allow model fits that are reliable. However, since we are only concerned with r_{d}, picking out reliable decompositions is not difficult. From Simard (priv. comm.), galaxy models with $B/T \leq 0.5$ (the B/T from the Sérsic bulge + exponential disk model) accurately model the disk component, and hence we consider all these galaxies. This is understandable since these galaxies are disk-dominated and their corresponding GIM2D models will likely yield reliable disk measurements. For models with $B/T > 0.5$, Simard (priv. comm.) recommends considering only galaxies with $P_{pS} < 0.32$, where P_{pS} represents the probability that a bulge+disk model is *not* required compared to a pure Sérsic model (Simard *et al.*, 2011). Thus $B/T > 0.5$ galaxies that have a high probability of requiring a bulge+disk model are also considered.

To avoid the effects of the SDSS point-spread function on the GIM2D disk model, we only allow disk models with $r_d > 2''.0$. Furthermore, we impose a strict face-on requirement such that all GIM2D model disks have inclination angles of less than 55 degrees. This corresponds to axis ratios greater than 0.6, a parameter space that has been shown by MacArthur *et al.* (2003) to produce no systematic variations on r_d when using 2D galaxy decompositions. Finally, we require that the fractional errors on r_d ($r_\mathrm{d,error}/r_\mathrm{d}$, where $r_\mathrm{d,error}$ is the formal error of r_d from GIM2D) be less than 2%. This number is approximately two standard deviations above the average $r_\mathrm{d,error}/r_\mathrm{d}$ of the BL sample. We choose this conservative cut in order to include only quality disk models.

We note that, although we only model a bulge and disk for these disk galaxies, $\sim 24\%$ of which are strongly barred, previous works have shown that, while bulge parameters may be affected by the presence of a bar, the disk scale length is not significantly affected (Erwin, 2005; Laurikainen *et al.*, 2005). This reliability is evident in the fact that our results are not sensitive to the choice of GIM2D bulge+disk model, i.e., both r_d from the $n = 4$ bulge+disk model and the Sérsic bulge+disk model produce the same results. Furthermore, the GIM2D formal errors on r_d are not significantly different from strongly barred systems ($p_\mathrm{bar} > 0.8$) and non-barred systems ($p_\mathrm{bar} < 0.05$).

We impose a final cut that eliminates all GIM2D models where the centers are offset from the input science images by more than one arscecond. Large offsets like these usually represent a bad fit, and, indeed, upon visual inspection, we find that almost all these cases contained bright point sources within the galaxy and/or diffraction spikes from nearby stars. Matching the GZ2D and BL samples to the GIM2D catalogs leave us with 13,328 and 1,159 disk galaxies, respectively.

3.2.4 MPA-JHU

Stellar masses and star formation rates are taken from the MPA-JHU DR7 release[24]. Stellar mass (M_*) estimates are calculated using the Bayesian methodology and model grids described in Kauffmann *et al.* (2003b). The models are fit to the broadband *ugriz* SDSS photometry, instead of the spectral indices from the $3''.0$ fiber aperture. These estimates are corrected for nebular emission and a Kroupa (2001) initial mass function is assumed.

Star formation rates (SFR) are based on the technique presented in Brinchmann *et al.* (2004). For their 'Star-Forming' class, which consists of 39,141 galaxies, they estimate the SFR from model fits that cover a wide range of star formation histories of several emission lines from the SDSS fiber. For 'Low S/N Star-Forming' class, which contains 29,115 galaxies, they convert the observed Hα luminosity into a SFR. And for the 'AGN', 'Composite' and 'Unclassifiable' classes, which contain a total of 66,986 galaxies, they use the D4000 value to estimate SFR/M_* and SFR. Aperture corrections follow the method of Salim *et al.* (2007), resulting in the SFR of the entire galaxy. The specific star formation rate (SSFR), a parameter that will be used throughout the paper, is defined to be the SFR divided by stellar mass; it was calculated by combining the SFR and M_* likelihood distributions as outlined in Appendix A of Brinchmann *et al.* (2004).

Matching the GZ2D and BL samples to the MPA-JHU catalog brings our final sample to 13,295 and 1,154, respectively. A detailed discussion of the completeness of the GZ2D and

---

[24] http://www.mpa-garching.mpg.de/SDSS/DR7/

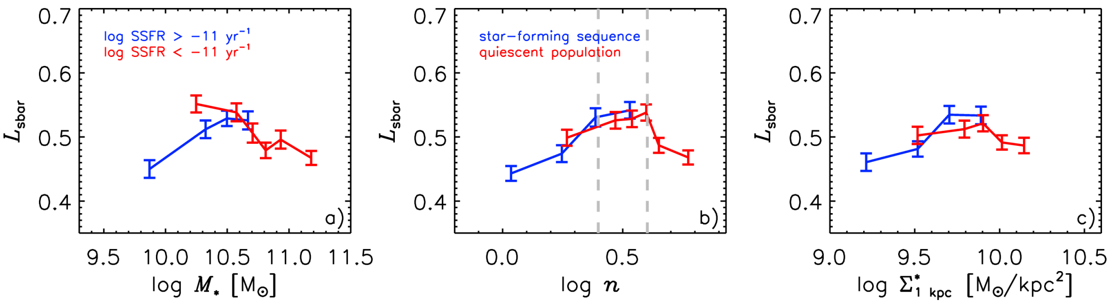

Figure 3.4: Average $L_{\rm sbar}$ plotted against: *a)* M_*, *b)* n, and *c)* $\Sigma^*_{1\ \rm kpc}$. Galaxies were split by their star formation state, namely, log SSFR > -11 yr^{-1} (star-forming; blue) and log SSFR < -11 yr^{-1} (quiescent; red). Each bin contains $\sim$ 100 galaxies. The error bars are given by $\sigma/\sqrt{N}$, where σ is the standard deviation of $L_{\rm sbar}$ per bin, and N is the total number of galaxies per bin. The vertical dashed lines in panel b are located at log $n = 0.4$ ($n = 2.5$) and log $n = 0.6$ ($n = 4$).

BL samples is presented in Appendix B. We find that while we are missing some low-mass quiescent disk galaxies, the effect is small and does not affect our results.

3.3 Results

3.3.1 Bar Likelihood Trends

In this section, we present the trends of bar likelihood with SSFR, stellar mass, and measures of bulge prominence.

The three panels of Fig. 3.3 plot both galaxy density and average $p_{\rm bar}$ in a 2D plane of: SSFR versus stellar mass (M_*; panel a), SSFR versus global Sérsic index (n; panel b), and SSFR versus central surface stellar mass density ($\Sigma^*_{1\ \rm kpc}$; panel c). The locations of the galaxies are shown by the contours. Bin sizes are adjusted so that they contain $\sim$ 100 galaxies each, and individual data points are shown for poorly populated bins. Each bin is colored by the average $p_{\rm bar}$ of the galaxies in it as indicated by the color bar.

The well-known bimodality between galaxies (even for disk galaxies) in the star-forming sequence and those in the quiescent population is clear in our sample and affects not only the galaxies' SSFR, baryonic mass, and bulge properties, but also their likelihood of being barred (Masters *et al.*, 2011). We find that there is a strong correlation between average p_{bar} and SSFR such that the average values of p_{bar} are larger for low SSFR disk galaxies (i.e., quiescent disk galaxies are more likely to host bars). The observed relationship between p_{bar} and SSFR is present even at fixed M_*, n, or $\Sigma^*_{1\ \mathrm{kpc}}$ (Fig. 3.3), indicating that this relationship is nearly independent of these galaxy properties.

Taking SSFR as a proxy for gas fraction (e.g., Kauffmann *et al.*, 2012) suggests that the underlying relationship is really between p_{bar} and gas content such that bar likelihood is increasing as gas fraction decreases. Similar trends between bar fraction and gas content were also observed by Masters *et al.* (2012).

We observe that the trends of the average bar likelihood with M_*, n, and $\Sigma^*_{1\ \mathrm{kpc}}$ depend on whether the disk galaxy is star-forming or quiescent, as is illustrated by Fig. 3.3. Thus we look in more detail at the observed trends within the star-forming ($\log\ \mathrm{SSFR} > -11\ \mathrm{yr}^{-1}$) and quiescent ($\log\ \mathrm{SSFR} < -11\ \mathrm{yr}^{-1}$) disk galaxy populations. We find:

- **Stellar Mass, M_* (Fig. 3.3a)** – There is a correlation between average p_{bar} and stellar mass within the star-forming disks such that p_{bar} is larger the larger their stellar mass. There is also an anti-correlation of p_{bar} with stellar mass within the quiescent population.

- **Sérsic Index, n (Fig. 3.3b)** – For the star-forming sequence, p_{bar} is strongly correlated with n (even more so than it is with M_*). Within the quiescent population, we see an inverse correlation between $p_{\rm bar}$ and n. This is an important point to note and might explain the contradictions between the results of previous studies, which found opposite trends of bar fraction with measures of bulge prominence from light profile shape (e.g., Masters *et al.* 2011 compared to Barazza *et al.* 2008). Moreover, this observation is in good agreement with theoretical predictions of bar formation as will be described in §3.4.

- **Central surface stellar mass density, $\Sigma^*_{1\ \rm kpc}$ (Fig. 3.3c)** – We find similar trends of $p_{\rm bar}$ with this parameter as between $p_{\rm bar}$ and n. Star-forming galaxies show a correlation between $p_{\rm bar}$ and $\Sigma^*_{1\ \rm kpc}$ (star-forming disks are more likely to host bars where the central density is higher), while quiescent galaxies show an anti-correlation (quiescent disks are more likely to host bars where the central density is lower)

3.3.2 Bar Length Trends

In this section we examine how bar length depends on galaxy properties. We define a scaled bar length, $L_{\rm sbar}$, as the bar length divided by a measure of disk size. We choose for this $2.2r_{\rm d}$ (2.2 semi-major axis exponential disk scale lengths) because this is where the rotation curve of a self-gravitating exponential disk reaches its maximum (Freeman, 1970). Hereafter, we will refer to the scaled bar length simply as the bar length unless stated otherwise.

Bars become longer over time as they transfer angular momentum from the bar to the outer disk and/or spheroid (halo and, whenever relevant, bulge). This secular evolution causes the host disk to expand and increase its scale length while the bar also grows. We will compare trends of bar length with those of $p_{\rm bar}$ to test if the trends we observe in the average value of $p_{\rm bar}$ in the galaxy population are due to the evolution of the bars, or the likelihood of bar formation in a galaxy.

Since the BL sample is more than an order of magnitude less numerous than the GZ2D sample, we find that breaking it up into small bins, as we did in Fig. 3.3 for $p_{\rm bar}$ results in no clear correlations. Since we found that the trends of $p_{\rm bar}$ had different properties depending on the SSFR of the galaxies, we split the BL sample into two subsamples (star-forming, or $\log\ {\rm SSFR} > -11\ {\rm yr}^{-1}$, and quiescent, or $\log\ {\rm SSFR} < -11\ {\rm yr}^{-1}$) to look at the trends of average $L_{\rm sbar}$. These trends are shown in Fig. 3.4.

This figure shows that in the star-forming sequence, the average value of $L_{\rm sbar}$ increases with all three properties (M_*, n, and $\Sigma^*_{1\ {\rm kpc}}$). In the quiescent population we find that the average bar length decreases with M_*. Curiously we find that the average bar length increases with n and $\Sigma^*_{1\ {\rm kpc}}$ up to a maximum value at around $\log\ n \approx 0.6$ ($n \approx 4$) and $\Sigma^*_{1\ {\rm kpc}} \approx 10^{9.8}$ $M_\odot/{\rm kpc}^2$ respectively, where the trend reverses.

3.4 Comparison to Theory

In this section, we compare our results in §3.3 with theoretical expectations of bar formation and evolution. We start with a short summary of theoretical results.

3.4.1 Theoretical Reminders

One can distinguish (at least) two phases in the lifetime of a bar: the formation phase and the secular evolution phase. AMR13 showed that these two phases are contiguous in gas-rich cases, while, for gas-poor ones, they are not. In the latter case, there are two further stages of relatively short duration in between the formation and secular evolution phases[25].

This is illustrated in Fig. 3.5, where we plot the bar strength, A_2, which is closely related to bar length, as a function of time for four simulations from AMR13. The two simulations in each panel have the same initial mass and velocity distribution of the baryonic and dark matter components. The only difference is the gas fraction, where the black and blue lines represent gas-poor and gas-rich simulations, respectively. The end of the bar formation phase is represented by the time when the steep increase of A_2 terminates, which is at times 2 – 2.5 Gyrs for the gas-poor simulations, and around 4.5 Gyrs for the gas-rich ones. These simulations illustrate that gas slows down bar formation considerably (AMR13). This is due both to an increase in the duration of the pre-bar phase (i.e., the phase during which the disk can still be considered as axisymmetric) and a decrease in the rate of the bar growth (i.e., an increase of the time it takes for the bar to end its growth phase), both being compared to the times of the equivalent phases in the gas-poor case.

The secular evolution phase, however, starts roughly at 4.5 Gyrs for all cases. In general, the duration of these phases, as well as the increase of bar strength that they imply, depend on the mass and velocity distribution of the baryonic and dark matter components within the galaxy, as well as on the gas fraction. Readers can find more information and a long list of relevant references in a recent review by Athanassoula (2013). It is also interesting to note in Fig. 3.5 that, for all times and in both phases, the bar in the gas-rich case is less strong than in the gas-poor one (see also Berentzen *et al.*, 2007).

Bar formation and evolution is influenced also by galactic bulges. Bulges, how-

---

[25] These two extra stages are related to the bar buckling phase (i.e., the formation of a boxy/peanut bulge), which is much less obvious in gas rich cases.

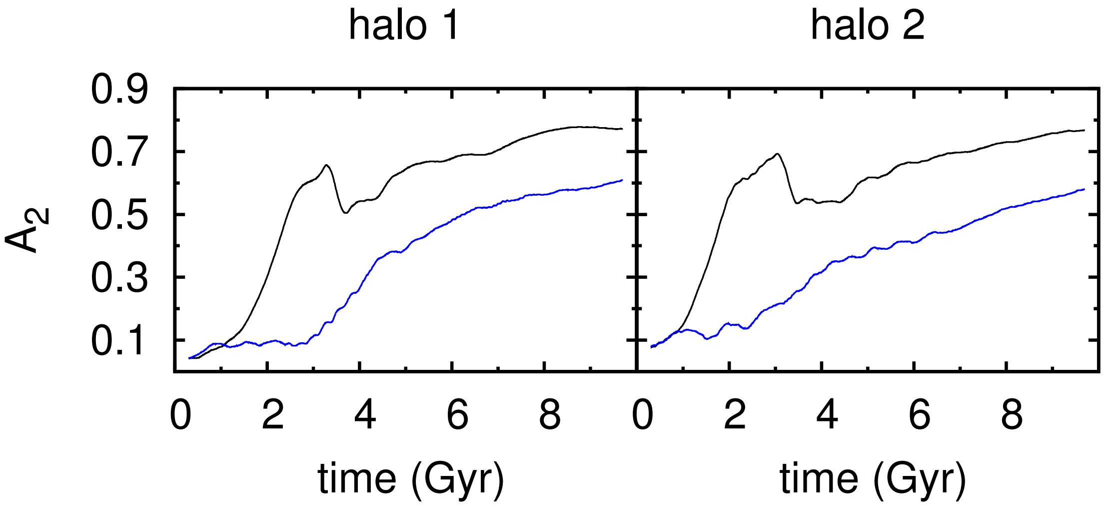

Figure 3.5:]
Bar strength, A_2, which can considered as a rough proxy for bar length, as a function of time for four simulations. Two simulations have a gas-rich disk (blue lines) while the other two have a gas-poor disk (black lines). The two panels correspond to different types of haloes: initially spherical (left panel) and initially triaxial (right panel). For a full description of these simulations and their results, see AMR13. These simulations show that bars grow slower and are less strong in the gas-rich case.

ever, are an inhomogeneous class of objects (Kormendy, 1993; Kormendy and Kennicutt, 2004; Athanassoula, 2005). Classical bulges have high Sérsic indices, typically around 4, but certainly above 2. Disky pseudobulges, on the other hand, have low Sérsic indices, typically around 1, and usually less than 2 (Fisher and Drory, 2010). The most popular scenario for the formation of disky pseudobulges in barred galaxies is that they are due to stars, and particularly, gas pushed inwards by the bar to the central parts of the disk. Here, the high density gas will give rise to star formation, so that the disky pseudobulges should be primarily composed of gas and young stars with a smaller fraction of old stars. Their extent is typically of the order of 1 kpc (Athanassoula, 1992; Heller and Shlosman, 1994; Fisher and Drory, 2010)[26].

---

[26] For completeness, we mention the boxy/peanut bulges, which, in fact, are part of the bar. Their Sérsic indices are smaller, or of the order of that of the disky pseudobulges. Given that all our decompositions here include only one or two components (§3.2.3), and bars are not included, and our sample excludes highly inclined systems, such

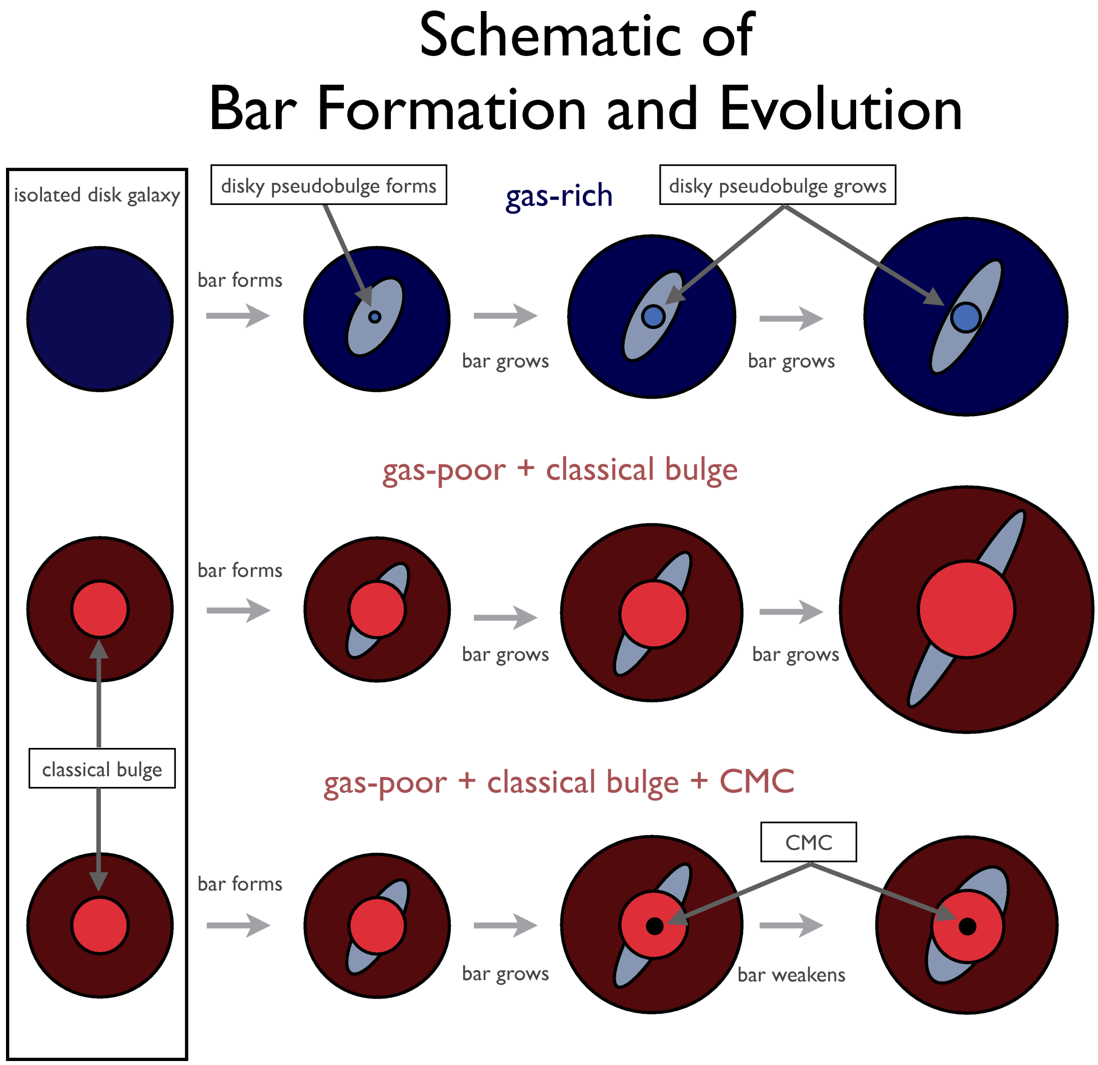

Figure 3.6: A schematic diagram of bar formation and evolution. *Top row* illustrates the gas-rich scenario, in which a bar forms and grows over time. As the bar enters the secular evolution phase, a disky pseudobulge is created. The growth of the disky pseudobulge follows that of the bar. *Middle row* illustrates the gas-poor scenario with a classical bulge. The evolution of the bar in the gas-poor case is faster than that of the gas-rich case. *Bottom row* illustrates the gas-poor scenario with a classical bulge and a central mass concentration (CMC). The development of a CMC weakens the bar.

These two different types of bulges have different dynamics and, therefore, different

---

bulges do not enter in our discussion. However, we do note that they may still be present in the sample and may not be well fit by our decompositions.

effects on the bar formation and evolution phases. Classical bulges predate the bar, so they will influence both phases. Their influence has many similarities to that of the dark matter halo. Namely, they slow down bar formation in the first phase, but, during the secular evolution phase, they help the bar grow by absorbing angular momentum, leading to stronger bars (Athanassoula and Misiriotis 2002, A03). Thus, simulations predict that bars in galaxies with classical bulges should be stronger than bars in galaxies without classical bulges, assuming all other properties are the same.

On the other hand, disky pseudobulges in barred galaxies are formed by material pushed inwards by the bar, i.e., they do not predate the bar and thus cannot influence its formation phase. Moreover, disky pseudobulges should not help the bar grow during the secular evolution phase either, since they cannot absorb angular momentum. This is because the radii of disky pseudobulges are considerably smaller than the corotation radius, and also because disky pseudobulges are flat (spherical-like density distributions, like the classical bulge or the halo, can absorb angular momentum). However, although disky pseudobulges do not affect bar formation or evolution, bars do affect disky pseudobulges. In fact, bar-driven secular evolution is the primary process of disky pseudobulge creation and growth (Kormendy and Kennicutt, 2004; Athanassoula, 2005). Thus, the theoretical prediction is that stronger bars push more gas inwards, resulting in more massive disky pseudobulges.

A visual approximation of bar formation and evolution is presented in Fig. 3.6.

3.4.2 The Effect of Gas Content on Bar Formation

We explain the trends we observe between the likelihood of disk galaxies being barred and their SSFR (present even at fixed M_*, n, or $\Sigma^*_{1\ \mathrm{kpc}}$; see Fig. 3.3) as being due to the effect of gas on bar formation. In the models, bars form later in disk galaxies with significant gas content, and after they form, they grow slower than disk galaxies with comparably less gas (AMR13 and Fig. 3.5). This predicts that the bar likelihood should be higher in gas-poor galaxies (i.e., the quiescent population), simply because some of the gas-rich galaxies (i.e., the star-forming sequence) have not yet formed their bars. Thus, taking SSFR as a tracer of gas content, then there is good agreement between simulation results and the trends we find (see also Masters *et al.*, 2012).

Within the star-forming sequence (defined here as $\log\ \mathrm{SSFR} > -11\ \mathrm{yr}^{-1}$) disk galaxies do not all have the same p_{bar}, but neither do they all have the same gas content. There are well known trends between SSFR, stellar mass, and gas content of disk galaxies (e.g., Catinella *et al.*, 2010; Saintonge *et al.*, 2011). The trend we observe here for p_{bar} to increase as SSFR declines (and M_* increases) can be explained as being due to decreasing amounts of gas in the disks of these galaxies. Indeed, Masters *et al.* (2012) showed that if you correct for the typical HI content of a disk galaxy, those galaxies with more HI than is expected for their stellar mass are less likely to host bars.

3.4.3 The Effects of Classical Bulges and Disky Pseudobulges on Bar Formation

We observe trends of bar likelihood with the Sérsic index (n, Fig. 3.3b) and central surface stellar mass density ($\Sigma^*_{1\ \mathrm{kpc}}$, Fig. 3.3c), where these latter two parameters are considered

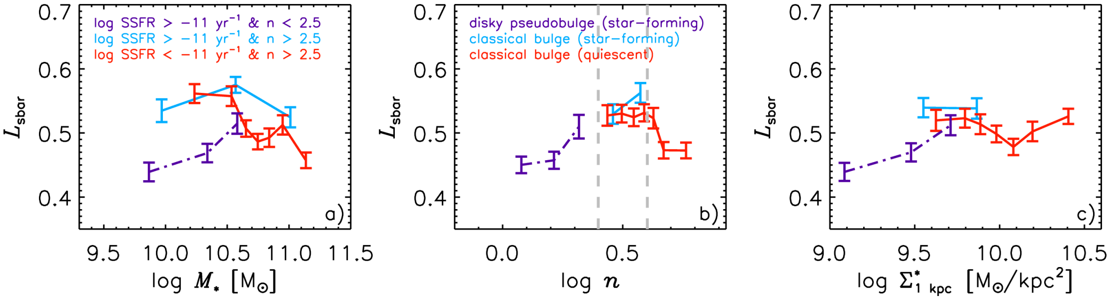

Figure 3.7: Average $L_{\rm sbar}$ plotted against: *a)* M_*, *b)* n, and *c)* $\Sigma^*_{1\ \rm kpc}$. The details of this figure are identical to that of Fig. 3.4, with the exception that each bin contains ~ 75 galaxies and also, galaxies are further separated by bulge type, as identified by n. Purple points represent the star-forming disky pseudobulge galaxies, light blue points represent the star-forming classical bulge galaxies, and red points represent the quiescent classical bulge galaxies. The correlations of $L_{\rm sbar}$ with n and $\Sigma^*_{1\ \rm kpc}$ for the disky pseudobulge galaxies match the predictions of bar-driven secular evolution.

to be measures of bulge prominence. In the star-forming sequence bar likelihood increases with both increasing n and $\Sigma^*_{1\ \rm kpc}$, while the opposite trend is observed in the quiescent population. In order to interpret these trends, we need to remember that there are two main types of bulges – the classical bulge and the disky pseudobulge, a distinction which will help explain this dichotomy.

The best way to distinguish these types of bulges involves the use of high resolution imaging of the bulges (e.g., Fisher and Drory, 2008), something that is not available for our large sample. However one can approximately separate the types with a threshold in the global galaxy Sérsic index (Drory and Fisher, 2007)[27]. Disky pseudobulges generally lie in galaxies with global $n < 2.5$ while classical bulges are found in galaxies with global $n > 2.5$. Although this method is less accurate than those using high resolution imaging, this is a simple option that is adequate for our purposes. Hence, we adopt this Sérsic threshold for the rest of the paper

---

[27] Gadotti (2009) advocates using the Kormendy relationship to separate classical bulges from disky pseudobulges. For this work, however, we choose to use the more simple global galaxy Sérsic threshold.

to distinguish the two types of bulges[28]. This threshold is illustrated with a vertical dashed line at $\log\ n = 0.4$ ($n = 2.5$) in Fig. 3.3b.

Our sample confirms the well known observation (e.g., Drory and Fisher, 2007) that quiescent (red) disk galaxies primarily have classical bulges while star-forming (blue) disk galaxies mainly have disky pseudobulges (see Fig. 3.3b). This suggests that the decreasing $p_{\rm bar}$ with n and $\Sigma^*_{1\ \rm kpc}$ observed in the quiescent disk galaxies is due to $p_{\rm bar}$ decreasing in galaxies with larger classical bulges, while the increasing $p_{\rm bar}$ with n and $\Sigma^*_{1\ \rm kpc}$ observed in star-forming disks shows that $p_{\rm bar}$ is larger in galaxies with more massive disky pseudobulges.

The classical bulge, like the halo, slows down bar formation due to it 'diluting' the non-axisymmetric forcing of the bar (Athanassoula, 2013). This predicts that bar likelihood should decrease with increasing prominence of the classical bulge, as we indeed observe.

Disky pseudobulges result from the material that a bar pushes inwards to the central part of the disk. Since these bulges formed after the bar, and are in fact, a product of the bar, they cannot influence the bar formation phase. However there is a clear link predicted between the existence of the bar and the amount of mass in the disky pseudobulge, (or central 1 kpc; Athanassoula 1992; Heller and Shlosman 1994; Fisher and Drory 2010). For galaxies of a given gas mass (or SSFR), a higher bar likelihood should result in more massive disky pseudobulges, as we observe (Figs. 3.3b and 3.3c).

---

[28] Of course, there are $n < 2.5$ galaxies that have no bulge (e.g., Simmons *et al.*, 2013). However, for simplicity, we consider all galaxies with $n < 2.5$ to contain a disky pseudobulge even if it might be a pure disk galaxy. This will not affect our discussion since pure disks and disky pseudobulges are closely related (see Kormendy and Kennicutt, 2004).

3.4.4 Evidence for Secular Evolution

Bar length trends (§3.3.2) can help us understand the secular evolution phase of the bar. We can safely assume that during the secular evolution phase of any non-interacting galaxy its bar length may be considered a proxy of bar age. However, this may not be true for any two galaxies, because the galaxy with the youngest bar can have the longest bar, provided its halo can absorb larger parts of the angular momentum emitted by the bar region (A03). Our comparisons, however, do not concern two galaxies but ensembles of a relatively large number of galaxies. For example in Fig. 3.4b we compare ensembles of galaxies with different n values. But the number of galaxies in each ensemble is sufficiently large for us to assume that galaxies with a variety of halo properties are included in a roughly similar manner in all ensembles. This subtle, but important point is intrinsic in our analysis and will be discussed further in §3.6.

The strongest $L_{\rm sbar}$ trends we observe are found within star-forming disk galaxies (the average $L_{\rm sbar}$ increases monotonically with M_*, n, and $\Sigma^*_{1\ \rm kpc}$; see Fig. 3.4). To better understand the underlying physical processes responsible for these trends, we separate the data in Fig. 3.4 by bulge type; this is shown in Fig. 3.7. Recall that galaxies with $n < 2.5$ are considered to contain disky pseudobulges while galaxies with $n > 2.5$ are considered to contain classical bulges. Note that quiescent galaxies with $n < 2.5$ are very rare, hence they are not shown.

During the secular evolution phase, bars become stronger, longer, and more efficient at funneling gas into the central regions of galaxies, leading to more massive disky pseudobulges (AMR13). This prediction matches our observations in Figs. 3.7b and 3.7c, where it is clear that $L_{\rm sbar}$ is correlated with n and $\Sigma^*_{1\ \rm kpc}$ for the disky pseudobulge galaxies (purple). These correlations give evidence for the secular evolution phase of bars.

The L_{sbar} trends with classical bulges are much more complex and also much less straightforward to interpret. Simulations show that classical bulges should foster secular evolution by absorbing some of the angular momentum emitted by the bar region (A03). Hence the expectation is that galaxies with more massive classical bulges should have longer bars, but also longer disk scale lengths.

Figs. 3.7b and 3.7c show that the classical bulge galaxies (light blue and red) generally have longer scaled bar lengths than galaxies without a classical bulge, i.e., the disky pseudobulge galaxies. However, there is little evidence of increasing scaled bar length with increasing n and $\Sigma^{*}{}_{1\text{kpc}}$. In fact, there actually appears to be a decrease in scaled bar length for log n larger than 0.6 (i.e., n larger than about 4, equivalent to a more concentrated light profile than the standard $r^{1/4}$ de Vaucouleurs profile). Similarly the scaled bar length stops increasing in the rightmost panel for $\Sigma^{*}_{1\text{kpc}}$ larger than roughly $10^{9.8}$ $\text{M}_{\odot}/\text{kpc}^{2}$ (although there seems to be an final increase in scaled bar length at the highest $\Sigma^{*}{}_{1\text{kpc}}$).

This decrease in scaled bar length with large n and $\Sigma^{*}_{1\ \text{kpc}}$ does not disagree with simulation results, and can be attributed to the presence of a very high central mass concentration (CMC)[29]. Indeed, our last averaged point is roughly at a log n value of 0.8, which corresponds to a Sérsic index of roughly 6.5. This could well be due to a luminosity spike in the center of the galaxy which would hamper the bar growth and evolution if it pre-existed the bar, or if grown later, that would bring a decrease of the bar length and strength (e.g., Shen and Sellwood, 2004;

---

[29] We note that this is just one of the possible reasons for this observed decrease. This could also correspond to the regime where the bulge is so massive that it has significantly delayed the onset of bar formation, resulting in a lack of bar evolution.

Athanassoula *et al.*, 2005). This strong CMC will thus bring a decrease of bar length at the highest values of n, as seen in Fig. 3.7b (and Fig. 3.4b).

Nevertheless, at least part of this decrease could be spurious and due to the fact that the bar component is not specifically included in our 2-component decompositions, which is more worrisome for galaxies with stronger and longer bars. To test it we scaled the absolute bar length with the r-band isophotal radius at 25 mag arcsec^{-2} from the SDSS pipeline and re-created Figs. 3.4 and 3.7. The results can be found in Appendix B.1. We find then that the decrease seen with the disk scale length at high n and $\Sigma^*_{1\ \mathrm{kpc}}$ is considerably lessened. We do not fully understand the bar length trends with the classical bulge galaxies at the highest n and $\Sigma^*_{1\ \mathrm{kpc}}$, more work needs to be done. Let us note, however, that the correlations of the scaled bar length with the disky pseudobulge galaxies are still present even when scaling with the isophotal radius, thus enhancing our confidence in the corresponding decompositions and trends.

3.5 Discussion

3.5.1 Are We Observing Secular Evolution?

In §3.3 and §3.4, we showed evidence which suggests that disky pseudobulges are more massive in populations of galaxies which are more likely to host bars and which host longer bars (specifically that average values of p_{bar} and L_{sbar} increased with n and $\Sigma^*_{1\ \mathrm{kpc}}$ for disky pseudobulge galaxies). We interpreted this as observational evidence of bar-driven secular evolution growing disky pseudobulges (Kormendy and Kennicutt, 2004; Athanassoula, 2005). Our interpretation hinges on the assumption that bar length traces the evolution of bars. This assumption is based on both simulations of bar growth as well as observational data. Elmegreen *et al.* (2007) showed that bar length mirrors bar strength (see also Block *et al.*, 2004). The simulations of bar growth shown in Fig. 3.5 – and a large number of others, as reviewed by Athanassoula (2013) – demonstrate that isolated bars typically grow stronger with time.

Furthermore, the simulations of AMR13 argue that bars in isolated galaxies are long-lived structures – in the ~ 10 Gyrs that their simulations covered, not one of their bars dissolved (see also Debattista *et al.* 2006 and Berentzen *et al.* 2007 for a similar conclusion). Recent zoom-in cosmological simulations by Kraljic *et al.* (2012) also support the idea that bars are long-lived structures. Their simulations show that most of the bars that formed at $z \leq 1$, when mergers have become less frequent, persist down to $z = 0$. Observational studies have now observed bars with modest frequencies out to $z \sim 1$ (Abraham *et al.* 1999; Jogee *et al.* 2004; Elmegreen *et al.* 2004; Sheth *et al.* 2008; Cameron *et al.* 2010; Melvin *et al.* 2014), and one upcoming study detects bars as far out as $z \sim 1.5$ (J. Herrington et al. 2013, submitted.), with the implication that many of the bars we observe in the local Universe could have formed at $z \sim 1$ or earlier. This gives a substantial time window for secular evolution to grow longer bars and stronger disky pseudobulges.

Previous works have shown a trend between bar length and Hubble type – that bars are longer in earlier type disks – and used this to argue that secular evolution had been observed (e.g., Athanassoula and Martinet, 1980; Elmegreen and Elmegreen, 1985; Martin, 1995; Regan and Elmegreen, 1997; Erwin, 2005; Laurikainen *et al.*, 2007; Elmegreen *et al.*, 2007; Menéndez-Delmestre *et al.*, 2007; Gadotti, 2011). Our result is novel in that it looked for trends of bar length with the central mass density in the very centers of galaxies, a quantity that is directly linked to secular evolution in models. Our sample is also nearly an order of magnitude larger than any previous study. Thus, we argue that our result is the best evidence yet for bar-driven secular evolution in disk galaxies.

Recent results from several high resolution simulations present mechanisms for the formation of disky pseudobulges that do not rely on secular evolution (Inoue and Saitoh, 2012b; Okamoto, 2013), but rather involve dynamical instability in clumpy galaxies or high-redshift starbursts. While the bulges of these simulations do have characteristics of local disky pseudobulges[30], our results here suggest that secular evolution does have a major effect, both in creating disky pseudobulges and in building up the stellar mass in the bulge region of barred galaxies.

Nevertheless, there are substantial numbers of disk galaxies that are non-barred and are hosting disky pseudobulges (Kormendy and Kennicutt, 2004). Up to a third or more of the local disk galaxy population is unbarred in even the most conservative reckoning. This observations argues that disky pseudobulges have more than one formation mechanism. Perhaps disky pseudobulges in non-barred galaxies were created through high redshift channels, while the disky pseudobulges in barred galaxies may have been created, and are still in the process of growing through bar-driven secular evolution, at much later times.

3.5.2 Can Bars Quench Star Formation?

The highest values of p_{bar} are found among quiescent galaxies with $n \sim 2.5$ (see Fig. 3.3b). Here we consider the question of whether these bars were formed in situ or if they could be implicated in the processes which turned these disk galaxies quiescent. We ask ‘were

---

[30] Not all bulges made from clump coalescence have characteristics of disky pseudobulges. For example, Elmegreen *et al.* (2008) show that their bulges made through clump coalescence have properties of classical bulges.

these bars formed in $n \sim 2.5$ quiescent galaxies, or did they form in star-forming galaxies (with $n \lesssim 2.5$) that evolved into the $n \sim 2.5$ quiescent disk galaxies?' We refer to this latter process as 'bar quenching' and explore this idea further.

Bars have been associated with enhanced central star formation in galaxies for decades (Hawarden *et al.*, 1986; Dressel, 1988; Friedli and Benz, 1993; Giuricin *et al.*, 1994; Huang *et al.*, 1996; Martinet and Friedli, 1997; Martin and Friedli, 1997; Ho *et al.*, 1997; Ellison *et al.*, 2011; Oh *et al.*, 2012; Wang *et al.*, 2012). This is a natural consequence of the evolution of gas in a disk galaxy under the influence of a bar. The bar-induced gravitational torques funnel gas into the centers of galaxies (Matsuda and Nelson, 1977; Simkin *et al.*, 1980; Athanassoula, 1992; Wada and Habe, 1992a, 1995; Friedli and Benz, 1993; Heller and Shlosman, 1994; Knapen *et al.*, 1995; Sakamoto *et al.*, 1999; Sheth *et al.*, 2005), where it should quickly form stars, thus enhancing the central star formation. If this secular evolution were efficient, it could accelerate the depletion of the gas supply within a considerable fraction of the disk, namely the region within corotation. If this process were not balanced by an increased inflow of cosmological gas, this would ultimately, produce a quiescent barred galaxy (Masters *et al.*, 2011, 2012).

Large surveys such as SDSS (Abazajian *et al.*, 2009), COSMOS (Scoville *et al.*, 2007), and AEGIS (Davis *et al.*, 2007) have painted a clear picture of the structural properties of quiescent galaxies – they are massive, centrally concentrated, and have high central velocity dispersions (e.g., Franx *et al.*, 2008; Bell *et al.*, 2012; Wake *et al.*, 2012b; Cheung *et al.*, 2012; Barro *et al.*, 2013; Fang *et al.*, 2013; Williams *et al.*, 2014). Cheung *et al.* (2012) recently found that the most distinguishing structural parameter of quiescent galaxies (compared to star-forming galaxies) is their central surface stellar mass density (within a radius of 1 kpc).

Almost all quiescent galaxies in the sample of Cheung *et al.* (2012) have high values of $\Sigma^*_{1\ \mathrm{kpc}}$, while star-forming galaxies mainly have low values of $\Sigma^*_{1\ \mathrm{kpc}}$. This is clear evidence that the process(es) that quench star formation in these galaxies are related to the buildup of the central stellar mass density (see also Fang *et al.*, 2013). We consider here if secular evolution is able to build high enough central densities to act as a quenching mechanism.

Indeed, Fig. 3.7c shows that the $\Sigma^*_{1\ \mathrm{kpc}}$ values of the disky pseudobulge galaxies overlap partly with the $\Sigma^*_{1\ \mathrm{kpc}}$ values of the classical bulge galaxies. The most massive of the disky pseudobulges we argue are grown by bar-driven secular evolution are comparable in central density to the smallest of the classical bulges. This suggests that secular evolution can build the high central densities that are observed in quiescent galaxies. This appears to be circumstantial evidence for an interesting, and potentially important galaxy evolution process – bar quenching. We caution, however, that our identification of disky pseudobulges in quiescent barred disk galaxies is based on global Sérsic fits. If it is indeed the case that there exist quiescent disk galaxies which host only disky pseudobulges, and show no evidence for classical bulges, this will be strong evidence for the process of 'bar quenching' having acted in these galaxies. However, more accurate identifications of disky pseudobulges are needed to verify this claim.

3.6 Conclusion

In this paper, we use hundreds of thousands of visual classifications measurements of galactic bars provided by "citizen scientists" through the Galaxy Zoo project (Lintott *et al.*, 2008, 2011; Willett *et al.*, 2013). We first select a sample of disk galaxies in which reliable bar classifications can be made – we call this the Galaxy Zoo 2 Disk (GZ2D) sample, which comprises 13,295 oblique (i.e., face-on or mildly inclined) disk galaxies in a volume limit to $z = 0.06$. This sample is similar to the GZ2 samples used previously to study trends of the bar fraction by Masters *et al.* (2011) and Masters *et al.* (2012). Strongly barred galaxies identified in GZ2 were part of a small Galaxy Zoo project which used a Google Sky interface to collect measurements of bar lengths (Hoyle *et al.*, 2011). In this paper we also make use of this Bar Length (BL) sample, which comprises 1,154 galaxies. We use these data to analyze the dependence of bar likelihood ($p_{\rm bar}$, a weighted and debiased fraction of GZ users identifying a bar, and which acts like a probability of a galaxy containing a visually identifiable bar; Willett *et al.* 2013) and scaled bar length ($L_{\rm sbar} = L_{\rm bar}/2.2r_d$; a measure of bar strength, linked to how evolved a bar is) on other galactic properties. Specifically we test how the likelihood and length of bars depend on specific star formation rate (SSFR; estimated through nebular emission lines from the SDSS fiber, and the broadband ugriz SDSS photometry, as measured by MPA-JHU) and inner galactic structure (i.e., bulge prominence) parameterized by global Sérsic index, n, as measured by GIM2D, and central surface stellar mass density, $\Sigma^*_{1\ {\rm kpc}}$, as estimated from a 1 kpc radius circular aperture projected onto SDSS images.

Our main observational results (§3.3) are:

1. There exists an anti-correlation between $p_{\rm bar}$ and SSFR; this relationship is present even at fixed M_*, n, or $\Sigma^*_{1\ {\rm kpc}}$.
2. The structural trends of $p_{\rm bar}$ are bimodal with SSFR. In the star-forming sequence, $p_{\rm bar}$ correlates with n and $\Sigma^*_{1\ {\rm kpc}}$, while in the quiescent population, $p_{\rm bar}$ anti-correlates with n

and $\Sigma^*_{1\ \mathrm{kpc}}$.

3. The structural trends of L_{sbar} are also bimodal with SSFR. Within the star-forming sequence, L_{sbar} correlates with n and $\Sigma^*_{1\ \mathrm{kpc}}$, in a similar way to p_{bar}. However within the quiescent population, L_{sbar} shows a rather different behavior, with a peak at values of $n \sim 4$ and $\Sigma^*_{1\ \mathrm{kpc}} \sim 10^{9.8}\ \mathrm{M}_\odot/\mathrm{kpc}^2$.

We compare these results to simulations of bar formation and evolution in §3.4. We find that the underlying physical processes become clearer upon separating these galaxies by those that contain disky pseudobulges ($n < 2.5$) and those that contain classical bulges ($n > 2.5$). This comparison reveals the following:

1. Assuming that SSFR is a good tracer of gas content, the anti-correlation of p_{bar} with SSFR is consistent with the expected effects of gas on bar formation. Simulations show that gas delays the formation of bars, thus many gas-rich galaxies simply have not yet formed bars, while most gas-poor disk galaxies have.

2. The observed trends of p_{bar} and L_{sbar} with n and $\Sigma^*_{1\ \mathrm{kpc}}$ for classical bulge galaxies are consistent with the effects of classical bulges and CMCs on bar formation and evolution. The gravitational forcing of classical bulges 'dilute' the non-axisymmetric forcing of the bar, which delays the formation of a bar. This diluting effect is more powerful in more massive classical bulges, resulting in a longer delay of bar formation. After the bar has formed, however, classical bulges are expected to promote *secular evolution* by absorbing the angular momentum emitted from the bar region; this process also scales with the mass of the bulge and leads to both longer bars and longer disk scale lengths.

Our results suggest that for Sérsic index up to roughly $n = 4$ the bar length may increase faster than the disk scale length. For yet higher values of n, a strong ensuing CMC could lead to a decrease of the bar strength by generating instabilities of the main family of bar-supporting orbits.

3. The correlations of p_{bar} and L_{sbar} with n and $\Sigma^{*}_{1\ \text{kpc}}$ for the disky pseudobulge galaxies are in agreement with the predictions of bar-driven secular evolution. Bars drive gas toward the centers of galaxies, where the gas should eventually form stars and give rise to disky pseudobulges. As bars grow stronger and longer, the ability to funnel gas grows stronger as well, resulting in more massive disky pseudobulges.

The comparison of the observational results we present here with simulations of bar formation and growth shows general agreement, indicating that many of the underlying physical processes of bar formation and evolution are understood. An implication of this is that we are confident in our basic understanding of the relationship between bars and their host galaxies. Bars are clearly not stagnant structures, rather they are dynamic, evolving, and furthermore directly influence the evolution of their host galaxies.

While this work only concerns the universe at $z \sim 0$, the ramifications of this idea reach far beyond the local universe. There is increasing evidence that bars have been present since $z \sim 1$ (Abraham *et al.* 1999; Jogee *et al.* 2004; Elmegreen *et al.* 2004; Sheth *et al.* 2008; Cameron *et al.* 2010; Melvin *et al.* 2014; J. Herrington et al. 2013, submitted.), indicating that the evolution of disk galaxies has been affected by bars for the last ~ 8 billion years. Moreover, if the observed evolution of bar fraction with redshift is extrapolated into the future (there is now an agreement that bar fraction increases towards lower z), then bars will soon be present in nearly all disk galaxies, and hence become an even more dominant driver of disk galaxy evolution.

We can not yet claim to understand all aspects of the symbiotic relationship between bars and their host galaxies. We do not fully understand the complicated behavior we observe between bar length and inner galactic structure in disk galaxies hosting classical bulges. Our tentative explanation is that these trends are due to the presence of CMCs, however this should be tested with much higher resolution imaging to probe the very centers of galaxies. Furthermore, in this work we have not explored many of the parameters that are predicted to affect bar formation and evolution (e.g., the dark matter halo and the velocity dispersion of the stars in the disk, Athanassoula and Sellwood 1986; A03). Even so, we found a good agreement between theory and observations and all observational trends could be well explained by simulations. This may be due to the large size of our sample, which allows for a variety of halo properties and of disk velocity dispersions in a roughly similar manner in all ensembles we compared. Finally, the role bars may play in processes which quench star formation is an interesting, and potentially important issue for galaxy evolution that warrants further study.

The most notable success in our comparison between observation and theory is the evidence we present for secular evolution. Unlike galaxy mergers, secular evolution is a slow and gentle process that is not immediately obvious in images. There has been previous observational evidence of secular evolution in galaxies (e.g., Athanassoula and Martinet, 1980; Courteau *et al.*, 1996; MacArthur *et al.*, 2003; Elmegreen *et al.*, 2007; Laurikainen *et al.*, 2009; Coelho and Gadotti, 2011; Sánchez-Janssen and Gadotti, 2013), however the combination of our large dataset and the observed correlations of bar likelihood and bar length with inner galactic structure for star-forming disk galaxies makes our results one of the most compelling pieces of evidence of not only the existence of secular evolution, but also of the role of ongoing secular processes on the evolution of disk galaxies.

Chapter 4

Galaxy Zoo: Bars are not Responsible for the Feeding of Active Galactic Nuclei at $0.2 < z < 1.0$

4.1 Introduction

Most simulations of galaxy evolution require active galactic nucleus (AGN) feedback to reproduce key observations, such as the color bimodality of galaxies (e.g., Springel *et al.*, 2005; Croton *et al.*, 2006). Yet, the mechanism that funnels gas toward the central supermassive black hole that feeds the AGN is still unknown (see Fabian 2012, Kormendy and Ho 2013, and Heckman and Best 2014 for recent reviews).

Major mergers are often cited as a key trigger for AGN activity (Sanders *et al.*, 1988; Barnes and Hernquist, 1991; Mihos and Hernquist, 1996; Di Matteo *et al.*, 2005; Hopkins *et al.*, 2005a,b). Although major mergers seem to drive the most luminous and rapidly accreting AGN

(Sanders *et al.*, 1988; Koss *et al.*, 2010; Kartaltepe *et al.*, 2010; Trump, 2011; Treister *et al.*, 2012; Hopkins *et al.*, 2013), low to moderate luminosity AGN, which make up the majority of AGN by number, seem to be fueled by processes that do not visibly disturb the disky structure of galaxies (Schawinski *et al.*, 2010; Cisternas *et al.*, 2011; Schawinski *et al.*, 2011; Simmons *et al.*, 2012; Kocevski *et al.*, 2012).

An obvious process that satisfies this constraint is secular evolution (Kormendy and Kennicutt, 2004; Athanassoula, 2013). A major driver of secular evolution in disk galaxies is large-scale bars[31], and they are predicted to affect galaxies in a variety of ways, including the fueling of AGN (Simkin *et al.*, 1980; Noguchi, 1988; Shlosman *et al.*, 1989, 1990; Wada and Habe, 1992b). The non-axisymmetric potential of a bar funnels interstellar gas into the central kpc (Athanassoula, 1992; Sakamoto *et al.*, 1999; Sheth *et al.*, 2005), where a possible nested bar may further funnel gas to the inner ~ 10 pc. From this distance, cloud-cloud collisions may lead to inflows onto the AGN accretion disk. Collectively, this scenario is known as "bars within bars" (Shlosman *et al.*, 1989, 1990; Hopkins and Quataert, 2010, 2011). Observations at low redshift, however, find no excess of bars in active galaxies (Ho *et al.* 1997; Mulchaey and Regan 1997; Malkan *et al.* 1998; Hunt and Malkan 1999; Regan and Mulchaey 1999; Martini and Pogge 1999; Erwin and Sparke 2002; Martini *et al.* 2003; Lee *et al.* 2012b; Oh *et al.* 2012; Cisternas *et al.* 2013, but see Knapen *et al.* 2000; Laine *et al.* 2002; Laurikainen *et al.* 2004, see Jogee 2006 for a review). There is also no direct correlation between large-scale bars and nuclear bars, with $\sim 30\%$ of all disk galaxies having a nuclear bar (Mulchaey and Regan, 1997; Regan and Mulchaey, 1999; Martini and Pogge, 1999; Erwin and Sparke, 2002; Laine *et al.*,

---

[31] Unless otherwise stated, we use "bars" to refer to large-scale (kpc-sized) structures.

2002). These results indicate that bars do not fuel AGN.

All previous observational work on the bar-AGN connection has been limited to the local universe, where the number density of AGN is low. Thus a compelling link between bars and AGN might still be found at *earlier* epochs, when the number density of AGN is higher (Ueda *et al.*, 2003; Silverman *et al.*, 2008; Aird *et al.*, 2010). In this work we focus on galaxies at $0.2 < z < 1.0$. The upper limit of $z = 1$ is chosen because we are confident that the Hubble Space Telescope optical imaging detects all large scale bars to $z = 1$ (see Sheth *et al.*, 2008; Melvin *et al.*, 2014).

We describe the data in §2. Our sample selection, and in particular, our selection of control samples of inactive galaxies is detailed in §3. §4 presents and discusses our main result that there is no statistically significant excess of bars in AGN hosts. Conclusions follow in §5. We assume a flat cosmological model with $H_0 = 70$ km s^{-1} Mpc^{-1}, $\Omega_m = 0.30$, and $\Omega_\Lambda = 0.70$ throughout this paper.

4.2 Data

Our sample is drawn from the AEGIS (Davis *et al.*, 2007), COSMOS (Scoville *et al.*, 2007), and GOODS-S (Giavalisco *et al.*, 2004) surveys. All three surveys have optical imaging from the Advanced Camera for Surveys on board the Hubble Space Telescope (HST/ACS) as well as catalogs of derived galaxy properties. In this work, we use measurements of stellar masses (M_*), spectroscopic redshifts (z), rest-frame colors ($U-B$ or $U-V$), and structural parameters (global Sérsic index n, effective radius r_e, and axis ratio b/a). These parameters

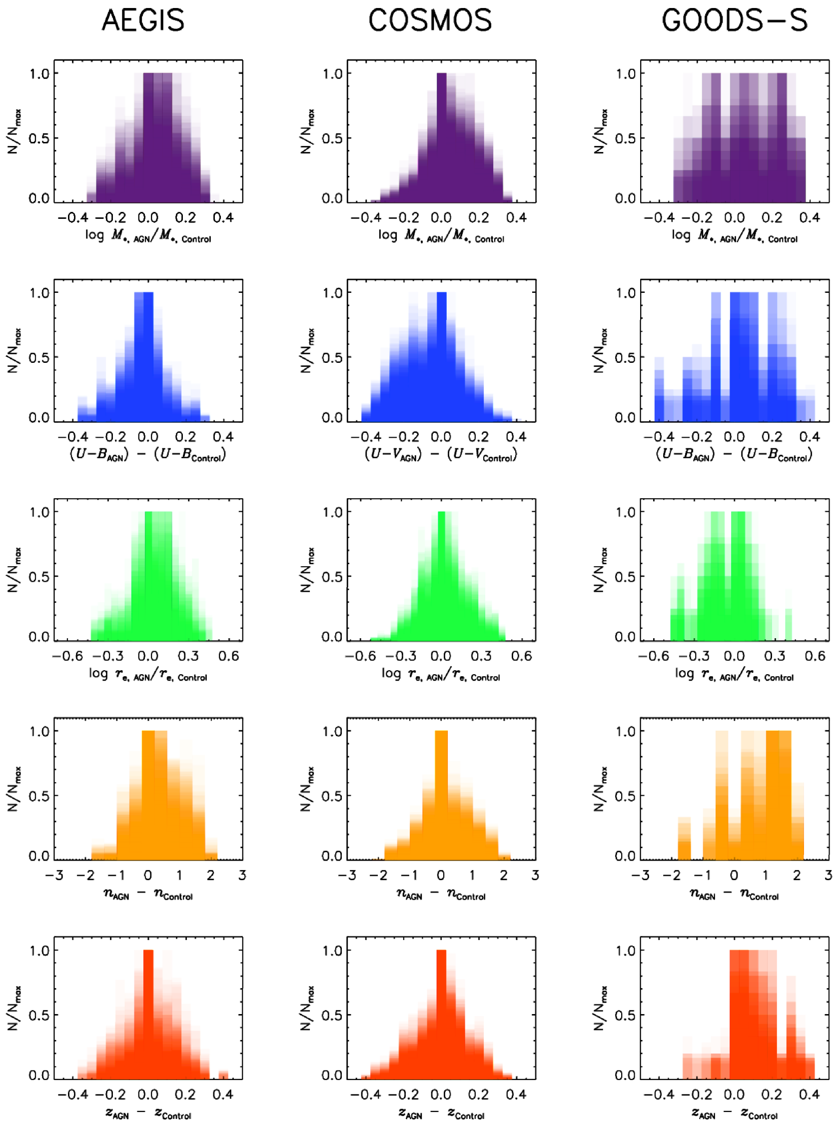

Figure 4.1: Each histogram shows the difference in the indicated parameter values between the AGN and their associated control galaxies. From top to bottom, the parameters are: stellar mass (M_*), rest-frame color ($U-B$ or $U-V$), effective radius (r_e), global Sérsic index (n), and spectroscopic redshift (z). Each panel overlays 100 histograms, one for each AGN-control sample realization. The shading reveals the amount of overlap. Most of the histograms peak around zero, implying that the AGN and control galaxies are generally well-matched. The histograms of GOODS-S are slightly broader and more skewed than those of AEGIS and COSMOS, which is due to the relatively small sample size of GOODS-S.

are used to select our parent sample of disk galaxies in §4.3.1. Readers are referred to the following works for the technical details behind these measurements: Cheung *et al.* (2012) for AEGIS; Lilly *et al.* (2009), Muzzin *et al.* (2013), and Griffith *et al.* (2012) for COSMOS; and Barro *et al.* (2011a), Williams *et al.* (2014), Guo *et al.* (2013), and Griffith *et al.* (2012) for GOODS-S.

To identify AGN, we use full-band (0.5-10 keV for AEGIS and COSMOS, 0.5-8 keV for GOODS-S) X-ray fluxes from deep Chandra observations described by Laird *et al.* (2009), Civano *et al.* (2012), and Xue *et al.* (2011) for AEGIS, COSMOS, and GOODS-S, respectively. We calculate X-ray luminosities using the equation $L_X = 4\pi d_L^2 f_x (1+z)^{\Gamma-2}$, where d_L is the luminosity distance, z is the redshift, f_x is the flux, and Γ is the power-law photon index. We set $\Gamma = 1.8$, which is a typical power-law photon index for intrinsic AGN spectra. In §4.3.2, we select AGN using these X-ray luminosities.

4.2.1 Galaxy Zoo: Hubble

Our work relies on bar identifications made possible by the Galaxy Zoo: Hubble citizen science project (GZH; Melvin *et al.* 2014). Volunteers were asked to visually classify the morphologies of galaxies at $z \sim 1$ based on HST/ACS optical imaging from the surveys listed above. Like the previous Galaxy Zoo project, Galaxy Zoo 2 (Willett *et al.*, 2013), GZH used a decision tree with multiple branches and nested, dependent questions.[32] These questions include, “Is there a sign of a bar feature through the center of the galaxy?”, which can only be reached if a volunteer identifies some type of a feature (e.g., clumps, spiral arms, rings, bars) or

---

[32] The complete decision tree is available at http://data.galaxyzoo.org/data.

a disk within a galaxy. Thus a galaxy must have a feature or a disk in order to be classified as barred.

Each galaxy is classified by at least 33 volunteers, with the median number of volunteers per galaxy being 47. These classifications produce vote percentages that we refer to throughout as "likelihoods"; e.g., if 25 out of 50 volunteers classified a galaxy as having a bar, then the bar likelihood is $p_{\rm bar} = 0.5$. Classifiers who consistently disagreed with the majority are significantly downweighted when calculating likelihoods (see Lintott *et al.*, 2008, 2011; Willett *et al.*, 2013).

GZH targets in AEGIS and COSMOS have HST/ACS F814W < 23.5 magnitude, and those in GOODS-S have HST/ACS F850LP < 23.5 magnitude. Although there are biases in all magnitude-limited samples, as the experiment that we are conducting is a relative comparison within each sample, it is weakly affected by any incompleteness and contamination within these samples.

4.2.1.1 Selecting Barred Galaxies

We consider galaxies to be barred if they have bar likelihoods greater than 0.5 ($p_{\rm bar} \geq 0.5$) and no obvious dust lanes[33] ($p_{\rm dust\ lane} < 0.5$; dust lanes may be mistaken for a bar). The bar threshold of $p_{\rm bar} = 0.5$ is based on previous Galaxy Zoo works that have shown it to be a reliable indicator of strong bar features (Masters *et al.*, 2011, 2012; Willett *et al.*, 2013; Melvin *et al.*, 2014).

To calculate the bar fraction, $f_{\rm bar}$, one divides the total number of barred galaxies by

---

[33] The exclusion of this criterion does not affect our conclusions

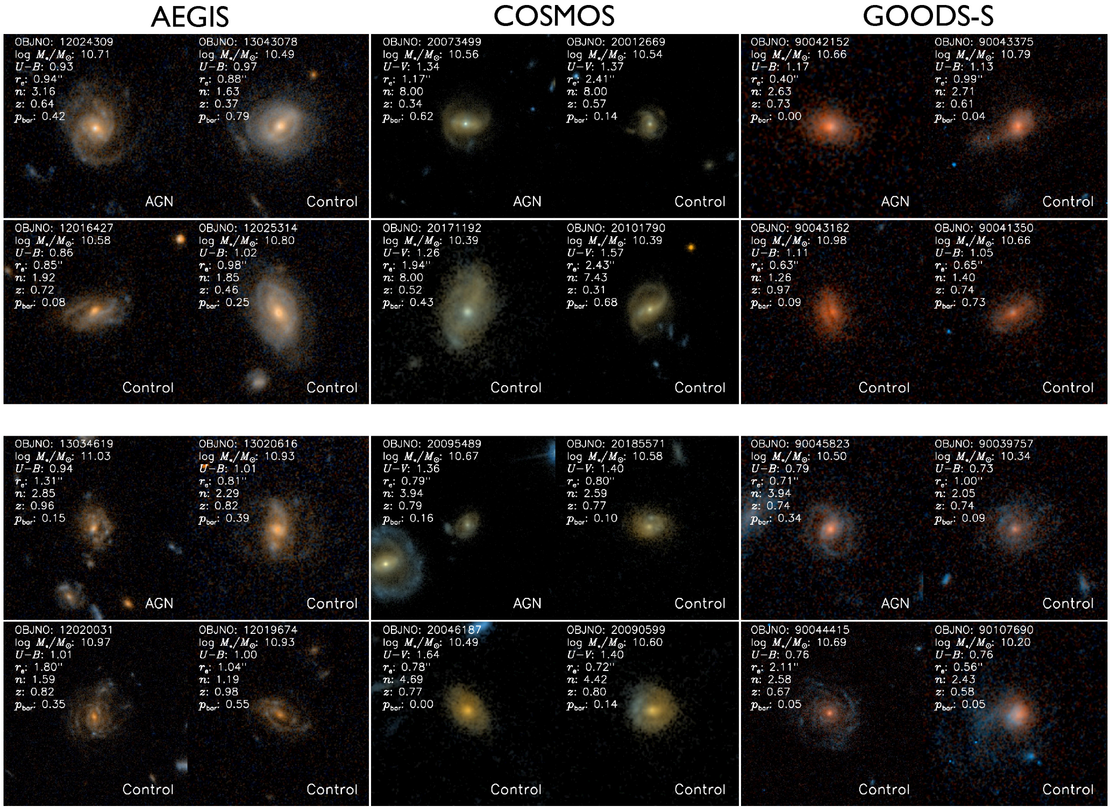

Figure 4.2: HST/ACS images of two matched sets of AGN-control galaxies for AEGIS (left), COSMOS (middle), and GOODS-S (right). Each AGN (upper-left image of each block) has three matched, non-AGN control galaxies. Galaxies with $p_{\rm bar} > 0.5$ are considered barred. Each set of AGN-control galaxies is similar in appearance, demonstrating the quality of our matching technique. Images are from Griffith *et al.* (2012).

the total number of disk galaxies in the sample. Varying the bar likelihood threshold between $0.3 \le p_{\rm bar} \le 0.6$ does not change our conclusions.

In our analysis, we also use the average bar likelihood, $\overline{p}_{\rm bar}$, defined as the average of all the bar likelihoods of a sample of galaxies. This parameter is another measure of bar presence and has been used by other studies (e.g., Skibba *et al.*, 2012; Casteels *et al.*, 2013; Cheung *et al.*, 2013).

4.3 Sample Selection

Since our study seeks to determine if AGN activity is linked with bars, we first construct a parent sample of face-on, disk-dominated objects whose bars can be robustly identified (§4.3.1). We then select AGN-hosting galaxies from this parent sample based on their X-ray luminosity (§4.3.2). Finally, we construct sets of matched AGN-control galaxies using these samples (§4.3.3). The number counts of these samples are listed in Table 4.1.

4.3.1 Face-on Disk Selection

The face-on disk samples for each field are defined by the following criteria:

1. $0.2 < z < 1.0$ – To obtain the most accurate X-ray luminosities and to identify broad-line AGN (which may contaminate their host galaxy measurements), we choose only galaxies with secure spectroscopic redshifts. Including photometric redshifts does not change our conclusions.

2. $b/a > 0.5$ – Since bars in highly inclined galaxies are difficult to identify, we exclude edge-on galaxies with global axis ratios less than or equal to 0.5.

3. $r_e > 8$ pixels – Selecting galaxies with $r_{\rm e}$ larger than 8 pixels, which corresponds to about twice the FWHM of the HST/ACS PSF, ensures that any bars with semimajor axes $\gtrsim 3$ kpc will be identified.

4. $N_{\rm Bar\ question}/N_{\rm Total} \geq 0.15$ – In order to answer the bar question, the GZH decision tree requires a volunteer to classify a galaxy as displaying some kind of feature or disk. Thus

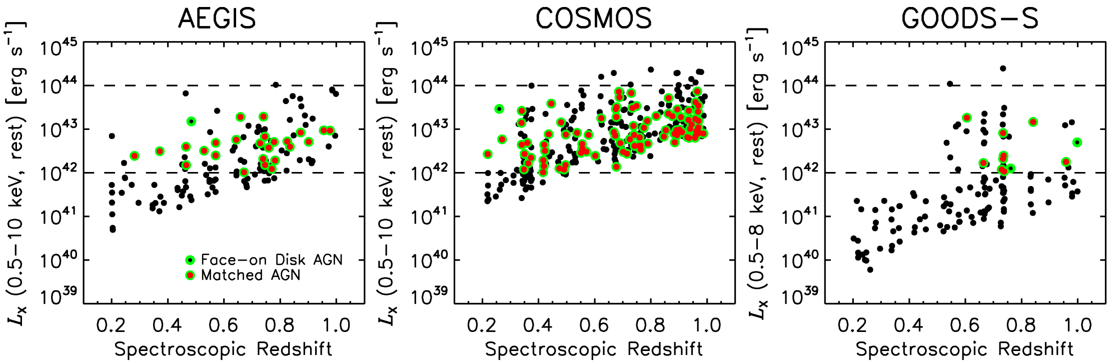

Figure 4.3: X-ray luminosity vs. spectroscopic redshift for all sources detected in the AEGIS (left), COSMOS (middle), and GOODS-S (right) surveys in our chosen redshift range (see §4.2). The dashed horizontal lines represent the lower and upper limits of our AGN selection. Our AGN samples, i.e., the red points encircled in green, are evenly distributed in $L_X - z$ space.

demanding that at least 15% of a galaxy's classifiers answer the bar question results in an effective selection for disk galaxies. Our result is not sensitive to the exact threshold, e.g., requiring $N_{\rm Bar\ question}/N_{\rm Total} \geq 0.75$ does not change our result.

5. $p_{\rm merge} < 0.65$ – In order to separate out the effects of mergers from our analysis, we choose non-interacting galaxies by requiring a merging likelihood less than 0.65 (Melvin *et al.*, 2014). This criterion eliminates a small fraction of our sample, and not applying this criterion does not affect our results.

4.3.2 AGN Selection

Out of these face-on disk samples, one from each survey, we select AGN hosts with X-ray luminosities 10^{42} erg s^{-1} $< L_X <$ 10^{44} erg s^{-1}. The lower limit removes starburst galaxies with weak X-ray emission, and the upper limit excludes quasars that may have optical point sources which would contaminate the other measurements of their host galaxies.

We also discard luminous unobscured AGN which might also contaminate the visible appearance of their host galaxy measurements. In AEGIS and COSMOS, we use broad emission lines since such AGN dominate the optical spectra of their host galaxies. There are zero broad-line AGN in AEGIS and five broad-line AGN in COSMOS, which we reject from our sample. GOODS-S lacks a public catalog of broad-line AGN, and so we instead use low X-ray hardness (HR < -0.3; Mainieri *et al.* 2007) as a proxy for unobscured AGN: this results in the rejection of one AGN. The rejection or inclusion of these six potential-contaminant AGN does not affect the conclusions.

Table 4.1 lists the final AGN count for each survey.

4.3.3 Control Selection

For each AGN host galaxy, we find three unique, non-AGN control galaxies from the *same* survey (AEGIS, COSMOS, or GOODS-S) that are matched in M_*, $U-B$[34], n, r_e, and z. These parameters have been shown to correlate with both AGN presence and bar presence (e.g., Kauffmann *et al.*, 2003a; Nandra *et al.*, 2007; Schawinski *et al.*, 2009b; Masters *et al.*, 2011; Cheung *et al.*, 2013) and thus must be controlled for in order to uncover any underlying bar-AGN connection.

For a given AGN host galaxy, we first select a pool of control galaxies satisfying the following conditions:

- $|\Delta \log M*| < 0.35$
- $|\Delta(U-B)| < 0.4$

---

[34] $U-V$ for COSMOS

- $|\Delta \log\, r_{\rm e}| < 0.48$
- $|\Delta n| < 2.0$
- $|\Delta z| < 0.4$

These limits are tuned in order to find enough control galaxies for each AGN. Our conclusions are not sensitive to the exact limits, e.g., reducing these limits by 50% does not change the conclusions.

With this initial pool of control galaxies, we perform a 5-stage matching process that iteratively reduces the pool until it reaches a final set of three unique and matched control galaxies. The first stage cuts the initial pool of control galaxies to the 15 closest matched galaxies in one of the matching parameters, i.e., $M_{*,\rm AGN}$, $U-B_{\rm AGN}$[21], $n_{\rm AGN}$, $r_{\rm e,AGN}$, or $z_{\rm AGN}$. Each successive stage matches the remaining control galaxies to one of the unused matching parameters and eliminates the three worst matched galaxies. Thus the second stage reduces the pool to 12, the third stage reduces the pool to 9, the fourth reduces the pool to 6, and finally, the fifth stage reduces the pool to 3. Ultimately, for each survey we have a control sample that contains no duplicates and is three times larger than the AGN sample (see Table 4.1).

This 5-stage matching process was performed for each AGN host in our sample. However, there were four AGN—one from AEGIS, one from COSMOS, and two from GOODS-S—that were discarded due to a lack of control galaxies for the AGN host. These host galaxies contained abnormally high n for their rest-frame colors and/or M_* compared to the pool of control galaxies. As the discarded AGN hosts have $p_{\rm bar} < 0.5$, their inclusion could serve only to lower the bar fraction in the AGN samples, bringing the AGN and control samples to even greater agreement in $f_{\rm bar}$ and $p_{\rm bar}$ (see Fig. 4.4). Thus they do not affect our conclusions.

The AGN and control samples that this matching technique produces are affected by the order in which we match the AGN hosts to the control galaxies and the order in which the matching parameters are used. In order to adequately sample the parameter space, we repeat this 5-stage matching technique 100 times for each survey, with each iteration randomly shuffling the order of the AGN hosts, the order of the control galaxies, and the order of the matching parameters. Ultimately, we generate 100 AGN samples and 100 control samples for each survey. For brevity and clarity, we define an "AGN-control sample" to be all AGN hosts and their corresponding control galaxies for a given survey and for a given matching iteration. We use the median counts and the resulting $f_{\rm bar}$ and $\overline{p}_{\rm bar}$ of the 100 AGN-control samples in presenting our results (see Table 4.1).

To demonstrate the quality of our matching procedure, Fig. 4.1 presents stacked histograms of the distribution of parameter differences between the AGN hosts and their matched control galaxies. Each panel stacks 100 translucent histograms, with each histogram representing one AGN-control sample. To elaborate, each histogram represents the difference in a parameter between each AGN and its three control galaxies for a given realization. The highly shaded regions represent the most populated parameter space, which are generally centered around 0, indicating that our matching technique works well. Note that the histograms of GOODS-S are slightly broader and more skewed than those of AEGIS and COSMOS. The relatively small sample size of GOODS-S (see Table 4.1) makes it difficult to identify well-matched control galaxies for the GOODS-S AGN hosts. However, §4.4 shows that the results from the GOODS-S sample are consistent with those of AEGIS and COSMOS, indicating that the skewness of the

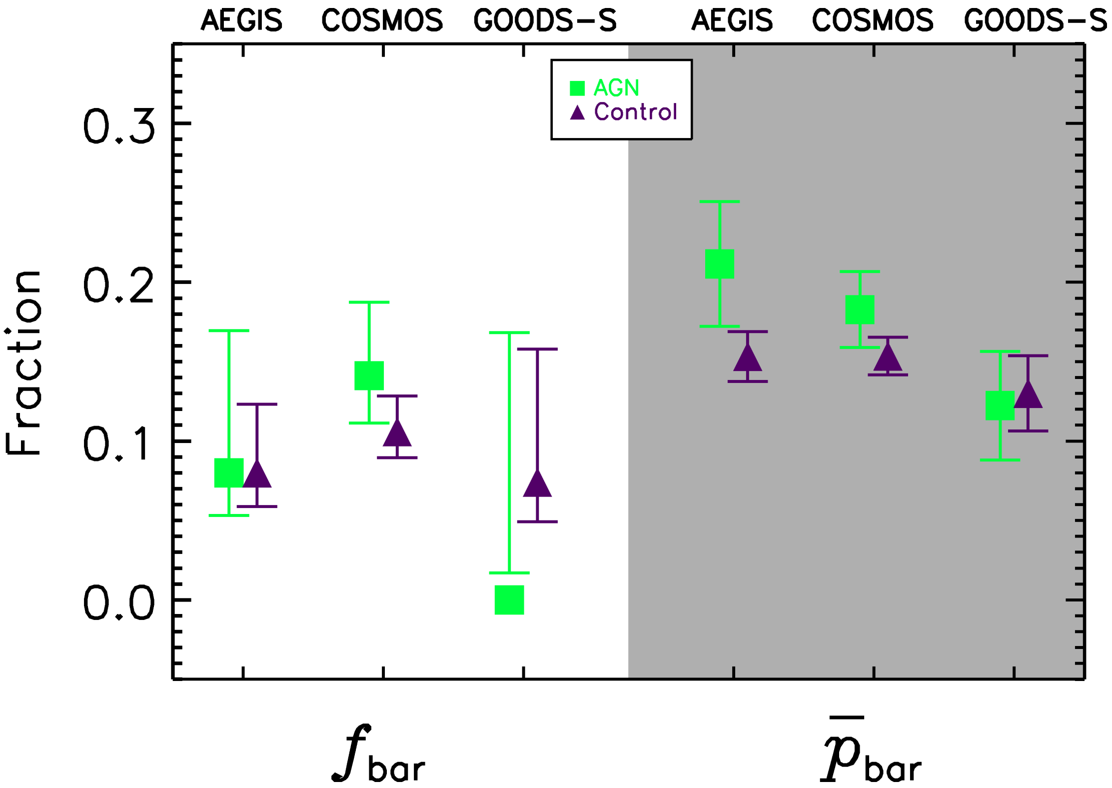

Figure 4.4: *Left*: The bar fraction, $f_{\rm bar}$, of the AGN (green squares) and control samples (purple triangles) for the AEGIS, COSMOS, and GOODS-S surveys. *Right*: The average bar likelihood, $\overline{p}_{\rm bar}$, of the AGN and control samples for the three surveys. The error bars on $f_{\rm bar}$ and $\overline{p}_{\rm bar}$ are the 68.3% binomial confidence limits and standard error, respectively. There is no statistically significant difference in $f_{\rm bar}$ or $\overline{p}_{\rm bar}$ between the AGN and non-AGN control samples across all three surveys, indicating that there is no excess of bars in AGN hosts.

GOODS-S AGN-control samples does not bias our analysis.

To further illustrate the quality of our matching technique, we show images of two matched sets of AGN-control galaxies from each survey in Fig. 4.2. Each set of AGN-control galaxies is reassuringly similar in appearance, confirming that our matching technique is reasonable.

The X-ray luminosity-redshift distribution of all X-ray sources in our chosen redshift range, i.e., from the second row of Table 4.1, is shown in Fig. 4.3. The black points encircled in

Table 4.1: Sample Statistics

Number	AEGIS	COSMOS	GOODS-S
Area (deg^2)	0.197	1.8	0.07
$0.2 < z < 1.0$	3,648	6,673	1,023
Face-on Disk	1,179	2,126	214
AGN	25	85	9
Control	75	255	27
Barred AGN	2	12	0
Barred Control	6	27	2
$f_{\text{bar, AGN}}$	$8.0^{+9.0}_{-2.7}\%$	$14.1^{+4.6}_{-3.0}\%$	$0.0^{+16.8}_{+1.7}\%$
$f_{\text{bar, Control}}$	$8.0^{+4.3}_{-2.1}\%$	$10.6^{+2.2}_{-1.6}\%$	$7.4^{+8.4}_{-2.5}\%$
$\overline{p}_{\text{bar, AGN}}$	$21.2 \pm 3.9\%$	$18.3 \pm 2.4\%$	$12.2 \pm 3.4\%$
$\overline{p}_{\text{bar, Control}}$	$15.3 \pm 1.6\%$	$15.4 \pm 1.2\%$	$13.0 \pm 2.4\%$

Note. — The first row lists the total area covered by each survey. The second row represents the total # of galaxies at $0.2 < z < 1.0$ with secure spectroscopic z's and HST/ACS imaging in our sample, and the third row represents the # of face-on disk galaxies that are in the second row. The rest of the table shows the median counts from the 100 AGN-control samples (see §3.3), and the resulting bar fraction, f_{bar}, and average bar likelihood, $\overline{p}_{\text{bar}}$.

green represent the AGN that satisfy our face-on disk criteria, and hence are eligible to undergo our matching process. The red points encircled in green represent the face-on disk AGN that have enough control galaxies, and thus are in our AGN samples. Fig. 4.3 shows that our AGN samples are evenly distributed in L_X-z space.

4.4 Results & Discussion

The main result of this paper is shown in Fig. 4.4, which plots the bar fraction, $f_{\rm bar}$, and the average bar likelihood, $\overline{p}_{\rm bar}$, of the AGN and non-AGN control samples for the AEGIS, COSMOS, and GOODS-S surveys. The uncertainties shown for $f_{\rm bar}$ are 68.3% binomial confidence limits, calculated using the beta distribution (Cameron, 2011). The uncertainties shown for $\overline{p}_{\rm bar}$ are calculated as $\sigma/\sqrt{N}$, where σ is the standard deviation of $p_{\rm bar}$, and N is the total number of galaxies.

We find no statistically significant enhancement in $f_{\rm bar}$ or $\overline{p}_{\rm bar}$ in AGN hosts compared to the non-AGN control galaxies. The probabilities that each survey's pair of $f_{\rm bar}$'s are different, given the binomial errors, are insignificant ($\lesssim 1\sigma$). Conducting a two-sample Kolmogorov-Smirnov (K-S) test on the $p_{\rm bar}$ distribution of each survey's AGN-control samples reveals that the AGN-control samples are consistent with being drawn from the same parent sample to the 99.9% level. Therefore, we conclude that *there is no excess of bars in AGN hosts*.

A slightly different, but related question is, "Are bars efficient fuelers of AGN?" We answer this question by studying the AGN fraction of barred and non-barred galaxies, as presented in Fig. 4.5. From our face-on disk sample (see §4.3.1), we select barred galaxies with the criteria described in §4.2.1.1. We then create a control sample of non-barred galaxies by demanding that $p_{\rm bar} < 0.05$ and by using our 5-stage matching technique that we described in §4.3.3. That is, for each barred galaxy, we find three non-barred galaxies matched in stellar mass, rest-frame color, size, Sérsic index, and redshift. Using the AGN criteria defined in §4.3.2, Fig. 4.5 shows that there is *no statistically significant excess of AGN among barred* *galaxies.*

At $z \sim 0$, several works have previously found no link between bars and AGN (Ho *et al.* 1997; Mulchaey and Regan 1997; Malkan *et al.* 1998; Hunt and Malkan 1999; Regan and Mulchaey 1999; Martini and Pogge 1999; Erwin and Sparke 2002; Martini *et al.* 2003; Lee *et al.* 2012b; Oh *et al.* 2012; Cisternas *et al.* 2013, but see Laine *et al.* 2002; Knapen *et al.* 2000; Laurikainen *et al.* 2004), and our results show that this absence of direct bar-driven AGN activity persists out to $z = 1$. Our chosen redshift range corresponds to an epoch where approximately half of the local supermassive black hole mass density was formed (Aird *et al.*, 2010), indicating that bars are not directly responsible for the buildup of at least half of the local supermassive black hole mass density. Moreover, the expected paucity of bars at $z > 1$ (Kraljic *et al.* 2012; Simmons et al. 2014, in preparation) indicates that bars were probably not associated with AGN at $z > 1$ either. Therefore, large-scale bars are likely not the primary fueling mechanism for supermassive black hole growth over cosmic time.

However, before ruling out bars as the primary fueling mechanism for supermassive black hole growth, one must ask if the bar–AGN connection can be concealed if a bar dissolves while a black hole is still accreting the bar-funneled gas. In the present analysis, we are assuming that the bar instantaneously funnels gas to the central black hole upon its formation, and moreover, that there is no delay in AGN activity.

The typical lifetimes of AGN and bars are uncertain. For AGN, the current estimates range from 10^6 to 10^8 years (Haehnelt and Rees 1993; Martini 2004, see Hanny's Voorwerp in Keel *et al.* 2012 for an example of an AGN with a short lifetime). For bars, early simulations

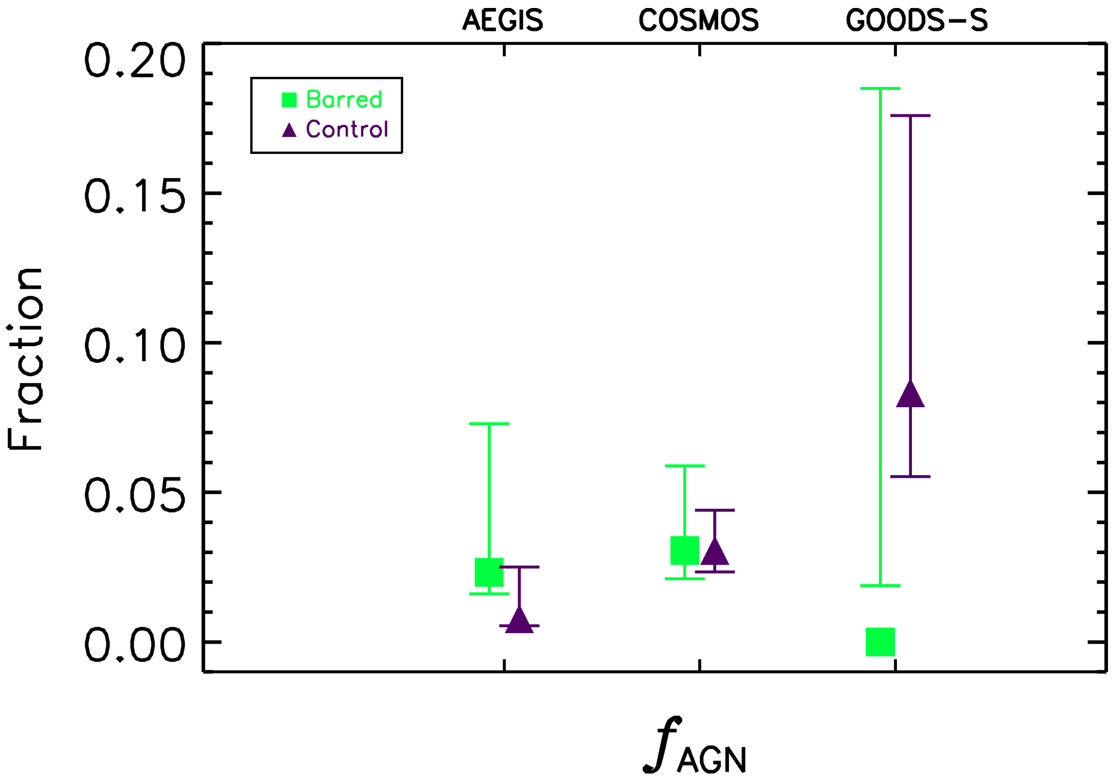

Figure 4.5: The AGN fraction, $f_{\rm AGN}$, of the barred (green squares) and control samples (purple triangles) for the AEGIS, COSMOS, and GOODS-S surveys. The error bars on $f_{\rm AGN}$ are the 68.3% binomial confidence limits. There is no statistically significant difference in $f_{\rm AGN}$ between the barred and non-barred control samples across all three surveys, indicating that there is no excess of AGN in barred galaxies.

of isolated disk galaxies by Bournaud and Combes (2002) indicate that they are short-lived, with a lifetime of 1–2$\times 10^9$ years. The latest simulations of isolated disk galaxies by Athanassoula *et al.* (2013), however, indicate that bars are long-lived, with a lifetime as long as 10^{10} years. This latter result is supported by recent zoom-in cosmological simulations by Kraljic *et al.* (2012), who show that bars formed at $z \approx 1$ generally persist down to $z = 0$. Despite the uncertainty of both AGN and bar lifetimes, even the shortest bar lifetime is an order of magnitude larger than the longest AGN lifetime, meaning that the bar-AGN connection is not likely to be concealed by short bar lifetimes.

Small-scale, nuclear bars may also fuel supermassive black hole growth. Unfortunately, we are unable to resolve such small structures in our images. However, work in the local universe shows that nuclear bars are not more frequent in AGN hosts compared to non-AGN hosts (Mulchaey and Regan, 1997; Regan and Mulchaey, 1999; Martini and Pogge, 1999; Erwin and Sparke, 2002; Laine *et al.*, 2002). This result mirrors that of large-scale bars, suggesting that nuclear bars do not fuel supermassive black hole growth at $z \sim 0$ either. Whether nuclear bars can fuel AGN at $z > 0$ will be left for future work.

Interestingly, studies of the relative angle between AGN accretion disks and host galaxy disks are consistent with our interpretation that bars do not fuel AGN. If AGN accretion disks are fueled by bar-funneled gas, then one would expect this gas to have an angular momentum vector that is parallel to the bulk of the gaseous disk of the galaxy. However, it appears that the accretion disks are randomly orientated with respect to their host galaxies (Ulvestad and Wilson, 1984; Kinney *et al.*, 2000; Schmitt *et al.*, 2002, 2003; Greenhill *et al.*, 2009), which fits with our interpretation that bars do not directly fuel AGN.

This misalignment could be interpreted even more generally—there simply may not be a galactic-scale black hole fueling mechanism. Instead, a collection of processes, including minor mergers (e.g., Kaviraj, 2014b,a), cooling flows (e.g., Best *et al.*, 2007) and multi-body interactions with star clusters or clouds (e.g., Genzel *et al.*, 1994), may work to transport gas into the vicinity of the black hole. This process, known as “stochastic fueling,” (Sanders, 1984) has been implemented in models that successfully reproduce observations of low to intermediate luminosity AGN (Hopkins and Hernquist, 2006; Hopkins *et al.*, 2013).

4.5 Conclusion

In this paper, we present the first study of the bar-AGN connection beyond the local universe. We combine Chandra and Galaxy Zoo: Hubble data in the AEGIS, COSMOS, and GOODS-S surveys to determine whether AGN are preferentially fed by large-scale bars at $0.2 < z < 1.0$.

Using GZH classifications and galaxy structural measurements, we select non-merging, face-on disk galaxies that have sizes large enough to accurately identify large-scale bars. From this face-on disk sample, we identify AGN with X-ray luminosity 10^{42} erg s^{-1} $< L_X < 10^{44}$ erg s^{-1}. We then construct control samples of non-AGN galaxies matched in stellar mass, rest-frame color, Sérsic index, effective radius, and redshift. With these samples, we find no statistically significant excess of barred galaxies in AGN hosts (and no excess of AGN in barred galaxies). The obvious interpretation is that AGN are not preferentially nor directly fed via large-scale bars at $0.2 < z < 1.0$.

Bibliography

Abazajian, K. N.; Adelman-McCarthy, J. K.; Agüeros, M. A.; Allam, S. S.; Allende Prieto, C.; An, D.; Anderson, K. S. J.; Anderson, S. F.; Annis, J.; Bahcall, N. A. and et al. The Seventh Data Release of the Sloan Digital Sky Survey. ApJS **182**, 543 (2009).

Abraham, R. G.; Merrifield, M. R.; Ellis, R. S.; Tanvir, N. R. and Brinchmann, J. The evolution of barred spiral galaxies in the Hubble Deep Fields North and South. MNRAS **308**, 569 (1999).

Abraham, R. G.; Valdes, F.; Yee, H. K. C. and van den Bergh, S. The morphologies of distant galaxies. 1: an automated classification system. ApJ **432**, 75 (1994).

Aguerri, J. A. L.; Méndez-Abreu, J. and Corsini, E. M. The population of barred galaxies in the local universe. I. Detection and characterisation of bars. A&A **495**, 491 (2009).

Aird, J.; Nandra, K.; Laird, E. S.; Georgakakis, A.; Ashby, M. L. N.; Barmby, P.; Coil, A. L.; Huang, J.-S.; Koekemoer, A. M.; Steidel, C. C. and Willmer, C. N. A. The evolution of the hard X-ray luminosity function of AGN. MNRAS **401**, 2531 (2010).

Alexander, D. M.; Swinbank, A. M.; Smail, I.; McDermid, R. and Nesvadba, N. P. H. Searching for evidence of energetic feedback in distant galaxies: a galaxy wide outflow in a z $\sim$ 2 ultraluminous infrared galaxy. MNRAS **402**, 2211 (2010).

Allen, P. D.; Driver, S. P.; Graham, A. W.; Cameron, E.; Liske, J. and de Propris, R. The Millennium Galaxy Catalogue: bulge-disc decomposition of 10095 nearby galaxies. MNRAS **371**, 2 (2006).

Ammons, S. M.; Rosario, D. J. V.; Koo, D. C.; Dutton, A. A.; Melbourne, J.; Max, C. E.; Mozena, M.; Kocevski, D. D.; McGrath, E. J.; Bouwens, R. J. and Magee, D. K. AGN Unification at z $\sim$ 1: u - R Colors and Gradients in X-Ray AGN Hosts. ApJ **740**, 3 (2011).

Arnouts, S.; Walcher, C. J.; Le Fèvre, O.; Zamorani, G.; Ilbert, O.; Le Brun, V.; Pozzetti, L.; Bardelli, S.; Tresse, L.; Zucca, E.; Charlot, S.; Lamareille, F.; McCracken, H. J.; Bolzonella, M.; Iovino, A.; Lonsdale, C.; Polletta, M.; Surace, J.; Bottini, D.; Garilli, B.; Maccagni, D.; Picat, J. P.; Scaramella, R.; Scodeggio, M.; Vettolani, G.; Zanichelli, A.; Adami, C.; Cappi, A.; Ciliegi, P.; Contini, T.; de la Torre, S.; Foucaud, S.; Franzetti, P.; Gavignaud, I.; Guzzo, L.; Marano, B.; Marinoni, C.; Mazure, A.; Meneux, B.; Merighi, R.; Paltani, S.; Pellò, R.; Pollo, A.; Radovich, M.; Temporin, S. and Vergani, D. The SWIRE-VVDS-CFHTLS surveys: stellar mass assembly over the last 10 Gyr. Evidence for a major build up of the red sequence between z = 2 and z = 1. A&A **476**, 137 (2007).

Athanassoula, E. The existence and shapes of dust lanes in galactic bars. MNRAS **259**, 345 (1992).

Athanassoula, E. What determines the strength and the slowdown rate of bars? MNRAS **341**, 1179 (2003).

Athanassoula, E. On the nature of bulges in general and of box/peanut bulges in particular: input from N-body simulations. MNRAS **358**, 1477 (2005).

Athanassoula, E. *Bars and secular evolution in disk galaxies: Theoretical input*, p. 305 (2013).

Athanassoula, E.; Lambert, J. C. and Dehnen, W. Can bars be destroyed by a central mass concentration?- I. Simulations. MNRAS **363**, 496 (2005).

Athanassoula, E.; Machado, R. E. G. and Rodionov, S. A. Bar formation and evolution in disc galaxies with gas and a triaxial halo: morphology, bar strength and halo properties. MNRAS **429**, 1949 (2013).

Athanassoula, E. and Martinet, L. A correlation between the lengths of bars and the sizes of bulges. A&A **87**, L10 (1980).

Athanassoula, E. and Misiriotis, A. Morphology, photometry and kinematics of N -body bars - I. Three models with different halo central concentrations. MNRAS **330**, 35 (2002).

Athanassoula, E. and Sellwood, J. A. Bi-symmetric instabilities of the Kuz'min/Toomre disc. MNRAS **221**, 213 (1986).

Baldry, I. K. Hubble's galaxy nomenclature. *Astronomy and Geophysics* **49**, 050000 (2008).

Baldwin, J. A.; Phillips, M. M. and Terlevich, R. Classification parameters for the emission-line spectra of extragalactic objects. PASP **93**, 5 (1981).

Bamford, S. P.; Nichol, R. C.; Baldry, I. K.; Land, K.; Lintott, C. J.; Schawinski, K.; Slosar, A.; Szalay, A. S.; Thomas, D.; Torki, M.; Andreescu, D.; Edmondson, E. M.; Miller, C. J.; Murray, P.; Raddick, M. J. and Vandenberg, J. Galaxy Zoo: the dependence of morphology and colour on environment. MNRAS **393**, 1324 (2009).

Barazza, F. D.; Jogee, S. and Marinova, I. Bars in Disk-dominated and Bulge-dominated Galaxies at z $\sim$ 0: New Insights from $\sim$3600 SDSS Galaxies. ApJ **675**, 1194 (2008).

Barmby, P.; Huang, J.-S.; Ashby, M. L. N.; Eisenhardt, P. R. M.; Fazio, G. G.; Willner, S. P. and Wright, E. L. A Catalog of Mid-Infrared Sources in the Extended Groth Strip. ApJS **177**, 431 (2008).

Barnes, J. E. and Hernquist, L. E. Fueling starburst galaxies with gas-rich mergers. ApJ **370**, L65 (1991).

Barro, G.; Faber, S. M.; Pérez-González, P. G.; Koo, D. C.; Williams, C. C.; Kocevski, D. D.; Trump, J. R.; Mozena, M.; McGrath, E.; van der Wel, A.; Wuyts, S.; Bell, E. F.; Croton, D. J.; Ceverino, D.; Dekel, A.; Ashby, M. L. N.; Cheung, E.; Ferguson, H. C.; Fontana, A.; Fang, J.; Giavalisco, M.; Grogin, N. A.; Guo, Y.; Hathi, N. P.; Hopkins, P. F.; Huang, K.-H.; Koekemoer, A. M.; Kartaltepe, J. S.; Lee, K.-S.; Newman, J. A.; Porter, L. A.; Primack, J. R.; Ryan, R. E.; Rosario, D.; Somerville, R. S.; Salvato, M. and Hsu, L.-T. CANDELS: The Progenitors of Compact Quiescent Galaxies at z $\sim$ 2. ApJ **765**, 104 (2013).

Barro, G.; Pérez-González, P. G.; Gallego, J.; Ashby, M. L. N.; Kajisawa, M.; Miyazaki, S.; Villar, V.; Yamada, T. and Zamorano, J. UV-to-FIR Analysis of Spitzer/IRAC Sources in the

Extended Groth Strip. I. Multi-wavelength Photometry and Spectral Energy Distributions. ApJS **193**, 13 (2011a).

Barro, G.; Pérez-González, P. G.; Gallego, J.; Ashby, M. L. N.; Kajisawa, M.; Miyazaki, S.; Villar, V.; Yamada, T. and Zamorano, J. UV-to-FIR Analysis of Spitzer/IRAC Sources in the Extended Groth Strip. II. Photometric Redshifts, Stellar Masses, and Star Formation Rates. ApJS **193**, 30 (2011b).

Bell, E. F. Galaxy Bulges and their Black Holes: a Requirement for the Quenching of Star Formation. ApJ **682**, 355 (2008).

Bell, E. F. and de Jong, R. S. Stellar Mass-to-Light Ratios and the Tully-Fisher Relation. ApJ **550**, 212 (2001).

Bell, E. F.; McIntosh, D. H.; Barden, M.; Wolf, C.; Caldwell, J. A. R.; Rix, H.-W.; Beckwith, S. V. W.; Borch, A.; Häussler, B.; Jahnke, K.; Jogee, S.; Meisenheimer, K.; Peng, C.; Sanchez, S. F.; Somerville, R. S. and Wisotzki, L. GEMS Imaging of Red-Sequence Galaxies at z$\sim$0.7: Dusty or Old? ApJ **600**, L11 (2004a).

Bell, E. F.; Phleps, S.; Somerville, R. S.; Wolf, C.; Borch, A. and Meisenheimer, K. The Merger Rate of Massive Galaxies. ApJ **652**, 270 (2006).

Bell, E. F.; van der Wel, A.; Papovich, C.; Kocevski, D.; Lotz, J.; McIntosh, D. H.; Kartaltepe, J.; Faber, S. M.; Ferguson, H.; Koekemoer, A.; Grogin, N.; Wuyts, S.; Cheung, E.; Conselice, C. J.; Dekel, A.; Dunlop, J. S.; Giavalisco, M.; Herrington, J.; Koo, D. C.; McGrath, E. J.; de Mello, D.; Rix, H.-W.; Robaina, A. R. and Williams, C. C. What Turns Galaxies

Off? The Different Morphologies of Star-forming and Quiescent Galaxies since z $\sim$ 2 from CANDELS. ApJ **753**, 167 (2012).

Bell, E. F.; Wolf, C.; Meisenheimer, K.; Rix, H.-W.; Borch, A.; Dye, S.; Kleinheinrich, M.; Wisotzki, L. and McIntosh, D. H. Nearly 5000 Distant Early-Type Galaxies in COMBO-17: A Red Sequence and Its Evolution since z$\sim$1. ApJ **608**, 752 (2004b).

Berentzen, I.; Heller, C. H.; Shlosman, I. and Fricke, K. J. Gas-driven evolution of stellar orbits in barred galaxies. MNRAS **300**, 49 (1998).

Berentzen, I.; Shlosman, I.; Martinez-Valpuesta, I. and Heller, C. H. Gas Feedback on Stellar Bar Evolution. ApJ **666**, 189 (2007).

Bertin, E. and Arnouts, S. SExtractor: Software for source extraction. A&AS **117**, 393 (1996).

Best, P. N.; von der Linden, A.; Kauffmann, G.; Heckman, T. M. and Kaiser, C. R. On the prevalence of radio-loud active galactic nuclei in brightest cluster galaxies: implications for AGN heating of cooling flows. MNRAS **379**, 894 (2007).

Bezanson, R.; van Dokkum, P. G.; Franx, M.; Brammer, G. B.; Brinchmann, J.; Kriek, M.; Labbé, I.; Quadri, R. F.; Rix, H.-W.; van de Sande, J.; Whitaker, K. E. and Williams, R. J. Redshift Evolution of the Galaxy Velocity Dispersion Function. ApJ **737**, L31 (2011).

Bigiel, F.; Leroy, A.; Walter, F.; Brinks, E.; de Blok, W. J. G.; Madore, B. and Thornley, M. D. The Star Formation Law in Nearby Galaxies on Sub-Kpc Scales. AJ **136**, 2846 (2008).

Birnboim, Y. and Dekel, A. Virial shocks in galactic haloes? MNRAS **345**, 349 (2003).

Birnboim, Y. and Dekel, A. Gravitational quenching by clumpy accretion in cool-core clusters: convective dynamical response to overheating. MNRAS **415**, 2566 (2011).

Blanton, M. R.; Eisenstein, D.; Hogg, D. W.; Schlegel, D. J. and Brinkmann, J. Relationship between Environment and the Broadband Optical Properties of Galaxies in the Sloan Digital Sky Survey. ApJ **629**, 143 (2005a).

Blanton, M. R.; Hogg, D. W.; Bahcall, N. A.; Baldry, I. K.; Brinkmann, J.; Csabai, I.; Eisenstein, D.; Fukugita, M.; Gunn, J. E.; Ivezić, Ž.; Lamb, D. Q.; Lupton, R. H.; Loveday, J.; Munn, J. A.; Nichol, R. C.; Okamura, S.; Schlegel, D. J.; Shimasaku, K.; Strauss, M. A.; Vogeley, M. S. and Weinberg, D. H. The Broadband Optical Properties of Galaxies with Redshifts $0.02 < z < 0.22$. ApJ **594**, 186 (2003).

Blanton, M. R. and Roweis, S. K-Corrections and Filter Transformations in the Ultraviolet, Optical, and Near-Infrared. AJ **133**, 734 (2007).

Blanton, M. R.; Schlegel, D. J.; Strauss, M. A.; Brinkmann, J.; Finkbeiner, D.; Fukugita, M.; Gunn, J. E.; Hogg, D. W.; Ivezić, Ž.; Knapp, G. R.; Lupton, R. H.; Munn, J. A.; Schneider, D. P.; Tegmark, M. and Zehavi, I. New York University Value-Added Galaxy Catalog: A Galaxy Catalog Based on New Public Surveys. AJ **129**, 2562 (2005b).

Block, D. L.; Buta, R.; Knapen, J. H.; Elmegreen, D. M.; Elmegreen, B. G. and Puerari, I. Gravitational Bar and Spiral Arm Torques from K_s-band Observations and Implications for the Pattern Speeds. AJ **128**, 183 (2004).

Bluck, A. F. L.; Conselice, C. J.; Buitrago, F.; Grützbauch, R.; Hoyos, C.; Mortlock, A. and Bauer, A. E. The Structures and Total (Minor + Major) Merger Histories of Massive Galaxies up to z $\sim$ 3 in the HST GOODS NICMOS Survey: A Possible Solution to the Size Evolution Problem. ApJ **747**, 34 (2012).

Blumenthal, G. R.; Faber, S. M.; Primack, J. R. and Rees, M. J. Formation of galaxies and large-scale structure with cold dark matter. Nature **311**, 517 (1984).

Borch, A.; Meisenheimer, K.; Bell, E. F.; Rix, H.-W.; Wolf, C.; Dye, S.; Kleinheinrich, M.; Kovacs, Z. and Wisotzki, L. The stellar masses of 25 000 galaxies at 0.2 $\leq$ z $\leq$ 1.0 estimated by the COMBO-17 survey. A&A **453**, 869 (2006).

Bournaud, F. and Combes, F. Gas accretion on spiral galaxies: Bar formation and renewal. A&A **392**, 83 (2002).

Bournaud, F.; Jog, C. J. and Combes, F. Multiple minor mergers: formation of elliptical galaxies and constraints for the growth of spiral disks. A&A **476**, 1179 (2007).

Bournaud, F.; Juneau, S.; Le Floc'h, E.; Mullaney, J.; Daddi, E.; Dekel, A.; Duc, P.-A.; Elbaz, D.; Salmi, F. and Dickinson, M. An Observed Link between Active Galactic Nuclei and Violent Disk Instabilities in High-redshift Galaxies. ApJ **757**, 81 (2012).

Brammer, G. B.; Whitaker, K. E.; van Dokkum, P. G.; Marchesini, D.; Franx, M.; Kriek, M.; Labbé, I.; Lee, K.-S.; Muzzin, A.; Quadri, R. F.; Rudnick, G. and Williams, R. The Number Density and Mass Density of Star-forming and Quiescent Galaxies at 0.4 $<=$ z $<=$ 2.2. ApJ **739**, 24 (2011).

Brinchmann, J.; Charlot, S.; White, S. D. M.; Tremonti, C.; Kauffmann, G.; Heckman, T. and Brinkmann, J. The physical properties of star-forming galaxies in the low-redshift Universe. MNRAS **351**, 1151 (2004).

Brown, M. J. I.; Dey, A.; Jannuzi, B. T.; Brand, K.; Benson, A. J.; Brodwin, M.; Croton, D. J. and Eisenhardt, P. R. The Evolving Luminosity Function of Red Galaxies. ApJ **654**, 858 (2007).

Bruzual, G. and Charlot, S. Stellar population synthesis at the resolution of 2003. MNRAS **344**, 1000 (2003).

Buitrago, F.; Trujillo, I.; Conselice, C. J.; Bouwens, R. J.; Dickinson, M. and Yan, H. Size Evolution of the Most Massive Galaxies at $1.7 < z < 3$ from GOODS NICMOS Survey Imaging. ApJ **687**, L61 (2008).

Buitrago, F.; Trujillo, I.; Conselice, C. J. and Häußler, B. Early-type galaxies have been the predominant morphological class for massive galaxies since only $z \sim 1$. MNRAS **428**, 1460 (2013).

Bundy, K.; Ellis, R. S.; Conselice, C. J.; Taylor, J. E.; Cooper, M. C.; Willmer, C. N. A.; Weiner, B. J.; Coil, A. L.; Noeske, K. G. and Eisenhardt, P. R. M. The Mass Assembly History of Field Galaxies: Detection of an Evolving Mass Limit for Star-Forming Galaxies. ApJ **651**, 120 (2006).

Bundy, K.; Fukugita, M.; Ellis, R. S.; Targett, T. A.; Belli, S. and Kodama, T. The Greater Impact of Mergers on the Growth of Massive Galaxies: Implications for Mass Assembly and

Evolution since z sime 1. ApJ **697**, 1369 (2009).

Bundy, K.; Scarlata, C.; Carollo, C. M.; Ellis, R. S.; Drory, N.; Hopkins, P.; Salvato, M.; Leauthaud, A.; Koekemoer, A. M.; Murray, N.; Ilbert, O.; Oesch, P.; Ma, C.-P.; Capak, P.; Pozzetti, L. and Scoville, N. The Rise and Fall of Passive Disk Galaxies: Morphological Evolution Along the Red Sequence Revealed by COSMOS. ApJ **719**, 1969 (2010).

Cameron, E. On the Estimation of Confidence Intervals for Binomial Population Proportions in Astronomy: The Simplicity and Superiority of the Bayesian Approach. PASA **28**, 128 (2011).

Cameron, E.; Carollo, C. M.; Oesch, P.; Aller, M. C.; Bschorr, T.; Cerulo, P.; Aussel, H.; Capak, P.; Le Floc'h, E.; Ilbert, O.; Kneib, J.-P.; Koekemoer, A.; Leauthaud, A.; Lilly, S. J.; Massey, R.; McCracken, H. J.; Rhodes, J.; Salvato, M.; Sanders, D. B.; Scoville, N.; Sheth, K.; Taniguchi, Y. and Thompson, D. Bars in early- and late-type discs in COSMOS. MNRAS **409**, 346 (2010).

Cano-Díaz, M.; Maiolino, R.; Marconi, A.; Netzer, H.; Shemmer, O. and Cresci, G. Observational evidence of quasar feedback quenching star formation at high redshift. A&A **537**, L8 (2012).

Capaccioli, M. Photometry of early-type galaxies and the R exp 1/4 law. In Corwin, Jr., H. G. and Bottinelli, L., eds., *World of Galaxies (Le Monde des Galaxies)* (1989), pp. 208–227.

Casteels, K. R. V.; Bamford, S. P.; Skibba, R. A.; Masters, K. L.; Lintott, C. J.; Keel, W. C.; Schawinski, K.; Nichol, R. C. and Smith, A. M. Galaxy Zoo: quantifying morphological indicators of galaxy interaction. MNRAS **429**, 1051 (2013).

Catinella, B.; Schiminovich, D.; Kauffmann, G.; Fabello, S.; Wang, J.; Hummels, C.; Lemonias, J.; Moran, S. M.; Wu, R.; Giovanelli, R.; Haynes, M. P.; Heckman, T. M.; Basu-Zych, A. R.; Blanton, M. R.; Brinchmann, J.; Budavári, T.; Gonçalves, T.; Johnson, B. D.; Kennicutt, R. C.; Madore, B. F.; Martin, C. D.; Rich, M. R.; Tacconi, L. J.; Thilker, D. A.; Wild, V. and Wyder, T. K. The GALEX Arecibo SDSS Survey - I. Gas fraction scaling relations of massive galaxies and first data release. MNRAS **403**, 683 (2010).

Cattaneo, A.; Dekel, A.; Devriendt, J.; Guiderdoni, B. and Blaizot, J. Modelling the galaxy bimodality: shutdown above a critical halo mass. MNRAS **370**, 1651 (2006).

Ceverino, D.; Dekel, A. and Bournaud, F. High-redshift clumpy discs and bulges in cosmological simulations. MNRAS **404**, 2151 (2010).

Cheung, E.; Athanassoula, E.; Masters, K. L.; Nichol, R. C.; Bosma, A.; Bell, E. F.; Faber, S. M.; Koo, D. C.; Lintott, C.; Melvin, T.; Schawinski, K.; Skibba, R. A. and Willett, K. W. Galaxy Zoo: Observing Secular Evolution through Bars. ApJ **779**, 162 (2013).

Cheung, E.; Faber, S. M.; Koo, D. C.; Dutton, A. A.; Simard, L.; McGrath, E. J.; Huang, J.-S.; Bell, E. F.; Dekel, A.; Fang, J. J.; Salim, S.; Barro, G.; Bundy, K.; Coil, A. L.; Cooper, M. C.; Conselice, C. J.; Davis, M.; Domínguez, A.; Kassin, S. A.; Kocevski, D. D.; Koekemoer, A. M.; Lin, L.; Lotz, J. M.; Newman, J. A.; Phillips, A. C.; Rosario, D. J.; Weiner, B. J. and Willmer, C. N. A. The Dependence of Quenching upon the Inner Structure of Galaxies at 0.5 <= z < 0.8 in the DEEP2/AEGIS Survey. ApJ **760**, 131 (2012).

Ciotti, L.; Ostriker, J. P. and Proga, D. Feedback from Central Black Holes in Elliptical Galaxies. I. Models with Either Radiative or Mechanical Feedback but not Both. ApJ **699**, 89 (2009).

Cisternas, M.; Gadotti, D. A.; Knapen, J. H.; Kim, T.; Díaz-García, S.; Laurikainen, E.; Salo, H.; González-Martín, O.; Ho, L. C.; Elmegreen, B. G.; Zaritsky, D.; Sheth, K.; Athanassoula, E.; Bosma, A.; Comerón, S.; Erroz-Ferrer, S.; Gil de Paz, A.; Hinz, J. L.; Holwerda, B. W.; Laine, J.; Meidt, S.; Menéndez-Delmestre, K.; Mizusawa, T.; Muñoz-Mateos, J. C.; Regan, M. W. and Seibert, M. X-Ray Nuclear Activity in S^4G Barred Galaxies: No Link between Bar Strength and Co-occurrent Supermassive Black Hole Fueling. ApJ **776**, 50 (2013).

Cisternas, M.; Jahnke, K.; Inskip, K. J.; Kartaltepe, J.; Koekemoer, A. M.; Lisker, T.; Robaina, A. R.; Scodeggio, M.; Sheth, K.; Trump, J. R.; Andrae, R.; Miyaji, T.; Lusso, E.; Brusa, M.; Capak, P.; Cappelluti, N.; Civano, F.; Ilbert, O.; Impey, C. D.; Leauthaud, A.; Lilly, S. J.; Salvato, M.; Scoville, N. Z. and Taniguchi, Y. The Bulk of the Black Hole Growth Since $z \sim 1$ Occurs in a Secular Universe: No Major Merger-AGN Connection. ApJ **726**, 57 (2011).

Civano, F.; Elvis, M.; Brusa, M.; Comastri, A.; Salvato, M.; Zamorani, G.; Aldcroft, T.; Bongiorno, A.; Capak, P.; Cappelluti, N.; Cisternas, M.; Fiore, F.; Fruscione, A.; Hao, H.; Kartaltepe, J.; Koekemoer, A.; Gilli, R.; Impey, C. D.; Lanzuisi, G.; Lusso, E.; Mainieri, V.; Miyaji, T.; Lilly, S.; Masters, D.; Puccetti, S.; Schawinski, K.; Scoville, N. Z.; Silverman, J.; Trump, J.; Urry, M.; Vignali, C. and Wright, N. J. The Chandra COSMOS Survey. III. Optical and Infrared Identification of X-Ray Point Sources. ApJS **201**, 30 (2012).

Coelho, P. and Gadotti, D. A. Bars Rejuvenating Bulges? Evidence from Stellar Population Analysis. ApJ **743**, L13 (2011).

Coil, A. L.; Newman, J. A.; Kaiser, N.; Davis, M.; Ma, C.-P.; Kocevski, D. D. and Koo, D. C. Evolution and Color Dependence of the Galaxy Angular Correlation Function: 350,000 Galaxies in 5 Square Degrees. ApJ **617**, 765 (2004).

Coil, A. L.; Weiner, B. J.; Holz, D. E.; Cooper, M. C.; Yan, R. and Aird, J. Outflowing Galactic Winds in Post-starburst and Active Galactic Nucleus Host Galaxies at $0.2 < z < 0.8$. ApJ **743**, 46 (2011).

Collister, A. A. and Lahav, O. ANNz: Estimating Photometric Redshifts Using Artificial Neural Networks. PASP **116**, 345 (2004).

Combes, F. and Elmegreen, B. G. Bars in Early Type and Late Type Galaxies. A&A **271**, 391 (1993).

Conroy, C. and Wechsler, R. H. Connecting Galaxies, Halos, and Star Formation Rates Across Cosmic Time. ApJ **696**, 620 (2009).

Conselice, C. J. Early and Rapid Merging as a Formation Mechanism of Massive Galaxies: Empirical Constraints. ApJ **638**, 686 (2006).

Cooper, M. C.; Aird, J. A.; Coil, A. L.; Davis, M.; Faber, S. M.; Juneau, S.; Lotz, J. M.; Nandra, K.; Newman, J. A.; Willmer, C. N. A. and Yan, R. The DEEP3 Galaxy Redshift Survey: Keck/DEIMOS Spectroscopy in the GOODS-N Field. ApJS **193**, 14 (2011).

Cooper, M. C.; Griffith, R. L.; Newman, J. A.; Coil, A. L.; Davis, M.; Dutton, A. A.; Faber, S. M.; Guhathakurta, P.; Koo, D. C.; Lotz, J. M.; Weiner, B. J.; Willmer, C. N. A. and Yan, R. The DEEP3 Galaxy Redshift Survey: the impact of environment on the size evolution of massive early-type galaxies at intermediate redshift. MNRAS **419**, 3018 (2012).

Cortese, L. and Hughes, T. M. Evolutionary paths to and from the red sequence: star formation and HI properties of transition galaxies at z $\sim$ 0. MNRAS **400**, 1225 (2009).

Couch, W. J. and Sharples, R. M. A spectroscopic study of three rich galaxy clusters at Z = 0.31. MNRAS **229**, 423 (1987).

Courteau, S.; de Jong, R. S. and Broeils, A. H. Evidence for Secular Evolution in Late-Type Spirals. ApJ **457**, L73 (1996).

Cowie, L. L.; Songaila, A.; Hu, E. M. and Cohen, J. G. New Insight on Galaxy Formation and Evolution From Keck Spectroscopy of the Hawaii Deep Fields. AJ **112**, 839 (1996).

Cox, T. J.; Jonsson, P.; Somerville, R. S.; Primack, J. R. and Dekel, A. The effect of galaxy mass ratio on merger-driven starbursts. MNRAS **384**, 386 (2008).

Croton, D. J.; Springel, V.; White, S. D. M.; De Lucia, G.; Frenk, C. S.; Gao, L.; Jenkins, A.; Kauffmann, G.; Navarro, J. F. and Yoshida, N. The many lives of active galactic nuclei: cooling flows, black holes and the luminosities and colours of galaxies. MNRAS **365**, 11 (2006).

Daddi, E.; Renzini, A.; Pirzkal, N.; Cimatti, A.; Malhotra, S.; Stiavelli, M.; Xu, C.; Pasquali, A.; Rhoads, J. E.; Brusa, M.; di Serego Alighieri, S.; Ferguson, H. C.; Koekemoer, A. M.;

Moustakas, L. A.; Panagia, N. and Windhorst, R. A. Passively Evolving Early-Type Galaxies at $1.4 \lesssim z \lesssim 2.5$ in the Hubble Ultra Deep Field. ApJ **626**, 680 (2005).

Darg, D. W.; Kaviraj, S.; Lintott, C. J.; Schawinski, K.; Sarzi, M.; Bamford, S.; Silk, J.; Proctor, R.; Andreescu, D.; Murray, P.; Nichol, R. C.; Raddick, M. J.; Slosar, A.; Szalay, A. S.; Thomas, D. and Vandenberg, J. Galaxy Zoo: the fraction of merging galaxies in the SDSS and their morphologies. MNRAS **401**, 1043 (2010).

Davis, M.; Faber, S. M.; Newman, J.; Phillips, A. C.; Ellis, R. S.; Steidel, C. C.; Conselice, C.; Coil, A. L.; Finkbeiner, D. P.; Koo, D. C.; Guhathakurta, P.; Weiner, B.; Schiavon, R.; Willmer, C.; Kaiser, N.; Luppino, G. A.; Wirth, G.; Connolly, A.; Eisenhardt, P.; Cooper, M. and Gerke, B. Science Objectives and Early Results of the DEEP2 Redshift Survey. In Guhathakurta, P., ed., *Discoveries and Research Prospects from 6- to 10-Meter-Class Telescopes II* (2003), vol. 4834 of *Society of Photo-Optical Instrumentation Engineers (SPIE) Conference Series*, pp. 161–172.

Davis, M.; Guhathakurta, P.; Konidaris, N. P.; Newman, J. A.; Ashby, M. L. N.; Biggs, A. D.; Barmby, P.; Bundy, K.; Chapman, S. C.; Coil, A. L.; Conselice, C. J.; Cooper, M. C.; Croton, D. J.; Eisenhardt, P. R. M.; Ellis, R. S.; Faber, S. M.; Fang, T.; Fazio, G. G.; Georgakakis, A.; Gerke, B. F.; Goss, W. M.; Gwyn, S.; Harker, J.; Hopkins, A. M.; Huang, J.-S.; Ivison, R. J.; Kassin, S. A.; Kirby, E. N.; Koekemoer, A. M.; Koo, D. C.; Laird, E. S.; Le Floc'h, E.; Lin, L.; Lotz, J. M.; Marshall, P. J.; Martin, D. C.; Metevier, A. J.; Moustakas, L. A.; Nandra, K.; Noeske, K. G.; Papovich, C.; Phillips, A. C.; Rich, R. M.; Rieke, G. H.; Rigopoulou, D.; Salim, S.; Schiminovich, D.; Simard, L.; Smail, I.; Small, T. A.; Weiner, B. J.; Willmer,

C. N. A.; Willner, S. P.; Wilson, G.; Wright, E. L. and Yan, R. The All-Wavelength Extended Groth Strip International Survey (AEGIS) Data Sets. ApJ **660**, L1 (2007).

De Propris, R.; Stanford, S. A.; Eisenhardt, P. R.; Holden, B. P. and Rosati, P. The Rest-Frame K-Band Luminosity Function of Galaxies in Clusters to z = 1.3. AJ **133**, 2209 (2007).

de Souza, R. E.; Gadotti, D. A. and dos Anjos, S. BUDDA: A New Two-dimensional Bulge/Disk Decomposition Code for Detailed Structural Analysis of Galaxies. ApJS **153**, 411 (2004).

Debattista, V. P.; Mayer, L.; Carollo, C. M.; Moore, B.; Wadsley, J. and Quinn, T. The Secular Evolution of Disk Structural Parameters. ApJ **645**, 209 (2006).

Debattista, V. P. and Sellwood, J. A. Constraints from Dynamical Friction on the Dark Matter Content of Barred Galaxies. ApJ **543**, 704 (2000).

Dekel, A. and Birnboim, Y. Galaxy bimodality due to cold flows and shock heating. MNRAS **368**, 2 (2006).

Dekel, A.; Sari, R. and Ceverino, D. Formation of Massive Galaxies at High Redshift: Cold Streams, Clumpy Disks, and Compact Spheroids. ApJ **703**, 785 (2009).

Di Matteo, T.; Springel, V. and Hernquist, L. Energy input from quasars regulates the growth and activity of black holes and their host galaxies. Nature **433**, 604 (2005).

Domínguez, A.; Primack, J. R.; Rosario, D. J.; Prada, F.; Gilmore, R. C.; Faber, S. M.; Koo, D. C.; Somerville, R. S.; Pérez-Torres, M. A.; Pérez-González, P.; Huang, J.-S.; Davis, M.;

Guhathakurta, P.; Barmby, P.; Conselice, C. J.; Lozano, M.; Newman, J. A. and Cooper, M. C. Extragalactic background light inferred from AEGIS galaxy-SED-type fractions. MNRAS **410**, 2556 (2011).

Dressel, L. L. Powerful warm infrared sources in early-type galaxies. ApJ **329**, L69 (1988).

Dressler, A. Galaxy morphology in rich clusters - Implications for the formation and evolution of galaxies. ApJ **236**, 351 (1980).

Dressler, A. and Gunn, J. E. Spectroscopy of galaxies in distant clusters. II - The population of the 3C 295 cluster. ApJ **270**, 7 (1983).

Driver, S. P.; Allen, P. D.; Graham, A. W.; Cameron, E.; Liske, J.; Ellis, S. C.; Cross, N. J. G.; De Propris, R.; Phillipps, S. and Couch, W. J. The Millennium Galaxy Catalogue: morphological classification and bimodality in the colour-concentration plane. MNRAS **368**, 414 (2006).

Driver, S. P.; Allen, P. D.; Liske, J. and Graham, A. W. The Millennium Galaxy Catalogue: The Luminosity Functions of Bulges and Disks and Their Implied Stellar Mass Densities. ApJ **657**, L85 (2007).

Drory, N. and Fisher, D. B. A Connection between Bulge Properties and the Bimodality of Galaxies. ApJ **664**, 640 (2007).

Ellison, S. L.; Nair, P.; Patton, D. R.; Scudder, J. M.; Mendel, J. T. and Simard, L. The impact of gas inflows on star formation rates and metallicities in barred galaxies. MNRAS **416**, 2182 (2011).

Elmegreen, B. G.; Bournaud, F. and Elmegreen, D. M. Bulge Formation by the Coalescence of Giant Clumps in Primordial Disk Galaxies. ApJ **688**, 67 (2008).

Elmegreen, B. G. and Elmegreen, D. M. Properties of barred spiral galaxies. ApJ **288**, 438 (1985).

Elmegreen, B. G.; Elmegreen, D. M. and Hirst, A. C. A Constant Bar Fraction out to Redshift z ˜ 1 in the Advanced Camera for Surveys Field of the Tadpole Galaxy. ApJ **612**, 191 (2004).

Elmegreen, B. G.; Elmegreen, D. M.; Knapen, J. H.; Buta, R. J.; Block, D. L. and Puerari, I. Variation of Galactic Bar Length with Amplitude and Density as Evidence for Bar Growth over a Hubble Time. ApJ **670**, L97 (2007).

Erwin, P. How large are the bars in barred galaxies? MNRAS **364**, 283 (2005).

Erwin, P. and Sparke, L. S. Double Bars, Inner Disks, and Nuclear Rings in Early-Type Disk Galaxies. AJ **124**, 65 (2002).

Eskridge, P. B.; Frogel, J. A.; Pogge, R. W.; Quillen, A. C.; Davies, R. L.; DePoy, D. L.; Houdashelt, M. L.; Kuchinski, L. E.; Ramírez, S. V.; Sellgren, K.; Terndrup, D. M. and Tiede, G. P. The Frequency of Barred Spiral Galaxies in the Near-Infrared. AJ **119**, 536 (2000).

Fabello, S.; Catinella, B.; Giovanelli, R.; Kauffmann, G.; Haynes, M. P.; Heckman, T. M. and Schiminovich, D. ALFALFA H I data stacking - I. Does the bulge quench ongoing star formation in early-type galaxies? MNRAS **411**, 993 (2011).

Faber, S. M.; Phillips, A. C.; Kibrick, R. I.; Alcott, B.; Allen, S. L.; Burrous, J.; Cantrall, T.; Clarke, D.; Coil, A. L.; Cowley, D. J.; Davis, M.; Deich, W. T. S.; Dietsch, K.; Gilmore, D. K.; Harper, C. A.; Hilyard, D. F.; Lewis, J. P.; McVeigh, M.; Newman, J.; Osborne, J.; Schiavon, R.; Stover, R. J.; Tucker, D.; Wallace, V.; Wei, M.; Wirth, G. and Wright, C. A. The DEIMOS spectrograph for the Keck II Telescope: integration and testing. In Iye, M. and Moorwood, A. F. M., eds., *Instrument Design and Performance for Optical/Infrared Ground-based Telescopes* (2003), vol. 4841 of *Society of Photo-Optical Instrumentation Engineers (SPIE) Conference Series*, pp. 1657–1669.

Faber, S. M.; Willmer, C. N. A.; Wolf, C.; Koo, D. C.; Weiner, B. J.; Newman, J. A.; Im, M.; Coil, A. L.; Conroy, C.; Cooper, M. C.; Davis, M.; Finkbeiner, D. P.; Gerke, B. F.; Gebhardt, K.; Groth, E. J.; Guhathakurta, P.; Harker, J.; Kaiser, N.; Kassin, S.; Kleinheinrich, M.; Konidaris, N. P.; Kron, R. G.; Lin, L.; Luppino, G.; Madgwick, D. S.; Meisenheimer, K.; Noeske, K. G.; Phillips, A. C.; Sarajedini, V. L.; Schiavon, R. P.; Simard, L.; Szalay, A. S.; Vogt, N. P. and Yan, R. Galaxy Luminosity Functions to z$\sim$1 from DEEP2 and COMBO-17: Implications for Red Galaxy Formation. ApJ **665**, 265 (2007).

Fabian, A. C. Observational Evidence of Active Galactic Nuclei Feedback. ARA&A **50**, 455 (2012).

Fang, J. J.; Faber, S. M.; Koo, D. C. and Dekel, A. A Link between Star Formation Quenching and Inner Stellar Mass Density in Sloan Digital Sky Survey Central Galaxies. ApJ **776**, 63 (2013).

Farrah, D.; Urrutia, T.; Lacy, M.; Efstathiou, A.; Afonso, J.; Coppin, K.; Hall, P. B.; Lonsdale, C.; Jarrett, T.; Bridge, C.; Borys, C. and Petty, S. Direct Evidence for Termination of Obscured Star Formation by Radiatively Driven Outflows in Reddened QSOs. ApJ **745**, 178 (2012).

Fisher, D. B. and Drory, N. The Structure of Classical Bulges and Pseudobulges: the Link Between Pseudobulges and SÉRSIC Index. AJ **136**, 773 (2008).

Fisher, D. B. and Drory, N. Bulges of Nearby Galaxies with Spitzer: Scaling Relations in Pseudobulges and Classical Bulges. ApJ **716**, 942 (2010).

Fisher, D. B. and Drory, N. Demographics of Bulge Types within 11 Mpc and Implications for Galaxy Evolution. ApJ **733**, L47 (2011).

Fisher, D. B.; Drory, N. and Fabricius, M. H. Bulges of Nearby Galaxies with Spitzer: The Growth of Pseudobulges in Disk Galaxies and its Connection to Outer Disks. ApJ **697**, 630 (2009).

Forbes, J.; Krumholz, M. and Burkert, A. Evolving Gravitationally Unstable Disks over Cosmic Time: Implications for Thick Disk Formation. ApJ **754**, 48 (2012).

Franx, M.; van Dokkum, P. G.; Schreiber, N. M. F.; Wuyts, S.; Labbé, I. and Toft, S. Structure and Star Formation in Galaxies out to z = 3: Evidence for Surface Density Dependent Evolution and Upsizing. ApJ **688**, 770 (2008).

Freeman, K. C. On the Disks of Spiral and so Galaxies. ApJ **160**, 811 (1970).

Friedli, D. and Benz, W. Secular evolution of isolated barred galaxies. I - Gravitational coupling between stellar bars and interstellar medium. A&A **268**, 65 (1993).

Friedli, D. and Benz, W. Secular evolution of isolated barred galaxies. II. Coupling between stars and interstellar medium via star formation. A&A **301**, 649 (1995).

Friedli, D.; Benz, W. and Kennicutt, R. On the influence of bars and star formation on galactic abundance gradients. ApJ **430**, L105 (1994).

Gadotti, D. A. Structural properties of pseudo-bulges, classical bulges and elliptical galaxies: a Sloan Digital Sky Survey perspective. MNRAS **393**, 1531 (2009).

Gadotti, D. A. Secular evolution and structural properties of stellar bars in galaxies. MNRAS **415**, 3308 (2011).

Gebhardt, K.; Bender, R.; Bower, G.; Dressler, A.; Faber, S. M.; Filippenko, A. V.; Green, R.; Grillmair, C.; Ho, L. C.; Kormendy, J.; Lauer, T. R.; Magorrian, J.; Pinkney, J.; Richstone, D. and Tremaine, S. A Relationship between Nuclear Black Hole Mass and Galaxy Velocity Dispersion. ApJ **539**, L13 (2000).

Gebhardt, K.; Faber, S. M.; Koo, D. C.; Im, M.; Simard, L.; Illingworth, G. D.; Phillips, A. C.; Sarajedini, V. L.; Vogt, N. P.; Weiner, B. and Willmer, C. N. A. The DEEP Groth Strip Survey. IX. Evolution of the Fundamental Plane of Field Galaxies. ApJ **597**, 239 (2003).

Genzel, R.; Hollenbach, D. and Townes, C. H. The nucleus of our Galaxy. *Reports on Progress in Physics* **57**, 417 (1994).

Gerke, B. F.; Newman, J. A.; Davis, M.; Marinoni, C.; Yan, R.; Coil, A. L.; Conroy, C.; Cooper, M. C.; Faber, S. M.; Finkbeiner, D. P.; Guhathakurta, P.; Kaiser, N.; Koo, D. C.; Phillips, A. C.; Weiner, B. J. and Willmer, C. N. A. The DEEP2 Galaxy Redshift Survey: First Results on Galaxy Groups. ApJ **625**, 6 (2005).

Giavalisco, M.; Ferguson, H. C.; Koekemoer, A. M.; Dickinson, M.; Alexander, D. M.; Bauer, F. E.; Bergeron, J.; Biagetti, C.; Brandt, W. N.; Casertano, S.; Cesarsky, C.; Chatzichristou, E.; Conselice, C.; Cristiani, S.; Da Costa, L.; Dahlen, T.; de Mello, D.; Eisenhardt, P.; Erben, T.; Fall, S. M.; Fassnacht, C.; Fosbury, R.; Fruchter, A.; Gardner, J. P.; Grogin, N.; Hook, R. N.; Hornschemeier, A. E.; Idzi, R.; Jogee, S.; Kretchmer, C.; Laidler, V.; Lee, K. S.; Livio, M.; Lucas, R.; Madau, P.; Mobasher, B.; Moustakas, L. A.; Nonino, M.; Padovani, P.; Papovich, C.; Park, Y.; Ravindranath, S.; Renzini, A.; Richardson, M.; Riess, A.; Rosati, P.; Schirmer, M.; Schreier, E.; Somerville, R. S.; Spinrad, H.; Stern, D.; Stiavelli, M.; Strolger, L.; Urry, C. M.; Vandame, B.; Williams, R. and Wolf, C. The Great Observatories Origins Deep Survey: Initial Results from Optical and Near-Infrared Imaging. ApJ **600**, L93 (2004).

Giuricin, G.; Tamburini, L.; Mardirossian, F.; Mezzetti, M. and Monaco, P. The nuclear 10 micron emission of spiral galaxies. ApJ **427**, 202 (1994).

Goto, T.; Yamauchi, C.; Fujita, Y.; Okamura, S.; Sekiguchi, M.; Smail, I.; Bernardi, M. and Gomez, P. L. The morphology-density relation in the Sloan Digital Sky Survey. MNRAS **346**, 601 (2003).

Governato, F.; Brook, C. B.; Brooks, A. M.; Mayer, L.; Willman, B.; Jonsson, P.; Stilp, A. M.; Pope, L.; Christensen, C.; Wadsley, J. and Quinn, T. Forming a large disc galaxy from a z <

1 major merger. MNRAS **398**, 312 (2009).

Governato, F.; Willman, B.; Mayer, L.; Brooks, A.; Stinson, G.; Valenzuela, O.; Wadsley, J. and Quinn, T. Forming disc galaxies in ΛCDM simulations. MNRAS **374**, 1479 (2007).

Graham, A. W. and Driver, S. P. A Concise Reference to (Projected) Sérsic $R^{1/n}$ Quantities, Including Concentration, Profile Slopes, Petrosian Indices, and Kron Magnitudes. PASA **22**, 118 (2005).

Greenhill, L. J.; Kondratko, P. T.; Moran, J. M. and Tilak, A. Discovery of Candidate H_2O Disk Masers in Active Galactic Nuclei and Estimations Of Centripetal Accelerations. ApJ **707**, 787 (2009).

Griffith, R. L.; Cooper, M. C.; Newman, J. A.; Moustakas, L. A.; Stern, D.; Comerford, J. M.; Davis, M.; Lotz, J. M.; Barden, M.; Conselice, C. J.; Capak, P. L.; Faber, S. M.; Kirkpatrick, J. D.; Koekemoer, A. M.; Koo, D. C.; Noeske, K. G.; Scoville, N.; Sheth, K.; Shopbell, P.; Willmer, C. N. A. and Weiner, B. The Advanced Camera for Surveys General Catalog: Structural Parameters for Approximately Half a Million Galaxies. ApJS **200**, 9 (2012).

Guedes, J.; Callegari, S.; Madau, P. and Mayer, L. Forming Realistic Late-type Spirals in a ΛCDM Universe: The Eris Simulation. ApJ **742**, 76 (2011).

Gunn, J. E. and Gott, III, J. R. On the Infall of Matter Into Clusters of Galaxies and Some Effects on Their Evolution. ApJ **176**, 1 (1972).

Guo, Y.; Ferguson, H. C.; Giavalisco, M.; Barro, G.; Willner, S. P.; Ashby, M. L. N.; Dahlen, T.; Donley, J. L.; Faber, S. M.; Fontana, A.; Galametz, A.; Grazian, A.; Huang, K.-H.; Kocevski,

D. D.; Koekemoer, A. M.; Koo, D. C.; McGrath, E. J.; Peth, M.; Salvato, M.; Wuyts, S.; Castellano, M.; Cooray, A. R.; Dickinson, M. E.; Dunlop, J. S.; Fazio, G. G.; Gardner, J. P.; Gawiser, E.; Grogin, N. A.; Hathi, N. P.; Hsu, L.-T.; Lee, K.-S.; Lucas, R. A.; Mobasher, B.; Nandra, K.; Newman, J. A. and van der Wel, A. CANDELS Multi-wavelength Catalogs: Source Detection and Photometry in the GOODS-South Field. ApJS **207**, 24 (2013).

Haehnelt, M. G. and Rees, M. J. The formation of nuclei in newly formed galaxies and the evolution of the quasar population. MNRAS **263**, 168 (1993).

Hao, L.; Jogee, S.; Barazza, F. D.; Marinova, I. and Shen, J. Bars in Starbursts and AGNs - A Quantitative Reexamination. In Jogee, S.; Marinova, I.; Hao, L. and Blanc, G. A., eds., *Galaxy Evolution: Emerging Insights and Future Challenges* (2009), vol. 419 of *Astronomical Society of the Pacific Conference Series*, p. 402.

Hawarden, T. G.; Mountain, C. M.; Leggett, S. K. and Puxley, P. J. Enhanced star formation - The importance of bars in spiral galaxies. MNRAS **221**, 41P (1986).

Heckman, T. and Best, P. The Co-Evolution of Galaxies and Supermassive Black Holes: Insights from Surveys of the Contemporary Universe. *ArXiv e-prints* (2014).

Heller, C. H. and Shlosman, I. Fueling nuclear activity in disk galaxies: Starbursts and monsters. ApJ **424**, 84 (1994).

Ho, L. C.; Filippenko, A. V. and Sargent, W. L. W. The Influence of Bars on Nuclear Activity. ApJ **487**, 591 (1997).

Hohl, F. Numerical Experiments with a Disk of Stars. ApJ **168**, 343 (1971).

Holley-Bockelmann, K.; Weinberg, M. and Katz, N. Bar-induced evolution of dark matter cusps. MNRAS **363**, 991 (2005).

Holmberg, E. A photographic photometry of extragalactic nebulae. *Meddelanden fran Lunds Astronomiska Observatorium Serie II* **136**, 1 (1958).

Hopkins, P. F.; Bundy, K.; Croton, D.; Hernquist, L.; Keres, D.; Khochfar, S.; Stewart, K.; Wetzel, A. and Younger, J. D. Mergers and Bulge Formation in ΛCDM: Which Mergers Matter? ApJ **715**, 202 (2010a).

Hopkins, P. F.; Bundy, K.; Hernquist, L.; Wuyts, S. and Cox, T. J. Discriminating between the physical processes that drive spheroid size evolution. MNRAS **401**, 1099 (2010b).

Hopkins, P. F.; Bundy, K.; Murray, N.; Quataert, E.; Lauer, T. R. and Ma, C.-P. Compact high-redshift galaxies are the cores of the most massive present-day spheroids. MNRAS **398**, 898 (2009a).

Hopkins, P. F.; Cox, T. J.; Younger, J. D. and Hernquist, L. How do Disks Survive Mergers? ApJ **691**, 1168 (2009b).

Hopkins, P. F. and Hernquist, L. Fueling Low-Level AGN Activity through Stochastic Accretion of Cold Gas. ApJS **166**, 1 (2006).

Hopkins, P. F.; Hernquist, L.; Cox, T. J.; Di Matteo, T.; Martini, P.; Robertson, B. and Springel, V. Black Holes in Galaxy Mergers: Evolution of Quasars. ApJ **630**, 705 (2005a).

Hopkins, P. F.; Hernquist, L.; Cox, T. J.; Dutta, S. N. and Rothberg, B. Dissipation and Extra Light in Galactic Nuclei. I. Gas-Rich Merger Remnants. ApJ **679**, 156 (2008).

Hopkins, P. F.; Hernquist, L.; Martini, P.; Cox, T. J.; Robertson, B.; Di Matteo, T. and Springel, V. A Physical Model for the Origin of Quasar Lifetimes. ApJ **625**, L71 (2005b).

Hopkins, P. F.; Kocevski, D. D. and Bundy, K. Do We Expect Most AGN to Live in Disks? *ArXiv e-prints* (2013).

Hopkins, P. F. and Quataert, E. How do massive black holes get their gas? MNRAS **407**, 1529 (2010).

Hopkins, P. F. and Quataert, E. An analytic model of angular momentum transport by gravitational torques: from galaxies to massive black holes. MNRAS **415**, 1027 (2011).

Hoyle, B.; Masters, K. L.; Nichol, R. C.; Edmondson, E. M.; Smith, A. M.; Lintott, C.; Scranton, R.; Bamford, S.; Schawinski, K. and Thomas, D. Galaxy Zoo: bar lengths in local disc galaxies. MNRAS **415**, 3627 (2011).

Huang, J. H.; Gu, Q. S.; Su, H. J.; Hawarden, T. G.; Liao, X. H. and Wu, G. X. The bar-enhanced star-formation activities in spiral galaxies. A&A **313**, 13 (1996).

Huang, J.-S.; Cowie, L. L.; Gardner, J. P.; Hu, E. M.; Songaila, A. and Wainscoat, R. J. The Hawaii K-Band Galaxy Survey. II. Bright K-Band Imaging. ApJ **476**, 12 (1997).

Hubble, E. and Humason, M. L. The Velocity-Distance Relation among Extra-Galactic Nebulae. ApJ **74**, 43 (1931).

Hubble, E. P. *Realm of the Nebulae* (1936).

Hunt, L. K. and Malkan, M. A. Morphology of the 12 Micron Seyfert Galaxies. I. Hubble Types, Axial Ratios, Bars, and Rings. ApJ **516**, 660 (1999).

Ilbert, O.; Salvato, M.; Le Floc'h, E.; Aussel, H.; Capak, P.; McCracken, H. J.; Mobasher, B.; Kartaltepe, J.; Scoville, N.; Sanders, D. B.; Arnouts, S.; Bundy, K.; Cassata, P.; Kneib, J.-P.; Koekemoer, A.; Le Fèvre, O.; Lilly, S.; Surace, J.; Taniguchi, Y.; Tasca, L.; Thompson, D.; Tresse, L.; Zamojski, M.; Zamorani, G. and Zucca, E. Galaxy Stellar Mass Assembly Between $0.2 < z < 2$ from the S-COSMOS Survey. ApJ **709**, 644 (2010).

Im, M.; Faber, S. M.; Gebhardt, K.; Koo, D. C.; Phillips, A. C.; Schiavon, R. P.; Simard, L. and Willmer, C. N. A. Are There Blue, Massive E/S0 Galaxies at $z<1$? Kinematics of Blue Spheroidal Galaxy Candidates. AJ **122**, 750 (2001).

Im, M.; Simard, L.; Faber, S. M.; Koo, D. C.; Gebhardt, K.; Willmer, C. N. A.; Phillips, A.; Illingworth, G.; Vogt, N. P. and Sarajedini, V. L. The DEEP Groth Strip Survey. X. Number Density and Luminosity Function of Field E/S0 Galaxies at $z < 1$. ApJ **571**, 136 (2002).

Inoue, S. and Saitoh, T. R. Natures of a clump-origin bulge: a pseudo-bulge like but old metal-rich bulge. MNRAS **422**, 1902 (2012a).

Inoue, S. and Saitoh, T. R. Natures of a clump-origin bulge: a pseudo-bulge like but old metal-rich bulge. MNRAS **422**, 1902 (2012b).

Jogee, S. The Fueling and Evolution of AGN: Internal and External Triggers. In Alloin, D., ed., *Physics of Active Galactic Nuclei at all Scales* (2006), vol. 693 of *Lecture Notes in Physics, Berlin Springer Verlag*, p. 143.

Jogee, S.; Barazza, F. D.; Rix, H.-W.; Shlosman, I.; Barden, M.; Wolf, C.; Davies, J.; Heyer, I.; Beckwith, S. V. W.; Bell, E. F.; Borch, A.; Caldwell, J. A. R.; Conselice, C. J.; Dahlen, T.; Häussler, B.; Heymans, C.; Jahnke, K.; Knapen, J. H.; Laine, S.; Lubell, G. M.; Mobasher, B.; McIntosh, D. H.; Meisenheimer, K.; Peng, C. Y.; Ravindranath, S.; Sanchez, S. F.; Somerville, R. S. and Wisotzki, L. Bar Evolution over the Last 8 Billion Years: A Constant Fraction of Strong Bars in the GEMS Survey. ApJ **615**, L105 (2004).

Kang, X.; Jing, Y. P.; Mo, H. J. and Börner, G. Semianalytical Model of Galaxy Formation with High-Resolution N-Body Simulations. ApJ **631**, 21 (2005).

Kannappan, S. J.; Guie, J. M. and Baker, A. J. E/S0 Galaxies on the Blue Color-Stellar Mass Sequence at z = 0: Fading Mergers or Future Spirals? AJ **138**, 579 (2009).

Kartaltepe, J. S.; Sanders, D. B.; Le Floc'h, E.; Frayer, D. T.; Aussel, H.; Arnouts, S.; Ilbert, O.; Salvato, M.; Scoville, N. Z.; Surace, J.; Yan, L.; Capak, P.; Caputi, K.; Carollo, C. M.; Cassata, P.; Civano, F.; Hasinger, G.; Koekemoer, A. M.; Le Fèvre, O.; Lilly, S.; Liu, C. T.; McCracken, H. J.; Schinnerer, E.; Smolčić, V.; Taniguchi, Y.; Thompson, D. J.; Trump, J.; Baldassare, V. F. and Fiorenza, S. L. A Multiwavelength Study of a Sample of 70 μm Selected Galaxies in the COSMOS Field. II. The Role of Mergers in Galaxy Evolution. ApJ **721**, 98 (2010).

Kauffmann, G.; Heckman, T. M.; De Lucia, G.; Brinchmann, J.; Charlot, S.; Tremonti, C.; White, S. D. M. and Brinkmann, J. Gas infall and stochastic star formation in galaxies in the local universe. MNRAS **367**, 1394 (2006).

Kauffmann, G.; Heckman, T. M.; Tremonti, C.; Brinchmann, J.; Charlot, S.; White, S. D. M.; Ridgway, S. E.; Brinkmann, J.; Fukugita, M.; Hall, P. B.; Ivezić, Ž.; Richards, G. T. and Schneider, D. P. The host galaxies of active galactic nuclei. MNRAS **346**, 1055 (2003a).

Kauffmann, G.; Heckman, T. M.; White, S. D. M.; Charlot, S.; Tremonti, C.; Brinchmann, J.; Bruzual, G.; Peng, E. W.; Seibert, M.; Bernardi, M.; Blanton, M.; Brinkmann, J.; Castander, F.; Csábai, I.; Fukugita, M.; Ivezic, Z.; Munn, J. A.; Nichol, R. C.; Padmanabhan, N.; Thakar, A. R.; Weinberg, D. H. and York, D. Stellar masses and star formation histories for 10^5 galaxies from the Sloan Digital Sky Survey. MNRAS **341**, 33 (2003b).

Kauffmann, G.; Heckman, T. M.; White, S. D. M.; Charlot, S.; Tremonti, C.; Peng, E. W.; Seibert, M.; Brinkmann, J.; Nichol, R. C.; SubbaRao, M. and York, D. The dependence of star formation history and internal structure on stellar mass for 10^5 low-redshift galaxies. MNRAS **341**, 54 (2003c).

Kauffmann, G.; Li, C.; Fu, J.; Saintonge, A.; Catinella, B.; Tacconi, L. J.; Kramer, C.; Genzel, R.; Moran, S. and Schiminovich, D. COLD GASS, an IRAM legacy survey of molecular gas in massive galaxies - III. Comparison with semi-analytic models of galaxy formation. MNRAS **422**, 997 (2012).

Kaviraj, S. The importance of minor-merger-driven star formation and black-hole growth in disk galaxies. *ArXiv e-prints* (2014a).

Kaviraj, S. The significant contribution of minor mergers to the cosmic star formation budget. MNRAS **437**, L41 (2014b).

Keel, W. C.; Lintott, C. J.; Schawinski, K.; Bennert, V. N.; Thomas, D.; Manning, A.; Chojnowski, S. D.; van Arkel, H. and Lynn, S. The History and Environment of a Faded Quasar: Hubble Space Telescope Observations of Hanny's Voorwerp and IC 2497. AJ **144**, 66 (2012).

Kennicutt, Jr., R. C. The star formation law in galactic disks. ApJ **344**, 685 (1989).

Kereš, D.; Katz, N.; Weinberg, D. H. and Davé, R. How do galaxies get their gas? MNRAS **363**, 2 (2005).

Khochfar, S. and Ostriker, J. P. Adding Environmental Gas Physics to the Semianalytic Method for Galaxy Formation: Gravitational Heating. ApJ **680**, 54 (2008).

Kinney, A. L.; Schmitt, H. R.; Clarke, C. J.; Pringle, J. E.; Ulvestad, J. S. and Antonucci, R. R. J. Jet Directions in Seyfert Galaxies. ApJ **537**, 152 (2000).

Knapen, J. H.; Beckman, J. E.; Heller, C. H.; Shlosman, I. and de Jong, R. S. The Central Region in M100: Observations and Modeling. ApJ **454**, 623 (1995).

Knapen, J. H.; Shlosman, I. and Peletier, R. F. A Subarcsecond Resolution Near-Infrared Study of Seyfert and "Normal" Galaxies. II. Morphology. ApJ **529**, 93 (2000).

Kocevski, D. D.; Faber, S. M.; Mozena, M.; Koekemoer, A. M.; Nandra, K.; Rangel, C.; Laird, E. S.; Brusa, M.; Wuyts, S.; Trump, J. R.; Koo, D. C.; Somerville, R. S.; Bell, E. F.; Lotz, J. M.; Alexander, D. M.; Bournaud, F.; Conselice, C. J.; Dahlen, T.; Dekel, A.; Donley, J. L.; Dunlop, J. S.; Finoguenov, A.; Georgakakis, A.; Giavalisco, M.; Guo, Y.; Grogin, N. A.; Hathi, N. P.; Juneau, S.; Kartaltepe, J. S.; Lucas, R. A.; McGrath, E. J.; McIntosh, D. H.; Mobasher, B.; Robaina, A. R.; Rosario, D.; Straughn, A. N.; van der Wel, A. and Villforth,

C. CANDELS: Constraining the AGN-Merger Connection with Host Morphologies at z $\sim$ 2. ApJ **744**, 148 (2012).

Koo, D. C.; Simard, L.; Willmer, C. N. A.; Gebhardt, K.; Bouwens, R. J.; Kauffmann, G.; Crosby, T.; Faber, S. M.; Harker, J.; Sarajedini, V. L.; Vogt, N. P.; Weiner, B. J.; Phillips, A. J.; Im, M. and Wu, K. L. The DEEP Groth Strip Survey. VIII. The Evolution of Luminous Field Bulges at Redshift z $\sim$ 1. ApJS **157**, 175 (2005).

Kormendy, J. A morphological survey of bar, lens, and ring components in galaxies Secular evolution in galaxy structure. ApJ **227**, 714 (1979).

Kormendy, J. Kinematics of extragalactic bulges: evidence that some bulges are really disks. In Dejonghe, H. and Habing, H. J., eds., *Galactic Bulges* (1993), vol. 153 of *IAU Symposium*, p. 209.

Kormendy, J. *Secular Evolution in Disk Galaxies*, p. 1 (2013).

Kormendy, J. and Ho, L. C. Coevolution (Or Not) of Supermassive Black Holes and Host Galaxies. ARA&A **51**, 511 (2013).

Kormendy, J. and Kennicutt, Jr., R. C. Secular Evolution and the Formation of Pseudobulges in Disk Galaxies. ARA&A **42**, 603 (2004).

Koss, M.; Mushotzky, R.; Veilleux, S. and Winter, L. Merging and Clustering of the Swift BAT AGN Sample. ApJ **716**, L125 (2010).

Kraljic, K.; Bournaud, F. and Martig, M. The Two-phase Formation History of Spiral Galaxies Traced by the Cosmic Evolution of the Bar Fraction. ApJ **757**, 60 (2012).

Kroupa, P. On the variation of the initial mass function. MNRAS **322**, 231 (2001).

Krumholz, M. R.; Dekel, A. and McKee, C. F. A Universal, Local Star Formation Law in Galactic Clouds, nearby Galaxies, High-redshift Disks, and Starbursts. ApJ **745**, 69 (2012).

Krumholz, M. R.; Leroy, A. K. and McKee, C. F. Which Phase of the Interstellar Medium Correlates with the Star Formation Rate? ApJ **731**, 25 (2011).

Laine, S.; Shlosman, I.; Knapen, J. H. and Peletier, R. F. Nested and Single Bars in Seyfert and Non-Seyfert Galaxies. ApJ **567**, 97 (2002).

Laird, E. S.; Nandra, K.; Georgakakis, A.; Aird, J. A.; Barmby, P.; Conselice, C. J.; Coil, A. L.; Davis, M.; Faber, S. M.; Fazio, G. G.; Guhathakurta, P.; Koo, D. C.; Sarajedini, V. and Willmer, C. N. A. AEGIS-X: Chandra deep survey (Laird+, 2009). *VizieR Online Data Catalog* **218**, 102 (2009).

Land, K.; Slosar, A.; Lintott, C.; Andreescu, D.; Bamford, S.; Murray, P.; Nichol, R.; Raddick, M. J.; Schawinski, K.; Szalay, A.; Thomas, D. and Vandenberg, J. Galaxy Zoo: the large-scale spin statistics of spiral galaxies in the Sloan Digital Sky Survey. MNRAS **388**, 1686 (2008).

Larson, R. B.; Tinsley, B. M. and Caldwell, C. N. The evolution of disk galaxies and the origin of S0 galaxies. ApJ **237**, 692 (1980).

Laurikainen, E.; Salo, H. and Buta, R. Comparison of Bar Strengths and Fractions of Bars in Active and Nonactive Galaxies. ApJ **607**, 103 (2004).

Laurikainen, E.; Salo, H. and Buta, R. Multicomponent decompositions for a sample of S0 galaxies. MNRAS **362**, 1319 (2005).

Laurikainen, E.; Salo, H.; Buta, R. and Knapen, J. H. Properties of bars and bulges in the Hubble sequence. MNRAS **381**, 401 (2007).

Laurikainen, E.; Salo, H.; Buta, R. and Knapen, J. H. Bars, Ovals, and Lenses in Early-Type Disk Galaxies: Probes of Galaxy Evolution. ApJ **692**, L34 (2009).

Laurikainen, E.; Salo, H. and Rautiainen, P. Comparison of bar strengths in active and non-active galaxies. MNRAS **331**, 880 (2002).

Lee, G.-H.; Park, C.; Lee, M. G. and Choi, Y.-Y. Dependence of Barred Galaxy Fraction on Galaxy Properties and Environment. ApJ **745**, 125 (2012a).

Lee, G.-H.; Woo, J.-H.; Lee, M. G.; Hwang, H. S.; Lee, J. C.; Sohn, J. and Lee, J. H. Do Bars Trigger Activity in Galactic Nuclei? ApJ **750**, 141 (2012b).

Lilly, S. J.; Le Brun, V.; Maier, C.; Mainieri, V.; Mignoli, M.; Scodeggio, M.; Zamorani, G.; Carollo, M.; Contini, T.; Kneib, J.-P.; Le Fèvre, O.; Renzini, A.; Bardelli, S.; Bolzonella, M.; Bongiorno, A.; Caputi, K.; Coppa, G.; Cucciati, O.; de la Torre, S.; de Ravel, L.; Franzetti, P.; Garilli, B.; Iovino, A.; Kampczyk, P.; Kovac, K.; Knobel, C.; Lamareille, F.; Le Borgne, J.-F.; Pello, R.; Peng, Y.; Pérez-Montero, E.; Ricciardelli, E.; Silverman, J. D.; Tanaka, M.; Tasca, L.; Tresse, L.; Vergani, D.; Zucca, E.; Ilbert, O.; Salvato, M.; Oesch, P.; Abbas, U.; Bottini, D.; Capak, P.; Cappi, A.; Cassata, P.; Cimatti, A.; Elvis, M.; Fumana, M.; Guzzo, L.; Hasinger, G.; Koekemoer, A.; Leauthaud, A.; Maccagni, D.; Marinoni, C.; McCracken, H.; Memeo, P.; Meneux, B.; Porciani, C.; Pozzetti, L.; Sanders, D.; Scaramella, R.; Scarlata, C.; Scoville, N.; Shopbell, P. and Taniguchi, Y. The zCOSMOS 10k-Bright Spectroscopic Sample. ApJS **184**, 218 (2009).

Lin, H.; Yee, H. K. C.; Carlberg, R. G.; Morris, S. L.; Sawicki, M.; Patton, D. R.; Wirth, G. and Shepherd, C. W. The CNOC2 Field Galaxy Luminosity Function. I. A Description of Luminosity Function Evolution. ApJ **518**, 533 (1999).

Lin, L.; Koo, D. C.; Weiner, B. J.; Chiueh, T.; Coil, A. L.; Lotz, J.; Conselice, C. J.; Willner, S. P.; Smith, H. A.; Guhathakurta, P.; Huang, J.-S.; Le Floc'h, E.; Noeske, K. G.; Willmer, C. N. A.; Cooper, M. C. and Phillips, A. C. AEGIS: Enhancement of Dust-enshrouded Star Formation in Close Galaxy Pairs and Merging Galaxies up to z $\sim$ 1. ApJ **660**, L51 (2007).

Lin, L.; Patton, D. R.; Koo, D. C.; Casteels, K.; Conselice, C. J.; Faber, S. M.; Lotz, J.; Willmer, C. N. A.; Hsieh, B. C.; Chiueh, T.; Newman, J. A.; Novak, G. S.; Weiner, B. J. and Cooper, M. C. The Redshift Evolution of Wet, Dry, and Mixed Galaxy Mergers from Close Galaxy Pairs in the DEEP2 Galaxy Redshift Survey. ApJ **681**, 232 (2008).

Lintott, C.; Schawinski, K.; Bamford, S.; Slosar, A.; Land, K.; Thomas, D.; Edmondson, E.; Masters, K.; Nichol, R. C.; Raddick, M. J.; Szalay, A.; Andreescu, D.; Murray, P. and Vandenberg, J. Galaxy Zoo 1: data release of morphological classifications for nearly 900 000 galaxies. MNRAS **410**, 166 (2011).

Lintott, C. J.; Schawinski, K.; Slosar, A.; Land, K.; Bamford, S.; Thomas, D.; Raddick, M. J.; Nichol, R. C.; Szalay, A.; Andreescu, D.; Murray, P. and Vandenberg, J. Galaxy Zoo: morphologies derived from visual inspection of galaxies from the Sloan Digital Sky Survey. MNRAS **389**, 1179 (2008).

Lotz, J. M.; Davis, M.; Faber, S. M.; Guhathakurta, P.; Gwyn, S.; Huang, J.; Koo, D. C.; Le Floc'h, E.; Lin, L.; Newman, J.; Noeske, K.; Papovich, C.; Willmer, C. N. A.; Coil, A.; Conselice, C. J.; Cooper, M.; Hopkins, A. M.; Metevier, A.; Primack, J.; Rieke, G. and Weiner, B. J. The Evolution of Galaxy Mergers and Morphology at $z < 1.2$ in the Extended Groth Strip. ApJ **672**, 177 (2008a).

Lotz, J. M.; Jonsson, P.; Cox, T. J.; Croton, D.; Primack, J. R.; Somerville, R. S. and Stewart, K. The Major and Minor Galaxy Merger Rates at $z < 1.5$. ApJ **742**, 103 (2011).

Lotz, J. M.; Jonsson, P.; Cox, T. J. and Primack, J. R. Galaxy merger morphologies and timescales from simulations of equal-mass gas-rich disc mergers. MNRAS **391**, 1137 (2008b).

Lynden-Bell, D. and Kalnajs, A. J. On the generating mechanism of spiral structure. MNRAS **157**, 1 (1972).

MacArthur, L. A.; Courteau, S. and Holtzman, J. A. Structure of Disk-dominated Galaxies. I. Bulge/Disk Parameters, Simulations, and Secular Evolution. ApJ **582**, 689 (2003).

Magorrian, J.; Tremaine, S.; Richstone, D.; Bender, R.; Bower, G.; Dressler, A.; Faber, S. M.; Gebhardt, K.; Green, R.; Grillmair, C.; Kormendy, J. and Lauer, T. The Demography of Massive Dark Objects in Galaxy Centers. AJ **115**, 2285 (1998).

Maier, C.; Lilly, S. J.; Zamorani, G.; Scodeggio, M.; Lamareille, F.; Contini, T.; Sargent, M. T.; Scarlata, C.; Oesch, P.; Carollo, C. M.; Le Fèvre, O.; Renzini, A.; Kneib, J.-P.; Mainieri, V.; Bardelli, S.; Bolzonella, M.; Bongiorno, A.; Caputi, K.; Coppa, G.; Cucciati, O.; de la Torre, S.; de Ravel, L.; Franzetti, P.; Garilli, B.; Iovino, A.; Kampczyk, P.; Knobel, C.; Kovač, K.; Le Borgne, J.-F.; Le Brun, V.; Mignoli, M.; Pello, R.; Peng, Y.; Perez Montero, E.; Ricciardelli, E.; Silverman, J. D.; Tanaka, M.; Tasca, L.; Tresse, L.; Vergani, D.; Zucca, E.; Abbas, U.; Bottini, D.; Cappi, A.; Cassata, P.; Cimatti, A.; Fumana, M.; Guzzo, L.; Halliday, C.; Koekemoer, A. M.; Leauthaud, A.; Maccagni, D.; Marinoni, C.; McCracken, H. J.; Memeo, P.; Meneux, B.; Porciani, C.; Pozzetti, L. and Scaramella, R. The Dependence of Star Formation Activity on Stellar Mass Surface Density and Sersic Index in zCOSMOS Galaxies at $0.5 < z < 0.9$ Compared with SDSS Galaxies at $0.04 < z < 0.08$. ApJ **694**, 1099 (2009).

Mainieri, V.; Hasinger, G.; Cappelluti, N.; Brusa, M.; Brunner, H.; Civano, F.; Comastri, A.; Elvis, M.; Finoguenov, A.; Fiore, F.; Gilli, R.; Lehmann, I.; Silverman, J.; Tasca, L.; Vignali, C.; Zamorani, G.; Schinnerer, E.; Impey, C.; Trump, J.; Lilly, S.; Maier, C.; Griffiths, R. E.; Miyaji, T.; Capak, P.; Koekemoer, A.; Scoville, N.; Shopbell, P. and Taniguchi, Y. The XMM-Newton Wide-Field Survey in the COSMOS Field. IV. X-Ray Spectral Properties of Active Galactic Nuclei. ApJS **172**, 368 (2007).

Malkan, M. A.; Gorjian, V. and Tam, R. A Hubble Space Telescope Imaging Survey of Nearby Active Galactic Nuclei. ApJS **117**, 25 (1998).

Martel, H.; Kawata, D. and Ellison, S. L. The connection between star formation and metallicity evolution in barred spiral galaxies. MNRAS **431**, 2560 (2013).

Martig, M.; Bournaud, F.; Teyssier, R. and Dekel, A. Morphological Quenching of Star Formation: Making Early-Type Galaxies Red. ApJ **707**, 250 (2009).

Martin, D. C.; Wyder, T. K.; Schiminovich, D.; Barlow, T. A.; Forster, K.; Friedman, P. G.; Morrissey, P.; Neff, S. G.; Seibert, M.; Small, T.; Welsh, B. Y.; Bianchi, L.; Donas, J.; Heckman, T. M.; Lee, Y.-W.; Madore, B. F.; Milliard, B.; Rich, R. M.; Szalay, A. S. and Yi, S. K. The UV-Optical Galaxy Color-Magnitude Diagram. III. Constraints on Evolution from the Blue to the Red Sequence. ApJS **173**, 342 (2007).

Martin, P. Quantitative Morphology of Bars in Spiral Galaxies. AJ **109**, 2428 (1995).

Martin, P. and Friedli, D. Star formation in bar environments. I. Morphology, star formation rates and general properties. A&A **326**, 449 (1997).

Martin, P. and Roy, J.-R. The influence of bars on the chemical composition of spiral galaxies. ApJ **424**, 599 (1994).

Martinet, L. and Friedli, D. Bar strength and star formation activity in late-type barred galaxies. A&A **323**, 363 (1997).

Martinez-Valpuesta, I.; Shlosman, I. and Heller, C. Evolution of Stellar Bars in Live Axisymmetric Halos: Recurrent Buckling and Secular Growth. ApJ **637**, 214 (2006).

Martini, P. QSO Lifetimes. *Coevolution of Black Holes and Galaxies* p. 169 (2004).

Martini, P. and Pogge, R. W. Hubble Space Telescope Observations of the CFA Seyfert 2 Galaxies: The Fueling of Active Galactic Nuclei. AJ **118**, 2646 (1999).

Martini, P.; Regan, M. W.; Mulchaey, J. S. and Pogge, R. W. Circumnuclear Dust in Nearby Active and Inactive Galaxies. II. Bars, Nuclear Spirals, and the Fueling of Active Galactic Nuclei. ApJ **589**, 774 (2003).

Masters, K. L.; Nichol, R. C.; Haynes, M. P.; Keel, W. C.; Lintott, C.; Simmons, B.; Skibba, R.; Bamford, S.; Giovanelli, R. and Schawinski, K. Galaxy Zoo and ALFALFA: atomic gas and the regulation of star formation in barred disc galaxies. MNRAS **424**, 2180 (2012).

Masters, K. L.; Nichol, R. C.; Hoyle, B.; Lintott, C.; Bamford, S. P.; Edmondson, E. M.; Fortson, L.; Keel, W. C.; Schawinski, K.; Smith, A. M. and Thomas, D. Galaxy Zoo: bars in disc galaxies. MNRAS **411**, 2026 (2011).

Matsuda, T. and Nelson, A. H. A galactic vacuum cleaner. Nature **266**, 607 (1977).

Melvin, T.; Masters, K.; Lintott, C.; Nichol, R. C.; Simmons, B.; Bamford, S. P.; Casteels, K. R. V.; Cheung, E.; Edmondson, E. M.; Fortson, L.; Schawinski, K.; Skibba, R. A.; Smith, A. M. and Willett, K. W. Galaxy Zoo: an independent look at the evolution of the bar fraction over the last eight billion years from HST-COSMOS. MNRAS **438**, 2882 (2014).

Menanteau, F.; Abraham, R. G. and Ellis, R. S. Evidence for evolving spheroidals in the Hubble Deep Fields North and South. MNRAS **322**, 1 (2001).

Mendez, A. J.; Coil, A. L.; Lotz, J.; Salim, S.; Moustakas, J. and Simard, L. AEGIS: The Morphologies of Green Galaxies at $0.4 < z < 1.2$. ApJ **736**, 110 (2011).

Menéndez-Delmestre, K.; Sheth, K.; Schinnerer, E.; Jarrett, T. H. and Scoville, N. Z. A Near-Infrared Study of 2MASS Bars in Local Galaxies: An Anchor for High-Redshift Studies. ApJ **657**, 790 (2007).

Mihos, J. C. and Hernquist, L. Dense stellar cores in merger remnants. ApJ **437**, L47 (1994).

Mihos, J. C. and Hernquist, L. Gasdynamics and Starbursts in Major Mergers. ApJ **464**, 641 (1996).

Minchev, I.; Famaey, B.; Combes, F.; Di Matteo, P.; Mouhcine, M. and Wozniak, H. Radial migration in galactic disks caused by resonance overlap of multiple patterns: Self-consistent simulations. A&A **527**, A147 (2011).

Moore, B.; Katz, N.; Lake, G.; Dressler, A. and Oemler, A. Galaxy harassment and the evolution of clusters of galaxies. Nature **379**, 613 (1996).

More, S.; van den Bosch, F. C.; Cacciato, M.; Skibba, R.; Mo, H. J. and Yang, X. Satellite kinematics - III. Halo masses of central galaxies in SDSS. MNRAS **410**, 210 (2011).

Morganti, R.; de Zeeuw, P. T.; Oosterloo, T. A.; McDermid, R. M.; Krajnović, D.; Cappellari, M.; Kenn, F.; Weijmans, A. and Sarzi, M. Neutral hydrogen in nearby elliptical and lenticular galaxies: the continuing formation of early-type galaxies. MNRAS **371**, 157 (2006).

Mortlock, A.; Conselice, C. J.; Hartley, W. G.; Ownsworth, J. R.; Lani, C.; Bluck, A. F. L.; Almaini, O.; Duncan, K.; Wel, A. v. d.; Koekemoer, A. M.; Dekel, A.; Davé, R.; Ferguson, H. C.; de Mello, D. F.; Newman, J. A.; Faber, S. M.; Grogin, N. A.; Kocevski, D. D. and Lai,

K. The redshift and mass dependence on the formation of the Hubble sequence at z $>$ 1 from CANDELS/UDS. MNRAS **433**, 1185 (2013).

Mulchaey, J. S. and Regan, M. W. The Fueling of Nuclear Activity: The Bar Properties of Seyfert and Normal Galaxies. ApJ **482**, L135 (1997).

Murray, N.; Quataert, E. and Thompson, T. A. On the Maximum Luminosity of Galaxies and Their Central Black Holes: Feedback from Momentum-driven Winds. ApJ **618**, 569 (2005).

Muzzin, A.; Marchesini, D.; Stefanon, M.; Franx, M.; Milvang-Jensen, B.; Dunlop, J. S.; Fynbo, J. P. U.; Brammer, G.; Labbé, I. and van Dokkum, P. A Public K_s -selected Catalog in the COSMOS/ULTRAVISTA Field: Photometry, Photometric Redshifts, and Stellar Population Parameters. ApJS **206**, 8 (2013).

Naab, T. and Trujillo, I. Surface density profiles of collisionless disc merger remnants. MNRAS **369**, 625 (2006).

Nair, P. B. and Abraham, R. G. A Catalog of Detailed Visual Morphological Classifications for 14,034 Galaxies in the Sloan Digital Sky Survey. ApJS **186**, 427 (2010a).

Nair, P. B. and Abraham, R. G. On the Fraction of Barred Spiral Galaxies. ApJ **714**, L260 (2010b).

Nandra, K.; Georgakakis, A.; Willmer, C. N. A.; Cooper, M. C.; Croton, D. J.; Davis, M.; Faber, S. M.; Koo, D. C.; Laird, E. S. and Newman, J. A. AEGIS: The Color-Magnitude Relation for X-Ray-selected Active Galactic Nuclei. ApJ **660**, L11 (2007).

Newman, J. A.; Cooper, M. C.; Davis, M.; Faber, S. M.; Coil, A. L.; Guhathakurta, P.; Koo, D. C.; Phillips, A. C.; Conroy, C.; Dutton, A. A.; Finkbeiner, D. P.; Gerke, B. F.; Rosario, D. J.; Weiner, B. J.; Willmer, C. N. A.; Yan, R.; Harker, J. J.; Kassin, S. A.; Konidaris, N. P.; Lai, K.; Madgwick, D. S.; Noeske, K. G.; Wirth, G. D.; Connolly, A. J.; Kaiser, N.; Kirby, E. N.; Lemaux, B. C.; Lin, L.; Lotz, J. M.; Luppino, G. A.; Marinoni, C.; Matthews, D. J.; Metevier, A. and Schiavon, R. P. The DEEP2 Galaxy Redshift Survey: Design, Observations, Data Reduction, and Redshifts. ApJS **208**, 5 (2013).

Noeske, K. G.; Weiner, B. J.; Faber, S. M.; Papovich, C.; Koo, D. C.; Somerville, R. S.; Bundy, K.; Conselice, C. J.; Newman, J. A.; Schiminovich, D.; Le Floc'h, E.; Coil, A. L.; Rieke, G. H.; Lotz, J. M.; Primack, J. R.; Barmby, P.; Cooper, M. C.; Davis, M.; Ellis, R. S.; Fazio, G. G.; Guhathakurta, P.; Huang, J.; Kassin, S. A.; Martin, D. C.; Phillips, A. C.; Rich, R. M.; Small, T. A.; Willmer, C. N. A. and Wilson, G. Star Formation in AEGIS Field Galaxies since z=1.1: The Dominance of Gradually Declining Star Formation, and the Main Sequence of Star-forming Galaxies. ApJ **660**, L43 (2007).

Noguchi, M. Gas dynamics in interacting disc galaxies - Fuelling of nuclei by induced bars. A&A **203**, 259 (1988).

Noguchi, M. Early Evolution of Disk Galaxies: Formation of Bulges in Clumpy Young Galactic Disks. ApJ **514**, 77 (1999).

Noordermeer, E.; van der Hulst, J. M.; Sancisi, R.; Swaters, R. A. and van Albada, T. S. The Westerbork HI survey of spiral and irregular galaxies. III. HI observations of early-type disk galaxies. A&A **442**, 137 (2005).

Oh, S.; Oh, K. and Yi, S. K. Bar Effects on Central Star Formation and Active Galactic Nucleus Activity. ApJS **198**, 4 (2012).

Okamoto, T. The origin of pseudo-bulges in cosmological simulations of galaxy formation. MNRAS **428**, 718 (2013).

Okamoto, T.; Eke, V. R.; Frenk, C. S. and Jenkins, A. Effects of feedback on the morphology of galaxy discs. MNRAS **363**, 1299 (2005).

O'Neill, J. K. and Dubinski, J. Detailed comparison of the structures and kinematics of simulated and observed barred galaxies. MNRAS **346**, 251 (2003).

Oosterloo, T.; Morganti, R.; Crocker, A.; Jütte, E.; Cappellari, M.; de Zeeuw, T.; Krajnović, D.; McDermid, R.; Kuntschner, H.; Sarzi, M. and Weijmans, A.-M. Early-type galaxies in different environments: an HI view. MNRAS **409**, 500 (2010).

Peng, C. Y.; Ho, L. C.; Impey, C. D. and Rix, H.-W. Detailed Structural Decomposition of Galaxy Images. AJ **124**, 266 (2002).

Peng, Y.-j.; Lilly, S. J.; Kovač, K.; Bolzonella, M.; Pozzetti, L.; Renzini, A.; Zamorani, G.; Ilbert, O.; Knobel, C.; Iovino, A.; Maier, C.; Cucciati, O.; Tasca, L.; Carollo, C. M.; Silverman, J.; Kampczyk, P.; de Ravel, L.; Sanders, D.; Scoville, N.; Contini, T.; Mainieri, V.; Scodeggio, M.; Kneib, J.-P.; Le Fèvre, O.; Bardelli, S.; Bongiorno, A.; Caputi, K.; Coppa, G.; de la Torre, S.; Franzetti, P.; Garilli, B.; Lamareille, F.; Le Borgne, J.-F.; Le Brun, V.; Mignoli, M.; Perez Montero, E.; Pello, R.; Ricciardelli, E.; Tanaka, M.; Tresse, L.; Vergani, D.; Welikala, N.; Zucca, E.; Oesch, P.; Abbas, U.; Barnes, L.; Bordoloi, R.; Bottini, D.;

Cappi, A.; Cassata, P.; Cimatti, A.; Fumana, M.; Hasinger, G.; Koekemoer, A.; Leauthaud, A.; Maccagni, D.; Marinoni, C.; McCracken, H.; Memeo, P.; Meneux, B.; Nair, P.; Porciani, C.; Presotto, V. and Scaramella, R. Mass and Environment as Drivers of Galaxy Evolution in SDSS and zCOSMOS and the Origin of the Schechter Function. ApJ **721**, 193 (2010).

Peng, Y.-j.; Lilly, S. J.; Renzini, A. and Carollo, M. Mass and Environment as Drivers of Galaxy Evolution. II. The Quenching of Satellite Galaxies as the Origin of Environmental Effects. ApJ **757**, 4 (2012).

Pierce, C. M.; Lotz, J. M.; Salim, S.; Laird, E. S.; Coil, A. L.; Bundy, K.; Willmer, C. N. A.; Rosario, D. J. V.; Primack, J. R. and Faber, S. M. Host galaxy colour gradients and accretion disc obscuration in AEGIS $z \sim 1$ X-ray-selected active galactic nuclei. MNRAS **408**, 139 (2010).

Poggianti, B. M.; Smail, I.; Dressler, A.; Couch, W. J.; Barger, A. J.; Butcher, H.; Ellis, R. S. and Oemler, Jr., A. The Star Formation Histories of Galaxies in Distant Clusters. ApJ **518**, 576 (1999).

Postman, M.; Franx, M.; Cross, N. J. G.; Holden, B.; Ford, H. C.; Illingworth, G. D.; Goto, T.; Demarco, R.; Rosati, P.; Blakeslee, J. P.; Tran, K.-V.; Benítez, N.; Clampin, M.; Hartig, G. F.; Homeier, N.; Ardila, D. R.; Bartko, F.; Bouwens, R. J.; Bradley, L. D.; Broadhurst, T. J.; Brown, R. A.; Burrows, C. J.; Cheng, E. S.; Feldman, P. D.; Golimowski, D. A.; Gronwall, C.; Infante, L.; Kimble, R. A.; Krist, J. E.; Lesser, M. P.; Martel, A. R.; Mei, S.; Menanteau, F.; Meurer, G. R.; Miley, G. K.; Motta, V.; Sirianni, M.; Sparks, W. B.; Tran,

H. D.; Tsvetanov, Z. I.; White, R. L. and Zheng, W. The Morphology-Density Relation in z ˜ 1 Clusters. ApJ **623**, 721 (2005).

Quintero, A. D.; Hogg, D. W.; Blanton, M. R.; Schlegel, D. J.; Eisenstein, D. J.; Gunn, J. E.; Brinkmann, J.; Fukugita, M.; Glazebrook, K. and Goto, T. Selection and Photometric Properties of K+A Galaxies. ApJ **602**, 190 (2004).

Rees, M. J. and Ostriker, J. P. Cooling, dynamics and fragmentation of massive gas clouds - Clues to the masses and radii of galaxies and clusters. MNRAS **179**, 541 (1977).

Regan, M. W. and Elmegreen, D. M. K-Band observations of barred spiral galaxies. AJ **114**, 965 (1997).

Regan, M. W. and Mulchaey, J. S. Using HUBBLE SPACE TELESCOPE Imaging of Nuclear Dust Morphology to Rule Out Bars Fueling Seyfert Nuclei. AJ **117**, 2676 (1999).

Robaina, A. R.; Bell, E. F.; van der Wel, A.; Somerville, R. S.; Skelton, R. E.; McIntosh, D. H.; Meisenheimer, K. and Wolf, C. The Merger-driven Evolution of Massive Galaxies. ApJ **719**, 844 (2010).

Roberts, M. S. and Haynes, M. P. Physical Parameters along the Hubble Sequence. ARA&A **32**, 115 (1994).

Robertson, B.; Bullock, J. S.; Cox, T. J.; Di Matteo, T.; Hernquist, L.; Springel, V. and Yoshida, N. A Merger-driven Scenario for Cosmological Disk Galaxy Formation. ApJ **645**, 986 (2006).

Saintonge, A.; Kauffmann, G.; Wang, J.; Kramer, C.; Tacconi, L. J.; Buchbender, C.; Catinella, B.; Graciá-Carpio, J.; Cortese, L.; Fabello, S.; Fu, J.; Genzel, R.; Giovanelli, R.; Guo, Q.; Haynes, M. P.; Heckman, T. M.; Krumholz, M. R.; Lemonias, J.; Li, C.; Moran, S.; Rodriguez-Fernandez, N.; Schiminovich, D.; Schuster, K. and Sievers, A. COLD GASS, an IRAM legacy survey of molecular gas in massive galaxies - II. The non-universality of the molecular gas depletion time-scale. MNRAS **415**, 61 (2011).

Sakamoto, K.; Okumura, S. K.; Ishizuki, S. and Scoville, N. Z. Bar-driven Transport of Molecular Gas to Galactic Centers and Its Consequences. ApJ **525**, 691 (1999).

Salim, S.; Charlot, S.; Rich, R. M.; Kauffmann, G.; Heckman, T. M.; Barlow, T. A.; Bianchi, L.; Byun, Y.-I.; Donas, J.; Forster, K.; Friedman, P. G.; Jelinsky, P. N.; Lee, Y.-W.; Madore, B. F.; Malina, R. F.; Martin, D. C.; Milliard, B.; Morrissey, P.; Neff, S. G.; Schiminovich, D.; Seibert, M.; Siegmund, O. H. W.; Small, T.; Szalay, A. S.; Welsh, B. Y. and Wyder, T. K. New Constraints on the Star Formation Histories and Dust Attenuation of Galaxies in the Local Universe from GALEX. ApJ **619**, L39 (2005).

Salim, S.; Fang, J. J.; Rich, R. M.; Faber, S. M. and Thilker, D. A. Galaxy-scale Star Formation on the Red Sequence: The Continued Growth of S0s and the Quiescence of Ellipticals. ApJ **755**, 105 (2012).

Salim, S. and Rich, R. M. Star Formation Signatures in Optically Quiescent Early-type Galaxies. ApJ **714**, L290 (2010).

Salim, S.; Rich, R. M.; Charlot, S.; Brinchmann, J.; Johnson, B. D.; Schiminovich, D.; Seibert, M.; Mallery, R.; Heckman, T. M.; Forster, K.; Friedman, P. G.; Martin, D. C.; Morrissey, P.; Neff, S. G.; Small, T.; Wyder, T. K.; Bianchi, L.; Donas, J.; Lee, Y.-W.; Madore, B. F.; Milliard, B.; Szalay, A. S.; Welsh, B. Y. and Yi, S. K. UV Star Formation Rates in the Local Universe. ApJS **173**, 267 (2007).

Sánchez-Janssen, R. and Gadotti, D. A. Evidence for secular evolution of disc structural parameters in massive barred galaxies. MNRAS **432**, L56 (2013).

Sanders, D. B.; Soifer, B. T.; Elias, J. H.; Madore, B. F.; Matthews, K.; Neugebauer, G. and Scoville, N. Z. Ultraluminous infrared galaxies and the origin of quasars. ApJ **325**, 74 (1988).

Sanders, R. H. Seyfert nuclei as short-lived stochastic accretion events. A&A **140**, 52 (1984).

Sanders, R. H. and Huntley, J. M. Gas response to oval distortions in disk galaxies. ApJ **209**, 53 (1976).

Schawinski, K.; Lintott, C.; Thomas, D.; Sarzi, M.; Andreescu, D.; Bamford, S. P.; Kaviraj, S.; Khochfar, S.; Land, K.; Murray, P.; Nichol, R. C.; Raddick, M. J.; Slosar, A.; Szalay, A.; Vandenberg, J. and Yi, S. K. Galaxy Zoo: a sample of blue early-type galaxies at low redshift. MNRAS **396**, 818 (2009a).

Schawinski, K.; Thomas, D.; Sarzi, M.; Maraston, C.; Kaviraj, S.; Joo, S.-J.; Yi, S. K. and Silk, J. Observational evidence for AGN feedback in early-type galaxies. MNRAS **382**, 1415 (2007a).

Schawinski, K.; Thomas, D.; Sarzi, M.; Maraston, C.; Kaviraj, S.; Joo, S.-J.; Yi, S. K. and Silk, J. Observational evidence for AGN feedback in early-type galaxies. MNRAS **382**, 1415 (2007b).

Schawinski, K.; Treister, E.; Urry, C. M.; Cardamone, C. N.; Simmons, B. and Yi, S. K. HST WFC3/IR Observations of Active Galactic Nucleus Host Galaxies at z $\sim$ 2: Supermassive Black Holes Grow in Disk Galaxies. ApJ **727**, L31 (2011).

Schawinski, K.; Urry, C. M.; Virani, S.; Coppi, P.; Bamford, S. P.; Treister, E.; Lintott, C. J.; Sarzi, M.; Keel, W. C.; Kaviraj, S.; Cardamone, C. N.; Masters, K. L.; Ross, N. P.; Andreescu, D.; Murray, P.; Nichol, R. C.; Raddick, M. J.; Slosar, A.; Szalay, A. S.; Thomas, D. and Vandenberg, J. Galaxy Zoo: The Fundamentally Different Co-Evolution of Supermassive Black Holes and Their Early- and Late-Type Host Galaxies. ApJ **711**, 284 (2010).

Schawinski, K.; Virani, S.; Simmons, B.; Urry, C. M.; Treister, E.; Kaviraj, S. and Kushkuley, B. Do Moderate-Luminosity Active Galactic Nuclei Suppress Star Formation? ApJ **692**, L19 (2009b).

Schaye, J. Star Formation Thresholds and Galaxy Edges: Why and Where. ApJ **609**, 667 (2004).

Schiminovich, D.; Catinella, B.; Kauffmann, G.; Fabello, S.; Wang, J.; Hummels, C.; Lemonias, J.; Moran, S. M.; Wu, R.; Giovanelli, R.; Haynes, M. P.; Heckman, T. M.; Basu-Zych, A. R.; Blanton, M. R.; Brinchmann, J.; Budavári, T.; Gonçalves, T.; Johnson, B. D.; Kennicutt, R. C.; Madore, B. F.; Martin, C. D.; Rich, M. R.; Tacconi, L. J.; Thilker, D. A.; Wild, V.

and Wyder, T. K. The GALEX Arecibo SDSS Survey - II. The star formation efficiency of massive galaxies. MNRAS **408**, 919 (2010).

Schiminovich, D.; Wyder, T. K.; Martin, D. C.; Johnson, B. D.; Salim, S.; Seibert, M.; Treyer, M. A.; Budavári, T.; Hoopes, C.; Zamojski, M.; Barlow, T. A.; Forster, K. G.; Friedman, P. G.; Morrissey, P.; Neff, S. G.; Small, T. A.; Bianchi, L.; Donas, J.; Heckman, T. M.; Lee, Y.-W.; Madore, B. F.; Milliard, B.; Rich, R. M.; Szalay, A. S.; Welsh, B. Y. and Yi, S. The UV-Optical Color Magnitude Diagram. II. Physical Properties and Morphological Evolution On and Off of a Star-forming Sequence. ApJS **173**, 315 (2007).

Schmitt, H. R.; Donley, J. L.; Antonucci, R. R. J.; Hutchings, J. B.; Kinney, A. L. and Pringle, J. E. A Hubble Space Telescope Survey of Extended [O III] λ5007 Å Emission in a Far-Infrared-Selected Sample of Seyfert Galaxies: Results. ApJ **597**, 768 (2003).

Schmitt, H. R.; Pringle, J. E.; Clarke, C. J. and Kinney, A. L. The Orientation of Jets Relative to Dust Disks in Radio Galaxies. ApJ **575**, 150 (2002).

Schwarz, M. P. The response of gas in a galactic disk to bar forcing. ApJ **247**, 77 (1981).

Scoville, N.; Aussel, H.; Brusa, M.; Capak, P.; Carollo, C. M.; Elvis, M.; Giavalisco, M.; Guzzo, L.; Hasinger, G.; Impey, C.; Kneib, J.-P.; LeFevre, O.; Lilly, S. J.; Mobasher, B.; Renzini, A.; Rich, R. M.; Sanders, D. B.; Schinnerer, E.; Schminovich, D.; Shopbell, P.; Taniguchi, Y. and Tyson, N. D. The Cosmic Evolution Survey (COSMOS): Overview. ApJS **172**, 1 (2007).

Sellwood, J. A. Galaxy models with live halos. A&A **89**, 296 (1980).

Sellwood, J. A. Secular evolution in disk galaxies. *Reviews of Modern Physics* **86**, 1 (2014).

Sellwood, J. A. and Wilkinson, A. Dynamics of barred galaxies. *Reports on Progress in Physics* **56**, 173 (1993).

Sersic, J. L. *Atlas de galaxias australes* (1968).

Shen, J. and Sellwood, J. A. The Destruction of Bars by Central Mass Concentrations. ApJ **604**, 614 (2004).

Shen, S.; Mo, H. J.; White, S. D. M.; Blanton, M. R.; Kauffmann, G.; Voges, W.; Brinkmann, J. and Csabai, I. The size distribution of galaxies in the Sloan Digital Sky Survey. MNRAS **343**, 978 (2003).

Sheth, K.; Elmegreen, D. M.; Elmegreen, B. G.; Capak, P.; Abraham, R. G.; Athanassoula, E.; Ellis, R. S.; Mobasher, B.; Salvato, M.; Schinnerer, E.; Scoville, N. Z.; Spalsbury, L.; Strubbe, L.; Carollo, M.; Rich, M. and West, A. A. Evolution of the Bar Fraction in COSMOS: Quantifying the Assembly of the Hubble Sequence. ApJ **675**, 1141 (2008).

Sheth, K.; Melbourne, J.; Elmegreen, D. M.; Elmegreen, B. G.; Athanassoula, E.; Abraham, R. G. and Weiner, B. J. Hot Disks and Delayed Bar Formation. ApJ **758**, 136 (2012).

Sheth, K.; Vogel, S. N.; Regan, M. W.; Thornley, M. D. and Teuben, P. J. Secular Evolution via Bar-driven Gas Inflow: Results from BIMA SONG. ApJ **632**, 217 (2005).

Shlosman, I.; Begelman, M. C. and Frank, J. The fuelling of active galactic nuclei. Nature **345**, 679 (1990).

Shlosman, I.; Frank, J. and Begelman, M. C. Bars within bars - A mechanism for fuelling active galactic nuclei. Nature **338**, 45 (1989).

Shlosman, I. and Noguchi, M. Effects of gas on the global stability of galactic disks - Radial flows. ApJ **414**, 474 (1993).

Silk, J. On the fragmentation of cosmic gas clouds. I - The formation of galaxies and the first generation of stars. ApJ **211**, 638 (1977).

Silverman, J. D.; Green, P. J.; Barkhouse, W. A.; Kim, D.-W.; Kim, M.; Wilkes, B. J.; Cameron, R. A.; Hasinger, G.; Jannuzi, B. T.; Smith, M. G.; Smith, P. S. and Tananbaum, H. The Luminosity Function of X-Ray-selected Active Galactic Nuclei: Evolution of Supermassive Black Holes at High Redshift. ApJ **679**, 118 (2008).

Simard, L.; Mendel, J. T.; Patton, D. R.; Ellison, S. L. and McConnachie, A. W. A Catalog of Bulge+disk Decompositions and Updated Photometry for 1.12 Million Galaxies in the Sloan Digital Sky Survey. ApJS **196**, 11 (2011).

Simard, L.; Willmer, C. N. A.; Vogt, N. P.; Sarajedini, V. L.; Phillips, A. C.; Weiner, B. J.; Koo, D. C.; Im, M.; Illingworth, G. D. and Faber, S. M. The DEEP Groth Strip Survey. II. Hubble Space Telescope Structural Parameters of Galaxies in the Groth Strip. ApJS **142**, 1 (2002).

Simkin, S. M.; Su, H. J. and Schwarz, M. P. Nearby Seyfert galaxies. ApJ **237**, 404 (1980).

Simmons, B. D.; Lintott, C.; Schawinski, K.; Moran, E. C.; Han, A.; Kaviraj, S.; Masters, K. L.; Urry, C. M.; Willett, K. W.; Bamford, S. P. and Nichol, R. C. Galaxy Zoo: bulgeless galaxies with growing black holes. MNRAS **429**, 2199 (2013).

Simmons, B. D.; Urry, C. M.; Schawinski, K.; Cardamone, C. and Glikman, E. Moderate-luminosity Growing Black Holes from $1.25 < z < 2.7$: Varied Accretion in Disk-dominated Hosts. ApJ **761**, 75 (2012).

Sirianni, M.; Jee, M. J.; Benítez, N.; Blakeslee, J. P.; Martel, A. R.; Meurer, G.; Clampin, M.; De Marchi, G.; Ford, H. C.; Gilliland, R.; Hartig, G. F.; Illingworth, G. D.; Mack, J. and McCann, W. J. The Photometric Performance and Calibration of the Hubble Space Telescope Advanced Camera for Surveys. PASP **117**, 1049 (2005).

Skibba, R. A.; Bamford, S. P.; Nichol, R. C.; Lintott, C. J.; Andreescu, D.; Edmondson, E. M.; Murray, P.; Raddick, M. J.; Schawinski, K.; Slosar, A.; Szalay, A. S.; Thomas, D. and Vandenberg, J. Galaxy Zoo: disentangling the environmental dependence of morphology and colour. MNRAS **399**, 966 (2009).

Skibba, R. A.; Masters, K. L.; Nichol, R. C.; Zehavi, I.; Hoyle, B.; Edmondson, E. M.; Bamford, S. P.; Cardamone, C. N.; Keel, W. C.; Lintott, C. and Schawinski, K. Galaxy Zoo: the environmental dependence of bars and bulges in disc galaxies. MNRAS **423**, 1485 (2012).

Smith, G. P.; Treu, T.; Ellis, R. S.; Moran, S. M. and Dressler, A. Evolution since $z = 1$ of the Morphology-Density Relation for Galaxies. ApJ **620**, 78 (2005).

Springel, V.; Di Matteo, T. and Hernquist, L. Black Holes in Galaxy Mergers: The Formation of Red Elliptical Galaxies. ApJ **620**, L79 (2005).

Springel, V. and Hernquist, L. Formation of a Spiral Galaxy in a Major Merger. ApJ **622**, L9 (2005).

Strateva, I.; Ivezić, Ž.; Knapp, G. R.; Narayanan, V. K.; Strauss, M. A.; Gunn, J. E.; Lupton, R. H.; Schlegel, D.; Bahcall, N. A.; Brinkmann, J.; Brunner, R. J.; Budavári, T.; Csabai, I.; Castander, F. J.; Doi, M.; Fukugita, M.; Győry, Z.; Hamabe, M.; Hennessy, G.; Ichikawa, T.; Kunszt, P. Z.; Lamb, D. Q.; McKay, T. A.; Okamura, S.; Racusin, J.; Sekiguchi, M.; Schneider, D. P.; Shimasaku, K. and York, D. Color Separation of Galaxy Types in the Sloan Digital Sky Survey Imaging Data. AJ **122**, 1861 (2001).

Strauss, M. A.; Weinberg, D. H.; Lupton, R. H.; Narayanan, V. K.; Annis, J.; Bernardi, M.; Blanton, M.; Burles, S.; Connolly, A. J.; Dalcanton, J.; Doi, M.; Eisenstein, D.; Frieman, J. A.; Fukugita, M.; Gunn, J. E.; Ivezić, Ž.; Kent, S.; Kim, R. S. J.; Knapp, G. R.; Kron, R. G.; Munn, J. A.; Newberg, H. J.; Nichol, R. C.; Okamura, S.; Quinn, T. R.; Richmond, M. W.; Schlegel, D. J.; Shimasaku, K.; SubbaRao, M.; Szalay, A. S.; Vanden Berk, D.; Vogeley, M. S.; Yanny, B.; Yasuda, N.; York, D. G. and Zehavi, I. Spectroscopic Target Selection in the Sloan Digital Sky Survey: The Main Galaxy Sample. AJ **124**, 1810 (2002).

Taylor, E. N.; Franx, M.; Brinchmann, J.; van der Wel, A. and van Dokkum, P. G. On the Masses of Galaxies in the Local Universe. ApJ **722**, 1 (2010).

Thomas, D.; Maraston, C.; Bender, R. and Mendes de Oliveira, C. The Epochs of Early-Type Galaxy Formation as a Function of Environment. ApJ **621**, 673 (2005).

Toomre, A. and Toomre, J. Galactic Bridges and Tails. ApJ **178**, 623 (1972).

Treister, E.; Schawinski, K.; Urry, C. M. and Simmons, B. D. Major Galaxy Mergers Only Trigger the Most Luminous Active Galactic Nuclei. ApJ **758**, L39 (2012).

Tremaine, S. and Weinberg, M. D. Dynamical friction in spherical systems. MNRAS **209**, 729 (1984).

Trujillo, I.; Conselice, C. J.; Bundy, K.; Cooper, M. C.; Eisenhardt, P. and Ellis, R. S. Strong size evolution of the most massive galaxies since z $\sim$ 2. MNRAS **382**, 109 (2007).

Trujillo, I.; Förster Schreiber, N. M.; Rudnick, G.; Barden, M.; Franx, M.; Rix, H.-W.; Caldwell, J. A. R.; McIntosh, D. H.; Toft, S.; Häussler, B.; Zirm, A.; van Dokkum, P. G.; Labbé, I.; Moorwood, A.; Röttgering, H.; van der Wel, A.; van der Werf, P. and van Starkenburg, L. The Size Evolution of Galaxies since $z \sim 3$: Combining SDSS, GEMS, and FIRES. ApJ **650**, 18 (2006).

Trump, J. R. Host Galaxy Morphology and the AGN Unified Model. *ArXiv e-prints* (2011).

Ueda, Y.; Akiyama, M.; Ohta, K. and Miyaji, T. Cosmological Evolution of the Hard X-Ray Active Galactic Nucleus Luminosity Function and the Origin of the Hard X-Ray Background. ApJ **598**, 886 (2003).

Ulvestad, J. S. and Wilson, A. S. Radio structures of Seyfert galaxies. VI - VLA observations of a nearby sample. ApJ **285**, 439 (1984).

Valenzuela, O. and Klypin, A. Secular bar formation in galaxies with a significant amount of dark matter. MNRAS **345**, 406 (2003).

van Driel, W. and van Woerden, H. Distribution and motions of atomic hydrogen in lenticular galaxies. XI - A summary of H I observations and evolutionary scenarios. A&A **243**, 71 (1991).

Vila-Costas, M. B. and Edmunds, M. G. The relation between abundance gradients and the physical properties of spiral galaxies. MNRAS **259**, 121 (1992).

Villa-Vargas, J.; Shlosman, I. and Heller, C. Dark Matter Halos and Evolution of Bars in Disk Galaxies: Varying Gas Fraction and Gas Spatial Resolution. ApJ **719**, 1470 (2010).

Wada, K. and Habe, A. Rapid gas supply to a nuclear region by self-gravitational instability in a weak barred potential. MNRAS **258**, 82 (1992a).

Wada, K. and Habe, A. Rapid gas supply to a nuclear region by self-gravitational instability in a weak barred potential. MNRAS **258**, 82 (1992b).

Wada, K. and Habe, A. Bar-driven fuelling to a galactic central region in a massive gas disc. MNRAS **277**, 433 (1995).

Wake, D. A.; Franx, M. and van Dokkum, P. G. Which galaxy property is the best indicator of its host dark matter halo properties? *ArXiv e-prints* (2012a).

Wake, D. A.; van Dokkum, P. G. and Franx, M. Revealing Velocity Dispersion as the Best Indicator of a Galaxy's Color, Compared to Stellar Mass, Surface Mass Density, or Morphology. ApJ **751**, L44 (2012b).

Wang, J.; Kauffmann, G.; Overzier, R.; Tacconi, L. J.; Kong, X.; Saintonge, A.; Catinella, B.; Schiminovich, D.; Moran, S. M. and Johnson, B. Quantifying the role of bars in the build-up of central mass concentrations in disc galaxies. MNRAS **423**, 3486 (2012).

Weiner, B. J.; Coil, A. L.; Prochaska, J. X.; Newman, J. A.; Cooper, M. C.; Bundy, K.; Conselice, C. J.; Dutton, A. A.; Faber, S. M.; Koo, D. C.; Lotz, J. M.; Rieke, G. H. and Rubin,

K. H. R. Ubiquitous Outflows in DEEP2 Spectra of Star-Forming Galaxies at z = 1.4. ApJ **692**, 187 (2009).

Weiner, B. J.; Phillips, A. C.; Faber, S. M.; Willmer, C. N. A.; Vogt, N. P.; Simard, L.; Gebhardt, K.; Im, M.; Koo, D. C.; Sarajedini, V. L.; Wu, K. L.; Forbes, D. A.; Gronwall, C.; Groth, E. J.; Illingworth, G. D.; Kron, R. G.; Rhodes, J.; Szalay, A. S. and Takamiya, M. The DEEP Groth Strip Galaxy Redshift Survey. III. Redshift Catalog and Properties of Galaxies. ApJ **620**, 595 (2005).

Willett, K. W.; Lintott, C. J.; Bamford, S. P.; Masters, K. L.; Simmons, B. D.; Casteels, K. R. V.; Edmondson, E. M.; Fortson, L. F.; Kaviraj, S.; Keel, W. C.; Melvin, T.; Nichol, R. C.; Raddick, M. J.; Schawinski, K.; Simpson, R. J.; Skibba, R. A.; Smith, A. M. and Thomas, D. Galaxy Zoo 2: detailed morphological classifications for 304 122 galaxies from the Sloan Digital Sky Survey. MNRAS **435**, 2835 (2013).

Williams, C. C.; Giavalisco, M.; Cassata, P.; Tundo, E.; Wiklind, T.; Guo, Y.; Lee, B.; Barro, G.; Wuyts, S.; Bell, E. F.; Conselice, C. J.; Dekel, A.; Faber, S. M.; Ferguson, H. C.; Grogin, N.; Hathi, N.; Huang, K.-H.; Kocevski, D.; Koekemoer, A.; Koo, D. C.; Ravindranath, S. and Salimbeni, S. The Progenitors of the Compact Early-type Galaxies at High Redshift. ApJ **780**, 1 (2014).

Williams, M. J.; Bureau, M. and Kuntschner, H. Secular evolution in action: central values and radial trends in the stellar populations of boxy bulges. MNRAS **427**, L99 (2012).

Williams, R. J.; Quadri, R. F.; Franx, M.; van Dokkum, P. and Labbé, I. Detection of Quiescent Galaxies in a Bicolor Sequence from Z = 0-2. ApJ **691**, 1879 (2009).

Woo, J.; Dekel, A.; Faber, S. M.; Noeske, K.; Koo, D. C.; Gerke, B. F.; Cooper, M. C.; Salim, S.; Dutton, A. A.; Newman, J.; Weiner, B. J.; Bundy, K.; Willmer, C. N. A.; Davis, M. and Yan, R. Dependence of galaxy quenching on halo mass and distance from its centre. MNRAS **428**, 3306 (2013).

Wuyts, S.; Förster Schreiber, N. M.; van der Wel, A.; Magnelli, B.; Guo, Y.; Genzel, R.; Lutz, D.; Aussel, H.; Barro, G.; Berta, S.; Cava, A.; Graciá-Carpio, J.; Hathi, N. P.; Huang, K.-H.; Kocevski, D. D.; Koekemoer, A. M.; Lee, K.-S.; Le Floc'h, E.; McGrath, E. J.; Nordon, R.; Popesso, P.; Pozzi, F.; Riguccini, L.; Rodighiero, G.; Saintonge, A. and Tacconi, L. Galaxy Structure and Mode of Star Formation in the SFR-Mass Plane from z $\sim$ 2.5 to z $\sim$ 0.1. ApJ **742**, 96 (2011).

Wuyts, S.; Labbé, I.; Schreiber, N. M. F.; Franx, M.; Rudnick, G.; Brammer, G. B. and van Dokkum, P. G. FIREWORKS U_{38}-to-24 μm Photometry of the GOODS Chandra Deep Field-South: Multiwavelength Catalog and Total Infrared Properties of Distant K_s-selected Galaxies. ApJ **682**, 985 (2008).

Xu, C. K.; Zhao, Y.; Scoville, N.; Capak, P.; Drory, N. and Gao, Y. Major-merger Galaxy Pairs in the COSMOS Field—Mass-dependent Merger Rate Evolution since z = 1. ApJ **747**, 85 (2012).

Xue, Y. Q.; Luo, B.; Brandt, W. N.; Bauer, F. E.; Lehmer, B. D.; Broos, P. S.; Schneider, D. P.; Alexander, D. M.; Brusa, M.; Comastri, A.; Fabian, A. C.; Gilli, R.; Hasinger, G.; Hornschemeier, A. E.; Koekemoer, A.; Liu, T.; Mainieri, V.; Paolillo, M.; Rafferty, D. A.; Rosati, P.; Shemmer, O.; Silverman, J. D.; Smail, I.; Tozzi, P. and Vignali, C. The Chandra Deep Field-South Survey: 4 Ms Source Catalogs. ApJS **195**, 10 (2011).

Yan, R.; Ho, L. C.; Newman, J. A.; Coil, A. L.; Willmer, C. N. A.; Laird, E. S.; Georgakakis, A.; Aird, J.; Barmby, P.; Bundy, K.; Cooper, M. C.; Davis, M.; Faber, S. M.; Fang, T.; Griffith, R. L.; Koekemoer, A. M.; Koo, D. C.; Nandra, K.; Park, S. Q.; Sarajedini, V. L.; Weiner, B. J. and Willner, S. P. AEGIS: Demographics of X-ray and Optically Selected Active Galactic Nuclei. ApJ **728**, 38 (2011).

Yang, Y.; Zabludoff, A. I.; Zaritsky, D. and Mihos, J. C. The Detailed Evolution of E+A Galaxies into Early Types. ApJ **688**, 945 (2008).

Zaritsky, D.; Kennicutt, Jr., R. C. and Huchra, J. P. H II regions and the abundance properties of spiral galaxies. ApJ **420**, 87 (1994).

Zheng, X. Z.; Bell, E. F.; Papovich, C.; Wolf, C.; Meisenheimer, K.; Rix, H.-W.; Rieke, G. H. and Somerville, R. The Dependence of Star Formation on Galaxy Stellar Mass. ApJ **661**, L41 (2007).

Appendix A

Completeness of Chapter 1

A.1 Surface Brightness Limits

One might be concerned that our ‘final’ sample may be missing low surface brightness galaxies; in this Appendix, we show that this is not the case. We demonstrate our ‘final’ and ‘starting’ samples’ surface brightness limits in Fig. A.1 by plotting the effective radius in arcseconds vs. V and I (see §2.3 for sample definitions). The master GIM2D sample is plotted in gray and the ‘starting’ and ‘final’ sample are overplotted in red and blue, respectively. In each panel, we draw two lines of constant surface brightness to give an idea of our samples’ surface brightness boundaries. There is obviously an edge to the distribution of the master GIM2D sample at low surface brightnesses. Whether this is a selection limit or a reflection of where real galaxies lie is unclear. But it is clear that the master GIM2D sample contains galaxies with the lowest surface brightnesses, indicating that our ‘starting’ and ‘final’ samples are sensitive to them.

In these plots, the relevant difference between the 'starting' and 'final' sample is the imposed mass limit of the 'final' sample. The main concern in terms of sample completeness boils down to whether the 'final' sample is missing massive low surface brightness galaxies. It is clear that there are many galaxies in 'starting' sample (and the master GIM2D sample) with much lower surface brightnesses than those in the 'final' sample. Hence if such massive low surface brightness galaxies existed, the 'final' sample should certainly contain them, thus our 'final' sample does not miss low surface brightness galaxies.

A.2 GIM2D Measurement Quaility

In this appendix, we show that the errors on the GIM2D measurements are well-behaved even at the sample limits. The most important quantities are the GIM2D model HST/ACS V and I magnitudes since every structural measurement is based on them. Fig. A.2 plots the V and I 1-σ errors as a function of V, I, and $\log M_*$. These errors are confidence limits derived through full Monte Carlo propagations of the parameter probability distributions computed by GIM2D (Simard *et al.*, 2002).

Shown are the master GIM2D catalog (gray), 'starting' sample (red), 'final' sample (blue), and galaxies within the 'final' sample with Sérsic indices $n < 1$ (pink). The 5-σ limiting magnitudes for the HST/ACS images are $V = 26.23$ and $I = 25.61$, consistent with the master GIM2D distribution. Within our 'final' sample, the limits of the magnitude distributions are ≈ 0.5 mag and ≈ 1.0 mag brighter than those limits, respectively. And most importantly, the V and I magnitude errors at the mass and magnitude limit of the 'final' sample are small, ≤ 0.06

mag, with the majority ≤ 0.03 mag.

To further illustrate the quality of the ‘final’ sample’s GIM2D fits, we plot in Fig. A.3 the 1-σ error of the Sérsic index, fractional 1-σ error of the effective radius, and the 1-σ error of the bulge-to-total ratio B/T (in the I band) as a function of V, I, and M_*. The errors of the Sérsic index measurements are almost all ≤ 0.2. A typical late-type galaxy has $n \sim 1$ while a typical early-type galaxy has $n \sim 4$. An error of 0.2 on n will not affect this division and hence these errors are tolerable. The errors on the effective radius measurements are presented as fractional errors, i.e., 1-σ effective radius error divided by the effective radius. Note that these radii are semimajor axis effective radii and not circularized effective radii. The fractional errors are small, almost all are $\leq 6\%$. The errors on the B/T are almost all ≤ 0.05. Most star-forming, blue galaxies in our ‘starting’ sample, which are presumably late-type, have $B/T \leq 0.10$ while most quiescent, red galaxies in our ‘starting’ sample, which are presumably early-type, have $B/T \geq 0.40$. Thus an error of 0.05 will not push blue galaxies to B/T values of red galaxies and vice versa. In summary, these plots demonstrate that our ‘final’ sample contain quality GIM2D measurements down to the mass and magnitude limits of the ‘final’ sample.

A.3 Sérsic Index Bias?

One might be concerned that the Sérsic index may be sensitive to surface brightness and stellar mass. Fig. A.4 plots the Sérsic index against these quantities. The top row is the μ in V and I. The vertical green dot-dashed line represents the approximate edge of the ‘final’ sample’s surface brightness distribution as seen in Fig. A.1. The contours represent the number

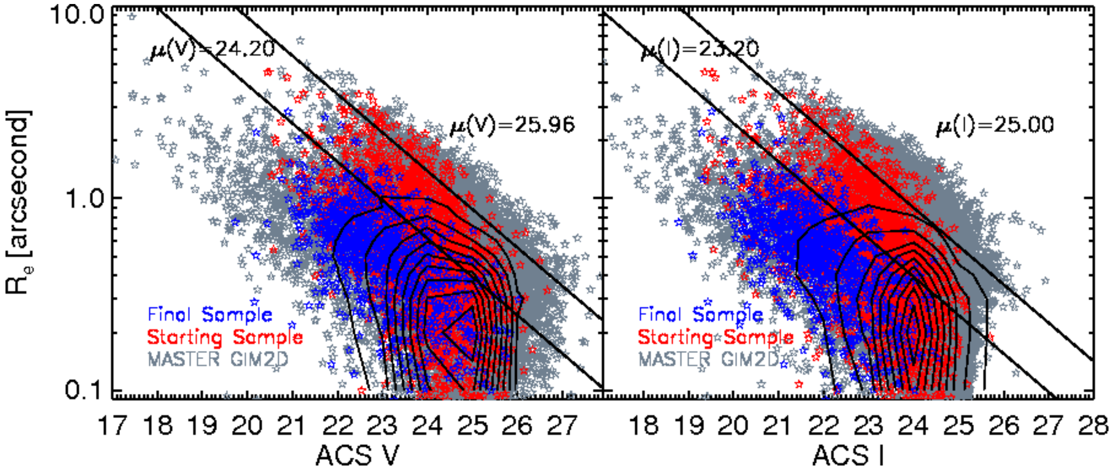

Figure A.1: Semimajor axis effective radius in arcsecond is plotted against V and I. The two lines of constant surface brightness in each panel roughly marks the edge of the 'starting' and 'final' samples' surface brightness distribution. The contours represent the number density of the master GIM2D sample.

density of the master GIM2D catalog, which clearly shows that the majority of these galaxies have low n. At faint μ, the 'starting' sample clearly has less $n > 3$ galaxies compared to the $n < 3$ population, but we would argue that is a reflection of the universe, i.e., high n galaxies generally have bright μ. For the 'final' sample, however, this proportional dearth of $n > 3$, faint μ galaxies seen in the 'starting' sample seems to have been greatly reduced.

We also plot the Sérsic index against stellar mass in the lower panel. At low stellar masses, the 'starting' sample also has less high n galaxies than low n galaxies. However, this absence does not seem as severe as with faint μ. And within our 'final' sample, it seems that this disparity in Sérsic populations have decreased. Moreover, it is important to note that even at the lowest masses, our 'final' sample still contains Sérsic index values across the entire possible range, indicating that GIM2D does not preclude high n fits for low mass galaxies. In fact, the absolute count of galaxies with Sérsic index $n > 3$ in every mass range is approximately the

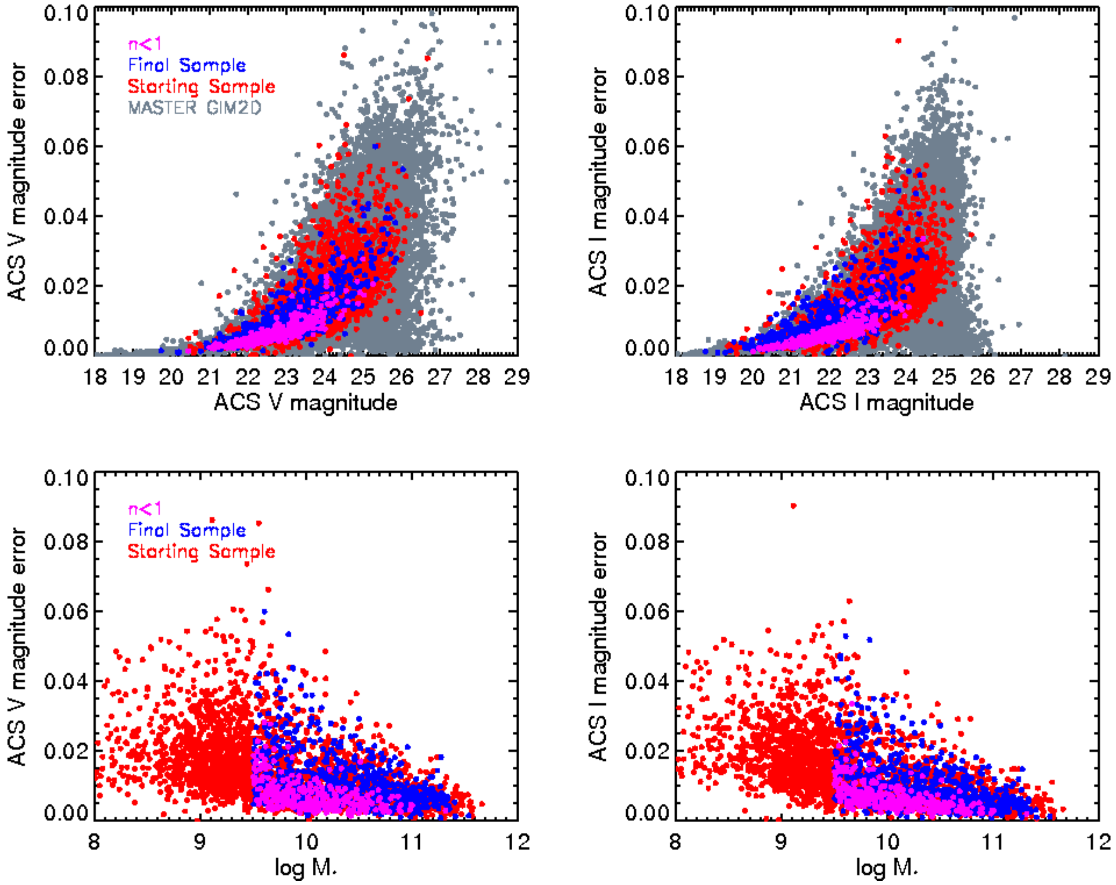

Figure A.2: V and I magnitude errors as a function of V, I, and log M_*.

same. Hence there is no predisposition against $n > 3$ galaxies in our 'final' sample. The fact that our 'final' sample has a large concentration of low n galaxies is most likely due to the fact that there are many late-type galaxies at low masses.

One might wonder how the low n galaxies fared near the limits of the data. As can be seen in Fig. A.4, the low n galaxies make up a significant fraction of our 'final' sample. To see the reliability of the measurements of these galaxies, we've highlighted this population ($n < 1$ galaxies in the 'final' sample) in magenta in several of the previous figures, specifically, Fig. A.2 and A.3. In most cases, these low n galaxies have errors consistent with the rest of the

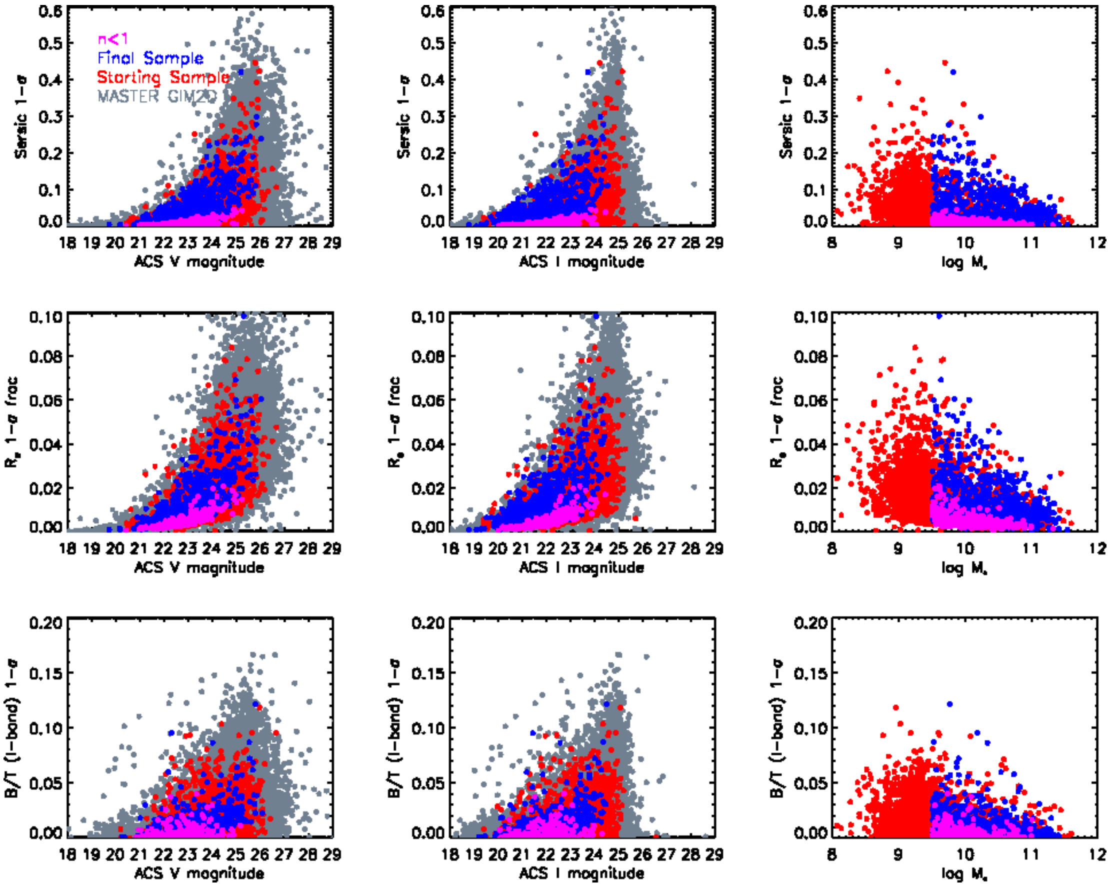

Figure A.3: Sérsic index error, effective radius fractional error, and bulge-to-total ratio errors as a function of V, I, and log M_*.

population, i.e., low n galaxies fare fine near the limits of our 'final' sample.

Table A.1: Galaxy Properties

DEEPID (1)	Q (2)	z (3)	M_B k-correct (4)	M_B Eqns. 2.3, 2.4 (5)	$U-B$ k-correct (6)	$U-B$ Eqn. 2.5 (7)	M_* J. Huang et al., in prep (8)	M_* Eqns. 2.6, 2.3, 2.4 (9)
13049654	4	0.20	-17.52	-17.49	0.77	0.77	9.14	9.19
13018599	4	0.79	-20.14	-20.13	1.14	1.14	10.56	10.42
12020067	4	0.45	-19.52	-19.38	0.62	0.65	9.38	9.49
12007757	4	0.99	-20.80	-20.91	0.89	0.83	10.09	10.12
13040619	4	0.71	-20.78	-20.96	1.34	1.24	10.81	10.82
13048556	4	0.61	-20.03	-20.48	0.64	0.59	9.53	9.75
13049852	4	0.57	-20.93	-21.01	1.44	1.39	10.93	10.94
13026131	-1	0.54	-18.73	-18.55	0.79	0.89	9.51	9.46

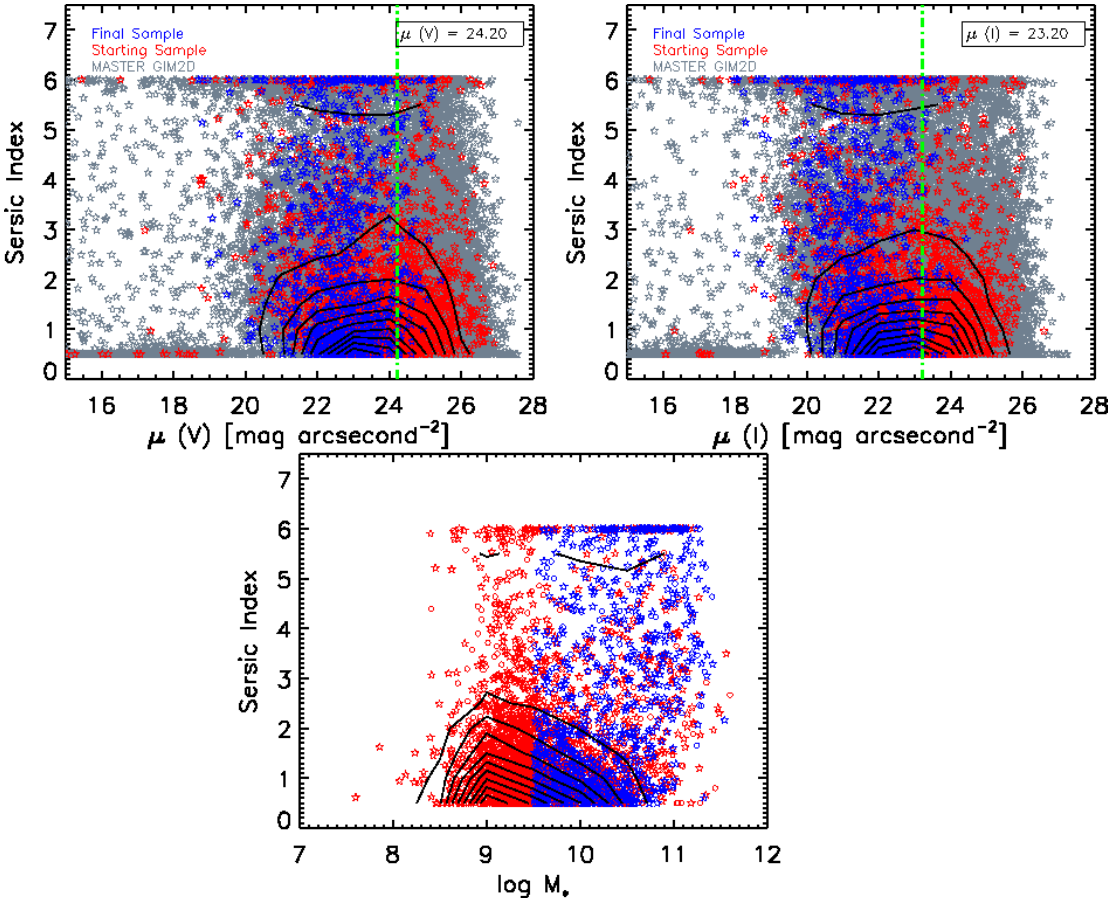

Figure A.4: Sérsic index is plotted against $\mu(V)$ and $\mu(I)$ in the top row. Contours represent the number density of the GIM2D master sample in gray. The vertical green dot-dashed line represents the approximate edge of our 'final' sample's surface brightnesses distribution (as seen in Fig. A.1). The bottom panel plots the Sérsic index against stellar mass. The 'final' sample does not show a strong disparity of high and low n populations at faint (low) surface brightness (mass).

Table A.1 (cont'd): Galaxy Properties

DEEPID (1)	Q (2)	z (3)	M_B k-correct (4)	M_B Eqns. 2.3, 2.4 (5)	$U-B$ k-correct (6)	$U-B$ Eqn. 2.5 (7)	M_* J. Huang et al., in prep (8)	M_* Eqns. 2.6, 2.3, 2.4 (9)
12020067	4	0.45	-19.52	-19.38	0.62	0.65	9.38	9.49
12015606	4	0.67	-20.77	-20.85	0.78	0.88	10.27	10.36
13058131	4	0.71	-20.84	-20.98	1.34	1.32	10.74	10.90
12016156	4	0.74	-19.47	-19.57	0.48	0.57	-1.00	9.37
13012297	4	0.81	-21.26	-21.19	1.23	1.24	10.92	10.94
12007918	4	0.66	-20.47	-20.45	0.63	0.68	9.79	9.90
13011795	-1	0.71	-19.81	-19.82	1.33	1.32	10.37	10.43
13064645	4	1.21	-22.56	-22.10	1.45	0.79	11.09	11.14

Table A.1 (cont'd): Galaxy Properties

DEEPID (1)	Q (2)	z (3)	M_B k-correct (4)	M_B Eqns. 2.3, 2.4 (5)	$U-B$ k-correct (6)	$U-B$ Eqn. 2.5 (7)	M_* J. Huang et al., in prep (8)	M_* Eqns. 2.6, 2.3, 2.4 (9)
12016799	3	0.68	-20.54	-20.54	1.16	1.12	10.67	10.53
12023870	-1	0.48	-18.78	-18.88	0.56	0.57	9.18	9.12
12004470	-1	0.46	-19.31	-19.15	0.29	0.53	9.13	9.17
12020439	4	0.58	-19.17	-18.97	0.74	0.66	10.03	9.27

Note. — Twenty randomly-selected galaxies from the catalog is shown. The entire catalog is available at: `http://people.ucsc.edu/~echeung1/data.html`. Col. (1): Unique DEEPID. Col. (2): Spectroscopic redshift quality code. Values of 3 and above are secure spectroscopic redshifts (see Newman *et al.*, 2013 for more details) and they comprise the spectroscopic sample. For values below 3, we use the photometric sample and their corresponding photometric redshifts. Col. (3): Best available redshift For those with $Q \geq 3$, these are spectroscopic z, those with $Q \leq 2$ are photometric z. Col. (4): Absolute B-band magnitude derived from k-correct. About $\approx 7\%$ have large error measurements, we use vales from Col. (5) for these objects. Col. (5): Absolute B-band magnitude derived from Eqns. 2.3, 2.4. Col. (6): $U-B$ rest-frame color derived from k-correct. About $\approx 7\%$ have large error measurements, we use vales from Col. (7) for these objects. Col. (7): $U-B$ rest-frame color derived from Eqn. 2.5. Col. (8): Stellar mass from J. Huang et al., in prep. $\approx 10\%$ of our sample have no corresponding M_*; they are marked by -1.00. We use Col. (9) for these objects. Col. (9): Stellar mass derived from Eqns. 2.6, 2.3, 2.4.

Table A.2: Subcomponent Properties

DEEPID (1)	M_B Bulge (2)	M_B Disk (3)	$U-B$ Bulge (4)	$U-B$ Disk (5)	M_* Bulge (6)	M_* Disk (7)
13049654	-15.95	-17.22	1.15	0.73	8.99	9.02
13018599	-19.17	-19.64	1.53	1.05	10.27	10.12
12020067	-18.85	-18.68	0.73	0.61	9.39	9.14
12007757	-20.30	-20.55	1.00	0.66	10.18	9.63
13040619	-19.62	-19.88	1.07	1.52	10.11	10.57
13048556	-19.15	-19.52	0.54	0.66	9.13	9.49
13049852	-19.33	-20.34	1.34	1.42	10.23	10.70
13026131	-17.65	-18.11	1.24	0.74	9.48	9.07
12020067	-18.85	-18.68	0.73	0.61	9.39	9.14
12015606	-19.84	-20.20	1.20	0.60	10.33	9.66
13058131	-19.60	-20.08	1.50	1.06	10.45	10.29
12016156	-18.85	-18.91	0.67	0.41	9.25	8.79
13012297	-21.05	-19.37	1.25	1.18	10.89	10.16
12007918	-19.91	-19.75	1.01	0.50	10.15	9.29

Table A.2 (cont'd): Subcomponent Properties

DEEPID (1)	M_B Bulge (2)	M_B Disk (3)	$U-B$ Bulge (4)	$U-B$ Disk (5)	M_* Bulge (6)	M_* Disk (7)
13011795	-18.66	-18.93	1.37	1.18	10.00	9.96
13064645	-21.00	-21.29	0.75	0.88	10.63	10.96
12016799	-20.27	-19.62	1.31	0.97	10.59	9.98
12023870	-18.35	-17.82	0.71	0.47	9.14	8.51
12004470	-18.40	-18.64	0.64	0.48	9.07	8.86
12020439	-18.26	-18.41	0.95	0.52	9.41	8.81

Note. — The same twenty randomly-selected galaxies from Table A.1 is shown. The entire catalog is available at: `http://people.ucsc.edu/~echeung1/data.html`. Col. (1): Unique DEEPID. Col. (2): Absolute *B*-band magnitude of bulge derived from Eqn. 2.3,2.4. Col. (3): Absolute *B*-band magnitude of disk derived from Eqn. 2.3-2.4. Col. (4): $U-B$ rest-frame color of bulge derived from Eqn. 2.5. Col. (5): $U-B$ rest-frame color of disk derived from Eqn. 2.5. Col. (6): M_* of bulge derived from Eqn. 2.3, 2.6. Col. (7): M_* of disk derived from Eqn. 2.3, 2.6.

Table A.3: GIM2D: Single n Catalog

DEEPID (1)	V (2)	I (3)	n (4)	e (5)	r_e (pixels) (6)	χ^2 V-band (7)	χ^2 I-band (8)
13049654	22.07	21.56	1.11	0.68	18.31	1.16	1.07
13018599	24.17	22.70	1.36	0.62	15.54	1.05	1.16
12020067	22.46	21.96	1.70	0.43	10.71	1.13	1.05
12007757	23.73	22.84	1.17	0.58	23.76	1.09	1.03
13040619	22.89	21.42	6.00	0.13	19.63	1.04	0.92
13048556	22.28	21.75	4.16	0.66	78.14	1.05	0.93
13049852	21.80	20.41	4.79	0.23	27.88	1.00	1.12
13026131	23.95	23.12	1.09	0.53	15.39	0.97	0.95
12020067	22.46	21.96	1.70	0.43	10.71	1.13	1.05
12015606	22.48	21.54	1.59	0.03	15.41	1.08	0.98
13058131	22.95	21.36	5.07	0.29	34.61	1.01	0.92
12016156	23.85	23.23	1.40	0.49	29.93	1.12	0.99
13012297	23.31	21.67	2.82	0.15	13.04	0.89	0.82
12007918	22.65	21.97	1.63	0.41	10.73	1.18	1.10

Table A.3 (cont'd): GIM2D: Single n Catalog

DEEPID (1)	V (2)	I (3)	n (4)	e (5)	r_e (pixels) (6)	χ^2 V-band (7)	χ^2 I-band (8)
13011795	24.10	22.51	5.94	0.30	16.12	0.88	0.81
13064645	23.97	22.49	5.99	0.25	12.85	0.96	0.93
12016799	23.02	21.76	1.36	0.46	21.21	1.15	1.09
12023870	23.13	22.70	4.64	0.46	8.98	1.21	1.18
12004470	22.71	22.34	1.66	0.41	5.67	1.62	1.48
12020439	23.69	23.09	1.32	0.68	6.24	1.10	1.15

Note. — The same twenty randomly-selected galaxies from Table A.1 is shown. The entire catalog is available at: `http://people.ucsc.edu/~echeung1/data.html`. Every value in this table is from the GIM2D decomposition that only fits for a single Sérsic index. These are the primary data we use throughout this paper, including the basic V and I of the galaxy. Col. (1): DEEPID. Col. (2): V-band magnitude of galaxy. Col. (3): I-band magnitude of galaxy. Col. (4): Sérsic index of galaxy. Col. (5): Ellipticity of galaxy. $e \equiv 1-b/a$, $b \equiv$ semiminoraxis, $a \equiv$ semimajoraxis) Col. (6): Effective radius of the galaxy measured along the major axis in units of pixels. Col. (7): χ^2 of fit in the V-band. Col. (8): χ^2 of fit in the I-band.

Table A.4: GIM2D: $n = 4$ Bulge Catalog

DEEPID (1)	V Bulge (2)	V Disk (3)	I Bulge (4)	I Disk (5)	B/T V-band (6)	B/T I-band (7)	r_e Bulge (pixels) (8)	r_d Disk (pixels) (9)	C V-band (10)	C I-band (11)	χ^2 V-band (12)	χ^2 I-band (13)
13049654	22.83	22.42	22.07	22.00	0.41	0.48	33.36	11.54	0.47	0.47	1.11	1.01
13018599	27.39	24.32	29.81	22.78	0.06	0.00	3.27	8.56	0.48	0.58	1.08	1.20
12020067	23.22	23.07	22.47	22.71	0.46	0.56	19.41	5.88	0.55	0.58	1.13	1.05
12007757	25.53	23.82	23.91	23.15	0.17	0.33	19.84	17.86	0.35	0.36	1.06	1.02
13040619	24.11	24.14	22.87	22.28	0.51	0.37	2.78	9.96	0.62	0.69	1.01	0.89
13048556	23.57	23.30	23.10	22.68	0.44	0.41	23.76	29.41	0.49	0.45	1.01	0.89
13049852	23.30	22.53	21.96	21.10	0.33	0.31	3.73	16.14	0.61	0.64	0.93	0.89

Table A.4 (cont'd): GIM2D: $n = 4$ Bulge Catalog

DEEPID (1)	V Bulge (2)	V Disk (3)	I Bulge (4)	I Disk (5)	B/T V-band (6)	B/T I-band (7)	r_{e} Bulge (pixels) (8)	r_{d} Disk (pixels) (9)	C V-band (10)	C I-band (11)	χ^2 V-band (12)	χ^2 I-band (13)
13026131	26.47	24.05	25.78	23.21	0.10	0.09	7.93	9.66	0.41	0.46	0.97	0.96
12020067	23.22	23.07	22.47	22.71	0.46	0.56	19.41	5.88	0.55	0.58	1.13	1.05
12015606	24.46	22.67	22.88	21.95	0.16	0.30	11.22	10.18	0.48	0.44	1.08	0.97
13058131	24.43	23.65	22.59	22.42	0.33	0.46	7.95	19.11	0.57	0.55	0.97	0.88
12016156	28.30	23.97	25.40	23.57	0.02	0.16	18.57	15.65	0.40	0.30	1.11	1.00
13012297	23.47	25.07	21.80	23.52	0.81	0.83	16.04	6.93	0.55	0.58	0.89	0.82
12007918	23.45	23.19	22.35	22.74	0.44	0.59	19.23	5.87	0.55	0.56	1.16	1.07

Table A.4 (cont'd): GIM2D: $n = 4$ Bulge Catalog

DEEPID (1)	V Bulge (2)	V Disk (3)	I Bulge (4)	I Disk (5)	B/T V-band (6)	B/T I-band (7)	r_{e} Bulge (pixels) (8)	r_{d} Disk (pixels) (9)	C V-band (10)	C I-band (11)	χ^2 V-band (12)	χ^2 I-band (13)
13011795	24.78	25.27	23.12	24.09	0.61	0.71	6.49	12.72	0.66	0.65	0.87	0.81
13064645	24.95	25.15	23.56	23.36	0.55	0.45	2.26	10.60	0.69	0.71	0.94	0.88
12016799	30.56	23.11	28.18	21.85	0.00	0.00	13.39	11.62	0.36	0.38	1.17	1.14
12023870	23.39	24.42	22.83	24.18	0.72	0.78	21.91	1.89	0.66	0.71	1.14	1.15
12004470	23.32	23.27	22.90	22.94	0.49	0.51	11.73	3.03	0.73	0.74	1.53	1.42
12020439	24.77	24.01	23.65	23.61	0.33	0.49	13.89	3.54	0.65	0.72	1.02	1.06

Note. — The same twenty randomly-selected galaxies from Table A.1 is shown. The entire catalog is available at: `http://people.ucsc.edu/~echeung1/data.html`. Every value in this table is from the GIM2D decomposition using a bulge and disk with Sérsic index of $n = 4$ and $n = 1$, respectively. Col. (1): DEEPID. Col. (2) & (3): V-band magnitude of bulge and disk. Col. (4) & (5): I-band magnitude of bulge and disk. Col. (6): B/T in V-band. Col. (7): B/T in I-band. Col. (8): Effective radius of major axis of bulge in units of pixels. Col. (9): Scale length of disk measured along major axis in units of pixel. Col. (10): Concentration with $\alpha = 0.3$ in V. Col. (11): Concentration with $\alpha = 0.3$ in I. Col. (12): Chi-squared of fit in V. Col. (13): Chi-squared of fit in I.

Table A.5: GIM2D: $n = 2$ Bulge Catalog

DEEPID (1)	V Bulge (2)	I Bulge (3)	V Disk (4)	I Disk (5)	B/T V-band (6)	B/T I-band (7)	r_e Bulge (pixels) (8)	r_e Disk (pixels) (9)	C V-band (10)	C I-band (11)	χ^2 V-band (12)	χ^2 I-band (13)
13049654	23.33	22.38	22.51	21.90	0.29	0.36	24.61	10.97	0.47	0.47	1.11	1.00
13018599	25.53	24.55	23.41	23.23	0.29	0.46	20.65	8.46	0.48	0.58	1.05	1.12
12020067	23.02	23.16	22.43	22.70	0.53	0.56	23.38	4.43	0.53	0.55	1.05	0.98
12007757	24.66	23.79	23.48	23.18	0.31	0.43	14.76	35.53	0.35	0.36	1.04	0.98
13040619	24.40	23.95	23.20	22.18	0.40	0.28	1.92	9.09	0.62	0.69	1.01	0.90
13048556	22.99	25.33	22.59	23.80	0.90	0.75	28.14	30.87	0.50	0.48	1.11	0.96
13049852	23.48	22.48	22.14	21.05	0.28	0.27	3.13	15.79	0.61	0.64	0.93	0.88

Table A.5 (cont'd): GIM2D: $n = 2$ Bulge Catalog

DEEPID (1)	V Bulge (2)	I Bulge (3)	V Disk (4)	I Disk (5)	B/T V-band (6)	B/T I-band (7)	r_e Bulge (pixels) (8)	r_e Disk (pixels) (9)	C V-band (10)	C I-band (11)	χ^2 V-band (12)	χ^2 I-band (13)
13026131	24.93	24.34	23.73	23.68	0.37	0.49	19.07	9.98	0.41	0.46	0.95	0.93
12020067	23.02	23.16	22.43	22.70	0.53	0.56	23.38	4.43	0.53	0.55	1.05	0.98
12015606	23.71	22.89	22.36	22.30	0.32	0.49	10.64	11.16	0.48	0.44	1.07	0.97
13058131	24.81	23.55	22.95	22.23	0.24	0.34	4.94	17.80	0.57	0.55	0.97	0.88
12016156	24.67	24.31	23.93	23.91	0.42	0.49	27.86	30.96	0.40	0.30	1.11	0.96
13012297	23.44	-99.99	21.80	-99.99	1.00	1.00	10.84	6.88	0.55	0.58	0.91	0.88
12007918	23.33	23.54	22.77	22.68	0.55	0.48	9.21	7.01	0.55	0.56	1.17	1.08

Table A.5 (cont'd): GIM2D: $n = 2$ Bulge Catalog

DEEPID (1)	V Bulge (2)	I Bulge (3)	V Disk (4)	I Disk (5)	B/T V-band (6)	B/T I-band (7)	r_e Bulge (pixels) (8)	r_e Disk (pixels) (9)	C V-band (10)	C I-band (11)	χ^2 V-band (12)	χ^2 I-band (13)
13011795	25.30	24.90	23.63	23.50	0.41	0.47	3.11	13.02	0.66	0.65	0.87	0.80
13064645	25.29	24.90	23.93	23.21	0.41	0.34	1.36	8.69	0.69	0.71	0.94	0.89
12016799	23.41	23.85	21.90	22.78	0.60	0.69	44.45	9.40	0.36	0.38	1.11	1.06
12023870	23.71	24.13	23.12	23.82	0.60	0.66	21.50	1.75	0.66	0.71	1.14	1.15
12004470	23.50	23.19	23.00	22.89	0.43	0.47	14.01	2.61	0.73	0.74	1.48	1.37
12020439	24.56	24.16	23.63	23.72	0.41	0.52	12.21	3.11	0.65	0.72	0.98	1.05

Note. — The same twenty randomly-selected galaxies from Table A.1 is shown. The entire catalog is available at: `http://people.ucsc.edu/~echeung1/data.html`. Every value in this table is from the GIM2D decomposition using a bulge and disk with Sérsic index of $n = 2$ and $n = 1$, respectively. Col. (1): DEEPID. Col. (2) & (3): V-band magnitude of bulge and disk. Col. (4) & (5): I-band magnitude of bulge and disk. Col. (6): B/T in V-band. Col. (7): B/T in I-band. Col. (8): Effective radius of major axis of bulge in units of pixels. Col. (9): Scale length of disk measured along major axis in units of pixel. Col. (10): Concentration with $\alpha = 0.3$ in V. Col. (11): Concentration with $\alpha = 0.3$ in I. Col. (12): Chi-squared of fit in V. Col. (13): Chi-squared of fit in I.

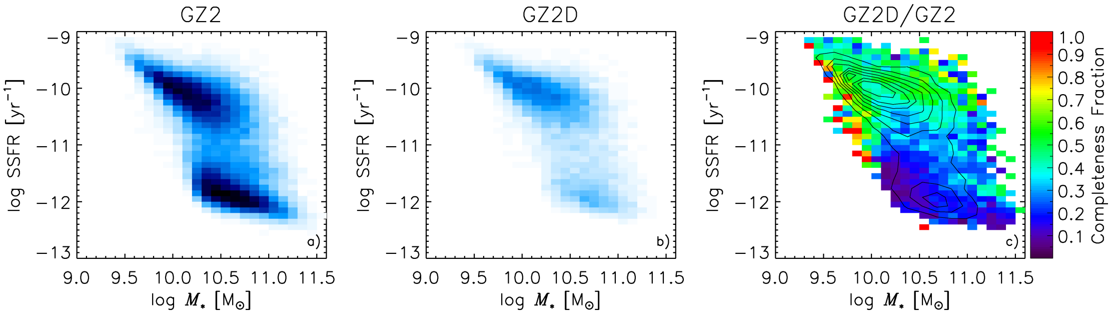

Figure B.1: The number density distribution of the: *a)* volume-limited parent Galaxy Zoo 2 (GZ2) sample and *b)* Galaxy Zoo 2 Disk (GZ2D) sample; both are scaled to the same. *c)*: The completeness of the GZ2D sample relative to the GZ2 sample. For each bin, we calculate the fraction of GZ2D galaxies in the GZ2 sample and color it according to the color bar to the right. The black contours outline the number density of the GZ2D sample and only bins with at least 2 GZ2 galaxies are shown. The completeness of GZ2D is bimodal such that it recovers $\sim 50\%$ of high SSFR ($> 10^{-11}$ yr^{-1}) galaxies and $\sim 20\%$ of low SSFR ($< 10^{-11}$ yr^{-1}) galaxies.

Appendix B

Completeness of Chapter 2

B.0.1 Galaxy Zoo 2 Disk Sample

The Galaxy Zoo 2 Disk (GZ2D) sample was selected on the basis of hundreds of thousands of visual morphological classifications collected via the Galaxy Zoo website. In order for a galaxy to be in this sample, the majority of volunteers classifying it must have identified

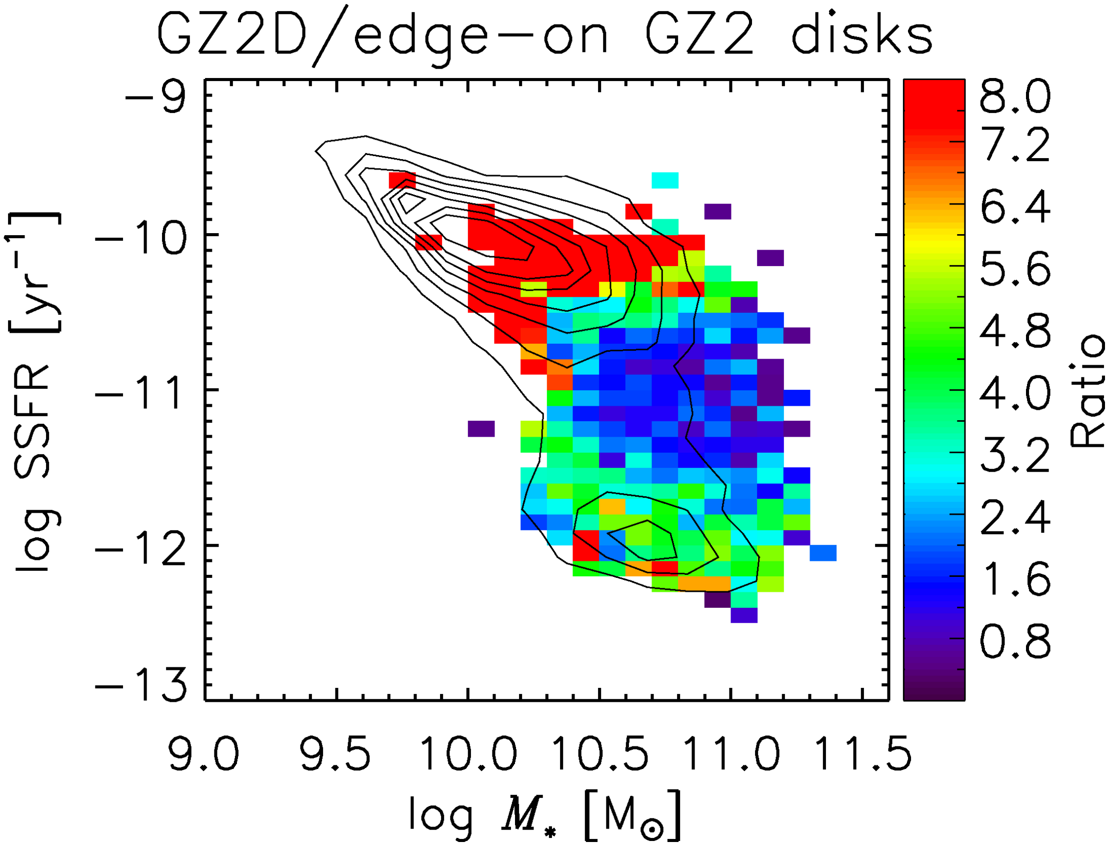

Figure B.2: The ratio of the number of galaxies in the GZ2D sample to the edge-on GZ2 disk sample. The black contours outline the number density distribution of the GZ2D sample. Only bins with $n \geq 2$ edge-on GZ2 galaxies are shown. GZ2D does not seem to be strongly biased against low mass quiescent disks.

'features' in it, and identified it as not being an edge-on disk (see Masters *et al.*, 2011; Willett *et al.*, 2013). In addition we apply an extra cut at $b/a > 0.5$ to ensure disks are face-on enough to identify bars. This results in a sample of disk galaxies with a broad mix in Hubble types. Objects might contain an obvious disk (e.g., SBc, Sc) or a subtle disk (e.g., S0). While we do not expect problems in identifying the former in any orientation, S0 galaxies are notoriously difficult (even for the most expert classifiers) to separate from ellipticals, if viewed face-on. We consider in this section if any face-on disk galaxies are missing from our sample. Presumably, if a galaxy had a bar, it would be readily identify as ‘featured’ and included in this sample, thus we assume any missing disk galaxies will be non-barred and therefore introduce potential biases into our results.

We use as a comparison sample, the volume-limited parent Galaxy Zoo 2 sample (see §3.2.2 for details of our initial Galaxy Zoo 2 sample) that the GZ2D sample was originally drawn from, as well as a sample of edge-on disk galaxies in which we expect all types of disks will be equally easy to identify. As a reminder, the parent Galaxy Zoo 2 sample has the following criteria:

1. $0.01 < z < 0.06$, where z is the SDSS spectroscopic redshift.
2. $M_r \leq -20.15$, where M_r is the rest-frame absolute Petrosian r-band magnitude.

Hereafter, this sample will be referred to as the Galaxy Zoo 2 sample, or simply, the GZ2 sample. We match the GZ2 sample to the MPA-JHU catalog for stellar masses and star formation rates, resulting in a total of 43,221 galaxies.

To identify edge-on disks, we use thresholds in the Galaxy Zoo vote fractions for ‘features of disk’ ($p_{\text{features}} > 0.5$) and for ‘edge-on disk’ ($p_{\text{edge-on}} > 0.80$), this is slightly more conservative that the recommended thresholds for selecting a ‘clean edge-on’ sample as given in Willett *et al.* (2013), but we do not expect the selection to introduce any bias with Hubble type for disk galaxies.

Fig. B.1 compares the number density distribution of the GZ2D sample (panel b) to that of the whole volume limited GZ2 sample (panel a). Both panels are scaled so that the blue scale indicates the same range of density and only bins with at least 2 galaxies are shown.

Using the GZ2 sample as the fiducial completeness standard, panel c displays the completeness of the GZ2D sample (i.e., the fraction of the GZ2 sample which is in GZ2D) as indicated by the legend. To aid the eye, contours of the GZ2D number density distribution are over-plotted. We point out that completeness levels of greater than 50% are not expected since the selection on axial ratio ($b/a > 0.5$) removes approximately half of all disk galaxies. In this plot we observe the expected bimodality, such that the completeness of high SSFR ($> 10^{-11}$ yr^{-1}; 'star-forming') galaxies is much higher ($\approx$ 50% complete) than it is for low SSFR ($< 10^{-11}$ yr^{-1}; 'quiescent') galaxies ($\approx$ 20% complete). This reveals the well know correlation between SSFR and morphology - that most star-forming galaxies have disks, and many quiescent galaxies are elliptical, so do not have obvious 'features' to be selected as part of the GZ2D sample.

This test, however, cannot reveal if the GZ2D sample represents a fair selection of all disks. To test that, we isolate a sample of edge-on disk galaxies in which we expect all disks (even S0s) will be identified. If the GZ2D sample is fairly representative of all disk galaxies, then the ratio of GZ2D (face-on disk) galaxies to the sample of edge-on disks should be uniform throughout the SSFR-mass diagram (this assumes all disk galaxies are randomly orientated, which we expect they should be, but also see Simard *et al.* 2011, and that the inclination introduces no systematic biases into estimates of SSFR or stellar mass, which is less clear).

Fig. B.2 compares the number density of the edge-on GZ2 disks to our GZ2D sample of mildy inclined or face-on disk galaxies. We show the ratio of the number of galaxies in the GZ2D sample to the edge-on GZ2 disks sample. Only bins with at least 2 galaxies from the edge-on GZ2 disks sample are shown and the black contours represent the number density distribution of the GZ2D sample. For high SSFR galaxies, there are $\sim$7 galaxies in the GZ2D sample for every edge-on GZ2 disk galaxy. This is likely due to a combination of the expected number ratios for edge-on and not edge-on disk galaxies (e.g., for random orientations, we expect one galaxy with $i > 85^{\circ}$ for every five with $i < 65^{\circ}$), and the possible effects of increased internal extinction in the egde-on sample causing SSFR to be underestimated. However we do not expect to be missing systematically any star-forming disk galaxies.

Because of the extinction of edge-on galaxies, the sample of low SSFR (log SSFR $<$ -11.6 yr^{-1}) edge-on GZ2 disks may contain a combination of truly low SSFR disks and reddened intermediate SSFR disks. However, we assume that the reddened intermediate SSFR contribution to the low SSFR regime of the edge-on GZ2 disks sample is uniform across stellar mass and only changes the absolute scaling of the number ratio between GZ2D and edge-on GZ2 disks. We therefore examine the uniformity of the low SSFR regime in Fig. B.2 to gauge whether the GZ2D sample is missing any quiescent disks.

The number ratio between edge-on quiescent disks and face-on quiescent disks is largely uniform (at ~ 5 oblique disks per edge-on disk). There is, however, hints of a small dearth in the GZ2D sample at low masses. Averaging the number ratios at low masses ($\log M_* <$ 10.6) reveals that we find $\approx 10\%$ less GZ2D galaxies compared to the average number ratios of the high mass quiescent disks. The total number of low mass quiescent galaxies in our sample is ≈ 900, so this suggests we may be missing ≈ 90 low mass quiescent disk galaxies. Presumably, if a galaxy had a bar, it would be readily spotted and included in this sample, thus we assume the missing disk galaxies are non-barred. We assume that the missing disks have values of n and $\Sigma^*_{1\text{ kpc}}$ typical for GZ2D galaxies of the same mass and SSFR. We find that the n and $\Sigma^*_{1\text{ kpc}}$ values of these low mass quiescent disks are roughly uniformly distributed, meaning that the

$p_{\rm bar}$ trends with n and $\Sigma^*_{1\ \rm kpc}$ for the quiescent population are unaffected by this incompleteness. We can estimate how many unbarred quiescent disk galaxies we are missing for every bin by simply dividing the total number of missing galaxies (≈ 90) by the total number of bins that the quiescent population spans in n and $\Sigma^*_{1\ \rm kpc}$, which turns out to be ~ 20 bins. Thus we are missing ≈ 5 unbarred quiescent disks in every $N = 100$ bin of n and $\Sigma^*_{1\ \rm kpc}$ (see Figs. 3.3b and 3.3c). Even if all five galaxies have $p_{\rm bar} = 0$ this would reduce the average $p_{\rm bar}$ in each bin by at most 5% (by simply adding 5 more galaxies in the denominator).

The number of missing low mass disks in the affected part of Fig. 3.3a works out to be ≈ 10 per low mass quiescent bin (there are ~ 10 bins in the low mass quiescent regime). Fig. 3.3a shows that the $p_{\rm bar}$ values for the low mass quiescent bins are ~ 0.60. Adding 10 non-barred ($p_{\rm bar} = 0$) disk galaxies to these bins, i.e., adding 10 galaxies to the denominator, reduces these $p_{\rm bar}$ values to ~ 0.50. Our qualitative results and interpretation are unaffected. Therefore, the missing non-barred low mass quiescent disks do not significantly influence our results.

B.0.2 Bar Length Sample

Unlike the GZ2D sample, there is not a concern that the BL sample is missing non-barred disks since, as the sample name implies, the BL (Bar Length) sample only contains barred disks. Nevertheless, we want to ensure that it is not suffering any selection bias.

Fig. B.3 shows the completeness of the BL sample relative to the GZ2D sample. The completeness of BL is approximately bimodal with SSFR. In the high SSFR regime ($\log\ {\rm SSFR} > -11\ {\rm yr}^{-1}$), the BL sample is $\sim 10\%$ complete, while in the low SSFR regime ($\log\ {\rm SSFR} <$

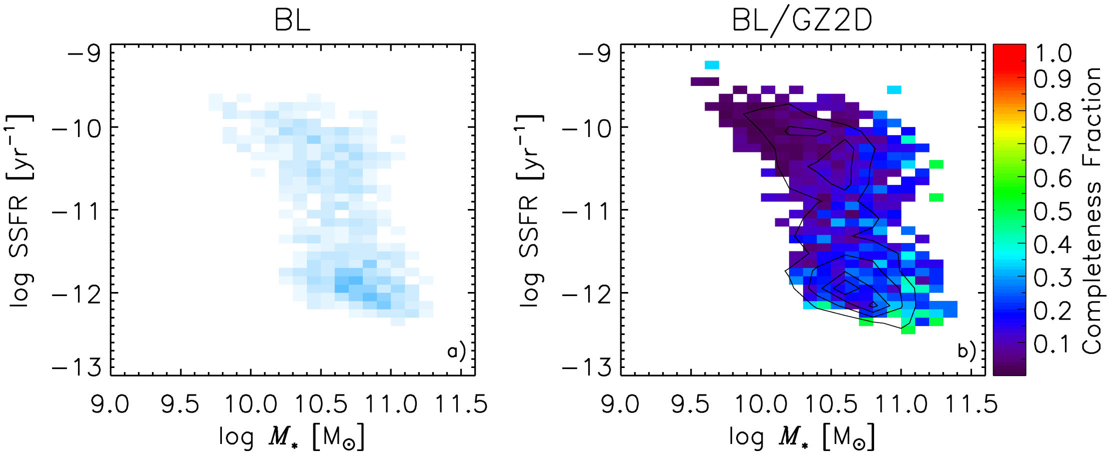

Figure B.3: *a)*: The number density distribution of the Bar Length (BL) sample scaled to a quarter of panel a of Fig 8. *b)*: The completeness of the BL sample relative to the GZ2D sample; the black contours in this panel represents the number density distribution of the BL sample. Only bins with 2 or more GZ2D galaxies are shown.

-11 yr^{-1}), it is $\sim 20\%$.

This completeness bimodality is reasonable because the BL sample is primarily composed of strong bars, which as illustrated in Fig. 3.3, strong bars mainly lie in the quiescent population. However, since our analysis splits the BL sample into star-forming and quiescent (i.e., Fig. 3.4 and Fig. 3.7), this difference in completeness should be inconsequential to our results and interpretations.

B.1 Bar Length Scaled by Isophotal Radii

Comparing the trends of bar length scaled by the isophotal radii (Fig. B.4 and B.5) to those of $L_{\rm sbar}$ (Fig. 3.4 and 3.7) shows a good agreement. The only noticeable differences are at the highest n and $\Sigma^*_{1\ {\rm kpc}}$, which is hard to interpret and may be due to a number of issues. These GIM2D disk scale lengths may be affected by the prominent bars present in

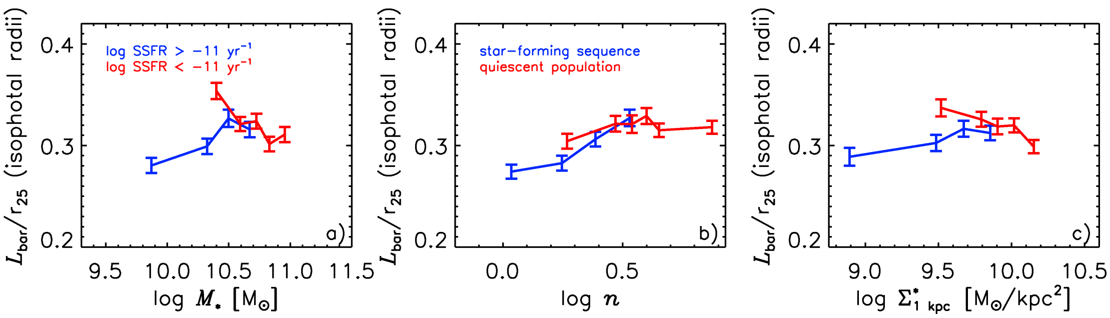

Figure B.4: Average bar length scaled by the isophotal radii, $L_{\rm bar}/{\rm r}_{25}$, plotted against: *a)* M_*, *b)* n, and *c)* $\Sigma^*_{1\ \rm kpc}$. Galaxies were split by their star formation state, namely, log SSFR > -11 yr^{-1} (star-forming; blue) and log SSFR < -11 yr^{-1} (quiescent; red). Each bin contains $\sim$ 100 galaxies. The error bars are given by $\sigma/\sqrt{N}$, where σ is the standard deviation of $L_{\rm sbar}$ per bin, and N is the total number of galaxies per bin.

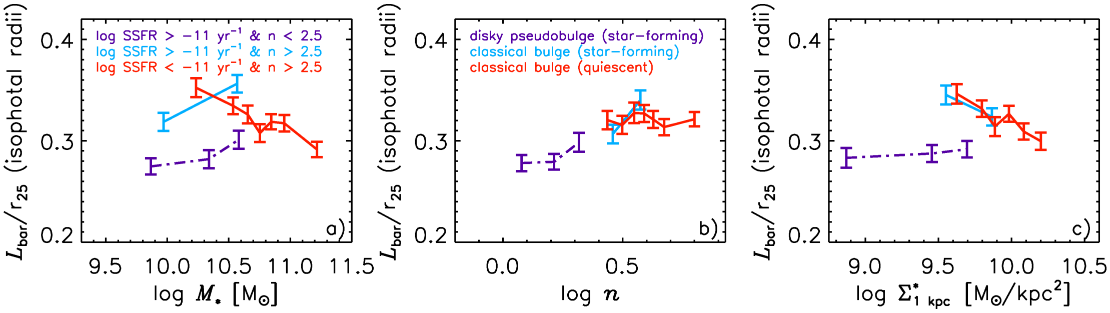

Figure B.5: Average $L_{\rm bar}/{\rm r}_{25}$ plotted against: *a)* M_*, *b)* n, and *c)* $\Sigma^*_{1\ \rm kpc}$. The details of this figure are identical to that of Fig. B.4, with the exception that each bin contains $\sim$ 75 galaxies and also, galaxies are further separated by bulge type, as identified by n. Purple points represent the star-forming disky pseudobulge galaxies, light blue points represent the star-forming classical bulge galaxies, and red points represent the quiescent classical bulge galaxies.

these galaxies. But the better sky background determination and better object deblending of the GIM2D decompositions could also lead to a more accurate measurement of the disk scale length. More work needs to be done to truly understand the differences, but this is outside the scope of this paper. Moreover, this paper does not put a strong emphasis on the bar length trends at the highest n and $\Sigma^*_{1\ \rm kpc}$, thus it does not affect our major conclusions.

B.2 R90/R50

Fig. B.6 shows the effects of using the Petrosian concentration index from SDSS, R90/R50, where R90 and R50 are the radii enclosing 90 and 50 % of the galaxy luminosity, respectively. The trends with $p_{\rm bar}$ in Fig. B.6a are almost identical to that with Sérsic index (Fig. 3.3b). Fig. B.6b and B.6c show that the trends with R90/R50 for the star-forming sequence, star-forming disky pseudobulge galaxies, and the star-forming classical bulge galaxies are the same as with n (Fig. 3.4b and 3.7b), i.e., $L_{\rm sbar}$ increases with increasing n or R90/R50.

For the quiescent population (Fig. B.6b) and the quiescent classical bulge galaxies (Fig. B.6c), however, there is a noticeable difference between the trends of $L_{\rm sbar}$ at the highest values of R90/R50 and n. Namely, while there is a decrease of $L_{\rm sbar}$ at the highest n (Fig. 3.4b and 3.7b), there seems to be a steady increase of $L_{\rm sbar}$ with increasing R90/R50. It is unclear why this is the case. It could be due to the improved sky background determination and object deblending in the fits of Simard *et al.* (2011) compared to the standard SDSS pipeline. However, no matter the reason, this minor difference does not affect the paper since we leave the interpretation of the bar length trends for the highest n values open.

Comparing the trends of bar length scaled by the isophotal radii between n (Fig. B.4b and B.5b) and R90/R50 (Fig. B.6d and B.6e) shows general agreement between all populations.

Thus the results from R90/R50 and n are largely similar, and the use of either would not change the main conclusions of the paper.

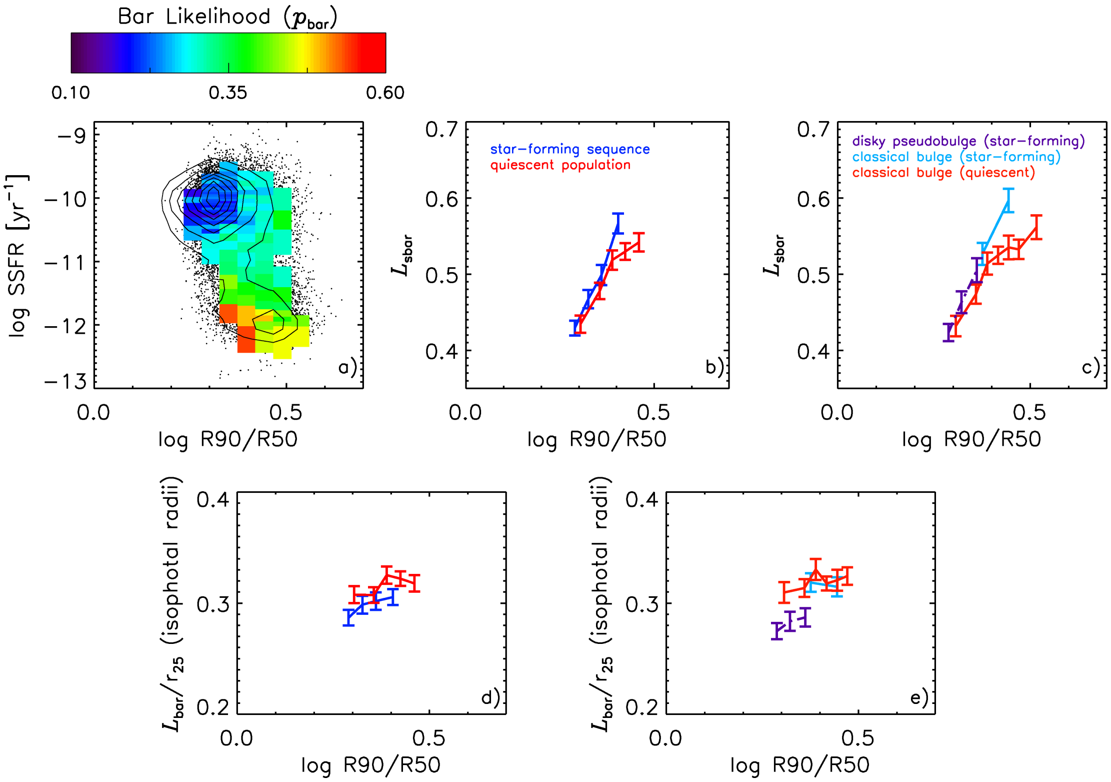

Figure B.6: Replacing Sérsic index with R90/R50. *a)* plots average p_{bar} in bins of SSFR and R90/R50. *b) & c)* plot bar length scaled by GIM2D bulge+disk model disk scale length vs. R90/R50. *d) & e)* plot bar length scaled by the isophotal radii vs. R90/R50.